Influencing the Properties of Excitons and Cavity-Polaritons in Transition Metal Dichalcogenide based Heterostructures

Daniel J. Gillard

A thesis submitted in partial fulfilment of the requirements for the degree of
Doctor of Philosophy

DEPARTMENT OF PHYSICS AND ASTRONOMY
FACULTY OF SCIENCE
THE UNIVERSITY OF SHEFFIELD

Submitted: March 2022

Preface

Declaration

I, *the author*, confirm that this thesis is my own work. I am aware of the University's *Guidance on the Use of Unfair Means* (www.sheffield.ac.uk/ssid/unfair-means). This work has not been previously presented for an award at this, or any other, university.

Publications arising from this work

- T.P. Lyons, **D.J. Gillard**, A. Molina-Sánchez, A. Misra, F. Withers, P.S. Keatley, A. Kozikov, T. Taniguchi, K. Watanabe, K.S. Novoselov, J. Fernández-Rossier, and A.I. Tartakovskii
"Interplay between spin proximity effect and charge-dependent exciton dynamics in $MoSe_2/CrBr_3$ *van der Waals heterostructures"*
Nature Communications, 2020, **Vol 11**, 6021
DOI: 10.1038/s41467-020-19816-4
http://www.nature.com/articles/s41467-020-19816-4

- **D.J. Gillard**, A. Genco, S. Ahn, T.P. Lyons, K.Y. Ma, A-R. Jang, T.S. Millard, A.A.P. Trichet, R. Jayaprakash, K. Georgiou, D.G. Lidzey, J.M. Smith, H.S. Shin, and A.I. Tartakovskii
"Strong exciton-photon coupling in large area $MoSe_2$ *and* WSe_2 *heterostructures fabricated from two-dimensional materials grown by chemical vapor deposition"*
2D Materials, 2020, **Vol. 8**, 011002
DOI: 10.1088/2053-1583/abc5a1
https://iopscience.iop.org/article/10.1088/2053-1583/abc5a1

- V. Kravtsov, A.D. Liubomirov, R.V. Cherbunin, A. Catanzaro, A. Genco, **D.J. Gillard**, E.M. Alexeev, T. Ivanova, E. Khestanova, I.A. Shelykh, A.I. Tartakovskii, M.S. Skolnick, D.N. Krizhanovskii, and I.V. Iorsh
"Spin-valley dynamics in alloy-based transition metal dichalcogenide heterobilayers"
2D Materials, 2021, **Vol 8**, 025011
DOI: 10.1088/2053-1583/abcf12
https://iopscience.iop.org/article/10.1088/2053-1583/abcf12

- T.P. Lyons, **D.J. Gillard**, C. Leblanc, J. Puebla, D.D. Solynshkov, L. Klompmaker, I.A. Akimov, C. Louca, P. Muduli, A. Genco, Y. Otani, G. Malpuech, and A.I. Tartakovskii
"Giant effective Zeeman splitting in a monolayer semiconductor realized by spin-selective strong light-matter coupling"
arXiv:2109.05859 (Submitted 2021)

Conference Contributions

- *"Band structure engineering in mono- and bi-layers of* $Mo_xW_{1-x}Se_2$ *alloys"*
Poster presentation, UK Semiconductors, Sheffield, 2018

- *"Band structure engineering in nano-layers of* $Mo_xW_{1-x}Se_2$ *and* $Mo_xW_{1-x}S_2$ *semiconducting alloys"*
Poster presentation, International Conference on the Physics of Semiconductors (ICPS), Montpellier, 2018

- *"Band structure engineering of* $Mo_xW_{1-x}Se_2$ *semiconducting alloys in nano-layers and heterostructures"*
Poster presentation, Graphene Study, Obergurgl, 2019

- *"Spin polarisation in* $MoSe_2$ *monolayer semiconductor by EuS magnetic proximity coupling"*
Poster presentation, TMD UK, Sheffield, 2019

- *"State specific magnetic proximity coupling in* $MoSe_2$ / $CrBr_3$ *van der Waals heterostructures"*

Oral presentation, Graphene Week, Helsinki, 2019

- *"Hybridised exciton-polaritons in moiré van der Waals heterostructures*

Poster presentation, Nanophotonics Winter School, Sheffield, 2020

Acknowledgements

It would be simply impossible to write a thesis without the people around me, both personal and professional. A small mention here will likely not do them justice, but for now it will have to do.

Firstly, I would like to thank the many collaborators that have had a direct input in the work presented here, and beyond. Special thanks to Chris Vickers, Phil Taylor, and Tom Ball, who have supplied my bath cryostat with a constant stream of liquid helium, and who have taught me a great deal of technical skills. I thank Jorge for hosting my visit to RIKEN, Japan.

I would like to thank everybody in our 2D materials group headed by Prof. Alexander Tartakovskii, with whom it has been a privilege to work and study. When I started my PhD, I joined a small group of hard working researchers who made me feel welcome and relaxed. Evgeny and Luca are two group members I did not spend a great deal of time actively working with, but nevertheless helped me when I needed and encouraged and aided my research progress. It was never a dull group meeting when they were discussing the finer details of their research. I had a small overlap of work in our Raman spectroscopy lab with Robbie, who was immensely fun to work with, even briefly. Toby is another person who I especially enjoyed working with. He has attempted to leave our group three times now, only to return again after a quick soul search. As such, Toby currently holds the record for the most leaving parties, which will be quite difficult to beat. Of all the people I have worked with over my time in Sheffield, it is Armando and Tom that have influenced my research the most, taking an active role in my experimental projects and academic development. It is safe to say that without their influence, my thesis and I would be far worse off.

Alessandro was the person who guided my initial training, from whom I learnt much about the fabrication and study of TMDs. The fabrication lab and my magneto-spectroscopy lab are adjacent and it was common to hear cheers of joy when a successful fabrication was completed, and even more common to hear shouts and curses that even non-Italian speakers could understand when a fabrication was not so successful. I last met Alessandro at Graphene Week, when I gave my first conference talk, and his support was greatly appre-

ciated. We bonded over our shared love of food and science fiction, and is someone I miss very much.

The remaining group consists of Panaiot, Pampos, and Oscar, with whom I have the pleasure of continuing my work with. I look forward to sharing a pizza and a few beers with them to celebrate the completion of this work, before continuing our research together in coming months and years... May they consist of many papers, laughs and beers.

On a personal note, I could not complete my PhD without the help and support of my friends and family. Nothing makes you realise the need for close personal relationships quite like having the world go into lock-down. My friends and my brothers especially have kept me sane throughout lock-down, sharing video calls and playing online games with them is a perfect way to de-stress. Ben and Ruth have been a welcome constant in my life here in Sheffield after my undergraduate degree finished, when lot of friends moved away for jobs, and continue to be some of my closest friends. Claire, my partner, is simply amazing and I cherish every moment we have together. Lastly, but definitely not least, I would like to thank my parents who instilled the foundation of my personality and my drive to better myself.

Dedications

I dedicate this thesis to the memory of four people who passed away during the final years of this work;

My friend and colleague Alessandro was the first person I met when I interviewed for my PhD in the 2D materials group. He, along with other members, showed me around the labs and confirmed that he was the type of person I wanted to work with. Passionately smart, dedicated, friendly, and most importantly, a complete nerd... he would never hesitate to play the Star Wars (Original) soundtrack at full volume while fabricating samples or argue which flaw in the latest trilogy was the biggest (There were so many). Alessandro was the person who trained me at the start of my PhD and began my journey towards the completion of this thesis. The news of his unexpected and sudden passing was a shock to our entire 2D Materials group, Sheffield University, and beyond. The lessons and knowledge that he shared continue to guide me.

It is a rare occasion that you meet someone and they change your complete outlook on life. I did not know Jenny for very long, and it really is a true shame. When I met my partner's mother, she was in the midst of a battle with Motor Neuron Disease. Her ability to brighten any room with her cheerfulness and continued fortitude throughout her illness is a lesson I take to heart every time I wake and step out of bed, a simple act that I took for granted for a very long time. She was always impressively practical for a person of her stature with no DIY task too big, it is the cruellest twist of fate that somebody so active should suffer such a debilitating disease. For my first, and last, birthday shared with Jenny I was gifted a flat cap, a gift that I must admit I had never even considered would suit me. I wear it almost every day.

My childhood, adolescence, and even adulthood, is filled with memories of arriving excitedly at my grandparents house at the start of the summer and Christmas holidays to be greeted with a big smile and a bigger hug. The very sense of who we are as people and the values we hold dearest are first nurtured from our family. My grandfather passed away after a long battle with Cancer and Alzheimer's, a one-two combination that would flaw even the healthiest of people. I don't remember my grandad getting sick once when I was younger. His dedication to his family is a trait impossible to overlook, from meticulously re-organising the dishwasher after we had rushed clearing up to get back to playing cards, to waking up early and serving us all cooked breakfast to order. I have visited my grandads house on only three occasions without being greeted by his warm embrace, I do not wish to do so again.

On the other side of my family, my grandmother was in and out of hospital and care homes for the better part of a year with various ailments associated with ageing before we were given the news that she had tested positive for COVID-19. This turned out to be one hurdle too far. She dealt with the passing of her husband, my grandfather, almost eleven years previous with a dignifying grief that was both reassuring and calming to a younger version of myself encountering the pain of loss for the first time. She continued to deal with being shuffled from care home to hospital and home again with the same dignity and understanding. My love of baking and cooking stems directly from sharing the kitchen with her as a young child and learning everything I could from an all knowing grandma. On that morning of my grandads funeral, I vividly remember her saying "It just doesn't seem real". Ten years on... it still doesn't.

One thing has become clear to me... Whilst I sat in the back of a black limousine feeling completely empty and wondering how I would get through the next couple of hours, I watched car after car stop in the middle of road and roundabout alike to let us pass slowly by and offer a small bow of the head... Is that there is a remedy for pain, Kindness. Simple, small acts of kindness have given me strength in my toughest moments. Through kindness, these four people made my world a better place. And as 2021 continues where 2020 ended, at one of our collectively most difficult moments, science and medicine will be the saviour of humans, and kindness will be the saviour of humanity, to make the entire world a better place.

"Our thought, our song
Will not die, will not perish…
Oh there, people, is our glory,
Glory of Ukraine!"

- Taras Shevchenko, 1860

Contents

REDACTED

List of Figures

REDACTED

List of Tables

REDACTED

Chapter 1

An introduction to two dimensional materials

Two dimensional materials were once considered to be theoretically impossible and due to critical thermal instabilities when separated from the bulk material. This changed when graphene was successfully isolated in 2004 by *A.K. Geim* and *K.S. Novoselov.*[1] For this work on graphene, and subsequent discoveries of the impressive properties, they were given the *Nobel Prize* in 2010. Graphene, along with a growing family of two-dimensional materials, possess very strong intralayer covalent bonds, while each individual layer within the material is only weakly bonded to the next through van der Waals attractions. Researchers have been taking advantage of this by effectively peeling away surface layers to obtain single, atomically thin, monolayers. The number of materials discovered with such properties has grown rapidly since the isolation of graphene, and now include electric conductors, insulators, direct and indirect band gap semiconductors, along with topological insulators, superconductors, and most recently, ferromagnetic and antiferromagnetic monolayers. The vast range of materials available has lead to an rapid increase in popularity resulting in a vast research field within condensed matter physics, with the cost of entry to the field remaining relatively low due to the lack of heavy costs attached to monolayer fabrication. In fact, almost anyone can produce monolayers from bulk crystals by way of micromechanical exfoliation with some blue sticky tape, completely bypassing the need for expensive lithography or epitaxial deposition technology in highly controlled nano-fabrication cleanrooms.

Much of the novel phenomena associated with 2D materials arises from the inherent geometry of monolayers. The reduced dimensionality and quantum confinement at the ultimate 2D limit provides a unique system to explore solid state physics and quantum phenomena, the resultant behaviour is discussed in chapter 2. One of the most attractive prospects is the adaptability and versatility associated with these materials, thanks to the weak interlayer van der Waals forces binding monolayers to adjacent layers or surfaces. A property that was once exploited for dry lubrication purposes is now used to adhere monolayers onto practically any conceivable substrate. This is not limited even to flat surfaces. Monolayers can be suspended across holes and gaps, draped over nanostructures and waveguides, integrated into photonic crystals, and even implanted into living tissue for biosensing. Possibly the most intriguing surface to combine with a monolayer, is another monolayer. Stacking different 2D materials together to form so-called *van der Waals heterostructures* opens un an unprecedented level of versatility. By choosing the layered materials carefully, van der Waals heterostructures can be readily designed to perform a potentially endless variety of functions, most commonly light emitting diodes, transistors and photodetectors, with device sizes at the nanometre scale.

The uncompromising versatility and low costs of 2D materials, combined with favourable mechanical properties, such as flexibility, provides a perfect platform to develop future technologies or miniaturise existing ones. Furthermore, recent advances in scalability and quality of monolayers, heterostructures, and devices, are rapidly bringing 2D materials towards mass production with commercial viability.

Motivation: Initiating a degree of control over light-matter interactions

The work carried out, and displayed, over the course of this work is motivated by the understanding of light-matter interactions, and in particular the attempts to gain a degree of control over the optical properties of the resultant interactions. Not only will this control provide a pathway to useful applications in information technology, but can also facilitate the investigations into fascinating non linear behaviour.

Scope of Thesis

This work will open with an insight into the current literature regarding transition metal dichalcogenides. Here we explore the very basics of the crystalline structural formation, with a focus on the electronic band structure and the concept of valleys and excitons which dictate the optical response of these atomically thin semiconductors. This introduction also inspects more recent investigations that are leading the field in fascinating new directions such as many body and non-linear phenomena. The next chapter will focus on the experimental techniques that are employed by the author in order to obtain and showcase the results presented in this work. Sample fabrication, both epitaxial and not, along with the laboratory equipment required to perform a variety of optical spectroscopy measurements are discussed here, before embarking onto the main results. Each chapter is designed as a self contained project with distinct discoveries whilst following the same overall theme of establishing an element of control over the optical and electronic properties of the devices sampled.

Chemical vapour deposition is an inherently scalable fabrication method which is normally overlooked for the production of TMD based devices of the highest optical quality. Chapter 4 demonstrates strong light matter coupling in two CVD grown $MoSe_2$ and WSe_2 devices for the first time, highlighting the recent advances made with the fabrication method. The CVD fabrication method is further validated through a substrate-wide analysis of flake orientation, showing how the epitaxial growth of monolayers directly onto hBN encourages a highly uniform growth orientation. This chapter is closed out by displaying a potential route towards scalable polariton device manufacturing through TMD embedded monolithic cavities.

Chapter 5 explores how the process of alloying can alter the band structure of TMDs in a controllable and predictable manner. A complete optical analysis study is performed on a range of alloy concentrations between $MoSe_2$ and WSe_2, producing a characteristic bowing of the excitonic resonances as the alloy content is tuned. This study confirms the high quality of alloyed TMD devices, especially high Mo alloys which demonstrate excitonic linewidths and Rabi splittings equal to that the pure materials. By understanding the band structure as the material composition is tuned, it is possible to select two materials to combine into a heterostructure that would encourage the hybridisation of intralayer and interlayer excitons, with a view of placing such a device into a microcavity to produce a population of polaritons with permanent dipole moment in a bid to study highly non linear phenomena. The investigation becomes slightly sidetracked when the discovery of such hybridised excitons in a different structure. The chapter is therefore concluded by placing the $MoSe_2$ / WS_2 heterostructure into the tunable microcavity where strong coupling is observed in such hybridised excitonic resonances.

REDACTED

REDACTED

The thesis is concluded with a brief outlook at potential research avenues in the near future and some of the studies already under way.

Chapter 2

Optical Properties of Transition Metal Dichalcogenides

This chapter will deliver a general discussion into the nature of TMDs and the properties that make these materials so promising. Specific attention will be made towards molybdenum diselenide ($MoSe_2$) and tungsten diselenide (WSe_2) monolayers, which form the basis of the devices studied in this thesis. These materials form direct-gap semiconducting analogues of graphene, presenting excellent and unique optical properties which provide a naturally attractive platform from which to build nanoscale opto-electronic and valley-tronic devices. The advantages of combining different layers together will form a theme throughout the studies displayed here, with further benefits when operating in the strong exciton-photon coupling regime.

2.1 Crystalline lattice structure of TMDs

Transition metal dichalcogenides (TMDs) have crystalline structures of the form MX_2 where M represents a transition metal atom (such as molybdenum or tungsten) and X is a chalcogen atom (such as sulphur, selenium or tellurium). Each layer of TMD possess a triatomic structure X-M-X, which is covalently bonded in a hexagonal lattice.[2,3] It is a point of note, that each chalcogen atom is only bonded to the nearest transition metal atom, and as such there are no dangling bonds outside of the lattice plane. The triatomic layers are bound together in 'bulk crystal' (Fig. 2.1a) form by a weak interlayer van der Waals force, which allows a single layer, or 'monolayer', to be easily isolated from the bulk material through micromechanical exfoliation.[1] Monolayer TMDs are most thermodynamically stable in a

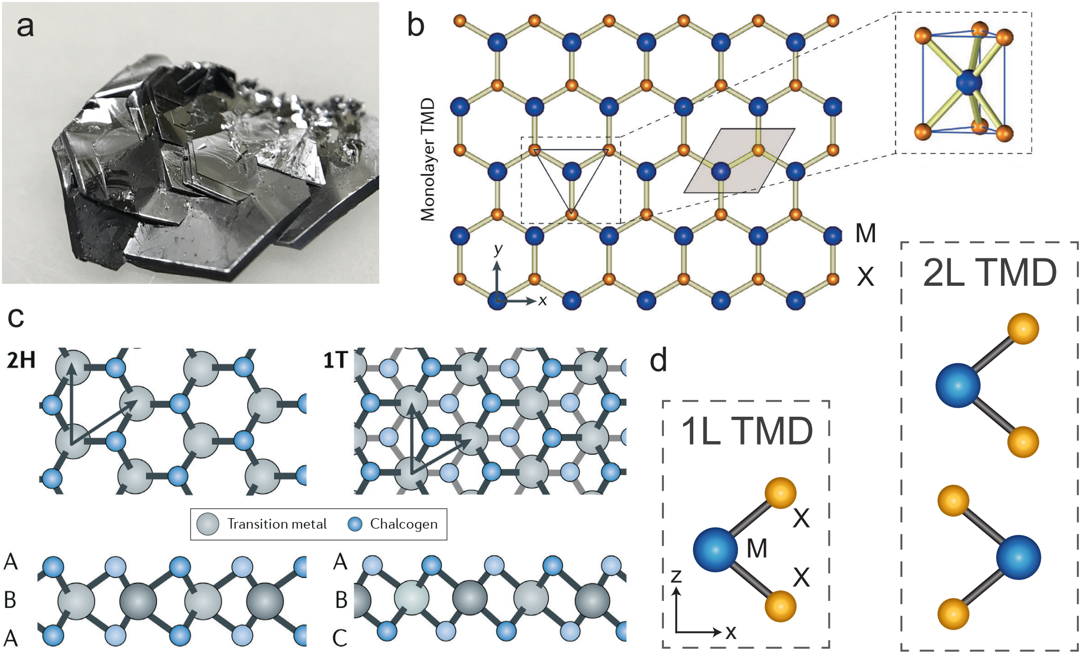

Figure 2.1: **a)** Image of MoSe$_2$ bulk crystal. Image from *2D Semiconductors*. **b)** Top view of a monolayer sheet, with primitive cell shaded in grey. *Inset:* Side view of the 2H-TMD, revealing the trigonal prismatic structure with lack of inversion centre. Image from Ref.[7] **c)** Comparison between 2H and 1T crystal phases of a monolayer. Image from Ref.[5] **d)** Side views of the primitive cells of a 2H-TMD monolayer (1L) and bilayer (2L). Inversion symmetry is broken in the monolayer, and restored in the bilayer. Image adapted from Ref.[8]

trigonal prismatic (2H crystal phase group) structure,[3,4,5] which have an out of plane mirror symmetry and a broken in plane inversion symmetry (Fig. 2.1b,c).[6] In this form, the two chalcogen atoms are vertically aligned in a stacking pattern described as A-B-A, as shown in figure 2.1c,d. A monolayer can also form in a metastable distorted octahedral 1T phase with A-B-C stacking pattern where the two chalcogen atoms are vertically offset (Fig. 2.1c).[3,5] However only 2H monolayers, with robust symmetry dependent properties are studied in this work.

The stacking of 2H monolayers creates an A-B-A-B... ordering such that the multilayer material is composed of alternating layers each rotated 180° from the last. The upper layer metal atom is positioned vertically above the lower layer chalcogen site, as shown in figure 2.1d, and likewise, the upper layer chalcogen site resides over the lower layer metal atom. Inversion symmetry is therefore maintained in the bilayer, where it is broken in the monolayer. This is most easily seen in figure 2.1b inset, whereby taking the metal atom as an inversion centre results in the six chalcogen atoms (with a position vector transformation $\mathbf{r}_i \to -\mathbf{r}_i$) being mapped onto a vacant site.[6,9]

2.2 Electronic band structure of TMDs

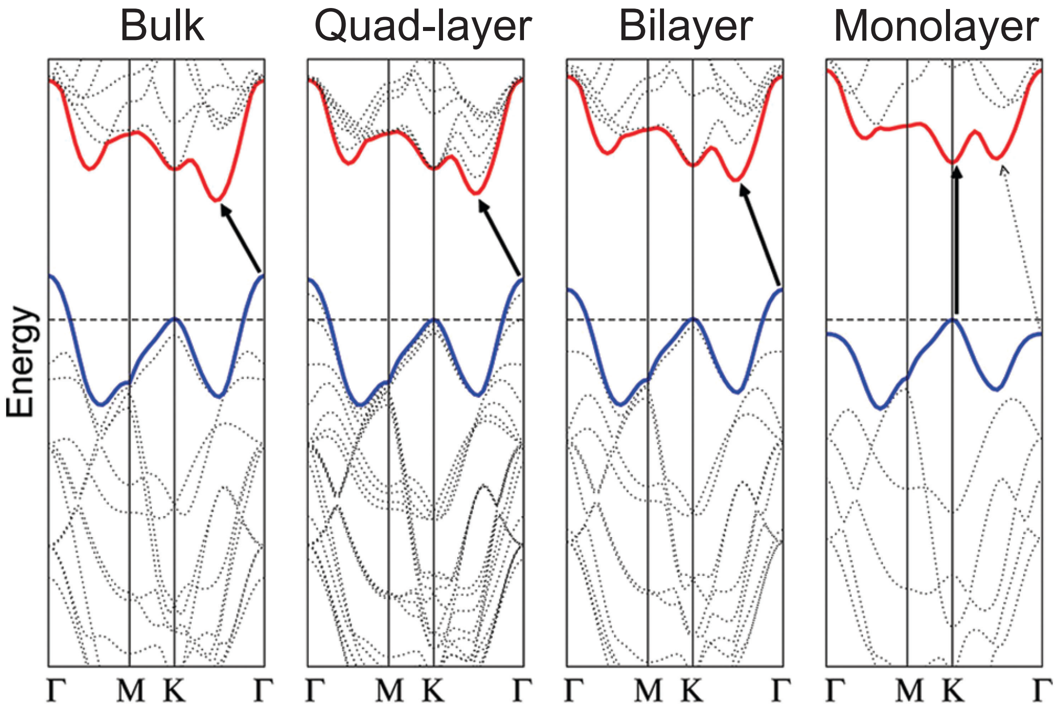

Figure 2.2: Electronic band structure of MoS_2 in the case of bulk, four layer, two layer, and single layer. The lowest energy inter-band transition (Bandgap) is marked with an arrow. The K point within the Brillouin zone is mostly unaffected by layer dependence, while the Γ_{VB} and Q_{CB} points are strongly affected by layer dependence. The bandgap transitions from momentum indirect in multilayers to momentum direct in monolayers. Image from Ref.[10]

An electronic band structure is formed when electrons move in an environment of periodic potentials such as a crystalline TMD lattice, with movement described by the Bloch function.[11] The resulting energy eigenvalues form a continuous band in momentum space. Due to the lattice periodicity, the electronic structure of the Brillouin zone can be considered the unit cell in energy-momentum space. With a lattice formed of different materials,

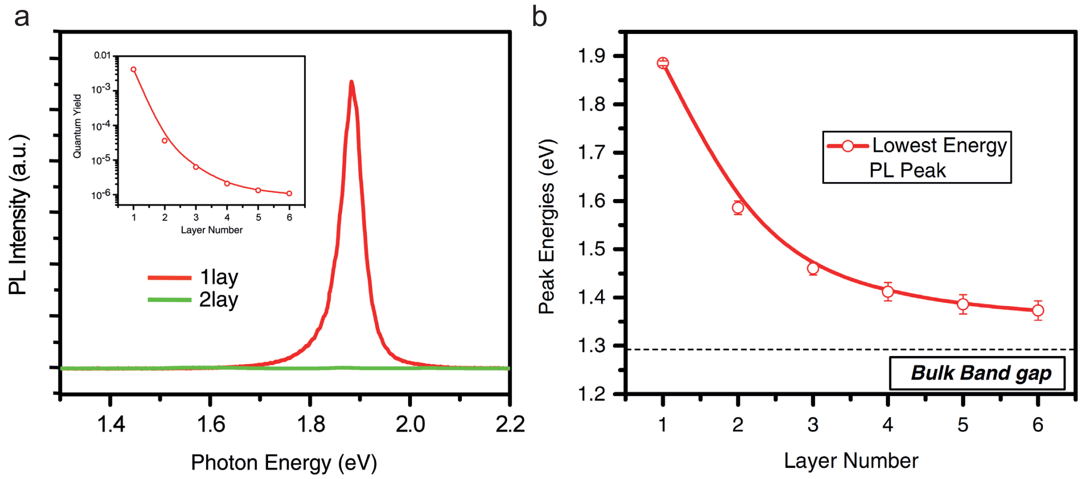

Figure 2.3: **a)** Intensity of photoluminescence observed from monolayer (Red) and bilayer (Green) MoS_2. *Inset:* PL quantum yield as a function of layer number. **b)** Bandgap energy, inferred from PL spectra, as a function of MoS_2 layer number. Image from Ref.[12]

the various electron orbitals are considered, to build up a convoluted band structure, as shown in figure 2.2 for the case of MoS_2 which is generally representative of TMDs.

In bulk form of TMD semiconductors, there exists a momentum offset between the valance band maximum (VBM), at the Γ point in the centre of the Brillouin zone, and the conduction band minimum (CBM), at the Q point of the Brillouin zone, halfway between the Γ and K points. This forms an indirect bandgap, as shown by the arrow in figure 2.2. At reducing layer numbers, the Γ_{VB} and Q_{CB} points are seen to shift in energy, while K remains mostly stationary. As the Γ point of the valance band is comprised of a combination of d_{z^2} transition metal orbitals and anti-bonding p_z chalcogen atom orbitals, while the K points are formed predominantly by d-orbitals of the metal atoms.[10,13,14,15,16,17] The electron states at K are therefore strongly localised to the plane of the transition metal atoms, reducing the spatial overlap with adjacent layers. Likewise, the Q point of the conduction band, is comprised of a combination of metal d-orbitals, and chalcogen p-orbitals.[14,15,16] As a result, the K points are mostly insensitive to changes in layer number, while the Γ_{VB} and Q_{CB} points undergo a significant shift when the number of layers is changed. This leads to the transition from momentum indirect, in multilayers, to momentum direct in monolayers, along with the associated increase in quantum yield and intensity of photoluminescence (PL) observed, initially, in MoS_2 (Fig. 2.3a). The increasing energy gap between the Γ_{VB} and Q_{CB} as the number of TMD layers is reduced, as reflected in figure 2.3b, where the lowest energy peak of MoS_2 is identified as monitored at various TMD thicknesses. At 1L, the lowest energy peak is the direct $K \rightarrow K$ transition.

2.3 Valley pseudospin, and optical selection rules

The shift from indirect to direct bandgap, as described in the previous section, results in a significantly better light-matter interaction from the monolayer when compared to bilayers and thicker. In a semiconducting material, when a photon of energy above the bandgap is absorbed, the photon energy is used in promoting an electron from the valance band to the conduction band, which leaves behind a 'hole' in the valance band of effective charge +1 (to the electron's -1). The electron then rapidly relaxes to the conduction band minimum. For a direct bandgap with no momentum offset between the CBM and VBM, the two charge carriers can easily recombine to release a photon of equivalent energy. However, since photons have effectively zero momentum, if there is an offset in k-space between the two band edges, the carriers cannot recombine due to carrying inequivalent momentum. Such an offset is compensated for via a momentum carrying phonon, but the involvement of an extra particle massively reduces the recombination efficiency. TMD monolayers are therefore significantly better for light-matter interactions.

The light-matter interactions of a TMD monolayer are dictated by the electronic band structure, in combination with governing optical selection rules. The Brillouin zone of a TMD monolayer is hexagonal in shape (in reciprocal space), with the conduction and valance band extrema positioned at the K points, at the edges (Fig 2.4a). Even though this produces a total of six K points, at each vertex of the hexagonal Brillouin zone, the three-fold symmetry of the TMD monolayer crystal lattice leads to a thrice repeating set of 2 inequivalent K points, nominally referred to $K+$ (K) and $K-$ (K'). At these points, the bands are quasi-parabolic and are commonly referred to as 'valleys', due to their shape.

In the out of plane c-axis, the spin projection of the charge carriers is well defined, due to the strong quantum confinement.[19] While the two $K\pm$ valleys are energy degenerate, the spin degeneracy is lifted due to a large spin-orbit coupling associated with the d-orbitals of the heavy transition metal atoms. Due to time reversal symmetry, the spin splitting is of opposite sign for opposite valleys, such that $E_{\uparrow}(K+) = E_{\downarrow}(K-)$ and $E_{\downarrow}(K+) = E_{\uparrow}(K-)$[17,19] as can be seen in figure 2.4. The orbitals forming the VBM at $K\pm$ consist of a mix of $d_{x^2} - dy^2$ and d_{xy}, which typically produce a spin splitting of hundreds of meV,[14,15,16,17] while the CBM is formed of just d_{z^2} orbitals and splitting of just tens of meV is observed. The splitting is also significantly larger ($\sim$ 400 meV) in W-type TMDs the Mo-type since tungsten is heavier than molybdenum.[17]

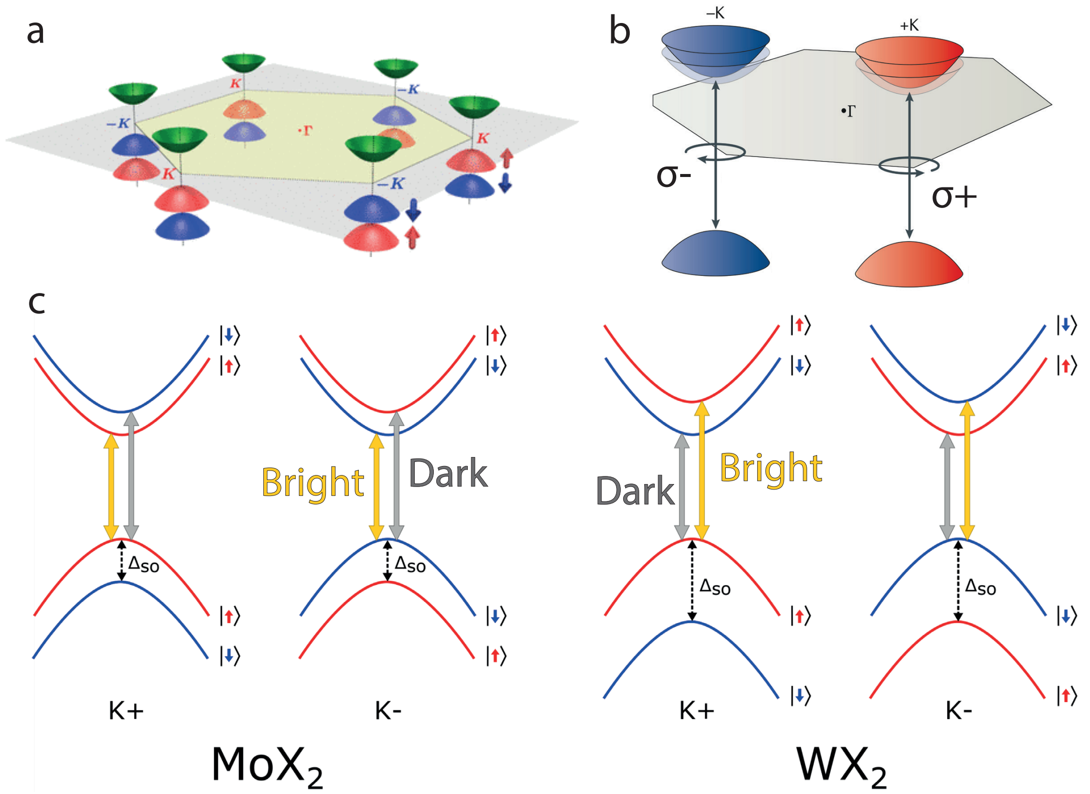

Figure 2.4: **a)** Hexagonal Brillouin zone of a monolayer TMD highlighting the spin-orbit splitting at the K± valleys. The smaller CB splitting is ignored here. Image from Ref.[6] **b)** Optical selection rules associated with the $K\pm$ valleys. Image from Ref.[7] **c)** Band valley structure of Mo-type and W-type TMD monolayers. Optically bright (spin allowed) transitions exist between CBM and VBM of same spin, while optically dark (spin forbidden) transitions exist between CBM and VBM of opposing spins. Image adapted from Ref.[18] Blue valleys indicate spin-down ($|\downarrow\rangle$) while red valleys indicate spin-up ($|\uparrow\rangle$).

The two valleys possess a valley degree of freedom, in that a charge carrier can occupy a state in either the $K+$ or $K-$. A carrier inherits a valley specific orbital magnetic moment with sign (±) depending on which valley it resides in. This is known as the valley pseudospin because it acts like a spin $\frac{1}{2}$ system. The K+ (K-) valley has valley pseudospin of $+\frac{1}{2}$ $(-\frac{1}{2})$. The combination of spin-orbit coupling and time reversal symmetry effectively locks the spin and valley degrees of freedom together since an electron of fixed energy can only occupy the valley of corresponding spin states. Single particle valley pseudospin is considered extremely robust, since a carrier would not only require a large amount of momentum transfer, but also an energetically costly spin flip and reversal of orbital angular momentum, associated with the valley states, in order to scatter between valleys. Since the spin-orbit splitting of the valance bands are significantly larger than that of the conduction band, and especially in W-type TMD monolayers, holes are seen to have particularly long valley lifetimes of $\sim$ ns at LT.[20] Notably, the suppressed valley scattering and associated long timescales have lead the concept of valleytronics, the exploitation of valley properties in storing and manipulating information through the valley degree of freedom in parallel with spintronics and spins and electronics and bits.[6,7,16]

The valley pseudospin has a remarkable effect on the interaction of TMD monolayers with light. In atomic physics, the optical transitions are dictated by angular momentum conservation rules, on the principle that the associated quantum numbers of the initial and final states are conserved. For TMD monolayers, the same rules apply also but with the additional concept of the valley orbital magnetic moment to consider.[21] The optical transition occurs across states of corresponding spin, such that the lowest energy bandgap transition is optically bright (spin allowed) in Mo-type TMDs, but optically dark (spin forbidden) in W-type TMDs as detailed in figure 2.4c. Furthermore, these constraints lead to a valley specific optical selection rule, as shown in figure 2.4b, that the $K-$ valley transitions couple only with σ^- circularly polarised light, and $K+$ with only σ^+.[6,21] It is therefore possible to optically address a specific valley through photon helicity, and perform valley specific measurements of TMD carriers simply through polarisation resolved spectroscopy as described in section 3.2.

2.4 Excitons in 2D materials

A single particle band structure is not sufficient to accurately describe the optical response of TMD monolayers. The solid state physics of TMD monolayers are dominated by two-body quasiparticles known as excitons. When a photon is absorbed by the direct band gap semiconductors, an electron is promoted from the filled valance band states to the empty conduction band leaving behind an empty state in a sea of filled states. This electron vacancy is known as a hole, with effective charge of +1 (to the electron charge of -1). In much the same way that an electron binds to an atomic nucleus, the electron and hole are attracted via electrostatic Coulomb forces.[18] Two common forms of exciton exist in crystalline semiconductors, with diverging properties which are determined by the size of the exciton, known as the Bohr radius, when compared to the unit cell of crystalline lattice. Frenkel type excitons,[22] often found in organic molecular crystals, are highly localised to a single atomic site, with Bohr radius a similar size to the unit cell. Wannier-Mott excitons are the opposite,[23,24] with large exciton Bohr radius many times large than the crystal unit cell, and are typically found in inorganic semiconductors where effective dielectric screening tends to reduce the Coulomb interactions between the electron-hole pair.[25,26]

2.4.1 Quasi-hydrogenic binding energy of excitons

In bulk TMD materials, the excitons formed are of the Wannier-Mott type, with large Bohr radius due to the effective screening of the surrounding material of dielectric constant ε_{3D}. As the number of layers is reduced, the amount of dielectric screening is likewise reduced. At the extreme 2D limit in monolayers, the effective dielectric constant is significantly lower $\varepsilon_{2D} < \varepsilon_{3D}$, leading to a small Bohr radius ($\sim$ 1 nm) and large binding energy ($\sim$ 0.5 eV).[27,28,29] In TMD monolayers, the excitons are therefore at the lower limit of the Wannier-Mott classification due to the small Bohr radii, verging more towards Frenkel like excitons. However, the excitons in TMD monolayers are still mobile within the crystal lattice and are therefore better described by the Wannier-Mott classification.

The binding energy of excitons in 2D semiconductors via Coulomb interaction is considered in the framework of the hydrogen Rydberg model:

$$E_B = \frac{\mu}{m_0} \frac{1}{\varepsilon_r^2} \frac{R_H}{n^2} = \frac{R_X}{n^2} \tag{2.1}$$

where m_0 is the rest mass of the electron (0.511 MeV), ε_r is the relative dielectric constant of the environment, R_H is the hydrogen Rydberg constant (13.6 eV),[25] and μ is the effective mass of an exciton:

$$\frac{1}{\mu} = \frac{1}{m_e^*} + \frac{1}{m_h^*} \tag{2.2}$$

with m_e^* and m_h^* the effective mass of the constituent electron and hole, respectively. To be stable against dissociation by interactions with thermally active phonons, the binding energy must be larger that the thermal energy such that $E_B > k_B T$, where k_B is the Boltzmann constant and T is the temperature. The associated Bohr radii is given by:

$$r_n = \frac{m_0}{\mu} \varepsilon_r n^2 a_H = n^2 a_X \tag{2.3}$$

where a_H is the hydrogen ground state Bohr radius. Excited exciton states have increasingly large Bohr radius and small binding energies. For an exciton to be generated through absorption of a photon, the photon energy must be equal to the free particle band gap minus the exciton binding energy:

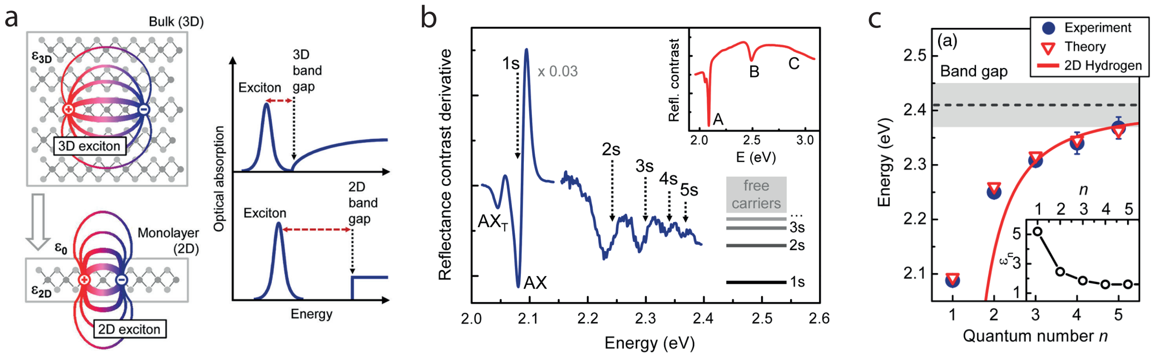

Figure 2.5: **a)** Comparison of Bohr radius in 3D and 2D systems shown in real-space. Bulk TMDs can be considered 3D systems with effective dielectric screening from the surrounding material. In monolayers, the reduced screening leads to a lower effective dielectric constant, and more strongly bound excitons with correspondingly small Bohr radius. The exciton optical absorption resonance energy is equal to the free particle band gap minus the exciton binding energy. **b)** Rydberg series of ground and higher exciton states shown through differential reflectivity $\frac{d}{dE}\left(\frac{\Delta R}{R}\right)$. The quantum numbers are labelled accordingly. **c)** Fitting of the observed transition energies (dots) to the hydrogenic Rydberg model (line) and subsequent nonhydrogenic Rydberg series (triangles) including an effective dielectric constant dependent on quantum number n (Inset). Images from Ref.[26]

$$E_\gamma = E_n = E_g^* - \frac{R_X}{n^2} \tag{2.4}$$

where E_g^* is the free particle band gap (energy required to create a free electron-hole pair). However, this differs from the absolute band gap measured as the energy gap between CBM and VBM by the so-called self energy term. This is nominally very similar in magnitude to the exciton binding energy with opposite sign such that the two mostly cancel out and the absorption peak is usually close in energy to the CBM to VBM absolute band gap.[18] For TMD monolayers, the optical band gap ranges from 650 to 800 nm (1.90 to 1.55 eV) depending on exact material composition.[30,31]

As shown in figure 2.5 the absorption signatures of excitonic Rydberg series up to n = 5 are detected in monolayer WS_2,[26] thanks to the large binding energies. However, when the energy peaks are fitted to the hydrogenic Rydberg series, a discrepancy appears for 1s and 2s excitons. This deviation is accounted for by considering a changing dielectric constant as a function of quantum number n, $\varepsilon_r(n)$ as seen in figure 2.5c.[26] The deviation arises due to the unique geometry of TMD monolayers, where the effective dielectric constant is massively dependent on the surrounding environment immediately outside the TMD monolayer, for example the type of substrate that the monolayer resides on, or if there is any contamination bubbles on the surface. The highly anisotropic dielectric screening therefore modifies the electric field between the carriers, which influences the binding energy of the exciton. This highlights the sensitivity of TMD monolayer to the surrounding environment. As a consequence, the optical signatures of a TMD monolayer exciton can slightly vary in energy between two samples of the same material.

2.4.2 Optical signatures of excitons

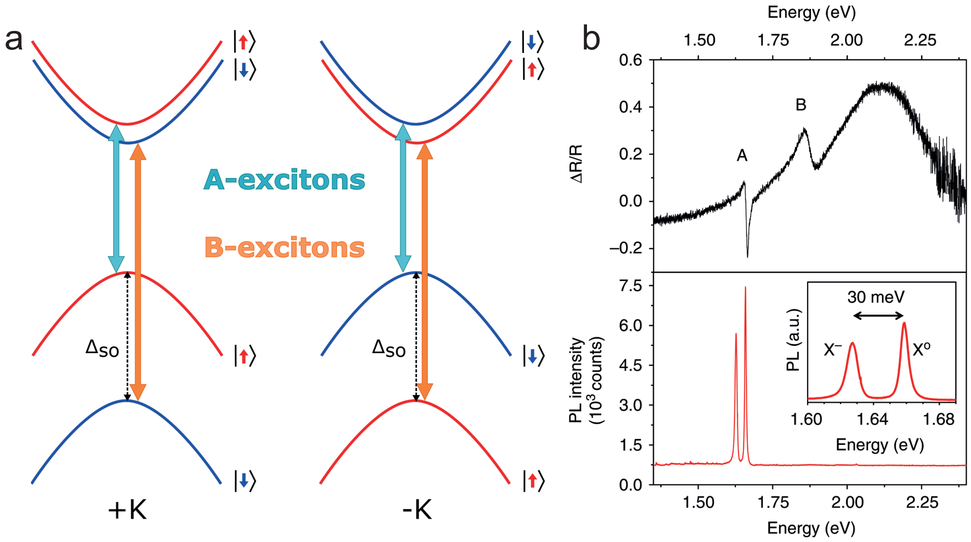

Figure 2.6: **a)** Band structure of the $K\pm$ points in a Mo-type monolayer showing the optically bright A and B excitonic resonances. Image adapted from Ref.[32] **b)** Optical signatures of the A and B excitons seen in reflectance contrast measurement, while PL (second panel) shows only neutral and charged A exciton emission. Image from Ref.[33]

As discussed earlier, the large spin-orbit coupling associated with the d-orbitals of the heavy transition metals lead to a spin dependent valance band splitting of hundreds of meV, while the optical selection rules are such that spin is conserved across the CB and VB. The combination of these effects leads to the appearance of two non-degenerate optically bright exciton resonances, from the spin-↑ CBM to spin-↑ VBM, and the spin-↓ CBM to spin-↓ VBM with energy difference influenced mostly by the valance band spin-orbit splitting.[30,33] These distinct exciton resonances are known as A-excitons and B-excitons, with A being the lower energy state, as shown in figure 2.6a. Further higher order complexes also exist (namely C- and D- excitons), however these are formed between non-ground states in the band structure originating from other orbitals.

Optical interactions with these resonances result in an absorption resonance at both A and B energies as shown in figure 2.6b, while despite optical excitation above B exciton energy the fast relaxation mechanics of excitons means that PL emission of the B exciton is not typically observed.[34] Reflectance contrast (RC) is a measure of absorption strength, which is nominally used to gain an insight into the spin-orbit coupling of the band structure. The PL emission spectra of TMD monolayers is dominated by the A excitonic resonance, with a second peak at slightly lower energy is also seen owing to charged exciton complexes.[33,35]

Charged excitons

Excitons, in the simplest form, are constructed of a single electron and single hole bound by attractive Coulomb forces to form a quasiparticle of combined charge $Q = 0$. However, more elaborate species not only exist, but are very common.[33] A bound state consisting of two electrons and a single hole will produce a charged excitonic resonance of overall charge Q = -1. Similarly, a state constructed of a single electron and two holes will form a charged exciton again, this time with a charge of $Q = +1$. These three-body resonances are commonly referred to as a trion.[33,35,38] In addition to two and three body states, four body states consisting of two electrons and two holes of zero overall charge ($Q = 0$) known as biexcitons,[39,40] along with five body 'quinton' states,[41,42] have been observed in TMD monolayers. These exciton species are shown schematically in figure 2.7a. To form trions, an additional amount of energy is required to bind the three charged particles together. As such, the trion emission X^- resonance is typically found at $\sim$ 20 to 30 meV offset from the neutral exciton X^0 (see bottom panel of Fig. 2.6b) owing to the additional binding energy.[33,43,44]

By introducing a back-gate, which provides control of the level of electrons and/or holes within a given monolayer, the population densities of the various exciton resonances is shown to depend on the level of excess charge (or doping) that is present within the monolayer band structure, as can be seen in figure 2.7b,c.[33,43,44] At diminishing doping levels, neutral excitons X^0 are the dominant exciton specie since there are no extra charges available to bind with, which is reflected in the PL emission spectra close to $V_g = 0$. As the back-gate voltage is increased, introducing a population of excess electrons in n-type doping, the photo-generated neutral excitons will readily bind to electrons and form negatively charged trions X^-. This is observed experimentally as an increase of X^- emission with simultaneous decrease of neutral exciton emission intensity. The opposite is seen with decreasing back-gate voltage, where p-type doping gives rise to an increase of positively

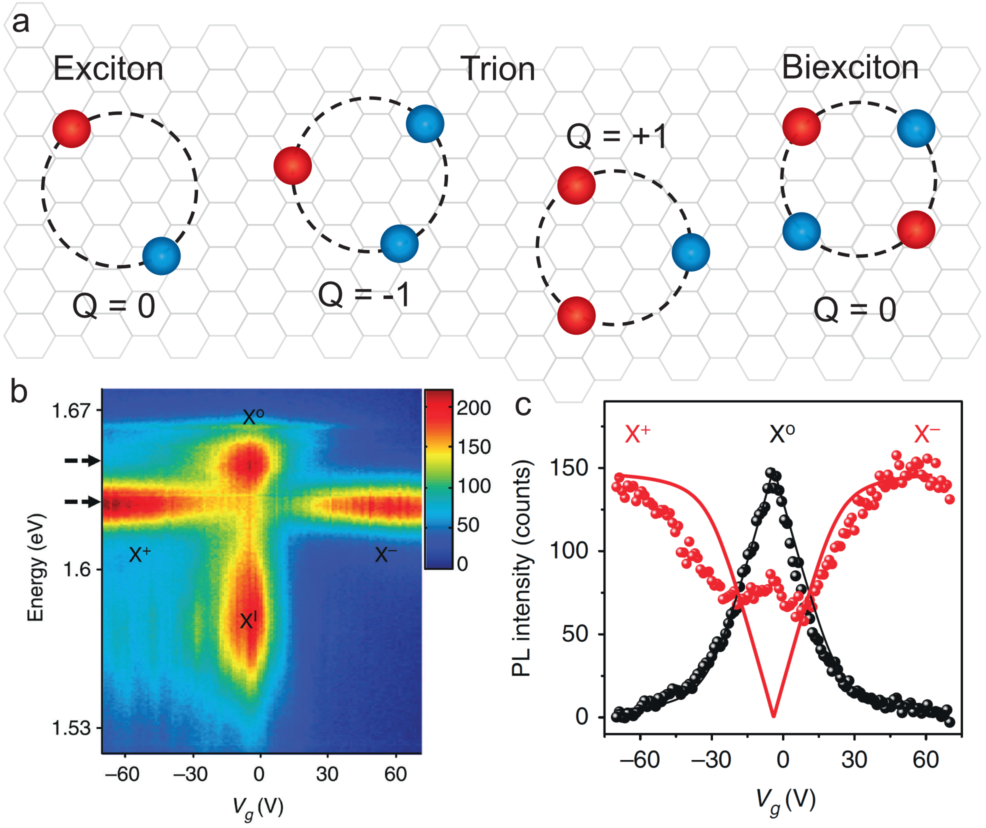

Figure 2.7: **a)** Schematic of the constituent particles that form (in order from left to right) the neutral exciton, negatively and positively charged trion, as well as the biexciton. The associated charge Q is also given. Image adapted from Refs.[18,36] **b,c)** PL emission from $MoSe_2$ as a function of back-gate voltage (V_g). As the voltage is dropped to negative (positive) values, the density of holes (electrons) present in the system increases, which encourages the formation of positively (negatively) charged trions X^+ (X^-), at the expense of neutral exciton emission, which decreases. The PL intensity profiles shown in c) are obtained at the neutral and charged exciton energies, highlighted by arrows in b). Low energy emission, X' is due to defect states. Image from Ref.[33]

charge exciton emission, at the expense of neutral excitons.[33] Biexciton formation requires very low doping, to suppress trion formation, along with a very high population density of neutral excitons achieved at large pumping powers.[39,40,41,42] An overview of the possible two- and three-body exciton configurations that readily form in TMD monolayers is given in figure 2.8.[37] Understanding, and controlling the population densities and dynamics will play a large part in the discussions throughout this thesis, especially in chapter 6.

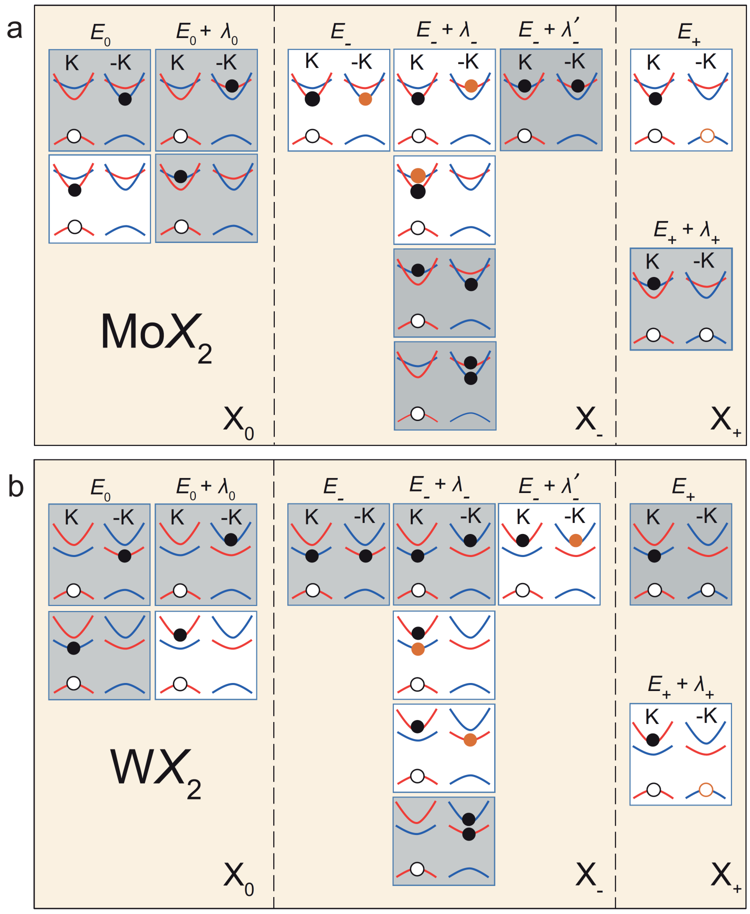

Figure 2.8: **a,b)** Exciton resonances found in a) MoX$_2$ and b) WX$_2$ TMD monolayers and the corresponding valley configurations of the constituent carriers. Red (Blue) curves show the spin-up (spin-down) valleys. Solid dots represent electrons, while empty dots are holes. For X^0 and X^-, (X^+) only excitons with hole (hole) residing in the K+ valley are shown (The reverse are also available). Optically bright excitons are shown with white background, while optically dark are shown with grey background. For the bright excitons, the recombining electron and hole are given in black and white respectively, and the excess carrier is shown in orange. Image from Ref.[37]

Temperature dependence of excitons

A lot of information can be gathered from the temperature dependencies of TMD monolayers, as they are heated from cryogenic temperatures up to ambient room temperature. Firstly, due to the differences in binding energy between the neutral and charged excitons, as the thermal energy is increased within the system, the trions begin to dissociate

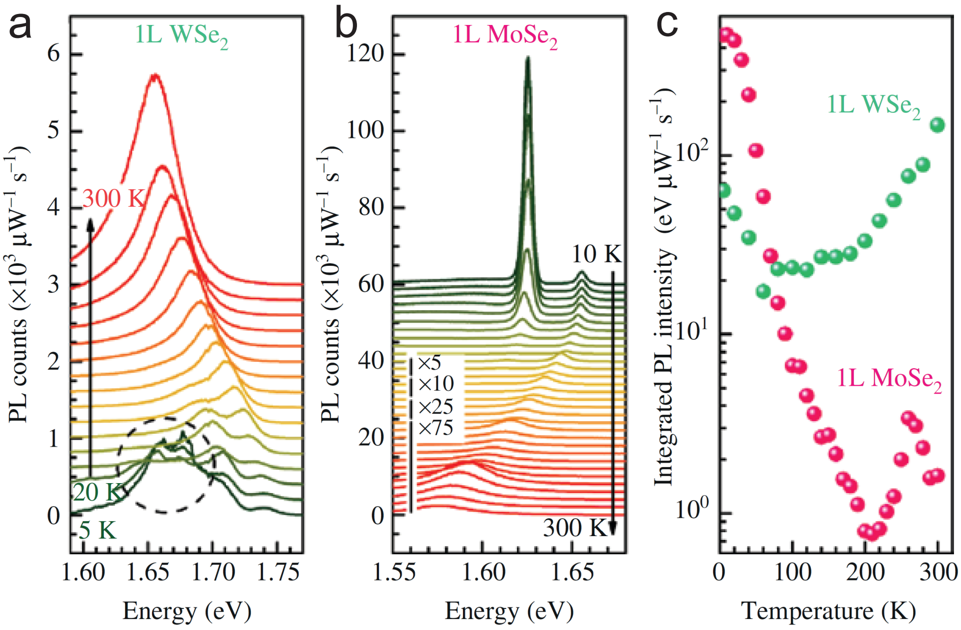

Figure 2.9: **a,b)** Temperature dependent PL emission from monolayer a) WSe_2 and b) $MoSe_2$. Trion peak is thermally dissociated by $T \approx 100K$. The circle in a) highlights the low energy band of localised defect states that serve as a radiative path out of the optically dark exciton ground state in W-type monolayers. **c)** Integrated PL intensity of the neutral exciton emission as temperature is increased with diverging trends observed for Mo-type and W-type TMD monolayers. Images from Ref.[45] using data from Ref.[46,47]

through interactions with thermally activated phonons much earlier than neutral excitons. The highly diverging response to temperature also highlights the differing band structure between Mo-type TMD monolayers and W-type (see Fig. 2.4c). Both can be clearly observed in figure 2.9 where the PL emission of $MoSe_2$ and WSe_2 is collected at increasing temperatures.[33,45,46,47]

The thermal energies of carriers residing in the valleys follow a Boltzmann distribution, such that an increasingly narrow distribution is found at temperatures approaching absolute zero. At cryogenic temperatures, the carriers are therefore well confined to the lowest energy state, i.e. electrons (holes) will relax to the conduction band minimum (valance band maximum). Depending on the spin states of the lowest energy transition between the band extrema, the radiative recombination efficiency of electron-hole pairs will be enhanced or suppressed. For example in $MoSe_2$, the lowest energy transition is spin-parallel, and therefore optically bright with large oscillator strength. Therefore funnelling electrons (holes) into the lowest energy configuration, via narrowed thermal distribution, will serve to increase radiative recombination efficiency and an associated increase in PL emission will be observed, as is the case in figure 2.9b. The opposite case is seen in WSe_2 (Fig. 2.9a), where the lowest energy transition is spin anti-parallel, or optically dark. At low temperatures, the carriers are confined to a radiatively inefficient state suppressing PL intensity. The spectra at this point is dominated by a band of low energy emission from excitons localised to perturbations of the WSe_2 band structure, such as phonon-replicas,[48,49] lattice defects,[50] and strain induced localisation of excitons.[51,52,53] The effects are also seen in highly disordered $MoSe_2$ monolayers,[33,54,55] such is shown in figure 2.7b. RC measurements offer a complementary insight into the excitonic behaviour and remains largely insensitive to these defect states. The integrated PL emission intensity as a function of temperature is shown in figure 2.9c, where the opposing trends are clear. In WSe_2, increasing the temperature such that the thermal energy distribution of electrons overlaps into the upper CB sub-band is accompanied with an increasing PL emission intensity. In both materials, the trion binding energy is quickly overcome by interactions with thermally activated phonons caused by the additional charge escaping from the bound state with neutral exciton such that only X^0 emission is observed at temperatures above ~ 100 Kelvin. The large binding energy of neutral excitons in 2D materials is shown as emission remains beyond room temperature, albeit with significant inhomogeneous broadening.[33,45,46,47]

2.4.3 Exciton valley pseudospin

The valley framework discussed previously in this chapter is slightly modified in the context of excitons, which needs to be considered due to the prevalence of excitons in TMD monolayer systems. Since an exciton (neutral, exciton-hole pair) can only be photo-generated within one valley due to the governing chiral optical selection rules, and as such inherit a valley degree of freedom from the constituent electron and hole. Optically bright excitons therefore behave as composite bosons with zero net charge (with dipole moment) and an optically addressable valley pseudospin, leading to the potential of all-optical information processing in a nano-scale device.

Exciton valley polarisation

Since optically bright excitons inherit the valley pseudospin from constituent carriers, it would follow that the robust suppression of valley scattering is likewise observed for excitons. Due to the chiral selection rules and optical addressability of excitons within a single valley, it is straight forward to measure the retention of valley polarisation through polarisation resolved spectroscopy. By pumping a monolayer band structure with σ^+ polarised laser

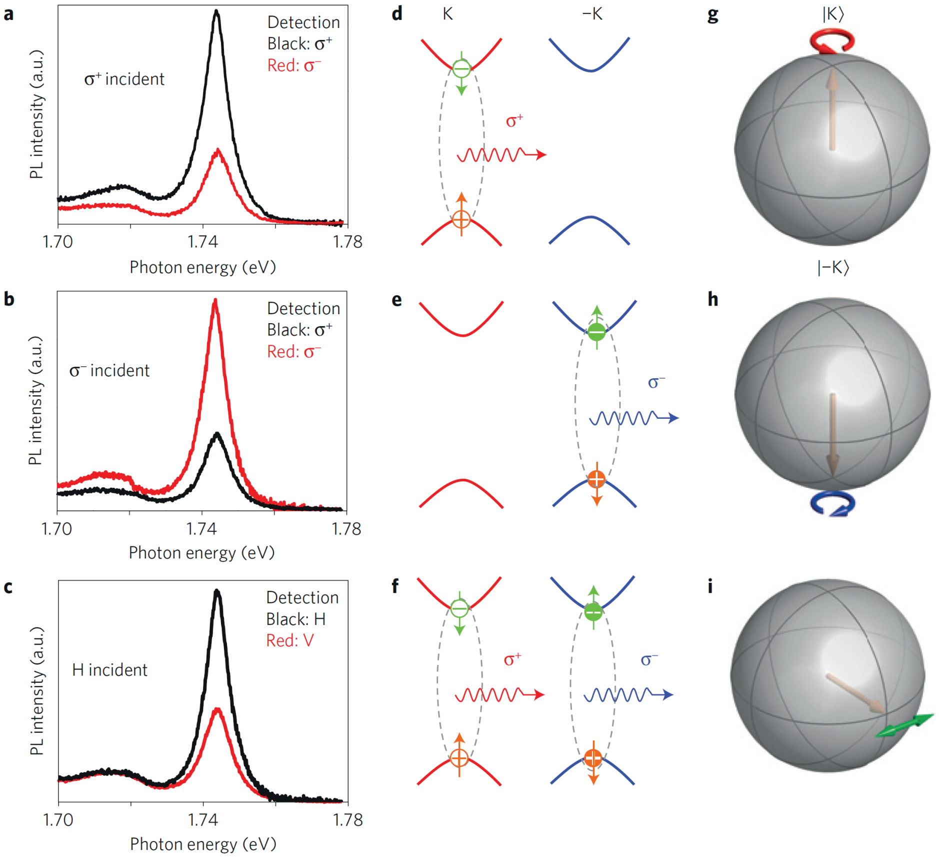

Figure 2.10: **a,b,c)** Polarisation resolved spectroscopy of the neutral exciton population in monolayer WSe_2 under different excitation and collection polarisations as defined in each panel. The valley polarisation of the injected excitons is retained in all cases, with $\sim 50\%$ valley polarisation observed. **d,e,f)** Simplified monolayer WSe_2 band structure, including corresponding exciton states for each polarisation regime. The electron and hole particle spin is shown (note this is distinct from the valley pseudospin shown in previous figures.) **g,h,i)** Bloch sphere vector notation for the corresponding valley states. Image from Ref.[8]

light creates excitons only in the $K+$ valley, initialising the valley polarisation of the exciton population.[19,36,56,57] The same applies for σ^- polarised laser to initialise excitons in $K-$ valley due to time reversal symmetries. Furthermore, due to valley coherence phenomena, pumping with linearly polarised light produces a population of excitons in both valleys, forming a linear superposition of valley states.[58,59,60,61] It can be useful to consider the exciton valley pseudospin as a vector within a Bloch sphere, with a vector pointing up to the north pole of the sphere being the $|K+\rangle$ valley state, while a vector pointing down to the south pole is the $|K-\rangle$ valley state. A vector positioned on the equator corresponds to a coherent superposition of the two.[8,58,59] For the valley pseudospin to be used successfully as an information processing mechanism in the same was as spin or cubits, it must be long lived such that the initialisation valley state remains well defined until recombination of the exciton. Exciting a sample with circularly polarised light and measuring the PL emission in a co- and cross-polarisation basis, as described in section 3.2, will determine the amount of valley polarisation retention across the radiative lifetime.[8,19,58] A significant difference in PL intensity between the co and cross polarised collections will indicate that some of the photo-generated excitons remained in the initialisation state before recombining. Figure 2.10 details such an experiment using monolayer WSe_2, with the corresponding valley pseudospin Bloch sphere vectors also shown (g-i). Clear intensity differences are observed for both circular polarisation excitations, as well as for linear excitation, indicating a relatively long valley lifetime or a short recombination lifetime. The specific amount of valley depolarisation that occurs is dependent on the ratio between the valley lifetime to radiative lifetime.

While these measurements show a successful retention of valley pseudospin, as required for information processing purposes, the amount of valley polarisation is far from unity,[2,62,63] while similar measurements performed on $MoSe_2$ show almost zero valley polarisation,[64] completely contradictory to the single particle model which results in valley relaxation lifetimes in the nanoseconds (compared to a radiative lifetime in the picoseconds). This is due to an exciton specific valley orbit coupling which results in a decoherence mechanisms effectively coupling the two $|K\pm\rangle$ valley states.[7,8,18,62,65]

The Coulomb interactions that the electron and hole are subject to can be categorised into two distinct contributions, direct and exchange. The direct Coulomb interaction determines the attraction between positive and negative distributions of charge, and is therefore responsible for the exciton binding energy.[18] It is also sensitive to the surrounding dielectric environment resulting in variations of exciton resonance energy when the TMD monolayer is placed on different substrates, thereby changing the dielectric environment.[66] The Coulomb exchange interaction, is separated into two further contributions, a short range (diagonal), and a long range (off-diagonal) interaction.[37] There are 10 exchange coupling terms, five of which are shown in figure 2.11c-e, and the others are obtained through time reversal symmetry. The right hand panels illustrate the the Feynman diagrams, while the left hand panels schematically illustrate the corresponding effects on the electron and hole valley configurations. Processes I and V are electron-electron exchange, where V is usually suppressed due to the energy mismatch arising form the CB spin-splitting, while II, III, and IV are electron-hole exchange interactions.[37] The short range Coulomb interaction originates from

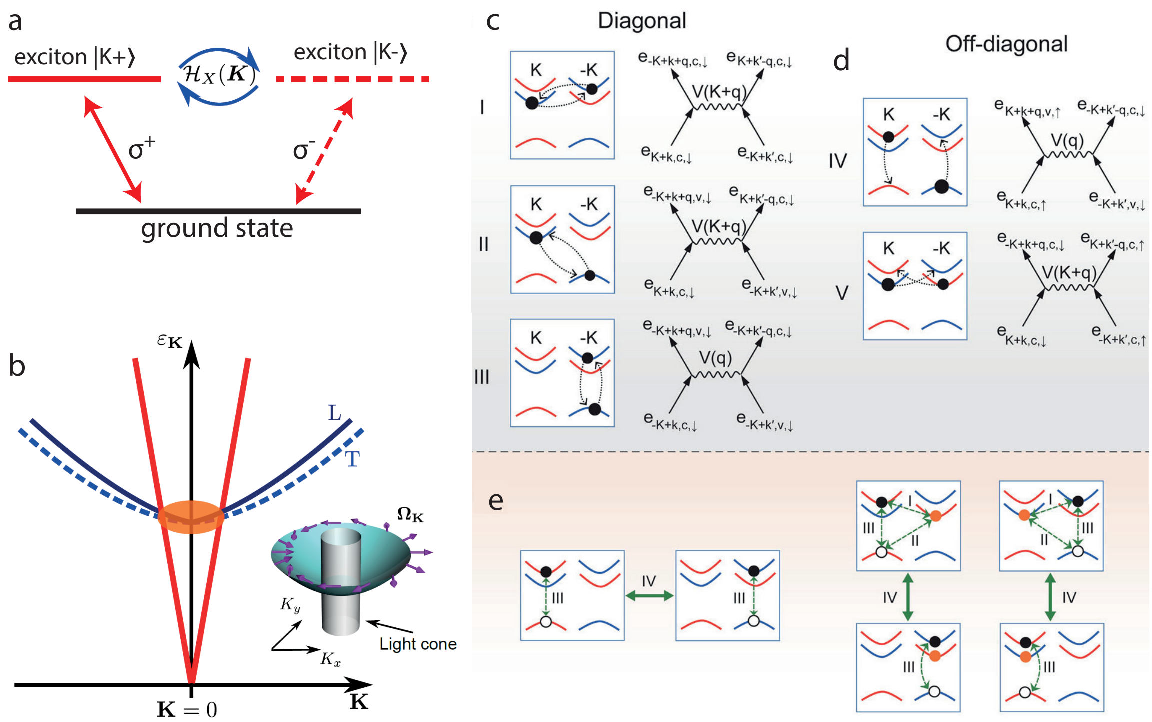

Figure 2.11: **a)** Coulomb exchange interaction $\mathcal{H}_X(\boldsymbol{K})$ effectively couples the two exciton valley pseudospin states $|K\pm\rangle$. Image adapted from Ref.[65] **b)** The LT splitting of the exciton dispersion and resultant effective magnetic field $\boldsymbol{\Omega_K}$ that acts on the valley pseudospin. Image from Ref.[65] **c)** The diagonal or short range exchange interactions that result in the fine structure splitting of excitons. **d)** The off-diagonal, or long range exchange interactions that result in a coupling between the two valley states. V is energetically unfavourable and IV is the dominant valley depolarisation mechanism. **e)** The processes involved for bight neutral excitons (left) and bright trions (right). Image from Ref.[37]

overlapping electron-hole wave-functions and, as such, is sensitive to the relative spin and valley indices due to the Pauli exclusion principle.[18] This short range interaction leads to an energy splitting between the singlet and triplet excitonic species, while also fortifies the spin-orbit coupling that energetically separates the optically bright and dark excitons.[18,62] It is the long range exchange interaction that is responsible for coupling the opposite valley states $|K\pm\rangle$, allowing efficient inter-valley scattering without the need for a spin-flip or momentum transfer through a Maialle-Silva-Sham mechanism.[7,8,18,62,65,67,68] The effect creates an energy splitting between excitons with dipole moment parallel (longitudinal) or perpendicular (transverse) to the in-plane centre-of-mass wave-vector $\boldsymbol{K} = (k_x, k_y)$, known as the L-T splitting (Fig. 2.11b).[2,37,62,63,65,67,68]

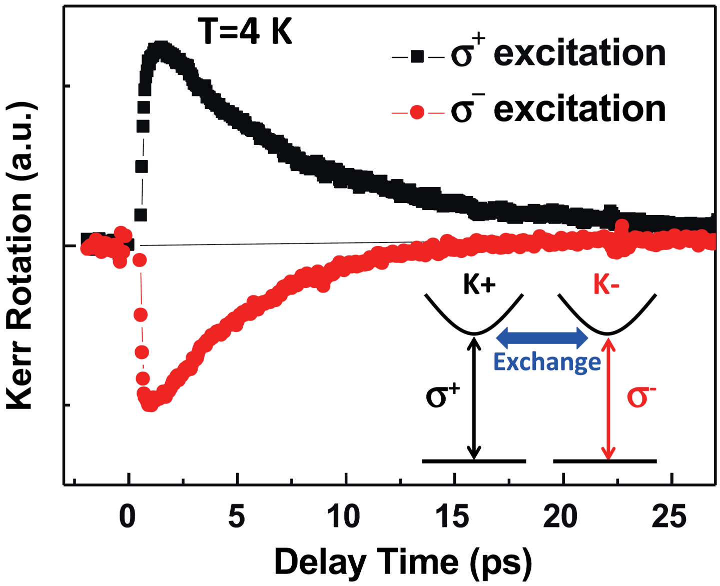

Figure 2.12: **a)** Rapid valley depolarisation (τ_v = (6 ± 0.1) ps) of a WSe_2 monolayer measured via Kerr rotation dynamics. Image from Ref.[69]

The effective Hamiltonian acting in the basis of $|K\pm\rangle$ states, as depicted in figure 2.11a, can be written as:[65]

$$\mathcal{H}_X(\boldsymbol{K}) = \frac{\hbar}{2}\left(\boldsymbol{\Omega_K} \cdot \boldsymbol{\sigma}\right) \tag{2.5}$$

where $\boldsymbol{\sigma} = (\sigma_x, \sigma_y)$ is the valley pseudospin vector composed of Pauli matrices and $\boldsymbol{\Omega_K} = (\Omega_x, \Omega_y)$ is the pseudospin precession frequency. The non-zero components are given by $\hbar\Omega_x = 2\alpha K^2 \cos(2\theta)$ and $\hbar\Omega_y = 2\alpha K^2 \sin(2\theta)$ where $\alpha(\boldsymbol{K})$ is the long distance Coulomb exchange coupling strength and θ is the angle between $\boldsymbol{K}$ and the in-plane axis x.[62,65] The splitting between the two longitudinal and transverse modes is therefore given by $\hbar\Omega_K = 2\alpha K^2$, where the coupling term becomes significantly weaker at large wave-vectors as $\alpha(K) \propto K^{-1}$.[65] The result is that the normally parabolic exciton dispersion picks us an energy splitting that is proportional to the wave-vector, $\hbar\Omega_K \propto K$, as shown in figure 2.11b.

$\boldsymbol{\Omega_K}$ acts as an effective magnetic field acting on the exciton centre of mass wave-vector $\boldsymbol{K}$ with a directional dependence that forms a double-winding in-plane orientation schematically presented in the inset to figure 2.11b. The MSS mechanism that produces this effective magnetic field is therefore responsible for the coupling the two valley pseudospin states

$|K\pm\rangle$ and leads to a lower than unity valley polarisation observed in TMD PL emission, despite robust optical selection rules and initialisation.[2,37,62,65,67,68] The resulting rapid valley depolarisation, as shown in figure 2.12 is of significant importance in chapter 6.

The valley Zeeman effect

The magnetic moment associated with the valley pseudospin is analogous to the Bohr magneton associated with conventional electron spin.[8] It has been discussed that the magnetic moment associated with the valleys take an equal magnitude of opposite sign at each valley state due to time reversal symmetry.[57] It is therefore possible to obtain a control over the valley pseudospin via an externally applied magnetic field, which has the effect of lifting the energy degeneracy between the two valley states. This effect is known as the valley Zeeman effect.[45,56,57,70,71,72]

The energy shift is not only dependent on the valley magnetic moment however, as contributions arising from conventional carrier spin as well as the magnetic moments of the metal d-orbitals that form the conduction and valance band edges need to be considered also. The sum of these three contributions will determine the total energy shift of the band structure, as shown in figure 2.13a,[70,71,72] while the energy splitting as observed by the optical response via PL emission (Fig. 2.13b) of each valley state arises from discrepancies between the total shift value of each valley shift.

For example, the Zeeman shift that occurs due to the spin magnetic moments (Black arrows in Fig. 2.13a.) causes the CB and VB sub-bands to move by the same amount (with oppose sign in the opposing K valley) since optical transitions conserve spin. Therefore the energy shift is applied to both initial and final states of a PL emission and the transition gap is still the same size. The value of the spin contribution is given by $\Delta_s = 2s_z\mu_B B$ (following the same notation given in Ref.[70]) where s_z is the spin projection in the z direction, μ_B is the Bohr magneton (5.79×10^{-5} eVT^{-1}), and B is the strength of the applied magnetic field.

The Zeeman shift from the atomic orbital moment does result in a shift in PL emission energy, as the conduction band edges are mainly composed of d-orbitals with $m = 0$, whereas the valance band edges are mostly $m = 2$ for the $K+$ valley, and $m = -2$ for the $K-$ valley.[70,71] This means that the conduction band is not shifted, while the valence band shift (purple arrows in Fig. 2.13a) is valley dependent with value $\Delta_a = 2\tau\mu_B B$, where τ is the valley index ($\tau = \pm1$ for the $K\pm$ valley) resulting in a net shift of $4\mu_B B$ between the valley PL emission.[70]

Finally, the Zeeman shift contribution from the valley magnetic moment (green arrows

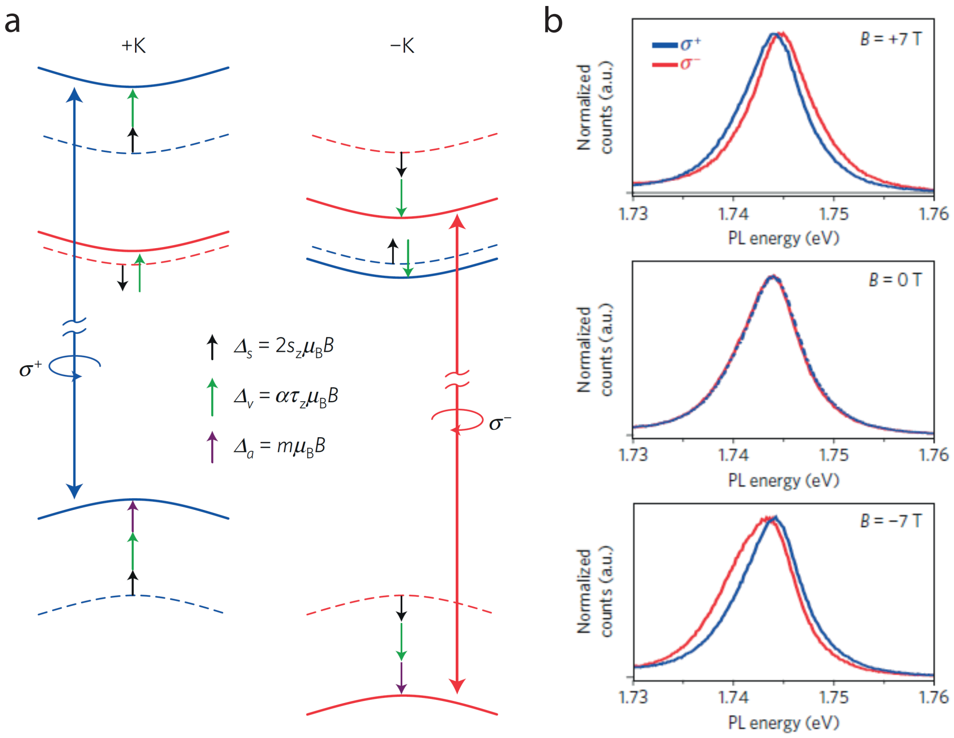

Figure 2.13: **a)** Schematic of the valley dependent energy shifts due to the three magnetic moment contributions. Black arrows show the carrier spin shift Δ_s, purple arrows show the atomic orbital moment shift Δ_a, while green arrows show the shift from the valley magnetic moment Δ_v. **b)** The resultant net exciton valley Zeeman shift measured through circularly polarisation resolved PL spectroscopy. Image from Ref.[70]

in Fig. 2.13a) is given by $\Delta_v = \alpha_{c,v}\tau\mu_B B$ where τ is again the valley index, and $\alpha_{c,v}$ is the valley g-factor and is dependent upon the effective masses of the conduction and valance bands with the expectation that nominally the two are equal such that $\Delta\alpha = \alpha_c - \alpha_v = 0$.[8] However, non-zero results have been found in a range of studies.[16,70,71,73] The valley magnetic moment leads to a shift of the $K+$ $(K-)$ valley sub-bands to higher (lower) energies, while the net shift of the optical resonances given by $2\Delta\alpha\mu_B B$.

Combining the results, the exciton valley Zeeman splitting between the opposite valleys is given by $\Delta_Z(B) = 2(2 - \Delta\alpha)\mu_B B$, with a linear valley dependent shift of the exciton resonance of $-\tau\Delta_z(B)/2$ such that the $K+$ valley exciton $(\tau = +1)$ is red-shifted with respect to the $K-$ valley exciton $(\tau = -1)$ for $B > 0$, and blue-shifted for $B > 0$, as is found in experimental observations of polarisation resolved PL emission of a WSe$_2$ monolayer under application of an external magnetic field (Fig. 2.13b). In the case shown here, the energy splitting is found to be $\Delta_z(B) = E_{\sigma^+} - E_{\sigma^-} \approx -1.8\mu_B B$, where the value -1.8 is termed the valley Zeeman g-factor.[70] Since this value is less than the -4 value as determined by the orbital magnetic moment Δ_a, this leads to the conclusion that the effective masses of the conduction band and valance bands are not equivalent in this sample. Typically though, a value of ∼ -4 is measured for neutral excitonic resonances in TMDs.[32,45,56,57,71,72,74] While measurements of the same effect in trions becomes more complicated with the presence of both spin-singlet and spin-triplet types of trions, as detailed by *Lyons, T.P., et. al.*[75]

2.4.4 Fermi polarons in highly doped monolayers

As the level of doping becomes increasingly large, the three-body model of charged excitons no longer adequately describes the optical response of the system. It is required to consider an exciton coupling not to a single carrier, but a Fermi-sea.[43,76,77,78,79,80,81] The interaction of a valley exciton with a Fermi sea of excess carriers characterised by a spin-singlet and spin-triplet interaction that effectively splits the exciton spectrum into a lower energy attractive exciton-polaron (normally identified as the trion branch) and a higher energy repulsive exciton-polaron (normally identified as the exciton branch), respectively (Fig 2.14c), with a linearly increasing splitting between the two polaron branches as the Fermi-level is increased further.[43,76,77,82] The three-body physics of a trion fails to explain this increasing energy splitting.

Figure 2.14a shows experimentally measured reflectance contrast of a gate controllable $MoSe_2$ monolayer, as the level of doping is tuned from zero producing a single absorption resonance from the neutral exciton in the absence of excess carriers, to heavily n-doped whereby the spin-triplet interactions between the excess carriers and exciton resonance transforms the latter into a repulsive polaron exhibiting a strong blue-shift and line broadening. At the same crossover point, a transfer of oscillator strength occurs from the repulsive polaron to an emerging second resonance originating from the spin-singlet interactions between the 2DEG and the dressed exciton forming the lower energy attractive polaron branch.[43,76,77,82] Due to the transfer of oscillator strength to the attractive polaron, the repulsive polaron becomes unidentifiable for very large doping levels ($\gtrsim 1 \times 10^{12}$ cm^{-2}).[76] The same results occur when the level of doping is tuned to highly p-doped, however monolayer TMDs are typically n-doped from the fabrication methods, so the consideration of p-doped materials is not continued in this work.[76]

Conceptually, in the valley states basis, a σ^+ attractive polaron can be thought of as a $K+$ valley exciton interacting with the spin-down two-dimensional electron gas within the $K-$ conduction band valley, as depicted in figure 2.14b, while the σ^+ repulsive polaron

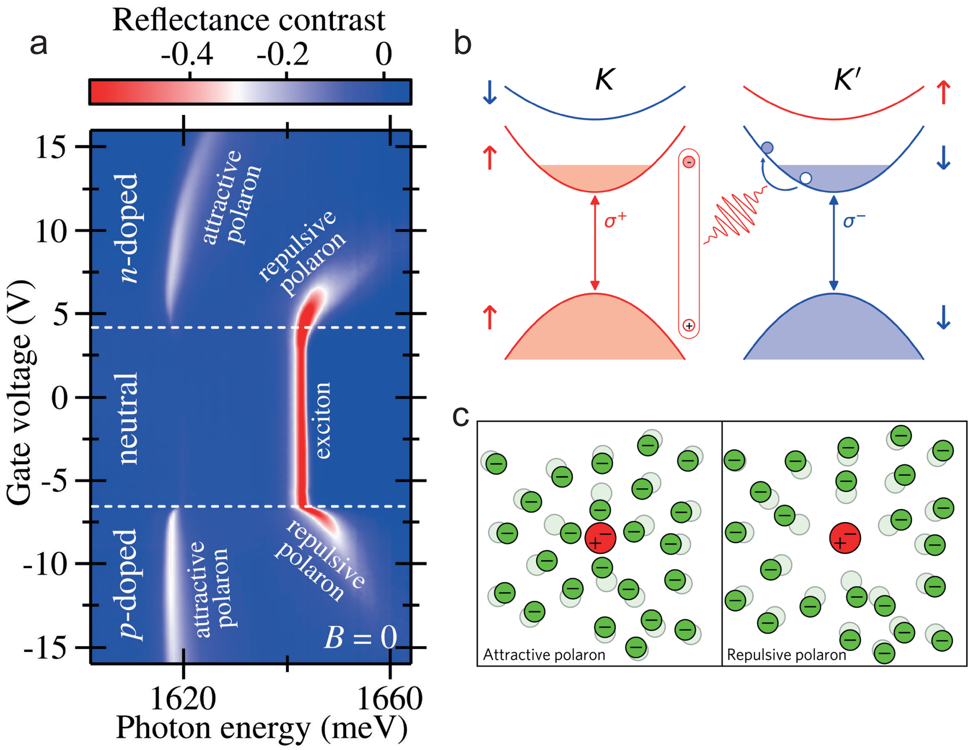

Figure 2.14: **a)** Reflectance contrast measurement of a $MoSe_2$ monolayer as function of gate voltage and doping level. Two distinct polaron regimes are found at high levels of p- and n-doping. Image from Ref.[82] **b)** Valley schematic of a highly n-doped Mo-type monolayer depicting an attractive (spin-singlet) interaction between a $K+$ valley exciton with the $K-$ 2DEG. Image from Ref.[83] **c)** Schematic representation of an attractive (spin-singlet) and repulsive (spin-triplet) interaction of a neutral exciton (red circle) within a Fermi-sea of itinerant electrons (green circles). Image from Ref.[43]

is the same $K+$ valley exciton interacting with the spin-up 2DEG within the same $K+$ CB valley.[83,84] The concept of Fermi-polarons is of vital importance in chapter 6 where the tuning of a spin-valley polarised CB 2DEG via an applied magnetic field leads to spin-valley selective strong coupling and the realisation of a robust all-optical topological gap.[84]

2.5 Alloying in TMDs

Alloying is the process of substituting a portion of lattice atoms with a different material, in effect controlling the precise chemical composition of a lattice, a powerful technique that first originates circa 2500 BC at the start of the Bronze age, and is widely used in the current generation of commercially available III-V semiconductor devices.[85] The concept of alloying is now starting to be applied to 2D semiconductors and TMD devices, with the promise of extensive tunability of the already exciting opto-electronic properties.[86,87,88,89,90,91] Possibly the most important consideration when producing an alloy of two materials is the structural differences between the two pure materials, if chemically replacing an atom (or set of atoms) within the lattice will cause large amounts of strain or introduce unwanted grain boundaries. While the family of 2D materials is vast and the range in band gaps and lattice constant are similarly large,[92] within the sub-group of TMDs, the lattice mismatch between MX_2 and WX_2 doesn't exceed 1%.[93,94] It is possible therefore to produce a purely crystalline lattice with the same symmetry, structural and physical properties as the pure TMDs with an arbitrary amount of atomic substitution of transition metal (or chalcogen) atoms with another type of TMD transition metal (or chalcogen) atoms.[95,96]

A variety of growth techniques are used to synthesise alloyed monolayers, from physical,[99] chemical,[102,103] and metal-oxide[104] vapour deposition techniques, along with chalcogen exchange processes.[97] These methods even provide a control of the alloy composition, during growth, leading to the production of monolayer flakes with a radial gradient of alloy concentration.[105] The main problem associated with these growth methods is the high density of defect states within the monolayers. It is therefore most common to synthesise alloyed TMD crystals in bulk form, and fabricate monolayers through micromechanical exfoliation (see section 3.1.1).[1,90] The alloys produced in bulk form are typically found to be almost perfectly mixed at an atomic scale, without any significant phase separation, as shown in figure 2.15b.[88,90,106]

The critical advantage that alloying has is that it allows fine control and continuous tuning of a material's optical and electrical properties, thereby creating a new degree of freedom. A method of characterising the tuning of a given property, for example PL emission energy, of an alloy is by using the bowing parameter:[89,90,107,108]

$$E_{PL}(Mo_xW_{1-x}Se_2) = xE_{PL}(MoSe_2) + (1-x)E_{PL}(WSe_2) - bx(1-x) \tag{2.6}$$

where x is the alloy composition between 0 and 1, $E_{PL}(MoSe_2)$ and $E_{PL}(WSe_2)$ is the emission energy of pure $MoSe_2$ and WSe_2 respectively, while b is the so-called bowing parameter. The bowing parameter is a useful metric by which to empirically describe the tuning curve, compare results with previous (and future) experiments, as well as estimating the composition required to reach a certain emission energy. Through alloying of TMDs it is possible to achieve a full continuous tuning of PL emission from ~ 1.6 eV ($MoSe_2$) to $\sim$

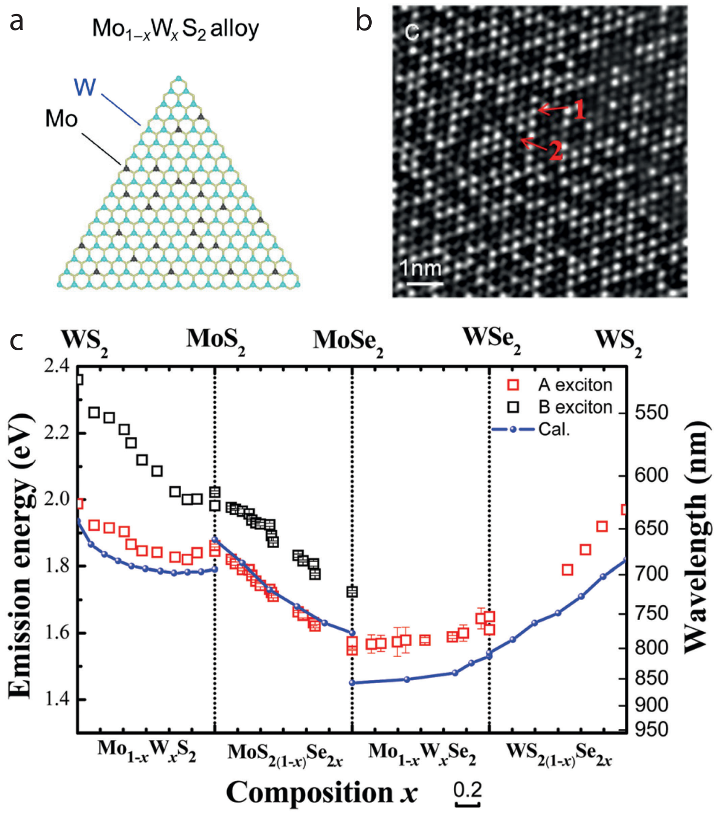

Figure 2.15: **a)** Schematic representation of a $MoWS_2$ alloyed monolayer. Blue dots represent W atoms, while grey dots are Mo atoms, and yellow dots are sulphur chalcogen atoms. Image from Ref.[97] **b)** STEM image with FFT filtering showing the mixture of Mo (2) and W (1) atoms within a $Mo_{0.47}W_{0.53}S_2$ alloyed monolayer. Image from Ref.[90] **c)** Tuning of PL emission energies across TMD based alloys. Image from Ref.[94] using experimental data from Refs.[88,90,95,98,99] and calculated data from Refs.[90,100,101]

2.0 eV (WS_2). Chapter 5 investigates the tuning of optical properties of $M_xW_{1-x}Se_2$ alloys through band structure engineering.

2.6 van der Waals Heterostructures

Due to the layered structure of the materials within the 2D semiconductor family, the process of combining multiple layers of different materials into a single device known as a van der Waals heterostructure (from the weak interlayer van der Waals bonding) becomes trivial.[36,109,110,111,112] The opto-electronic properties of the constructed device not only

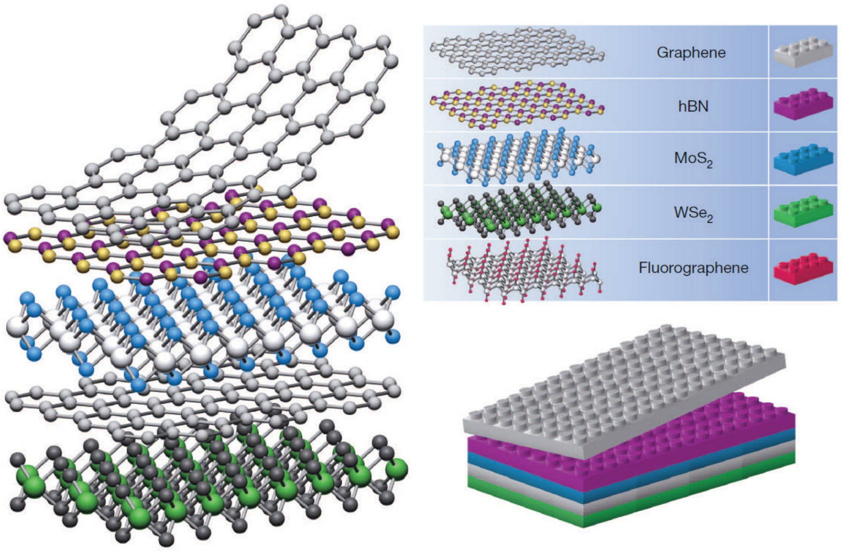

Figure 2.16: **a)** The ease of stacking different 2D materials together to form a complex van der Waals heterostructure is likened to building Lego® structures. Image from Ref.[110]

inherited from the constituent materials but also in how the materials interact with each other, such that novel phenomena,[36,113,114] and new avenues for potential applications, can be explored.[36,115,116,117]

A 2D material is formed through very strong covalent bonds within a layer forming a very strong crystalline lattice structure, while the van der Waals (vdW) forces between the layers (interlayer) is relatively weak in comparison. This allows a material to be placed onto almost any surface, including other 2D materials, without consideration for dangling bonds or lattice mismatch which blight the construction of similar multilayered structures using conventional III-V semiconductors. Figure 2.16 shows a graphical representation of an example vdW heterostructure (HS) created with multiple different 2D materials such as semimetallic graphene, insulating hexagonal boron nitrate (hBN), and TMD monolayers, in analogy to stacking bricks of Lego® together.[110] Of course, it is not *quite* that simple in reality, but recent advances in fabrication methods (Sec. 3.1) means that, at least conceptually, the analogy remains valid.

2.6.1 hBN encapsulation

One of the most simple form of heterostructure, is built through hBN encapsulation on one or both sides of the active TMD monolayer.[118] Hexagonal boron nitrate is an atomically flat, insulating material, making it a near-ideal surface for 2D materials which are inherently sensitive to the surrounding dielectric environment.[26,118] Not only does the layer insulate the active TMD from charge disorder within a given substrate,[119,120,121] but also provides a perfectly uniform dielectric environment. The combination of these effects leads to the optical and electronic properties of a monolayer to be much closer to the intrinsic limit, unperturbed by external effects from the surrounding environment, as demonstrated by *Ajayi, O.A., et. al.*,[118] where the linewidth of $MoSe_2$ neutral exciton emission is reduced from a respectable 9 meV, when placed directly on a substrate of SiO_2 (Fig. 2.17a), to a near intrinsic 3 meV, when fully encapsulated with hBN on the same SiO_2 substrate (Fig. 2.17b). hBN also forms a protective layer, separating the active material (or materials) from ambient conditions, especially useful for materials that degrade rapidly when in contact with air or moisture.[122] The benefits of hBN encapsulation are explored further in chapter 4.

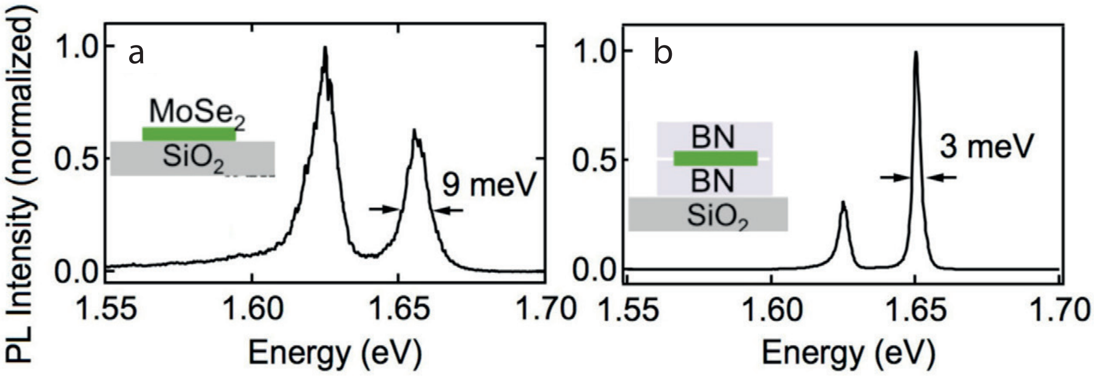

Figure 2.17: **a, b)** PL emission of a $MoSe_2$ monolayer when positioned a) directly on a SiO_2 substrate and b) fully encapsulated with surrounding hBN layers. The result is a much narrower X^0 linewidth due to reduced spatial and dielectric inhomogeneity. Image from Ref.[118]

2.6.2 Interlayer excitons

By combining two (or more) TMD monolayers together, the possibility exists that an exciton's constituent charge carriers are located in separate layers forming an interlayer exciton,[124,125,126,127,128,129,130] in contrast to an intralayer exciton where the charges reside entirely within the single monolayer, as shown schematically in figure 2.18a. For interlayer excitons to readily form, the band alignment between the two materials need to encourage the flow of CB electrons into one material layer, while holes are channelled into the other layer forming an atomically thin pn-junction.[123,124,126,130] This is type II band alignment,

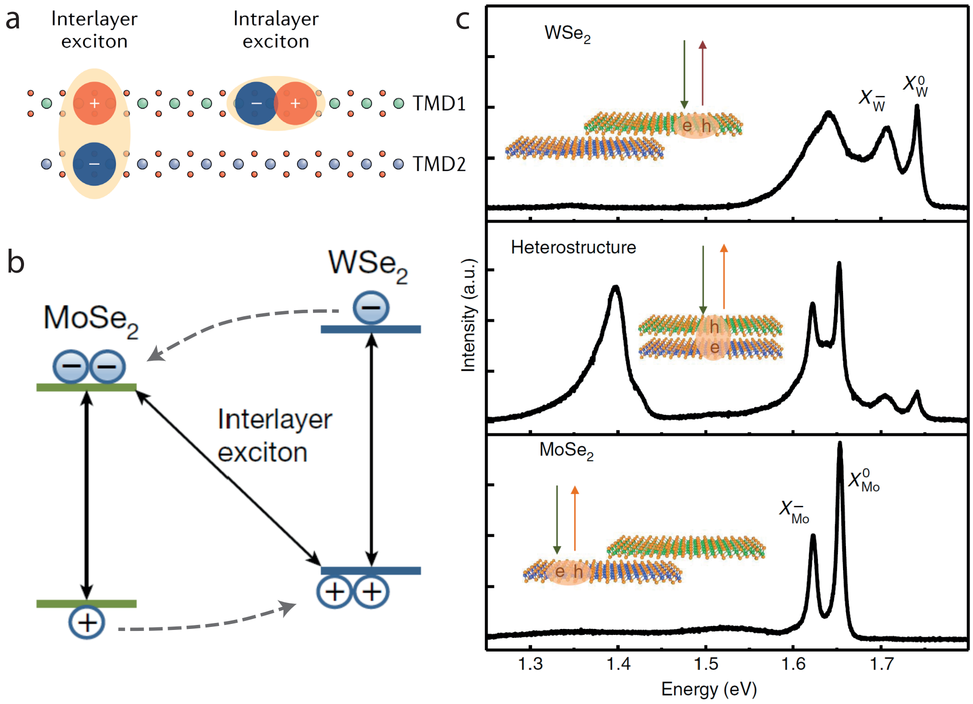

Figure 2.18: **a)** Schematic representation of an interlayer exciton, with either constituent carrier in a different TMD layer, and an intralayer exciton residing completely within a single TMD layer. Image from Ref.[114] **b)** Type II band alignment of a MoSe$_2$ / WSe$_2$ heterostructure with interlayer exciton highlighted. Due to the band offsets, electrons will flow from the WSe$_2$ CB into the MoSe$_2$ CB, while holes will flow the opposite way from the MoSe$_2$ VB to the WSe$_2$ VB. Image from Ref.[123] **c)** PL emission from the WSe$_2$ layer (top panel), heterostructure where the interlayer exciton peak visible at lower energy (middle panel), and the MoSe$_2$ monolayer (bottom panel). Image from Ref.[124]

as demonstrated by figure 2.18b using a MoSe$_2$ / WSe$_2$ heterojunction as an example. The PL emission from such a heterostructure is shown in figure 2.18c, where a new low energy peak observed only within the heterostructure region shows the existence of the interlayer exciton. the higher energy peaks are due to intralayer excitons and can also be seen in the corresponding monolayer regions.[124,130]

Previously much research has been carried out with separated charges in electrically biased single[131] and coupled double quantum wells,[132,133] and continues to be an active area of research.[134,135,136,137] The spatial separation of the charge carriers distinguishes the interlayer excitons (IX), from the intralayer (or direct) excitons (DX). The consequent of such is the reduced overlap of carrier wave-function alters the opto-electronic properties of the IX. The physical separation of the electron hole pair leads to a large permanent electric dipole moment,[129] while the reduced wave-function overlap results in extremely long lifetimes (∼ ns).[124,138] This combination means that the IX has a much larger interaction strength with other excitons than the intralayer exciton does, and has been touted as a method of exploring enticing many body phenomena such as Bose-Einstein condensation and superfluidity of excitons.[131,139,140]

The process of hybridising interlayer excitons with intralayer excitons with particular attention to the resulting optical properties is discussed further in chapter 5.

2.6.3 Moiré patterns and twist-angle dependence of heterostructure properties

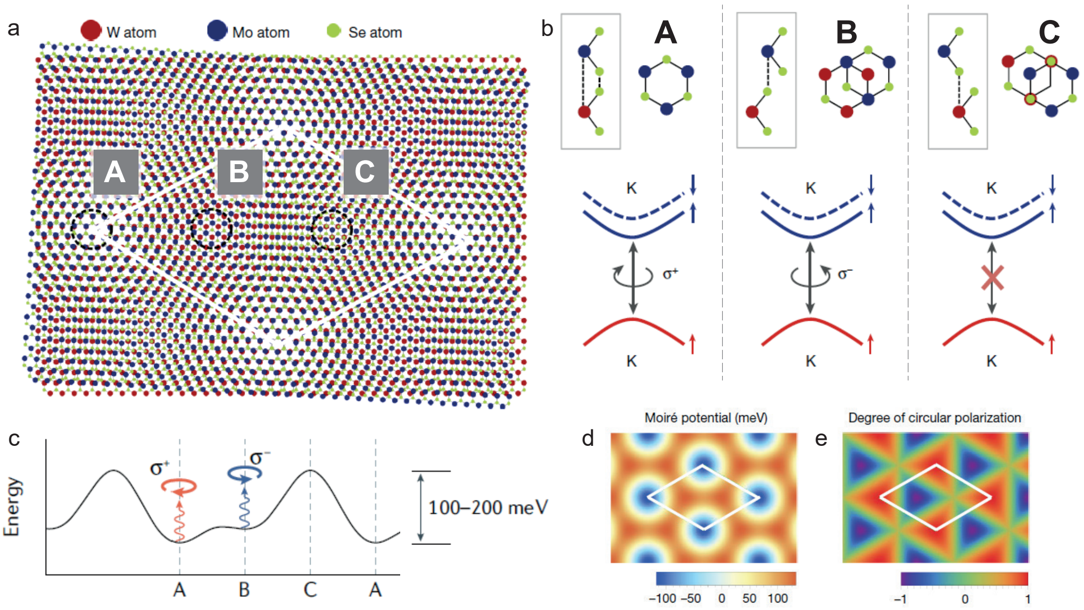

Figure 2.19: **a)** Graphical recreation of two monolayers with relative twist angle and the resultant moiré pattern. The periodically repeating moiré supercell is highlighted in white, with several points of high symmetry labelled here A, B and C. **b)** The moiré pattern causes different stacking orders within the heterostructure, which results in different chiral optical coupling for the interlayer excitons. Points A and B provide oppositely circular polarised IX emission, while point C results in a dipole forbidden transition for out of plane emission. **c)** The periodic potential resulting from the moiré superlattice, with points A, B, and C highlighted. Image from Ref.[114] using data from Ref.[141] **d)** 2D spatial colourmap of the same periodic moiré potential. **e)** 2D colourmap of the spatially resolved degree of circular polarisation. Red represents σ^+ emission, while blue is σ^-. All other images from Ref.[123]

Since a heterostructure is formed of two overlapping hexagonal lattices patterns, if there is a small lattice mismatch or twist angle between the two layers, then a superpattern is formed simply from the geometry of the overlapping lattices known as moiré patterns.[113,114,123,142,143,144] Three points of high symmetry appear within the superlattice pattern, denoted A, B, C in figure 2.19. The changing stacking order between the three points results in three different couplings between the interlayer excitons and chiral photons (Fig. 2.19b). For example, points A and B result in photon emission of opposite helicities when an interlayer exciton recombines, while point C results in a dipole forbidden transition for out of plane IX emission, with elliptically polarised emission in between the high symmetry points.[114,123,141]

As the stacking order gradually changes between the three high symmetry points, the interlayer spatial separation also changes, causing a varying potential energy landscape based of the moiré pattern.[114,123,141] Since the pattern has repeating periodicity, the potential is also periodic leading to the creation of a moiré Brillouin zone (Fig. 2.20c).[113]

Figure 2.20a shows how the periodicity of the super-lattice is highly dependent on the relative twist angle of the two independent layers.[113] In a similar way, the lattice mismatch between two crystalline structures also leads to varying moiré supercell sizes. In heterobilayers of closely matched lattice constants, the moiré period can exceed 100 nm in real space. In reciprocal space, this leads to the IX exciton dispersion relation being modulated by a very compressed moiré potential.[114] The resulting PL emission is extremely narrow[146,147] due to interlayer excitons trapped in very localized moiré potential wells.[114,141] Likewise, the opposite is true, for high relative twist angles or lattice mismatches, the moiré periodicity in real space becomes smaller, leading to a broadening of the exciton dispersion modulation in k-space.[114] In these systems, such as $MoSe_2$ / WS_2 (Fig. 2.20b), additional absorption features are observed owing to a folding of excitonic bands as the moiré Brillouin zone and standard TMD monolayer Brillouin zones are reconciled.[113,142] It is suggested that the band folding brings additional excitonic modes that would normally reside outside of the light cone, and are therefore dark, in structures without in-plane periodicity.[113,114] In heterobilayers with nearly resonant conduction band edges where the interlayer and intralayer excitons are nearly degenerate, the band folding leads to a hybridisation between the two excitonic species. Figure 2.20d shows the twist angle dependence of these extra absorption resonances in $MoSe_2/WS_2$ as calculated and measured by *Alexeev, E.M., et. al.*[113], while *Ruiz-Tijerina, D.A., et. al.,*[143] calculates similar dependencies on a range of TMD based heterobilayers. For a hybridised specie of intra-inter-layer exciton, the large oscillator strength of the intralayer exciton and permanent dipole moment of the interlayer

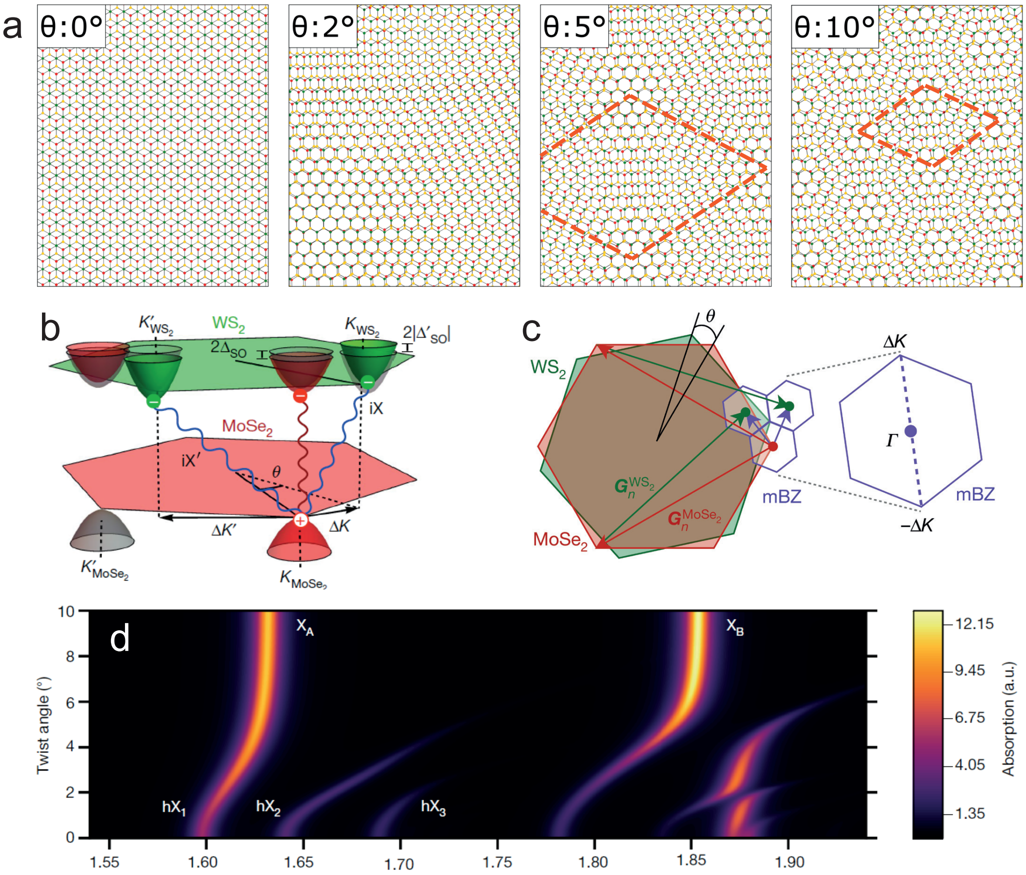

Figure 2.20: **a)** Twist angle dependence of the moiré pattern produced by two identical overlapping lattices. The moiré supercell is highlighted in red. At small twist angles the moiré unit cell is large, and shrinks as the twist angle is increased. Image from Ref.[145] **b)** Schematic of the valley structure of a twisted $MoSe_2$ / WS_2 heterostructure. $MoSe_2$ valleys are shown in red, while the WS_2 CB valleys are in green. **c)** The result of the moiré potential is reciprocal space is the creation of a repeating moiré Brillouin zone with $\pm\Delta K$ the k-space offset between the WS_2 CB and $MoSe_2$ VB. **d)** Calculated excitonic resonances as a function of increasing twist angle for a $MoSe_2$ / WS_2 HS. At small twist angles, a hybridisation occurs between the $MoSe_2$ DX and IX, as a result of moiré effects. Images from Ref.[113]

exciton are merged, forming a highly interacting optically bright particle with the potential to explore fascinating non-linear phenomena in both excitonic and polaritonic regimes.[148]

The possible implications of twist angle on opto-electronic properties of heterostructures are investigated in chapters 4 and 5, along with an attempt to couple the moiré hybridised interlayer excitons with cavity photons.

2.7 Optical microcavities

An optical microcavity is formed by confining light between two highly reflective mirrors separated by a length on the scale of the wavelength of confined light. The confined light takes the form of a standing wave with stationary nodes at the mirror/cavity interface, while the length of the cavity dictates the wavelength of the standing waves. In this work, the mirror is formed of a distributed Bragg reflector (DBR), which is formed of alternating high refractive index n_H and low refractive index n_L dielectric layers. At each interface between layers, the reflectivity is defined as:[149]

$$r = \frac{n_L - n_H}{n_L + n_H} \tag{2.7}$$

The reflectivity of a mirror can be enhanced for a given wavelength of light by choosing the thickness of each layer such that any two reflections of layer i, and $i+1$ will constructively interfere. Over an entire periodic structure, the DBR forms a photonic band gap which prevents the transmission of waves across a small range about a desired wavelength leading to near unity reflectivity. In order to create such a condition, the phase shift at each reflective interface must be $\Delta\phi_r = \pi$. The phase shift can be calculated as:[149,150]

$$\Delta\phi_r = \frac{4\pi}{\lambda} d_{H,L} n_{H,L} \tag{2.8}$$

where λ is the desired working wavelength of the cavity and $d_{H,L}$ is the thickness of the high (H), and low (L), refractive index layers respectively. It is therefore found that:

$$d_{H,L} = \frac{\lambda}{4n_{H,L}} \tag{2.9}$$

is the required thickness of the high and low refractive index layers for a desired wavelength. With increasing number, N, pairs of high and low index layers leads to a total reflectivity given by:[149]

$$R = \left(\frac{1 - \frac{n_1}{n_2}\left(\frac{n_L}{n_H}\right)^{2N}}{1 + \frac{n_1}{n_2}\left(\frac{n_L}{n_H}\right)^{2N}} \right)^2 \tag{2.10}$$

where n_1 and n_2 are the reflective indices of the dielectric environment at either side of the DBR. Nominally, the cavity will be placed within a vacuum, which the DBR is grown onto a plinth of fused silica, which gives a value of $n_1 = 1$ and $n_2 = 1.5$.

The difference between the two refractive indices of the DBR layers establishes the spec-

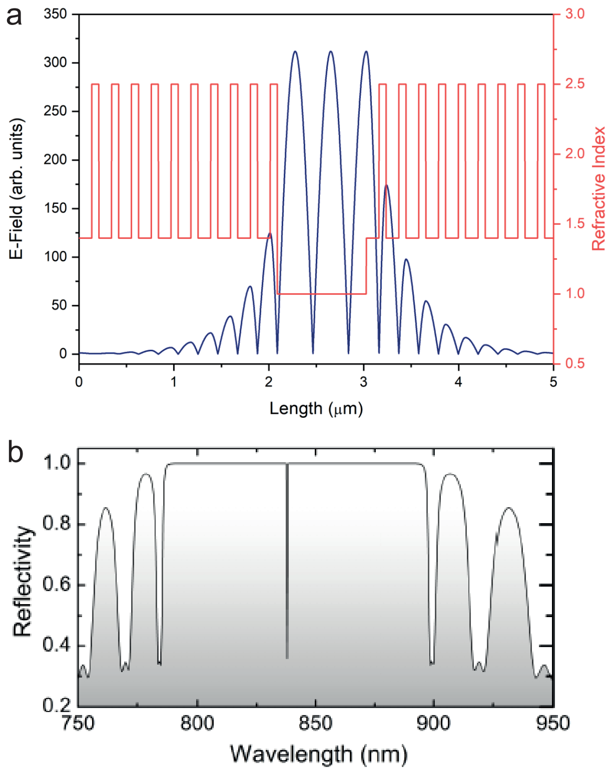

Figure 2.21: **a)** Basic 1D simulation using *CAMFR*[151] based on the transfer matrix method (TMM) to calculate the electric field profile of a microcavity for a given DBR design. **b)** The reflectivity spectrum of a given cavity, with near unity reflectivity across the DBR stopband and cavity mode visible. Image adapted from Ref.[152]

tral width of the photonic band gap, often referred to as the stopband, with a dependence such that:[149]

$$\Delta_{sb} = \frac{\lambda \Delta_n}{\pi n_{eff}} \tag{2.11}$$

where $\Delta n = n_H - n_L$ is the DBR refractive index contrast, while $n_{eff} = \left(\frac{1}{n_H} + \frac{1}{n_L}\right)^{-1}$ is the effective refractive index across the DBR depth. It is therefore quite simple to design an optical microcavity for a specific central wavelength, stopband, and reflectivity by choosing the DBR layer materials, number of layers, and layer thicknesses carefully. Figure 2.21b shows an example reflectivity spectrum of a DBR cavity with high reflective stopband clearly visible. It is common to design a cavity around the intended use, for example with TMD monolayers, the central wavelength will need to be close to excitonic resonance. Furthermore, the direction of light can be influenced by having one DBR have a fewer number of layers than the other side, creating an unbalanced reflectivity such that the majority of the PL emission can be guided towards an objective lens and optical collection path.

Due to ease of production, as well as good optical transmission properties, SiO_2 is typically used as the low index dielectric material with $n_L \approx 1.4$, while Ta_2O_5 or Nb_2O_5 are used as the high index material with $n_H \approx 2.3$ and ≈ 2.5, respectively. For a set of materials, the electric profile of the optical microcavity can easily be tested using the transfer matrix method.[153] Figure 2.21a shows a rudimentary example of such a cavity simulation. The simulation shows that the standing wave profile of the electric field has a node or antinode at each dielectric interface. For the DBR that terminates into the cavity with a high index layer (left of figure), the electric field strength is minimal at this interface. While there is a maximum electric field strength at the interface with the opposite DBR, which terminates with a low refractive index layer. The cavity is designed such that a TMD monolayer can be placed directly on the DBR since the terminating layer is of low refractive index, corresponding to an electric field maxima, which will maximise the light-matter coupling.

The discussion so far is applicable to planar microcavities, which provide a useful basis in which to estimate the behaviour of a microcavity. However, the majority of the experiments in this work are performed with a hemispherical top DBR, which has the effect of focussing the electric strength profile of the cavity photonic modes in all three spatial dimensions to form a zero-dimensional cavity.[154,155] The result it that the cavity mode volume is much smaller, which enhances the light-matter interactions. The concave mirrors are formed by growing the DBRs onto fused silica substrates, with an array hemispherical indents already milled into it via focussed ion beam (FIB).[154] The resultant DBR is shown in figure 2.22a,b as imaged by scanning electron microscope and bright-field optical microscope imaging, while the shape profile is also provided (Figure 2.22c-e), displaying sub-nanometre surface roughness of the concave feature leading to a high cavity quality factor.[154,155]

The hemispherical DBR slightly modifies the electrical field profile within the cavity and instead becomes describable by a series of discrete Gaussian longitudinal modes, each accompanied by a set of higher order transverse modes. These modes are required to satisfy a cavity round trip phase shift $\Delta\phi(k, L_{opt})$ equal to 2π, or integer multiple of:[149,152,156]

$$\Delta\phi(k, L_{opt}) = 2kL_{opt} + \Delta\phi_{DBR}(k) = 2\alpha\pi \tag{2.12}$$

where k is the wave-number, L_{opt} is the optical length of the cavity, ϕ_{DBR} is the sum of the reflection phase shifts of the two DBR mirrors, which remains constant for a given set

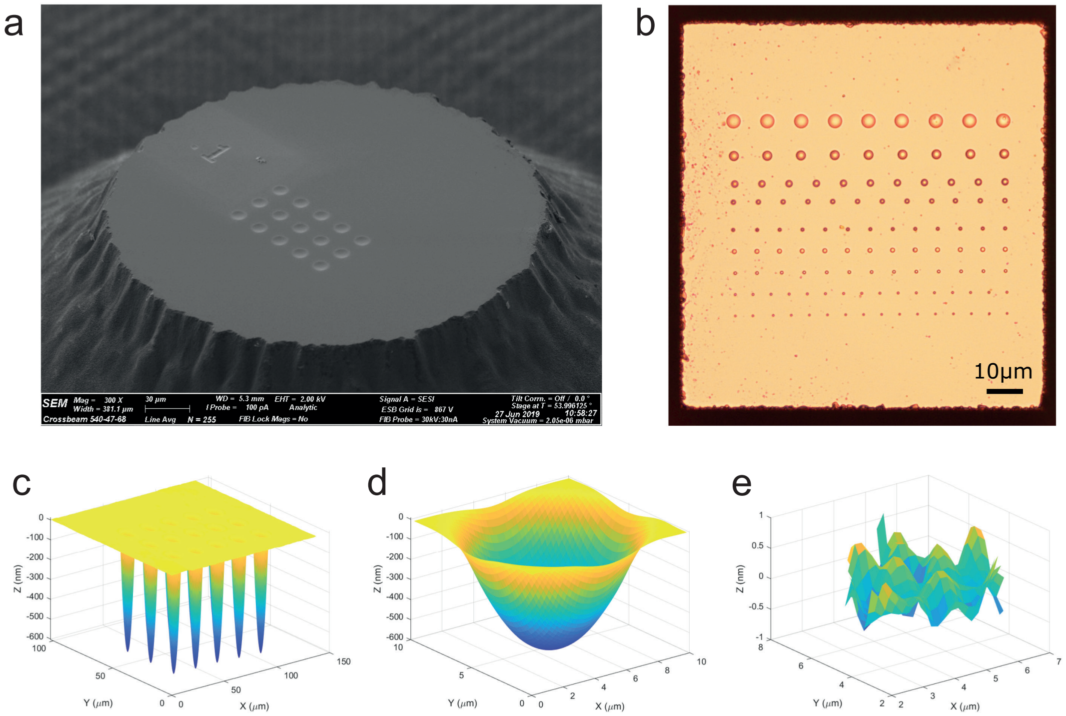

Figure 2.22: **a)** Scanning electron microscope image of an array of identical concave features with radius of curvature $\sim 20\ \mu$m. The image if taken directly after milling, before DBR growth. The plinth design lets the two mirrors be positioned very close together, even without *perfect* parallel alignment. **b)** Optical microscope image of a DBR. A range of differently sized concave fixtures are provided, with largest radius of $\sim 20\ \mu$m. Fabrication of DBR is performed by collaborators at *The University of Oxford*. **c)** Profilometry data for the array of features shown in a). Each has nearly identical shape and depth. **d)** Shape profile of a single concave feature. **e)** Residual roughness after an ideal polynomial function is removed from d), indicating the sub-nm roughness and high uniformity acheived through focussed ion beam milling. Images from *Oxford HighQ*.

of DBRs, and α is an integer. A general description of the eigenfrequencies of the confined electric field within the cavity is given by:[149,152,156]

$$\nu_{qmn} = \frac{c}{2n_{cav}L_{opt}}\left[q + \frac{(m+n+1)}{\pi}\cos^{-1}\left(1 - \frac{L_{cav}}{RoC}\right)\right] \tag{2.13}$$

where c is the speed of light, n_{cav} is the refractive index within the cavity (which in an open cavity is 1), q is the longitudinal and m,n are the transverse Gaussian mode indices, while RoC is the radius of curvature of the hemispherical top mirror, and L_{cav} is the cavity

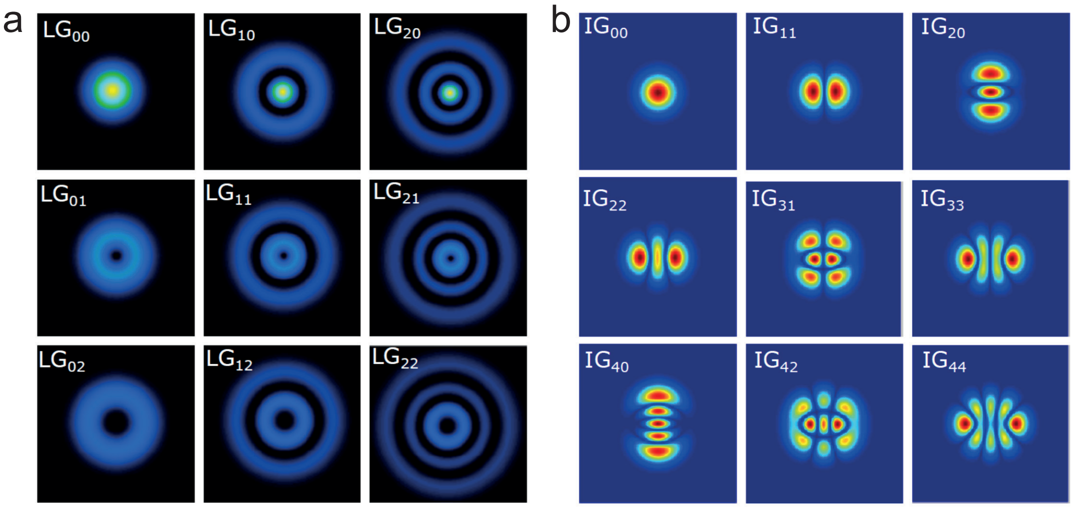

Figure 2.23: **a)** The first nine Laguerre-Gaussian cylindrical mode profiles LG_{lp}.[157,158,159] **b)** Examples of Ince-Gaussian elliptical mode profiles IG_{lp} that are likely to be present in the cavity thanks to imperfect alignment or slight ellipticity of the concave DBR.[157,159]

length, which is distinct from the optical length because the cavity mode penetrates into the DBR mirrors before being fully reflected. L_{opt} is therefore a combination of L_{cav} and the combined cavity penetration depths ($> 1\mu$m). While it is impossible to directly measure the optical cavity length, it can be determined by finding the frequency difference between two adjacent longitudinal cavity modes ($\Delta q = 1, m = n = 0$) and rearranging the above equation 2.13, to find:

$$L_{opt} = \frac{c}{2n_{cav}\Delta\nu} \tag{2.14}$$

The largest difference here, compared to a planar microcavity, is that the eigenfrequencies are dependent on the specific curvature of the top mirror, since the boundary condition forces the phase-front of the propagating beam to match the RoC of a given mirror. The Gaussian modes are supported within the cavity if the condition $L_{cav} < RoC$ is satisfied, which focusses the Gaussian modes to a minimum beam waist at the planar mirror surface. In this work, the RoC is always 20 μm, such that the beam waist at the planar mirror, or TMD sample will be $\sim 1\mu$m in diameter, providing a much better spatial resolution than the standard laser spot size ($\sim 2.4\mu$m).

Figure 2.23a shows the set of discrete photonic states allowed in a hemispherical cavity, corresponding to Laguerre-Gaussian mode profiles,[149,156,158,160] however, the cavity is

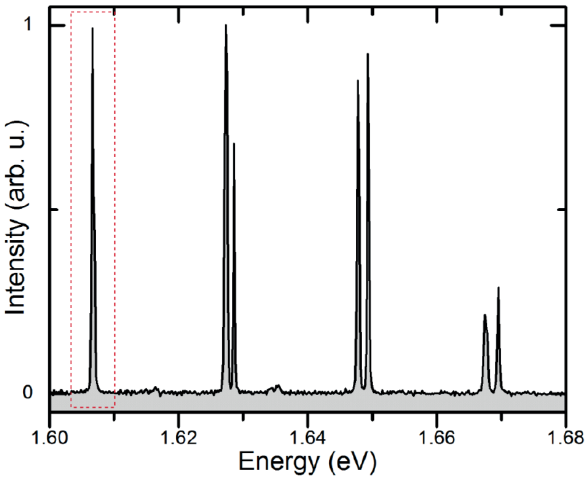

Figure 2.24: An example PL spectrum of a cavity embedded TMD, with cavity mode far from exciton resonance. The ground state longitudinal cavity mode is highlighted with higher order transverse modes also visible.

rarely completely symmetrical. The cavity instead supports a set of elliptical solutions corresponding to Ince-Gaussian mode profiles,[157,159] which are given in figure 2.23b as a comparison. This perturbation from perfect electrical field profile is mitigated since only the ground state longitudinal mode (LG_{00} or IG_{00}), with minimal differences between the cylindrical and elliptical solutions, is studied in this work. Furthermore, *Dufferwiel, S., et. al*[154] image a set of cylindrical modes using the same experimental setup as presented in this work, suggesting that a perfectly symmetrical cavity is indeed achievable. Figure 2.24 shows a PL spectrum of the cavity used in this work, with the ground state longitudinal mode highlighted. By slowly changing the cavity length, the allowed eigenfrequency is shifted towards resonance with a TMD exciton resonance. The enhanced light confinement found in optical microcavities provides the perfect environment to explore a rich field of phenomena observed only in the strong light-matter coupling regime.

2.7.1 Exciton-polaritons

In the previous sections, the unique physical properties of excitons in transition metal dichalcogenides has been explored, most notably displaying a very large oscillator strength, leading to a strong absorption of light.[12,36,161] In the ultimate case of light-matter interactions, TMD exciton resonances strongly couple with cavity photonic modes to form a polariton, graphically represented in figure 2.25.[162,163,164] Strong coupling occurs between

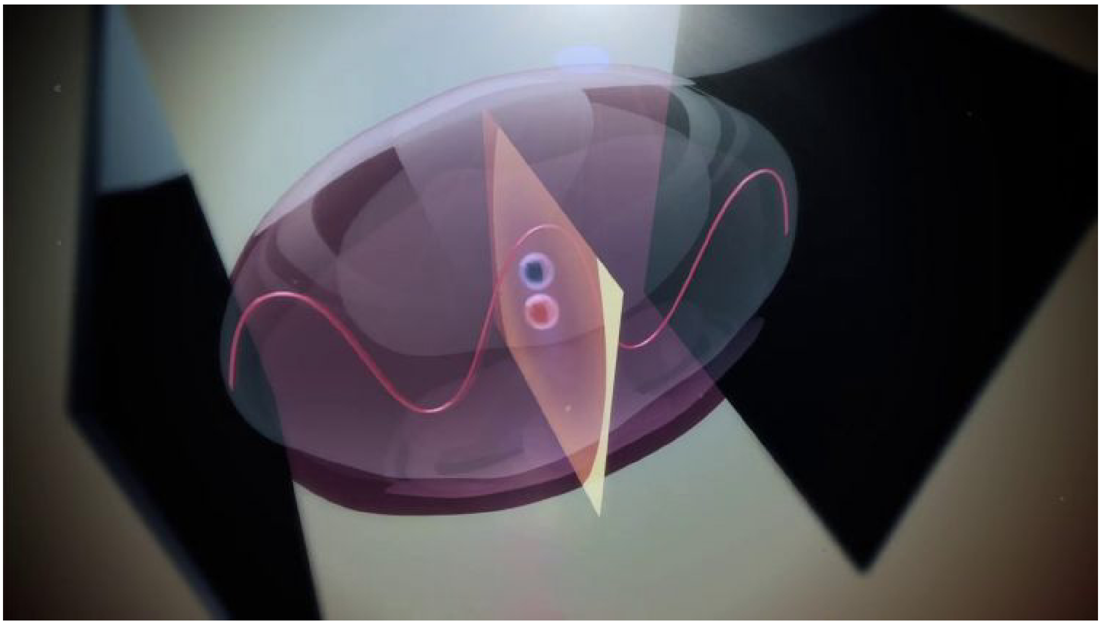

Figure 2.25: Graphical representation of strong light-matter coupling between a TMD exciton and cavity photon to form a new quasiparticle known as a polariton. Image credit to *The University of Sheffield*.

the excitonic and photonic resonance through a cyclical transfer of energy, corresponding to a repeated absorption and re-emission of a cavity photon by a TMD exciton. This energy transfer can be adequately described by a classical coupled oscillator model, as schematically shown in figure 2.26a.[152,155,161] In this case, the electric field of the cavity mode $\boldsymbol{E}$, and the dielectric polarisation of the TMD monolayer excitons $\boldsymbol{P}$ are represented by two oscillators, with uncoupled frequencies ω_c and ω_x respectively, with a coupling term V_R that determines the interaction strength. The system is therefore described by two equations of motion:[152,155,161]

$$\begin{aligned} \imath\frac{d\boldsymbol{E}}{dt} &= (\omega_c - \imath\gamma_c)\,\boldsymbol{E} + V_R\boldsymbol{P} \\ \imath\frac{d\boldsymbol{P}}{dt} &= (\omega_x - \imath\gamma_x)\,\boldsymbol{P} + V_R\boldsymbol{E} \end{aligned} \tag{2.15}$$

where $\gamma_{c,x}$ are the oscillator damping terms for the cavity and exciton, respectively. In physical terms, these are the linewidths of the cavity mode and excitonic absorption resonances. Figure 2.26b shows the system applied to a cavity embedded TMD exciton, where γ_c is shown as a photon escaping the cavity through less than unity reflectivity of

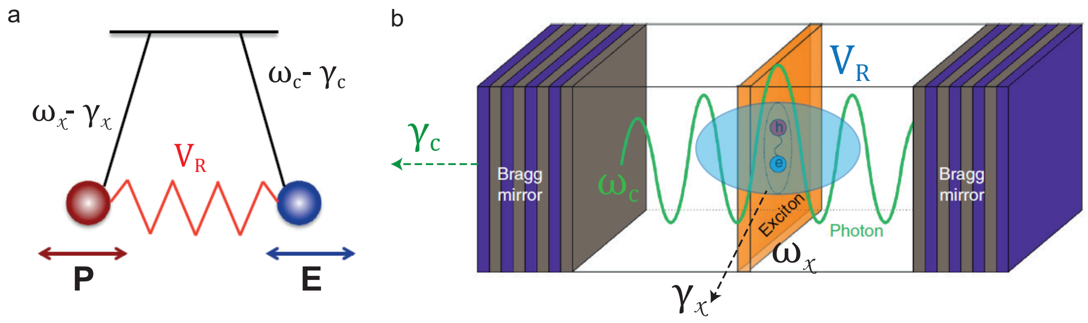

Figure 2.26: **a)** Coupled oscillator model describing the cyclical energy transfer within a polariton. The electric field of the photonic cavity mode $\boldsymbol{E}$ and dielectric polarisation of a TMD monolayer due to an exciton $\boldsymbol{P}$ with oscillation frequencies of ω_c, e and damping $\gamma_{c,x}$ respectively are coupled by an interaction potential V_R. **b)** Overall schematic of a polariton system described in physical terms with $\gamma_{c,x}$ describing photon tunnelling and non radiative exciton decay respectively. Images adapted from Ref.[161]

the mirrors, while γ_x describes a non radiative decay of an exciton. Both of which leads to a loss of energy in the polariton system. The two independent oscillators are characterised as possessing a harmonic time dependence such that $\boldsymbol{E}, \boldsymbol{P} \propto e^{-\imath\omega t}$, and solving eqs. 2.15 leads to:[152,161]

$$(\omega - \omega_c + \imath\gamma_c)\,(\omega - \omega_x + \imath\gamma_x) = V_R^2 \tag{2.16}$$

where the solution provides the two eigenfrequencies $\omega_\pm$ of the coupled oscillator model.[165,166,167] At the resonant frequency, $\omega_x = \omega_c = \omega_0$, the eigenfrequencies become:[152,161]

$$\omega_\pm = \omega_0 - \imath\frac{\gamma_c + \gamma_x}{2} \pm \sqrt{V_R^2 - \left(\frac{\gamma_c - \gamma_x}{2}\right)^2} \tag{2.17}$$

At this point, the fundamental definition of strong coupling is found. In the condition that $2V_R < |\gamma_c - \gamma_x|$ then the square root term becomes imaginary and the two oscillators are weakly coupled.[161] In this regime the cavity affects the local optical density of states as experienced by the exciton dipole, leading to a Purcell-like enhancement or suppression of the radiative decay rate.[152,168,169] While the condition that $2V_R > |\gamma_c - \gamma_x|$ leads to the strong coupling regime. The term in the square root is real, and an energy splitting appears between the two eigenfrequencies forming a characteristic anti-crossing about the resonance.[152,155,161,170] It is then possible to define the two resultant higher and lower energy eigenmodes, as the upper and lower polariton branches respectively. This anti-crossing is a signature of strong coupling regime, and signals the onset of polariton formation. The energy separation of the two polariton branches at resonance is given by the Rabi splitting:

$$\hbar\Omega_R = \sqrt{4V_R^2 - (\gamma_c - \gamma_x)} \tag{2.18}$$

where Ω_R is the Rabi frequency at which the energy is transferred. This energy splitting can be experimentally measured as a method of determining the strength of the coupling between exciton and cavity photon in a given polariton system. In some cases however, a broad linewidth, comparable to the energy splitting, may be present for the two polariton branches leaving the anti-crossing unresolvable, even if the system is defined (as above) to be in a strong coupling regime. The coupling strength V_R is influenced by the physical properties of the two separate systems, the microcavity quality factor and mode volume along with the exciton oscillator strength. For this reason, TMD based polaritons typically produce much larger Rabi splittings than those observed with III-V quantum wells due to the very large oscillator strengths of TMD excitons.[161,171] It should be noted that the upper polariton branch (UPB) is not usually observed in other systems such as perovskites and organics due to, comparatively, much faster non-radiative UPB relaxation times associated with smaller exciton binding energies.[171,172,173,174,175,176,177] The loss mechanisms for the cavity photons depend mostly on the reflectivity of the mirrors forming the cavity, but also the stability of the system, while excitonic losses are entirely caused by non-radiative decay mechanisms, such as lattice disorder and phonon induced scattering.[152,155,161,170]

Strong coupling in TMD based devices has been observed with a variety of materials and cavity geometries in recent years,[43,84,170,178,179,180] while this work will consider the cases of a microcavity formed by planar DBR as a bottom mirror, combined with one of either a concave hemispherical DBR top mirror already described in this section, or a planar silver mirror. Both are demonstrated in chapter 4, while the 0D cavity is used throughout.

Chapter 3

Experimental Methods

In the previous chapter, we have examined the physical processes that underpin the investigations into TMD based devices that will be reported later on. This chapter focusses on how these processes are observed within the laboratory. Starting from the exfoliation of monolayer TMDs and how these are identified, to fabrication of more complex structures. Moving onto how the various experiments are actually performed, considering the optical apparatus and devices required to extract the observational information from the materials. The analytical methods used to translate the raw observational information into easy to understand graphics with obvious physical interpretations, are discussed in subsequent relevant chapters.

3.1 Fabrication methods

3.1.1 Micro-mechanical exfoliation of TMD monolayers

Discovery of the ability to isolate stable monolayers of graphene,[1,181] using a technique termed *micromechanical exfoliation* (informally as the 'scotch tape method'), away from the bulk graphite was awarded the 2010 Nobel prize for opening up a new avenue in which to explore similarly layered materials.

As discussed in chapter 2, bulk transition metal dichalcogenides have a similar layered crystalline structure to graphene, whereby the intralayer structure is held together through very strong covalent bonds, whereas the van der Waals force keeping the layers together are, relatively, very weak, therefore allowing isolation of monolayers through micromechanical exfoliation. This scotch tape method uses an adhesive tape, of strong enough adhesion to overcome the van der Waals interlayer forces, to lift up surface layers from the bulk

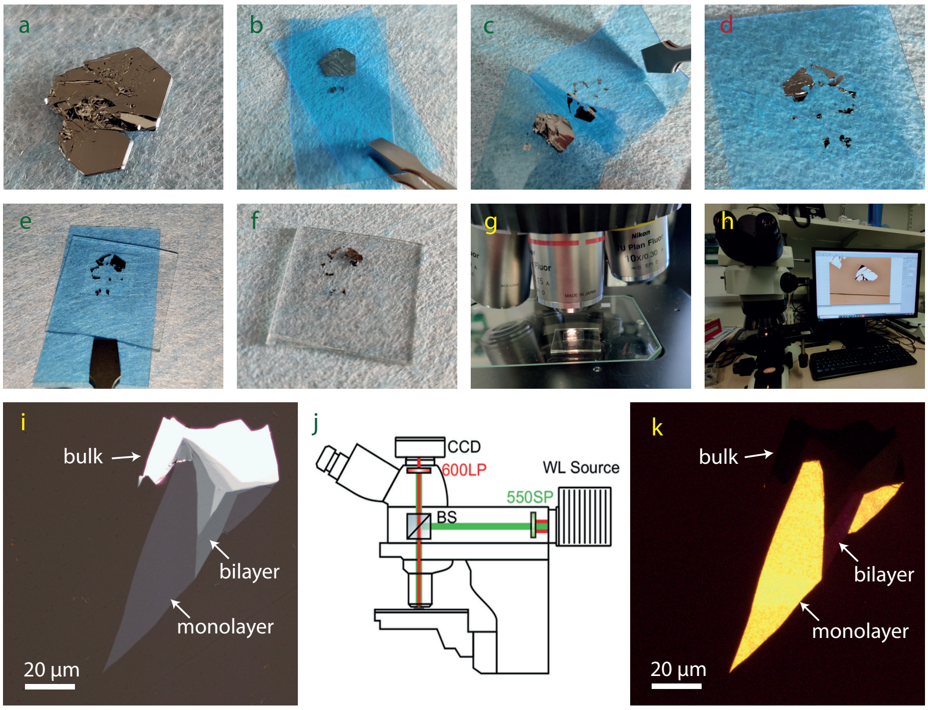

Figure 3.1: **a-f)** Micro-mechanical exfoliation. a) Photograph of the bulk crystal as purchased from HQGraphene. b) A small amount of material, separated initially by tweezers from the bulk crystal is placed between two pieces of blue 'scotch' tape. c) Peeling the tape apart lifts a small portion of the material away from the bulk crystal. d) After multiple repetitions, the material is thinned down. e) The TMD is transferred to a target substrate of PDMS atop a glass slide. f) The sample is fully exfoliated onto PDMS and ready to be flake-searched. **g-k)** Flake search and monolayer identification. g, h) The PMDS/TMD sample is placed under a microscope objective lens which can be viewed using both an eye-piece and also on the computer. i) Optical image of a monolayer and bilayer TMD on the PDMS substrate. The monolayer, bilayer and bulk areas of the flake have been highlighted. j) Schematic of a modified optical microscope to allow photoluminescence detection. Image from Ref.[130]. k) PL Image from the modified optical microscope. The monolayers are easily visible up due to the increased quantum yield of monolayers compared to bilayers and thicker. (Scale bar visible in i and k is 20 μm).

crystal (Fig. 3.1a-c). The peeled tape is covered in material with thicknesses ranging down to the monolayer, which can then be pressed onto a target substrate and peeled away again, leaving both monolayers and thicker material on the desired substrate (Fig. 3.1d-f). For TMDs, the target substrate is usually a small square of polydimethylsiloxane (PDMS) polymer due to its favourable viscoelastic properties which encourages the production of large area monolayer flakes, typically of more than 10 μm x 10 μm. A target substrate of many different materials can be used with trade-offs on typical flake size and transferability (see Sec. 3.1.3).

Due to the TMD monolayers being only a few atoms thick, they are completely invisible to the naked eye. As such, searching for freshly exfoliated monolayers must be done with the aid of an optical microscope (see Sec. 3.2.1). The identification of flakes suitable for further study is achieved by methodically searching through the substrate (Fig. 3.1g-i). A monolayer can be instantly identified by a simple modification of the optical microscope using a 550 nm short pass filter in the excitation path, providing a light source above the TMD band gap, combined with a 600 nm long pass filter to block the excitation light, isolates the PL emission from the monolayer sample (Fig. 3.1j,k). This is an incredibly useful tool as the monolayers have a very low optical contrast when sitting atop a PDMS substrate. Bilayers and thicker material are much more visible in the bright field mode owing to a higher optical contrast of multiple layers when compared to a single layer. In the PL mode, the bulk material disappears completely. And while the bilayer is very faint due to the lower quantum yield of the indirect band-gap,[10] it can also be seen at higher exposure times or applying an analogue gain (Fig. 3.1i,k).[130]

Despite being the earliest method of isolating monolayers, micromechanical exfoliation remains the best way to obtain high quality monolayer samples.[182] Other methods, such as chemical vapour deposition (CVD) as detailed later in Sec. 3.1.4, while having progressed significantly,[170,183,184,185] remain behind the leading exfoliated flakes. Problems do persist though, most notably with the low yield of monolayer flakes for each round of exfoliation, which can be time consuming to prepare and clean the area before exfoliation to minimise external contamination, or even require expensive glove boxes with inert gases to provide the ultimate stable environment for fabrication. This is compounded by the need for particular substrates on which to exfoliate. Glass or metal, for example, leave the monolayers almost entirely transparent.[181] Typically, therefore, exfoliation is completed onto a thin layer (order of 100 nm) of dielectric film or polymer atop an opaque base substrate such as silicon, where the optical interference effects of the thin film provide an enhanced optical contrast of monolayer to the base substrate, dramatically improving the visibility of said monolayers.

The most reliable method of identifying layer thickness is atomic force microscopy (AFM). However AFM is usually a very slow process and measuring across an entire substrate is simply not viable. It is mostly used with materials that have a very low optical contrast and maybe also maintain an indirect band gap at the monolayer limit, therefore being insensitive to PL imaging. Layered materials such as III-VI post-transition metal chalcogenides (InSe, GaSe, etc), for example, require AFM imaging in order to determine layer number.[186]

For materials that are sensitive to PL such as monolayer TMDs, imaging with an adapted optical microscope, as shown in figure 3.1j, is by far the quickest method of identifying suitable flakes for further study. Combined with the sub-micron resolution of the optical microscope and CMOS camera, the level of detail visible within an image, beyond initial identification, an intuitive assessment of the sample can be made instantly. Cracks and folds that may not be visible or easily missed in the standard bright field viewing are instantly revealed in PL imaging. Furthermore, the intensity and uniformity of the emission across a monolayer flake can help deduce the domain sizes or optical quality. For example, figure 3.1k shows a typical PL image of a monolayer TMD sample. In this case there are two areas of monolayer visible, with the larger area on the left seeming to have a higher uniformity and intensity than the smaller are on the right. Beyond this, within the larger monolayer to the left, there is a central section (close to the intersection of monolayer, bilayer and substrate) with even higher uniformity and intensity, suggesting that this sub-area, or domain, possesses the highest optical quality of the flake. The quality and crystalline uniformity of domains within a monolayer is inherited directly from the initial growth of the bulk material, where exfoliation simply isolates individual layers from the bulk crystal. Enhancements in exfoliation techniques (and user skill levels) allow for larger monolayers, with fewer cracks and folds introduced through the mechanical nature of the technique, along with minimal introduction of external contaminants such as dust, but development of growth techniques is also imperative.

Recent advances in flake searching technology has started to avoid the need to manually search through large areas of exfoliated waste material for monolayers, by using a motorised xyz-stage below the microscope objective and developing a flake identification algorithm, the process of flake searching can be fully automated.[187] Ultimately however, the fundamental flaws of micromechanical exfoliation are unlikely to be overcome in the drive towards large scale production of monolayer flakes and devices. The lack of control over flake size and position, as well as the inherently low yield and scalability means that scotch tape method alone is not suitable for the production commercially viable TMD based devices.

3.1.2 Flake transfer via viscoelastic stamping

Micromechanical exfoliation produces high quality monolayer flakes, however it is impossible to control the size and position of the flakes being found. While you can exfoliate onto a variety of target substrates with various trade-offs in terms of average flake sizes, visibility for flake searches and transferability. I have already briefly discussed exfoliating onto PDMS

(Sec. 3.1.1) however measurements and studies of the monolayer TMD devices are usually carried out at liquid helium temperatures. Studying a material placed on top of a polymer at LT is not viable as high thermal expansion coefficients generally associated with polymers would induce large stresses in the monolayer sample and likely break it apart. Exfoliation directly onto a solid, opaque substrate with low thermal expansion coefficient, such as silicon (for flake search visibility reasons, a thin film of dielectric SiO_2 on top of the silicon is conventional) is a commonly used option when looking at an initial low temperature characterisation of monolayers due to the reduced number of fabrication steps involved. Even so, the same problems persist in terms of control over flake size and position (not necessarily an issue for initial characterisation of a material), as well as a tendency to result in smaller area monolayers when compared to exfoliation onto polymers. Again, not really an issue so long as the monolayer sample is larger that the laser spot size. However, for slightly more complex studies, it is usually suitable to have control over the size, shape and even surrounding material. It is possible to simply keep exfoliating and flake searching until an ideal sample monolayer is found for the required experiment.

It has been hinted at that, generally, PDMS is used as the initial target substrate for exfoliation, and for good reason. The viscoelasticity of PDMS means that the level of viscosity is directly dependent upon the swiftness of the stress applied.[188] For example, if a stress is applied quickly the viscosity of the material increases, and the level of adhesion increases as a direct consequence. The opposite is true also, that if a stress is applied very slowly, the PDMS 'relaxes' and the adhesion reduces. It can therefore be possible to control whether a PDMS stamp releases or retains any exfoliated flakes on it's surface by varying the amount of applied vertical tension. Consequently, it follows that by bringing a piece of PDMS with exfoliated material into contact with another substrate, and peeling off very slowly the exfoliated material will be transferred onto the target substrate.[109] As such the transfer process is detailed in figure 3.1. To introduce a level of control the PDMS and target substrate are placed onto two independent micromechanical xyz-stages and held in place using vacuum. This allows the chosen flake to be exactly aligned with the required position on the target substrate below. A rotation stage is introduced to further increase control over the relative angle between flake and substrate, a property that is becoming increasingly important in certain heterostructures[113,114,144,148,189] (Fig. 3.1c,d). A microscope with long working distance objective lenses is used to view the procedure (It therefore helps that the PDMS and glass slide are both transparent) and a hotplate can help encourage successful transfers by slightly melting the PDMS and further decreasing viscosity. In the setup pictured in figure 3.1d, the z-stage of the transfer arm (where the

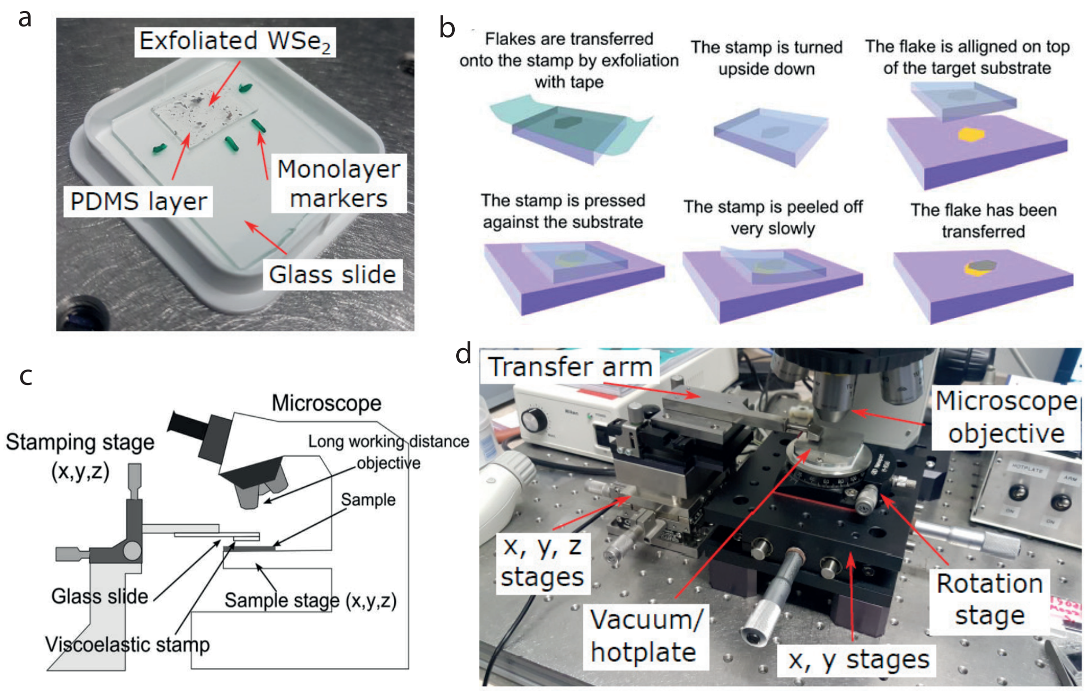

Figure 3.2: **a)** Exfoliated WSe$_2$ Exfoliated onto a PDMS stamp, on top of a glass slide, ready to be transferred. It can useful to add monolayer markers in order to help re-find the flake on the transfer setup. **b)** Graphic describing the step-by-step transfer process, from exfoliation to fully transferred. Image from Ref.[109] **c, d)** Schematic (c), from Ref.[109], and photograph (d) of the transfer setup. The glass slide is placed on the transfer arm, and controlled with micromechanical x and y linear stages as well as θ and ϕ tilt stages. For added control, the z stage has been replaced with a piezo controller. The target substrate is placed on the sample stage, which is controlled with x, y, z, and rotation stages. A hotplate is added to the sample stage to encourage transfer success rates. The transfer process is viewed using a long working distance microscope objective.

PDMS and chosen exfoliated flake initially resides) is controlled by a piezo stepper controller for ultimate vertical precision and control.

Figure 3.3 shows example flakes that have been exfoliated onto PDMS (Fig. 3.3a,b) and subsequently transferred onto a silicon substrate with 90 nm SiO$_2$ dielectric film (Fig. 3.3c,d). A separate WS$_2$ flake has been transferred onto a distributed Bragg reflector (DBR) (Fig. 3.3e,f). The difference in colour is not only due to the flakes being of two distinct materials (with slightly different band gap energies) but also the individual substrates having different properties.[130] The DBR, for example, enhances red colours due to having a reflectivity stop-band centred about (in this case) 600 nm, whereas the SiO$_2$/Si is opaque.

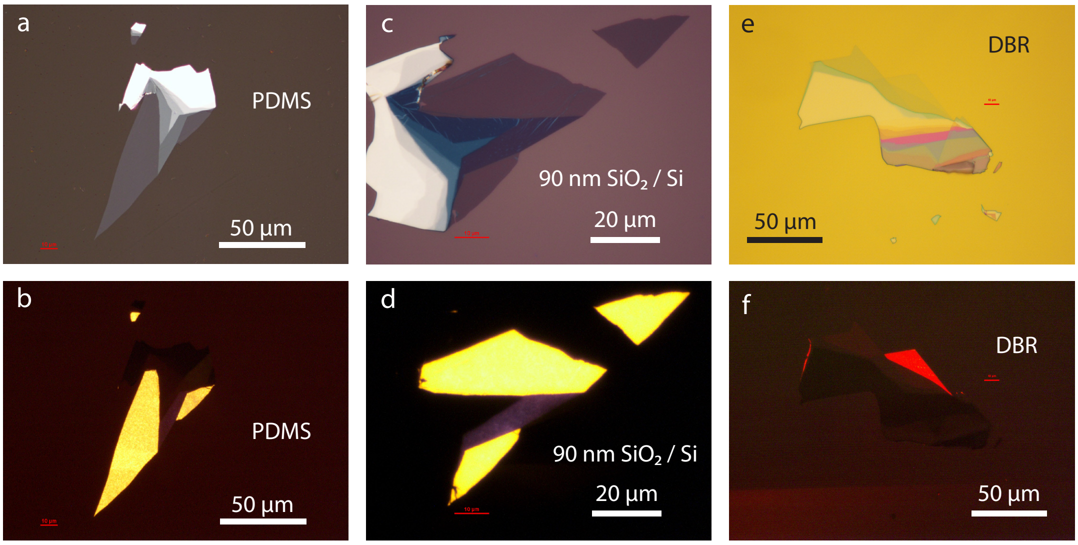

Figure 3.3: **a, b)** Example monolayer flake exfoliated onto PDMS imaged in a) normal optical microscope at 20x magnification, and b) PL imaging also at 20x magnification highlighting the monolayer. Scale bar in a) and b) is 50 μm. **c, d)** The flake is transferred onto a substrate of 90 nm SiO_2/Si ready for low temperature optical spectroscopy measurements. The flake is imaged at 50x magnification in c) normal microscope and d) PL imaging. Scale bar visible in c) and d) is 20 μm. **e, f)** A different flake (WS_2) has been transferred onto a DBR substrate ready for cavity measurements. The flake is imaged at 20x magnification in normal e) and PL f) imaging modes. Scale bar visible in e) and f) is 50 μm.

Another property that is highlighted is the differences in optical contrast and visibility of the monolayers in normal bight-field imaging (Fig. 3.3a,c,e). This shows why exfoliation is never completed directly onto a DBR substrate, as flake search would be near impossible. Furthermore, DBRs possess a lower adhesion than both PDMS and silicon meaning a lower yield with smaller average sizes (transfer success rates onto DBRs are generally lower than onto silicon because of this) and are also vastly more expensive per substrate further highlighting the benefit of using PDMS as an intermediary step when fabricating monolayers.

3.1.3 Fabrication of van der Waals heterostructures

Exfoliating TMD monolayers onto PDMS polymer stamps is a very easy way to regularly obtain relatively large area (> 10 μm x 10 μm) flakes that can be transferred to a target substrate for further study. However, when the fabrication of more complex structures is required by combining multiple monolayers together in TMD based *van der Waals het-*

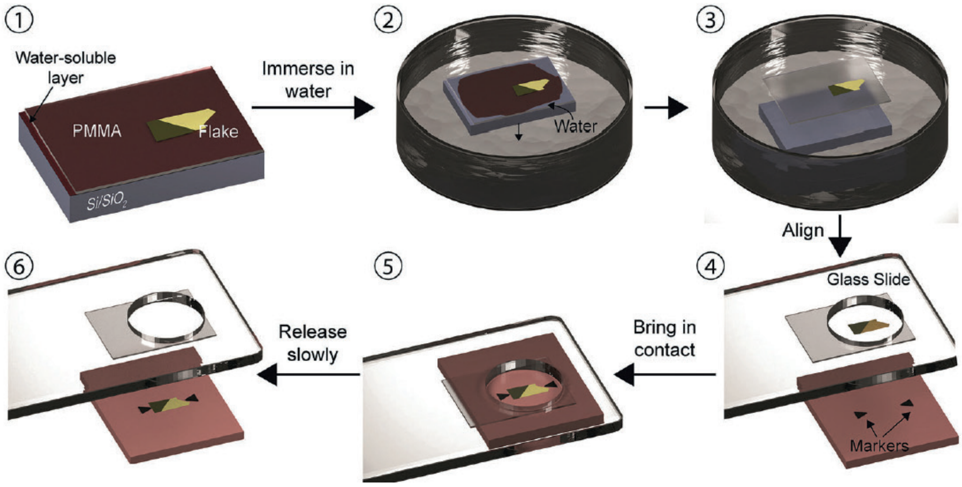

Figure 3.4: A step by step graphical representation of a wet transfer method using PMMA. Image from Ref.[192].

erostructures,[110,111,190,191] PDMS is no longer ideal. In this case the strong level of adhesion (greater than the interlayer coupling van der Waals forces) that makes PDMS so useful for exfoliation and individual monolayer transfers also makes it difficult to deposit a flake onto another flake. The target bottom monolayer is more likely to be picked up off the target substrate than have the transfer monolayer dropped on top.

For building a heterobilayer (two individual monolayers fabricated as a two layer device) it is common to use a hydrophobic polymer layer such as Poly(methyl methacrylate) (PMMA) with sacrificial water soluble layer of polymethylglutarimide (PMGI) via a wet transfer method as detailed in figure 3.4. Here, a Si/SiO$_2$ wafer substrate is spin coasted with PMGI and PMMA to be subsequently exfoliated onto with TMD monolayers. After flake search has been completed and a suitable monolayer found, the PMMA and monolayer flake is separated from the Si/SiO$_2$ by dissolving the PMGI layer in de-ionized (DI) water. The hydrophobic PMMA floats on the surface of the water to be lifted using a specialised glass or metallic slide with an aperture over which the membrane and monolayer rests. The hole causes the membrane to be stretched as it dries making the transfer process easier. The slide is then upturned and mounted on the transfer microscope, with the monolayer positioned directly above the unfinished heterostructure (or indeed, a blank substrate of choosing) and lowered slowly until contact is made. The target substrate is then heated to $\sim 65°C$ in order to soften the PMMA membrane and promote adhesion to the target substrate or flake, and very slowly lifted away completing the transfer, and or heterostructure.[119,185,192]

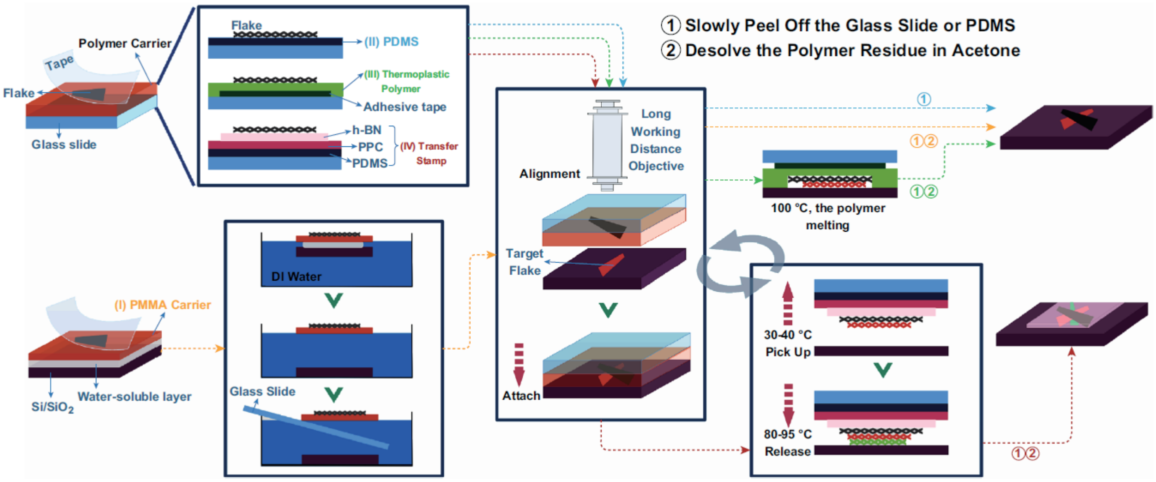

Figure 3.5: A comprehensive guide to fabrication of heterostructures using various methods. Each coloured dashed line represents a different fabrication style, with each step of the fabrication method shown within the outlined boxes, starting from exfoliation on the left, to the final heterostructure on the right. Image from Ref.[185].

There are, of course, more than just one method of heterostructure construction. A comprehensive guide to various heterostructure fabrication methods is shown in figure 3.5. In a 'bottom up' method, the lowest material of the final heterostructure is exfoliated or transferred onto the target substrate, and the next layers are deposited, one by one, on top. For a 'top down' method, the uppermost layer is exfoliated first, and then using that top layer, the next layer is picked up from its exfoliation substrate, and so on, until the heterostructure is completed and deposited onto a target substrate. PMMA wet transfer method detailed in figure. 3.4 is an example of the bottom up fabrication.

Top down fabrication is generally used when more than two layers are being stacked into a complex heterostructure. Here, a layer of polycarbonate (PC) or polypropylene carbonate (PPC) is coated or gently stretched onto a PDMS stamp, upon which a thin hexagonal boron nitride (hBN) flake is exfoliated. Using the hBN/PPC(PC)/PDMS stamp, it is possible to pick up a TMD monolayer from a hard inert surface, such as silicon wafers or glass, due to the stronger adhesion of PPC(PC). The van der Waals forces between the hBN and monolayer hold the two materials together, but the adhesion of PPC(PC) means that the vdW stack is lifted as opposed to being deposited. This process is then repeated until the desired heterostructure is completed, at which point the entire stack can be deposited onto the final layer of hBN and final target substrate. To make sure the heterostructure is deposited, the PPC(PC) is heated to high temperatures causing the

PPC(PC) to separate from the PDMS and glass slide. The unwanted PPC(PC) membrane is then washed away with a combination of chloroform and isopropyl alcohol (IPA). Thanks to the hBN top layer, the heterostructure is protected from the chemicals.[120,185,192,193] The main advantage of the top down method is the cleanliness of the interfaces between each layer since the only contact with other materials is with the hard inert surface upon which it is exfoliated onto, and the flake which collects it into the heterostructure. Other fabrication methods involve sticky polymers such as PDMS and/or PMMA which has been shown to leave contaminants such as hydrocarbons and other chemical adsorbates on the surface of the monolayers which drastically reduce the electrical coupling between the two layers.[190,194] This is somewhat mitigated in any interface by a tendency for the contaminants to group into isolated bubbles between the layers,[190] leaving much of the interface atomically clean.[195] This is why the use of hBN encapsulation is so common when studying even single monolayers. Thanks to its layered structure, hBN interface layers provide an atomically flat surface, far smoother than typical dielectric or metallic surfaces, and therefore acts as an ideal substrate beneath the active monolayer.[119] Indeed, it has been shown that encapsulation with hBN provides a uniform dielectric screening of the Coulomb interaction, reducing spatial inhomogeneity in the exciton resonance, and hence lowering the emission linewidth.[118,196] Moreover, the hBN layer isolates the TMD flake from potential adverse effects originating from the underlying substrate, for example trapped charges in SiO_2 can introduce unwanted doping effects.[119] Furthermore, encapsulation of the flake with hBN layers both above and below provides excellent protection against damaging environmental effects, or chemical washes required to remove residual polymers, which could otherwise lead to degradation of the monolayers and introduce associated losses in PL intensity and inhomogeneous line broadening effects.[66] While some of the adverse affects of PMMA or PDMS polymer contamination can be mitigated through hBN encapsulation when using the bottom up fabrication method, creating heterostructures using PPC(PC) top down fabrication completely avoids any potential contaminants at the layer interfaces, ultimately providing the best interlayer coupling and highest quality devices.[120,185,192,193]

3.1.4 Chemical vapour deposition

Chemical vapour deposition (CVD) is the leading alternative fabrication method for monolayer TMDs, which looks to remedy some of the shortcomings associated with micromechanical exfoliation as discussed in the previous section.[197] Originally developed during a drive for thin film semiconductors after World War II,[198,199,200,201,202] the CVD growth method has seen a recent resurgence due to the growing interest in scalable semiconducting

TMD monolayers.[170,197,203,204] The growth method has been evolved and refined since its inception, such that large scale TMD monolayers grown via CVD synthesis is now commonplace.[205,206,207,208]

In general the process involves a heated substrate on which thin films are formed via chemical reactions of catalytic salt sources and volatile gas-phase precursors on the substrate surface under very low pressures.[197,203,204,209] Figure 3.6a shows a graphical representation of such process. One of the major benefits of CVD growth over other monolayer synthesis techniques such as molecular beam epitaxy,[210] and metal organic vapour phase epitaxy,[211] other than the cost and relative simplicity, is that a process based on a chemical reaction is inherently controllable.[204] Meaning that the purity of the finished material will be simply dependent on the purity of the input materials (assuming no unwanted products from the reaction, which can normally be mitigated by choosing different reactants) and that the reaction rates can be controlled by altering the environment. The fine tuning of each element within the process results in a manipulation of the deposited material's properties.[204] For example, altering the temperature of the furnace, the pressure and flow rate of the gas (or gases) along with the amount and granularity of (in this case) Se and WO_3 powders all have obvious effects upon the chemical process and speed. Beyond these initial variables however, there are some less apparent, but still controllable, variables that can produce a remarkable difference in outcome. *Zhang, Y., et. al.*[206] found that, while maintaining all other variables as constant, having a small distance between source and substrate led to consistently obtaining few-layer WS_2 flakes with large domain sizes, whilst a larger source substrate distance would produce monolayer flakes with small domain sizes. It was also found that introducing H_2 as a carrier gas along with Ar, the previously saw-tooth edged WS_2 domain shapes become sharp-edged triangles, as is demonstrated in figure 3.6b.

Ultimately, through accurate manipulation of the growth parameters, the production of large area TMD monolayers can be batch produced in an inherently scalable manner.[205,206,207,208] Figure 3.6b shows an example of CVD grown WSe_2 flakes across a 5 μm x 5 μm substrate studied later in this work (Chapt. 4). Furthermore, by introducing a second flow direction and increased authority over growth parameters during epitaxial growth procedure via pre-programmable modulations, it is possible to grow multiple TMD materials onto the same substrate, in the same batch. Figure 3.6c depicts a graphical schematic of a growth chamber capable of synthesising vertical and(or) in-plane heterostructures in-situ.[127,204,212,213,214,215,216,217,218] Fabrication of non-epitaxial multilayer structures requires a layer by layer construction process that is often wasteful of both time and material. CVD synthesis now provides a perfect solution through in situ epitaxial growth of large scale

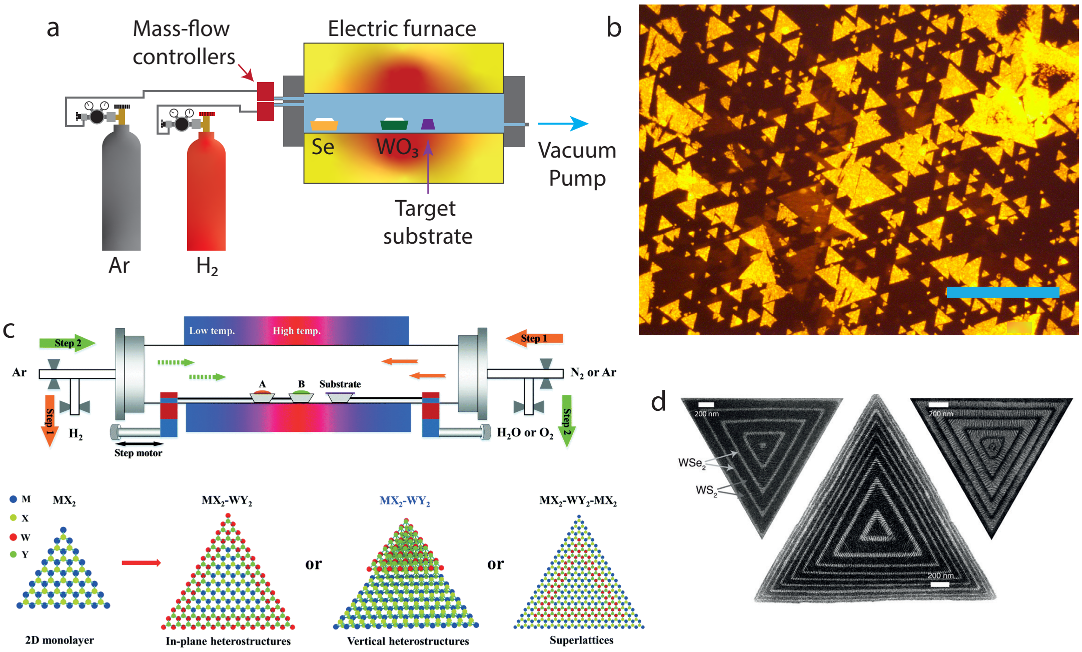

Figure 3.6: **a)** Graphic representation of a chemical vapour deposition growth chamber. Image adapted from Ref.[209] **b)** PL image of CVD grown WSe_2 monolayers. Scale bar is 50 μm. Image from Ref.[170] **c)** Schematic of CVD growth chamber allowing multiple materials to be grown simultaneously onto the same substrate. By altering flow rate and direction it is possible to grow in situ TMD complexes such as in plane and vertical heterostructures as well as super-lattices. Image from Ref.[212] **d)** SEM image of an in-plane WSe_2 / WS_2 super-lattice grown via CVD. Scale bar is 200 nm. Image from Ref.[213]

heterostructure devices. Figure 3.6d provides an SEM image of an in-plane WSe_2/WS_2 super-lattice grown using CVD techniques demonstrating the incredible fine control of in-plane widths of the constituent materials, here just a few 10s of nm thick.[213] Further investigations focus on the growth of alloyed TMD monolayers[99,219,220] (Chapter 5) details the benefits of alloying in TMD materials) or control over the crystallographic orientation of the characteristic triangle shaped islands.[170,187] Historically however, CVD synthesis has resulted in generally poor quality monolayers when compared to exfoliated flakes, but recent progresses have lead to observations of strong exciton-photon coupling in CVD grown monolayer $MoSe_2$,[170] MoS_2,[221] and now WSe_2.[170]

3.1.5 Growth and deposition specifications for samples used in this thesis

Due to the systematic approach to the advancement of CVD growth parameters, it is important to divulge the specifics of each successful growths. Hence, included is a list of the growth parameters for the synthesised materials on which chapter 4 is based. The procedures are also available in *D.J. Gillard, et. al.*[170]

Growth of single layer $MoSe_2$ and transfer to SiO_2/Si

Fabrication method described here is performed by Seongjoon Ahn, Kyung Yeol Ma, A-Rang Jang, and Hyeon Suk Shin at Ulsan National Institute of Science and Technology, South Korea for use in the publication D.J. Gillard, et. al.[170] *and included here with permission.*

MoO_3 (99.97%, Sigma Aldrich) and Se (99.999%, Alfa Aesar) were used as precursors for the growth. 60 mg of MoO_3 powder was placed in the centre of the furnace and 150 mg of Se was placed at the upstream entry. To minimize the intense evaporation of the MoO_3, the crucible that contained the precursor was partially covered by a SiO_2/Si wafer. The target substrate of c-plane sapphire was placed beside the crucible containing MoO_3. The tube furnace was evacuated for 30 minutes and subsequently repleted with the Ar gas. Ambient pressure is reached before the furnace was heated to 600 °C for 18 minutes under a steady flow of Ar gas (60 sccm) and H_2 gas (12 sccm). As the furnace temperature reached 600 °C, the upstream entry of the tube was heated to 270 °C, using a heating belt, as to vaporise Se. Finally, the furnace temperature was raised to 700 °C, and maintained for 1 hour to facilitate the $MoSe_2$ growth. Upon completion, the tube furnace was cooled to room temperature whilst maintaining Ar flow, without H_2. Polystyrene was used to transfer $MoSe_2$ on top of the DBR in order to maintain sample quality.

Growth of single layer WSe_2 on hBN

Fabrication method described here is performed by Seongjoon Ahn, Kyung Yeol Ma, A-Rang Jang, and Hyeon Suk Shin at Ulsan National Institute of Science and Technology, South Korea for use in the publication D.J. Gillard, et. al.[170] *and included here with permission.*

Initially, hBN was grown on c-plane sapphire (see Below). WO_3 (99.998%, Alfa Aesar) and Se (99.999%, Alfa Aesar) were used as precursors for the growth of single layer WSe_2. 120 mg of WO_3 powder, mixed with a small amount of NaCl to reduce the influence of humidity, was placed in the centre of the furnace and 300 mg of Se was placed at the upstream entry. The target substrate of multilayer hBN on sapphire was placed beside the crucible that contained WO_3. The tube furnace was evacuated for more than 30 min before being heated to 800 °C for 24 minutes under a steady flow of Ar gas (120 sccm) and H_2 gas (20 sccm). As the furnace temperature reached 800 °C, the upstream entry of the tube was heated to 270 °C, using a heating belt, as to vaporise Se. Finally, the furnace temperature was raised to, and maintained at, 870 °C for 1 hour to facilitate WSe_2 growth. Upon completion, the tube furnace was cooled to room temperature whilst maintaining Ar flow, without H_2. In order to maintain sample quality, polystyrene was used to transfer the WSe_2 / hBN stack to the DBR.

Growth of large area hBN

Fabrication method described here is performed by Seongjoon Ahn, Kyung Yeol Ma, A-Rang Jang, and Hyeon Suk Shin at Ulsan National Institute of Science and Technology, South Korea for use in the publication D.J. Gillard, et. al.[170] *and included here with permission.*

Multilayer hBN with an AA' stacking order was grown by remote inductively coupled plasma chemical vapour deposition method. A 2-inch c-plane sapphire was used as a substrate for the hBN growth. The substrate was placed in the centre of a 2-inch alumina tube furnace of CVD. A borazine (Gelest, Inc.) precursor flask was placed in a water bath at -15 °C. The bath temperature before the growth of hBN was increased up to 25 °C. Before the growth of multilayer hBN, the furnace was heated to 1220 °C under flow of Ar gas (10 sccm). Plasma was generated at a power of 30 W under a flow of borazine (0.2 sccm) and Ar (10 sccm) gases for 30 mins. Atomic force microscopy and transmission electron microscopy measurements confirmed that the thickness of hBN was 1.2 nm, approximately 3 layers. In addition, the hBN sample shows quite good thickness uniformity over the 2-inch sapphire substrate according to the Raman and UV absorption spectra measured at nine random points over the 2-inch hBN film.

Dielectric mirror fabrication

Fabrication method described here is performed by Aurélien A P Trichet and Jason M Smith at University of Oxford, UK for use in the publication D.J. Gillard, et. al.[170] *and included here with permission.*

Highly reflecting distributed Bragg reflectors (DBRs) are deposited on silica substrates by ion beam sputtering. The DBRs are comprised of 13 pairs of quarter wavelength SiO_2/Ta_2O_5 layers, terminating with SiO_2, of thicknesses 129 and 89 nm (refractive index 1.45 and 2.10, respectively). The DBRs are designed for a centre wavelength of 750 nm and a stop-band width of 200 nm.

Using focused Gallium ion beam milling into a planar fused silica substrate, the concave shaped template for the top mirror is formed.[222] The nominal radius of curvature of the concave mirror was 20 μm, prompting a beam waist of around 1 μm[155,223] on the focal plane.

Fabrication of monolithic cavities

Fabrication method described here is performed by Rahul Jayaprakash and Kyriacos Georgiou at University of Sheffield, UK for use in the publication D.J. Gillard, et. al.[170] *and included here with permission.*

The monolithic cavity has been fabricated by depositing a SiO_2 film of 98nm on top of the CVD-grown monolayers, which were previously transferred on a 13 pairs SiO_2/Ta_2O_5 DBR grown by ion beam assisted sputtering on a sapphire substrate. In order to minimize the potential damages on the monolayers, the silica layer covering the TMDs has been grown at room temperature by using an e-beam deposition system. For the top mirror, a semi-transparent layer of Au (thickness: 50 nm) has been thermally evaporated, completing the cavity.

3.2 Optical Measurements

3.2.1 Optical microscope imaging

Once a sample monolayer or heterostructure device has been fabricated, the first step is always to check the sample for obvious damage with the optical microscope imaging. The use of optical microscopes with regards to flake searching and monolayer identification has already been discussed (Sec. 3.1). This section will continue that discussion, and identify further uses of the microscope while examining the fabricated samples and devices. The optical microscopes available to the author have three primary modes, two of which has been mentioned already, bright field, dark field, and photoluminescence imaging. It is easy to switch between the three modes using a sets of filters that rotate into and out of the optical paths within the main body of the microscope. Likewise, the different objectives are attached to a rotating housing that can be switched around to view the samples at various magnifications. A variable intensity white light source provides illumination of the imaged samples. The samples to be viewed are placed onto a stage with full xyz translation control to allow easy focus and flake searching. Figure 3.7a shows a schematic of the optical microscope with a 550 short-pass filter in the illumination path (between the white light source and the sample) and a 600 long-pass filter in the collection path (between the sample and the CMOS camera) to allow PL imaging to take place, as detailed in section. 3.1. Figure 3.7g,h show example PL images of a TMD bilayer at different exposure times. Figure 3.7b provides a photograph of the microscope with live image feed from the connected computer while in bright field imaging mode. Figure 3.7c-e provide images taken in bright field at 5x, 20x, 100x optical magnifications of a TMD bilayer sample. Saving images at multiple magnifications is helpful later when the sample is placed in the experimental setups and the flake location within the substrate area is required once again.

The third mode, not yet discussed, is the 'dark field' mode. In this setting, the white light source is spatially filtered, using a obstruction target, such that only a perimeter disc of illumination light is channelled towards the objective lens. This disc will therefore meet the sample with large incident angle as the periphery of the objective lens will introduce the largest refraction when focussing light onto the sample. Figure 3.7f shows the resultant image in dark field mode. The illumination light with large incidence angle reflects of the edges of the sample,with the intensity corresponding to the thickness of edge. This mode is most useful for viewing multilayered heterostructures, with or without hBN encapsulation, where overlapping of similar materials might result in a convoluted image in bright field, or indeed when the sample or substrate material hinders the optical contrast between substrate and sample such as monolayer TMD on DBR substrates (Fig. 3.3).

3.2.2 Photoluminescence and reflectance contrast spectroscopy

The principles of photoluminescence and reflectance contrast (absorption) with respect to TMD monolayers have been detailed in chapter 2. This section will discuss the implementation of PL and RC spectroscopy in the laboratory. The general configuration of a PL/RC setup consists of optical components that guide an excitation light onto the sample to be absorbed. The emission is collected and guided towards a spectrometer where a diffraction grating disperses the collected light with respect to wavelength. A select range of wavelengths are focussed onto a high resolution charge-coupled device (CCD), which digitally records the intensity of the photoluminescence as a function of emission wavelength. In the reflectivity regime, a broad-band white light source is directed towards the sample, and the reflected light minus any absorption from the sample is directed towards the spectrometer. When normalised against a reflection spectrum without any absorption, such that $\Delta RC = (R_{sub} - R_{sample})/R_{sub}$ where R_{sub} is the reflected light from the substrate only (without any absorption), and R_{sample} is the reflection with sample absorption, the reflectance contrast, ΔRC, provides a spectrum of the absorbed light as a function of wavelength. Together, the PL and RC regimes provide a complete picture of the sample optical

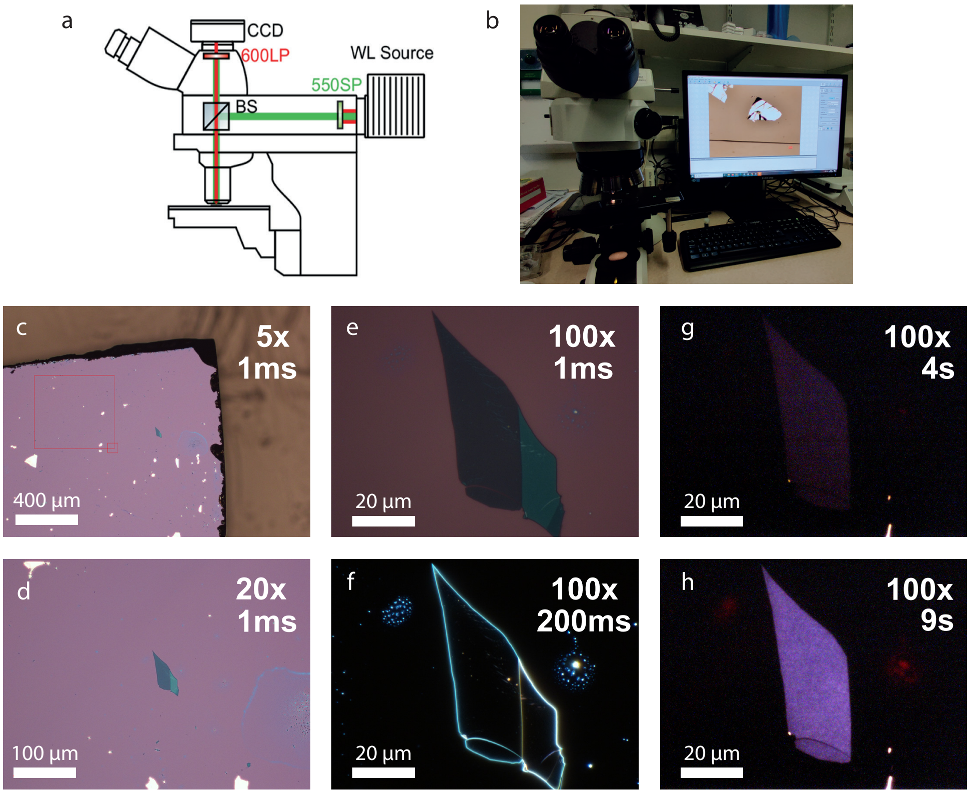

Figure 3.7: Optical Microscope Imaging. **a)** Schematic of a modified optical microscope to enable PL Imaging of exfoliated flakes. Image from Ref.[130] **b)** Photograph of the Optical microscope in use. **c)** Image taken of a TMD bilayer sample at 5 times magnification in normal bright light configuration. For bright light, the exposure time is normally the lowest setting available at 1 ms. **d)** Image of the same flake at 20x magnification. **e)** Image of the same flake at 100x magnification. **f)** Image of the same flake using the 'dark-field' configuration. In this configuration, the light is incident at an angle to the sample, and the edges of the flake are highlighted. Due to the reduction in light intensity, a longer exposure time of a few hundred ms is required. **g)** Image of the same flake again, this with the PL configuration as shown in a). The photoluminescence signal from the sample can be seen in a modified optical microscope when a long exposure is taken. Typically a few seconds are required, however with bilayers slightly longer may be needed. Analogue gain can also be applied to amplify the image intensity. **h)** The same image using optimal acquisition settings for a bilayer TMD sample.

response.

TMD monolayers possess a unique band structure which combines a spin-valley locking effect and robust chiral selection rules, allowing a researcher to probe a single K± valley through polarisation resolved spectroscopy. Optically obtaining chiral photon helicities is achieved through a combination of polarising optics. The optics used are shown in figure 3.8.

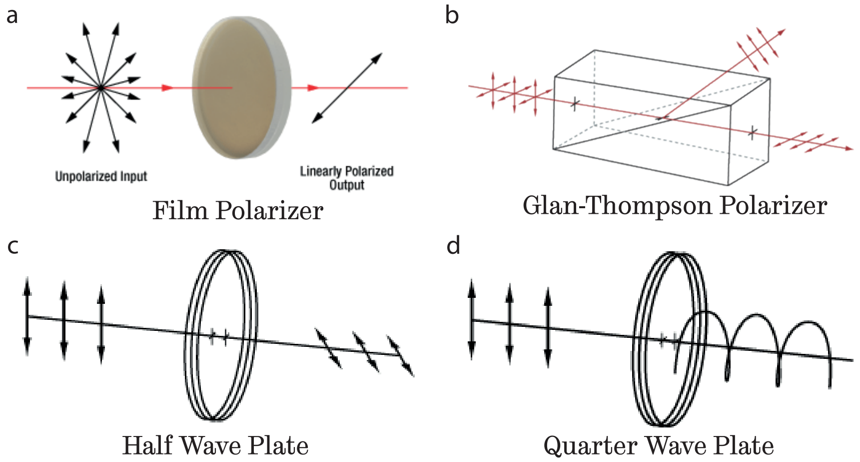

Figure 3.8: Schematic of the polarisation optics used for low temperature polarisation resolved magneto-optical spectroscopy. **a)** Schematic of a thin film linear polariser. **b)** Schematic of a Glan-Thompson linear polariser. In general, linear polarisers filter the incident beam transmitting only a single angle of polarisation. **c)** A half wave plate rotates the polarisation axis of a beam. Rotating a HWP changes the amount of rotation by which the linearly polarised light is altered. **d)** A quarter wave plate (QWP) will turn an incident linearly polarised beam into a circularly polarised beam. Images are from *Thorlabs LTD* webpage.

A linear polariser, in general, filters out all but one plane of polarisation and so converts unpolarised (or randomly polarised) light into linearly polarised light. There are many designs of linear polariser with varying effectiveness, two of which are shown in figures 3.8a and b. Thin film polarisers typically exploit interference effects to absorb light that is polarised perpendicular to the transmission axis, and offer a large range of options both in terms of performance and price, with polymer based films being a much cheaper option than embedded nanoparticles. A Glan-Thompson polariser exploits the polarisation dependence of Brewster's angle reflections at the intersection of two cemented crystals. Other methods of producing linearly polarised light include using birefringent crystals to separate the two orthogonal polarisations and then deflect or block the unwanted axis, and arrays of parallel or holographic wire grids that reflect light with an electric field-vector parallel to the wire while transmitting light with an electric field vector perpendicular to the wire grid.

Wave-plates are made out of birefringent materials for which the index of refraction is different for the two orthogonal polarisation components, effective slowing one polarisation component in respect to the other, introducing a phase shift between the slow axis and the fast axis. This phase shift can be actively selected by changing the thickness of a given birefringent material. In the case of a half wave plate, such that a $\pi(+n)$, where n is an integer, phase shift is introduced, the effect is that the polarisation axis of any incident linearly polarised light can be rotated to any necessary angle. For a circularly (or elliptically) polarised beam, the helicity of the light is reversed. A quarter wave plate introduces a phase shift of $^{\pi}/_{2}$ $(+n)$, which has the effect of converting linearly polarised light into circularly polarised light (and visa versa). By changing the relative angle of incoming polarisation axis to the fast axis of the QWP, it is possible to achieve $\sigma^{\pm}$ photon helicity with ±45° relative angle, or even leave the linearly polarised light unaffected when there is no relative angle between incident beam polarisation and fast axis.

3.2.3 Low temperature magneto-optical spectroscopy in a tunable microcavity

Low temperature magneto-photoluminescence spectroscopy is performed by mounting the sample in a liquid helium bath cryostat with free space optical access and a superconducting magnet coil. A full schematic of the experimental setup is given in figure 3.9. The excitation source used here is a 637 nm (1.946 eV) continuous wave diode laser, which produces photons with significantly higher energy than the absorption edges of both $MoSe_2$ and WSe_2. The TMD monolayers will therefore readily absorb the laser light and generate electron-hole pairs. For other materials, diode lasers of different wavelengths can also be installed. Using a motorised linear gradient neutral density (ND) filter at the laser diode, gives precise control over the laser power being introduced to the optics and sample. Furthermore, combining the motorised ND filter with a power meter in a feedback loop, allows the laser power control to be automated and self correcting providing the setup with highly stabilised laser power. This is necessary for long exposure cavity scans, where uncontrollable variations in the lab environment, such as air temperature and humidity, along with movement of the optical fibre, can cause the laser power to drift over time.

The laser beam is then focussed into a single mode optical fibre, effectively cleaning the diode's distorted beam into a symmetric spot with a Gaussian intensity profile reflecting that of the fibre's single transmission mode. The other end of the fibre is coupled and collimated, via an aspherical lens, to the free space optics board that resides above the helium bath cryostat (see figure 3.10a,b). Two adjustable mirrors provide full alignment of the optical path and guide the laser towards the polarisation optics. A 650 nm short pass

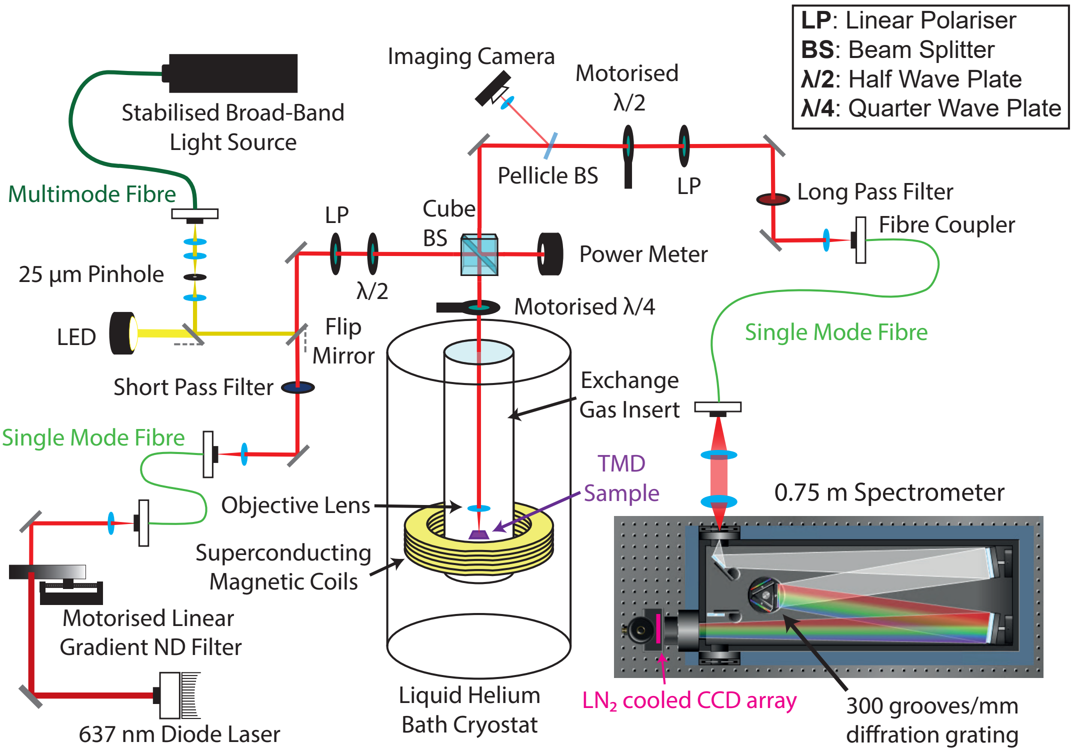

Figure 3.9: Schematic of the experimental setup used for low temperature polarisation resolved magneto-optical spectroscopy. It is capable of performing fully automated polarisation resolved optical spectroscopy with automatically stabilized laser power, due to the three motorized stages, with a stable long term environment owing to the liquid helium bath cryostat. Spectra are acquired using a low noise, high sensitivity nitrogen cooled charge-coupled device with 1340 by 400 pixels of 20 μm pixel size. A 300 grooves per mm diffraction grating is used to provide a 0.09 nm per pixel spectral resolution. Acronyms are expanded in the key (Top right). A full description of the experimental setup is detailed in the text.

filter blocks higher order laser modes as well as any luminescence originating from the fibre material. A flip mirror provides a second excitation path, which is occupied in this case by a broad-band white light source for RC measurements, and LED light for live viewing of the sample via a combination of pellicle (8:92) beam splitter with reflection directed at an imaging camera. The multimode fibre used here is to maximise the intensity of the beam, as the white light source is of significantly lower power than the laser diode. The 25 μm pinhole is used to clean the optical path into a symmetrical spot. To keep the laser beam path impervious to misalignment, the white light path is aligned using two separate mirrors to the laser beam path. Alignment of the beams is necessary to ensure the beam enters the objective lens centrally with perpendicular incidence, which best retains the spot symmetry of the beam profile (see Fig. 2.23) as it is focussed onto the sample.

A combination of Glan-Thompson linear polariser (LP) and half wave plate ($\lambda/2$) provides the excitation path with linearly polarized light at a customisable angle relative to the sample. The excitation beam then encounters a 50:50 beam splitter (BS), which reflects and transmits the beam in two equal amounts. The transmitted component is used to measure the laser beam power, and the reflected component (of equal power) is directed towards the objective lens and TMD sample. Just after the beam splitter, a motorised quarter wave plate ($\lambda/4$) converts the linearly polarised light into one of σ^+, σ^-, or maintains linear polarisation, such that each valley (K±) can be optically addressed independently or simultaneously. The motorisation of this QWP means that the polarisation selection can be automated as part of a larger cavity scan script written in *National Instruments LabVIEW* software. The excitation beam is focussed onto the sample with an achromatic doublet with a focal length of 7.5 mm. The objective lens has a numerical aperture of 0.31 (diameter of 5 mm), corresponding to a diffraction limited spot size of 1.2 μm with 637 nm laser wavelength. However the spot size measured as FWHM of the intensity profile of the focussed spot is ≈ 2.4 μm, due to a cumulative influences of the various optics in place along the optical excitation path.

Emission from the TMD sample consists of a combination of emission from both valleys. As such the circularly polarised light is reconverted to linearly polarised light by the QWP. The $\lambda/4$ will simultaneously covert both σ^+ and σ^- PL emission into two orthogonally linearly polarised components to be (partially) transmitted through the cube beam splitter. The subsequent HWP, in combination with the final LP, is used to selectively allow one orthogonal polarisation component at a time by positioning the fast axis of the HWP either parallel or 45° to the LP transmission axis. The motorised stage is used in combination with the motorised QWP to provide fully automated access of the valley selective excitation and emission of the TMD sample.

A 700 nm long pass filter allows only PL emission wavelengths through to the collection fibre, effectively blocking the 637 nm laser light along with any other background light under 700 nm wavelength.

The collection beam is refocussed into a second single mode fibre, which again has the effect of cleaning the optical path to a symmetric Gaussian profile. Through alignment with a final two mirrors, the collection path is adapted to closely overlap the excitation spot on the sample. In doing so, the intensity of collected PL is maximised whilst simultaneously minimising background light originating outside the intended excitation spot, improving both the signal to noise ratio and the spatial resolution of the setup. Finally, the fibre is directed towards the spectrometer bench where the fibre output is collimated and refocussed onto the spectrometer entrance slit of 100 μm. Through a series of two concave mirrors and diffraction grating, the polychromatic beam is converted into a set of monochromatic images of the entrance slit organised linearly by wavelength that are focussed onto the CCD pixel array. The 1340 x 400 array of 20 μm sized pixels that make up the CCD is cooled to -120°C, by a small tank of liquid nitrogen, in order to minimise dark counts. While the diffraction can be switched to different ratings, the 300 grooves/mm grating is used here providing a spectral range of $\sim$ 120 nm with spectral resolution of $\sim$ 0.09 nm per pixel. During each CCD exposure, photon counts from each column of pixels are vertically binned together such that signal to noise ratio is enhanced in the final spectrum. Background counts can be removed by subtracting a reference spectrum of same acquisition parameters with excitation/detection spot positioned on the sample substrate away from the active TMD material.

The sample being measured is placed inside a vacuum tube which is then inserted into the liquid helium bath cryostat. The ambient air is pumped out from the tube insert to ultra high vacuum pressures to stop damaging condensation from occurring on the sample and electronics at these temperatures. A small amount of He gas is pumped into the tube insert as an exchange gas, in order to thermally couple the sample to the liquid helium in the bath cryostat. Figure 3.10c provides a photograph of the exchange gas insert where the sample is placed onto a stack of 5 piezo nano-positioners which control the vertical, lateral, and tilt axis of the sample. The three extra piezo nano-positioners above the sample, control the top DBR mirror providing a method of introducing (or removing) the top mirror to (from) the optical path when the tunable microcavity is (isn't) required. The laser, white-light source, and LED are all focussed through real time observation of the laser spot size using the imaging camera while moving the sample plane in the z axis.

Magneto-optical spectroscopy

Introducing a magnetic field whilst performing photoluminescence and reflectance contrast spectroscopy is a powerful experimental ally to study the magneto-optical response of the TMD semiconducting materials, providing a new insight into the physical processes at play within a TMD monolayer. The B-field is introduced by way of superconducting coils positioned close to the sample, as detailed in figures 3.9 and 3.10. In this particular setup, there are three coils within the bath cryostat. One large coil produces a magnetic field in

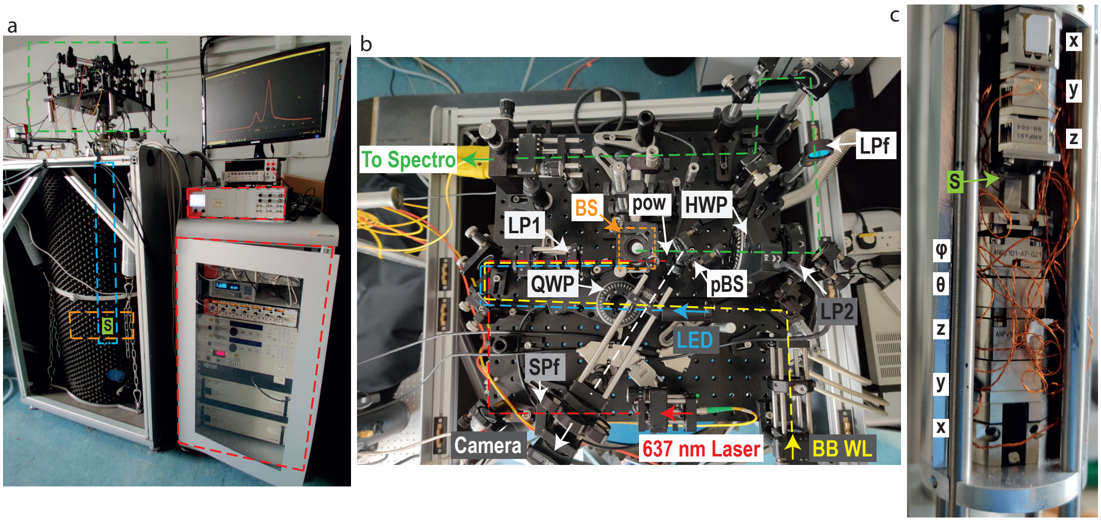

Figure 3.10: Photographs of the experimental setup used for low temperature polarisation resolved magneto-optical spectroscopy. **a)** Image of the overall setup when in use. The optical board, is highlighted in green, with the control box for the magnet and piezo-electric stages in red. The position of the exchange gas insert is estimated with a blue outlining, with the superconducting magnetic coils in orange. The sample position is estimated with a green S. The results of the measurements are observed through a spectrometer connected to a computer and outputted through the monitor seen. **b)** Photograph of the optical board from above, with a graphical schematic overlay of the optical path and instruments. **c)** Photograph of the sample insert. The piezo control stages are visible and labelled. The sample device position is highlighted with a green S.

the Faraday geometry (Perpendicular to the sample plane, AKA Out-of-plane) up to a field strength of 9 Tesla, while the other two smaller coils combine to produce a 4.5 T field in the Voigt geometry (Parallel to the sample plane, AKA In-plane). It is also possible to linearly combine the two B-field vectors to produce a field vector in any given direction up to 4.5 T. The magnets can be used in two settings; *ramping* mode, where the field strength is actively modified between each exposure by increasing (or decreasing) the current through the coils; and *persistent* mode, whereby a superconducting element effectively short circuits the coil, creating an infinite current loop with zero resistance. The current doesn't decay in this situation, and so a stable fixed magnetic field strength is maintained during automated cavity PL experiments. Figure 3.10a shows the control unit and high voltage power unit for the superconducting coils outlined in red, along with the control unit for the 8 piezo nano-positioners, temperature control, helium level indicator along with electrical control for any contacts that the sample may have. The majority of these functions can be controlled via computer and automated into *NI LabVIEW* scripts.

Tunable microcavity

The last part of the experimental puzzle is put into place by the two DBR mirrors, controlled fully via the aforementioned piezo nano-positioners visible in figure 3.10c. The bottom mirror is controlled by a 5-axis piezo-actuator stack, the first three stages control the xyz translational motion, while another two stages control the tilt alignment. The top mirror is positioned using a 3-axis piezo-actuator stage controlling the xyz translational motion. When combined and aligned the two highly reflective DBRs produce a tunable optical microcavity. The top mirror has a concave shape, with nominal radius of 20 μm, which confines the photonic mode in all three spatial dimensions to produce a 0D tunable cavity.[154] Details of the DBR mirrors are found in chapter 2. A cavity scan is then performed by simply modifying the z-axis piezo voltage which controls the cavity length and photonic mode energy, collecting PL or EC spectra at each step of cavity length. The tunable cavity measurements can be performed with heating or magnetic fields (when in persistent mode) to expand to experimental ability of this setup.

3.2.4 Additional spectroscopy experiments using a flow cryostat

The bath cryostat provides a long term stable environment for a sample being measured over several days or weeks when a large number of experiments are required of the same sample. However, the potential benefits of the bath cryostat are generally outweighed when simpler and quicker experiments are required. For example changing samples in the bath cryostat can take several days, requiring the exchange gas insert tube to warm up to ambient temperatures before being opened and exposed to air. Inserting the room temperature tube into the helium bath causes significant boil off. Furthermore, the specifics of the bath cryostat are fixed, such that transmission experiments are simply not possible, and the heating plate competes against the cooling power of the exchange gas, limiting the heater range to a maximum of ~ 70 K. For a larger amount of adaptability in terms of experimental freedom, or for simple fast PL and RC measurements, it is often more appropriate to employ the use of a flow cryostat. The sample is placed in a small vacuum chamber upon a fixed stage and thermally coupled to a cold finger, in which the liquid helium is pumped through. The fixed stage has a heating element which provides thermal control from 4.2 K to room temperature (higher temperatures are available, but are not used). The vacuum chamber while sample residing inside is placed on an optical bench with the optics constructed in the surrounding area, allowing a large amount of experimental freedom to change optics or introduce further optical paths and diode laser wavelengths. The objective lenses are also easily interchanged as they reside outside the vacuum chamber, with the only constraint is that a large working distance is required. Typically this allows a higher (nominally 0.55) numerical aperture to be installed, with better spatial resolution of the measurements, when compared to the 0.31 NA lens installed in the bath cryostat. For PL and RC measurements, the setup is practically identical in terms of optics used with the bath cryostat as described by figure 3.9.

k-space Imaging of Monolithic Cavities

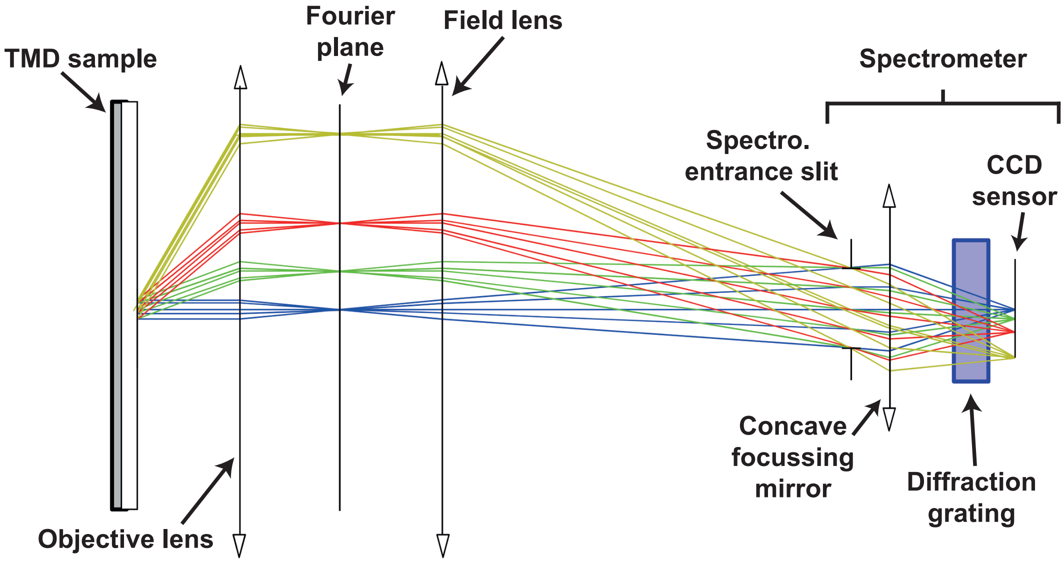

Figure 3.11: Schematic of the focussing optics used to capture angle resolved PL. It should be noted that this schematic is for illustration purposes only and does not reflect accurate lens positions or beam paths. Image adapted from Ref.[224].

In chapter 4, the measurement of a monolithic cavity PL spectra is performed with the use of the flow cryostat. Details of how the cavity is constructed is given in section 3.1.5. A monolithic cavity has no inherent tuning of the cavity length, but by measuring PL across a range of emission angles relative to the sample plane, the effective cavity length will be larger for bigger angles. This is the basis of k-space (or Fourier space) imaging. In terms of optics, This is achieved by introducing an additional lens, labelled in figure 3.11 as 'field lens' which focusses an image of the Fourier plane onto the spectrometer entrance slit. The slit here effectively selects only the section of the Fourier space at $k_x = 0$, resulting in a final image on the CCD displaying the PL spectra as a function of k_y on the y-axis and energy in x-axis. The conversion from k_y to angles is carried out by considering $k_y \approx \sin\theta$ with the knowledge that the maximum k_y, detected at the extremes of the CCD sensor, will be equal to the objective NA = 0.55. In chapter 4, the PL spectra are matched to TMM simulations to reinforce accurate conversions between CCD pixel number, k_y, and angle.

Chapter 4

Strong coupling in $MoSe_2$, and WSe_2, based heterostructures grown by chemical vapour deposition

The work detailed in this chapter lead to the publication D.J. Gillard, et. al.[170]

The previous chapter has introduced some of concepts needed to understand what makes TMD monolayers so unique, with potential benefits for opto-electronics, such as high binding energies, very large oscillator strengths, broken inversion symmetry, and spin-valley locking of the optically addressable K and K' (also commonly referred to as K+ and K-, referring to the $\sigma^{\pm}$ polarisation of light associated with each valley).[8,38,225]

The unique properties seen in TMD monolayers can be further enriched through the integration of 2D semiconductors within optical microcavities to engage in a strong exciton-photon coupling regime.[43,155,161,180,226,227,228] As discussed in chapter 2, TMD based polaritons acquire novel properties that arise from the unique band structure and resulting valley degree of freedom of excitons in TMD monolayers,[68,229] displaying enhanced valley coherence due to the coupling with long lived cavity photonic modes.[230,231] As such, efficient propagation of polaritons in monolayer TMDs have been recently observed, with diffusion lengths of up to 20 μm demonstrated in room temperature WS_2,[232] while valley-dependent divergence of polariton diffusion has been observed in $MoSe_2$ at cryogenic temperatures, where the polarisation resolved polaritons spread towards opposite in-plane directions due to the exciton valley Hall effect.[233]

Polaritons in TMDs provide a system that allows highly non-linear phenomena already observed,[226,234,235] and there is further effort being directed towards the realisation of Bose-Einstein condensation,[115,234] polariton lasing[236,237] and optical parametric oscillation[238] so far observed in other material systems. These phenomena, when entwined with the valley degree of freedom, of TMDs, could be exploited to create large scale all optical polariton circuits and quantum networks.[239,240]

The scalability of TMD based devices becomes an inherent difficulty when the most common fabrication method involves micromechanical exfoliation, which often results in lesser sized flakes, which severely hinders the scalability and reproducibility of any devices fabricated in this manner. Chemical vapour deposition (CVD) growth techniques provide an alternative fabrication method and that have the ability to produce substrate-wide homogeneous coverage of monolayer islands,[196] along with the developing capability to grow complex multilayered heterostructures, in-situ.[204] therefore completely bypassing the, often wasteful, mechanical transfers necessary to complete the fabrication of exfoliated equivalents and thereby minimizing the possibility of external contamination.

CVD offers, therefore, a very beneficial and inherently scalable method of producing large scale TMD based devices. Because of which, CVD-grown MoS_2 and WS_2 flakes have been used in polaritonic devices working at room temperature already.[180,241] Nonetheless, optimisation of polariton valley properties requires low structural disorder and narrow exciton spectral linewidths, which until recently[170] have only been demonstrated in exfoliated $MoSe_2$ and WSe_2 monolayer flakes operating at low temperatures.[43,68,155,161,226,227,230] Access to low temperature regimes in high quality TMD structures provides a path towards highly non-linear trion-polaritons[84,226,235] or Fermi-polaron-polaritons.[43,76,77,242] Such resonances require precise control and stability of charged excitons, as well as utilisation of suitable heterostructures.[43]

In this chapter, two CVD-grown fully encapsulated devices are studied. The first device employs $MoSe_2$ as the active semiconductor layer, while the other uses WSe_2. The hBN used to encapsulate the substrate wide monolayers are also grown using CVD techniques. The first heterostructure, HS1, is shown in figure 4.1. The $MoSe_2$ flakes are grown onto a sapphire substrate, and mechanically transferred onto an appropriate planar DBR. The few-layer hBN film is subsequently transferred on top of the $MoSe_2$ layer. The transfers are carried out using a substrate sized polystyrene membrane which picks up the many thousands of $MoSe_2$ islands in their entirety to be transferred in a single process. The second heterostructure (Fig. 4.2) is similarly compiled, with the exception that the WSe_2 monolayers are grown directly onto a few layer hBN film substrate. The hBN/WSe_2 stack is then transferred together onto the DBR and, again, is subsequently topped with few layer hBN to complete the full encapsulation.

It has already been demonstrated, that encapsulation of exfoliated TMD with thin hBN implements a uniform dielectric screening of the Coulomb interactions, which reduces the spatial inhomogeneity of an exciton, narrowing the spectral linewidth.[118,196] In addition, the TMD layers gain a level of protection from damage and contamination from external sources, that could otherwise degrade the sample quality and device integrity.[122]

Furthermore, the growth of TMD monolayers directly onto a hBN substrate is also beneficial as a step towards single-crystal epitaxial growth,[187,243] an achievement so far limited to just a few TMD materials, namely MoS_2,[244] WS_2,[245] and more recently WSe_2.[243] Through careful procedural adjustments of the CVD growth conditions, for example with control of nucleation and lateral growth times, significant progresses in optical and electrical quality has been accomplished compared to the same material grown on sapphire.

4.1 Initial optical characterisation of the heterostructures

Observing the structures under an optical microscope in ambient conditions, as described in section 3.2.1, provides an initial characterisation of the room temperature PL emission across a large area of the device along with an indication of the general morphology of the structures. The optical microscope PL images of HS1 and HS2 are given in figures 4.1b and 4.2b respectively. In HS1, the $MoSe_2$ monolayers can be seen as characteristic triangular shaped island with an average lateral width of 8 , as well as numerous regions where multiple flakes merge into a single island of monolayer exceeding 100 μm in lateral size. HS2 is much the same, with a slightly larger average flake width, determined to be 11 μm, again with notable areas of merged triangles forming monolayer islands of over 100 μm in size.

A sufficiently abundant and homogeneous monolayer coverage of the substrate is required for scaleable fabrication, for example constructing large arrays of identical heterostructure devices, such as transistors or photodetectors. The monolayer coverage, calculated by dividing the total area of monolayer across the sample by the total substrate area, is a useful metric to compare different samples. A substrate-scale PL imaging analysis protocol (discussed further in Sec. 4.2) is used to identify the monolayers in HS1 and HS2 from the substrate, such that the monolayer coverage value of 14% for HS1 and 22% for HS2 can be determined.

The two heterostructures are characterised further with reflectance contrast and photoluminescence spectroscopy at room ($\sim$ 290 K) and low temperatures ($\sim$ 4 K), which is

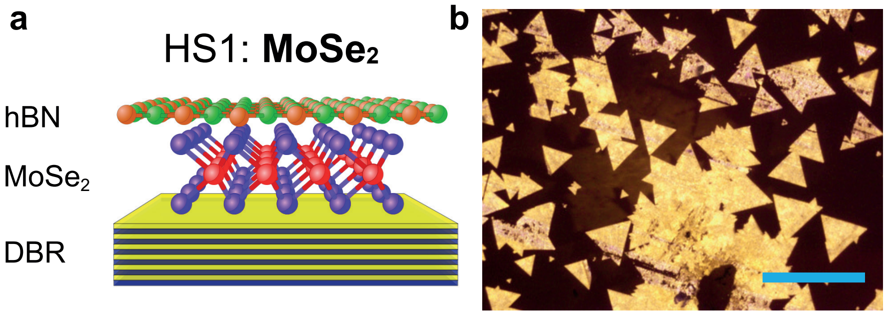

Figure 4.1: **a)** Schematic of the first CVD-grown heterostructure labelled HS1. **b)** Optical microscope PL image of HS1 taken in ambient conditions using a 50x objective lens. Scale bar = 50 μm.

displayed in figures 4.3 and 4.4. PL spectroscopy measurements are carried out using an off resonant continuous wave (cw) laser at a power of $\sim$ 20 μW (Sec: 3.2). The considerable intensity of the room temperature excitonic PL emission highlights the large exciton binding energy associated with TMD monolayers.[225] The exciton emission peak observed in HS1 by the monolayer $MoSe_2$ is located about a central peak energy of 1.579 eV with full-width-half-maxima (FWHM) linewidth of 40 meV, while in HS2 the WSe_2 exciton PL peak is found at 1.670 eV with similar FWHM linewidth of 45 meV. The values are typical for $MoSe_2$ and WSe_2 monolayers at room temperatures.

When the TMD devices are lowered in temperature to $\sim$ 4 K (the boiling point of liquid helium, see Sec 3.2), the monolayers' excitonic emission becomes narrowed and blue shifted to 1.671 eV in HS1 ($MoSe_2$) and 1.759 eV in HS2 (WSe_2). This peak, and that at

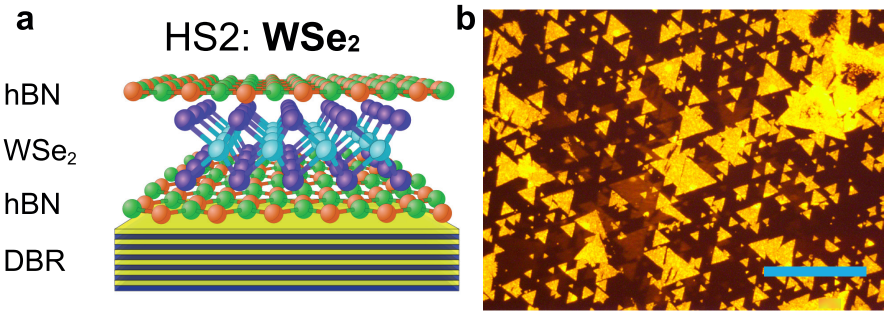

Figure 4.2: **a) a)** Schematic of the second CVD-grown heterostructure labelled HS2. **b)** Optical microscope PL image of HS2 taken in ambient conditions using a 50x objective lens. Scale bar = 50 μm.

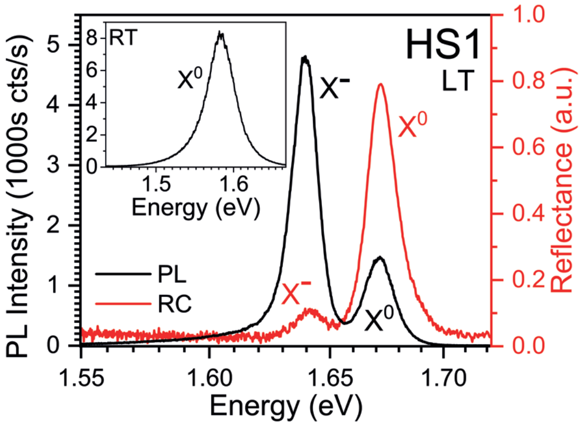

Figure 4.3: Optical characterisation of HS1 at T∼ 4 K. Inset shows PL spectra at room temperature. PL and reflectance contrast (RC) spectra are shown in black and red, respectively. PL cw excitation conditions: λ_{exc} = 660 nm, P = 20 μW.

room temperature is emission from the simplest excitonic resonance, the neutral exciton X^0. The second peak, labelled X^- is formed by the charged excitonic (or trion) emission (Sec. 2.4) and is nominally found 20-30 meV below the neutral exciton peak.[33,35,68,155] Here the trion forms at 1.639 eV in HS1 and 1.726 eV in HS2. It has already been discussed how the relative peak intensities of the two excitonic resonances is greatly influenced by the density of free carriers present in the structures.[38] As discussed in section 2.4, the WSe_2 PL emission seen at lower energies, below ∼ 1.70 eV, has been previously attributed to various excitonic complexes, including exciton-phonon side-bands,[48] spin dark excitons,[246] and localised states.[50]

The two heterostructure devices display a X^0 linewidth of 13 meV and 21 meV for CVD grown $MoSe_2$ (HS1) and WSe_2 (HS2) respectively, along with 12 meV and 20 meV for X^- emission from the two monolayers. The linewidth of an excitonic resonance in TMD monolayers is, in general, heavily affected by the level of structural disorder and density of defects within the material's crystal lattice.[241] The spectral shapes and linewidths demonstrated here improve upon previous CVD grown monolayers, as reported by *Zhang, X., et. al.*[243] and *Lippert, S., et. al.*[247]. Furthermore they are comparable to exfoliated flakes functioning at low temperature without encapsulation.[33,118,155,196,230] The optical quality demonstrated by HS1 and HS2 therefore suggests that CVD growth is a viable fabrication method capable of producing heterostructures of comparable quality to mechanically exfoliated flakes.

Reflectance contrast (RC) measurements are also performed using a broad band white light source and calculated as $\Delta R/R = (R_{sub} - R_{HS})/R_{sub}$, where R_{HS} is the reflectance of

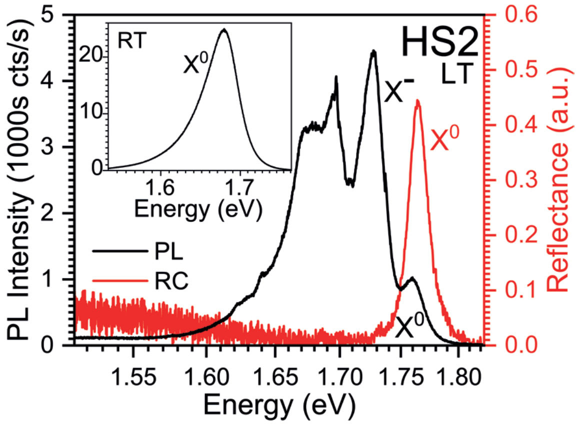

Figure 4.4: Optical characterisation of HS2 at T≈ 4 K. Inset shows PL spectra at room temperature. PL and reflectance contrast (RC) spectra are shown in black and red, respectively. PL cw excitation conditions: λ_{exc} = 532 nm, P = 20 μW.

the active heterostructure, and R_{sub} is the reflectance of the bare substrate away from the absorbing media. This is displayed in red in figures 4.3 and 4.4, which reveals a dominant $MoSe_2$ absorption peak of the neutral exciton in HS1 at 1.672 eV with width of 14 meV, with a smaller trion absorption peak at 1.642 eV with a linewidth of 13 meV.

The relative peak height, i.e. the strength of the absorption, is strictly related to the oscillator strength of individual excitonic transitions, with X^0 being much more intense than X^- in $MoSe_2$ (HS1) due to a relatively low doping level.[56,77,242] The X^0 absorption peak of WSe_2 (HS2) at 1.764 eV is slightly broader than in HS1, with a linewidth of 24 meV, following the trend observed for the PL regime, which is an indication of the greater structural disorder present in CVD-grown WSe_2.

4.2 Luminous object analysis

Further insights into the optical qualities of the two heterostructures being studied here can be found by performing substrate scale optical imagine analysis of the devices involving a luminous object identification method developed by *Severs-Millard, T., et. al.*[187] Separating the active monolayer areas from the inactive empty substrate area by employing a colour threshold technique across multiple optical PL images across the entire substrate, reveals a total of 16999 individual luminous $MoSe_2$ objects are discovered across HS1, and 14205 WSe_2 islands across HS2. Figure 4.5 displays the number of monolayer islands identified in each heterostructure as a function of increasing object area. The average (mean) area of all

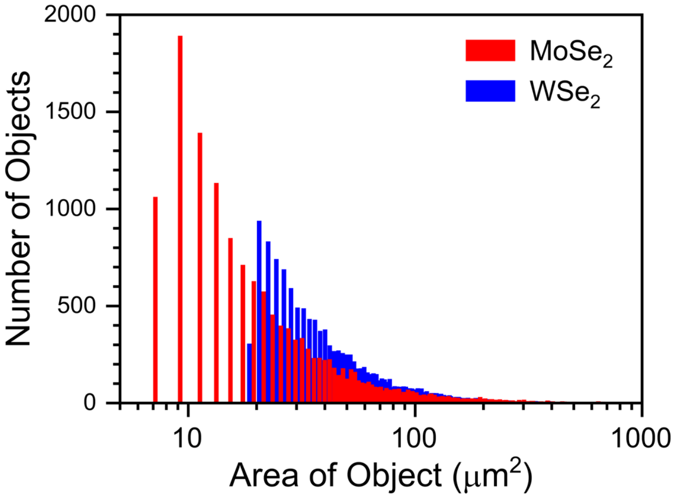

Figure 4.5: **a)** Histogram showing the distribution of areas of isolated objects for both $MoSe_2$ (HS1) and WSe_2 (HS2), presented in red and blue respectively.

the objects identified in HS1 is 71.3 μm^2 and 171.7 μm^2 in HS2. The number of objects in each optical PL image used, along with the average area of the objects within said images can be used to construct a heatmap (Figs. 4.6 and 4.7) of object density and size across the entire substrates, giving easy identification of potential areas of interest. The image thresholding that identifies luminous monolayer objects is adaptable to optimize identification of any heterostructure or device, and so different camera settings, and emission wavelengths (colours) are accounted for accordingly.

For the construction of large arrays of individual heterostructure devices, merged monolayers will not be of great use. When considering only objects that resemble equilateral triangles, an average area of 46.6 μm^2 (80.7 μm^2) is found from 8089 (8391) individual monolayers across HS1 (HS2), leading to an average lateral width of 7.9 μm (10.9 μm). This corresponds to 21% (17%) of the total monolayer coverage being formed of isolated triangular objects.

Figs. 4.1(b) and 4.2(b) provide an example optical PL image used to extract the luminous object properties. From these images it is possible to see that the bright triangular monolayer islands appear to have a preferred angular orientation on the device substrate.

After identifying all the triangular objects across the two heterostructures, it is possible to calculate the flake orientation relative to the horizontal axis of the microscope image. In order to maximize accuracy, only islands with shape close to equilateral triangles are analysed in terms of angular orientation.

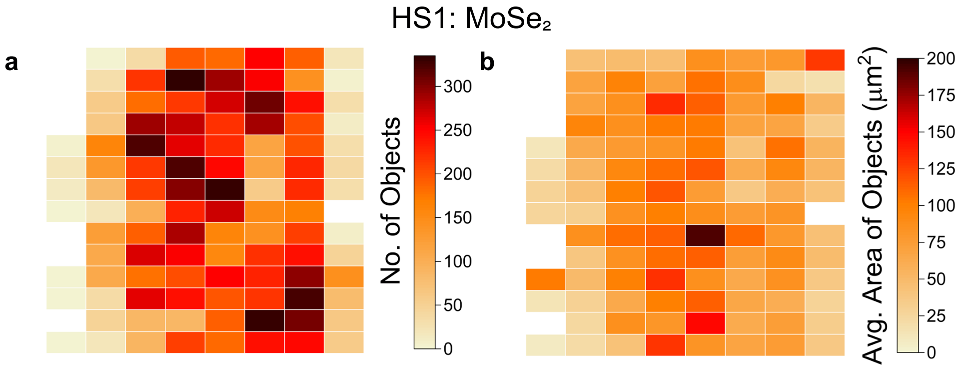

Figure 4.6: **a, b)** Heatmaps of $MoSe_2$ (HS1) displaying the density (a) and average size (b) of all individual luminous objects contained within a single 20x magnification image (385 μm x 289 μm). Empty images with no objects present as white spaces.

The histograms in Fig. 4.8 depict the number of luminous triangular islands identified as a function of orientation angle. Both CVD grown $MoSe_2$ (HS1), and WSe_2 (HS2) present a significant amount of uniformity in terms of object orientation, a signature of epitaxial growth. For the CVD growth of WSe_2 directly onto hBN, as shown in Fig. 4.8c, there are two preferred orientation angles that can be seen clearly. This is expected from a sample with a three-fold symmetry and triangular morphology presenting two possible opposite growth directions rotated 180° to one another. The observed bi-directional orientation

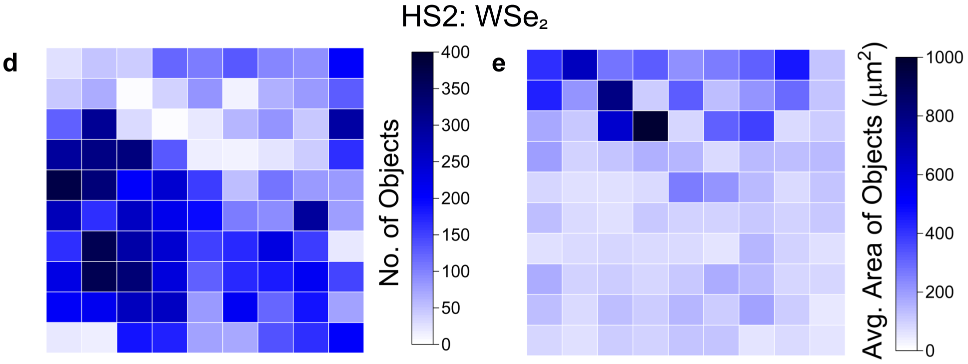

Figure 4.7: **a, b)** Heatmaps of WSe_2 (HS2) demonstrates the density (a) and average size (b) of objects within a single 20x magnification image (497 μm x 373 μm).

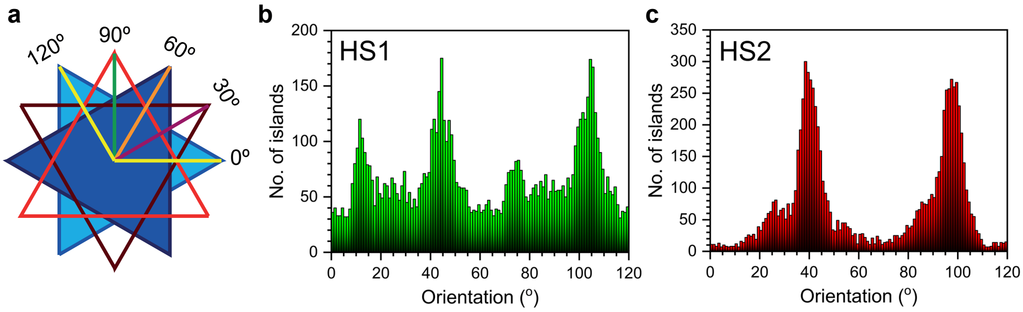

Figure 4.8: **a)** Schematic showing flake orientations at different angles relative to the horizontal axis of the microscope images. **b, c)** Analysis of flake orientation. Islands of monolayer TMD are identified and the orientation extracted using methodology as described in previous investigations.[187] Both b) HS1 and c) HS2 show two main peaks situated 60° apart, equivalent to two opposite growth configurations rotated by 180° due to the three fold symmetry of equilateral triangles. HS1 also shows two extra peaks situated at 30° from the main peaks.

preference is a direct consequence of the hexagonal crystal structure of the underlying growth substrate and has also been observed in previous studies of MoS_2, WS_2, and WSe_2 monolayers grown by CVD onto hBN.[187,243,244,245] As for the growth of $MoSe_2$ onto c-plane sapphire, as detailed in Fig. 4.8b, there are four peaks observed in the angular distribution, where two dominant peaks indicate the preferred flake orientations, found at 60° relative to the other, along with two lesser preferred angles at 30° offset from the dominant peaks. Both two, and four preferential growth directions have been seen in TMDs grown via CVD onto c-plane sapphire.[248,249] Control of, or at least an ability to predict, the relative angle of the flake's growth at the synthesis stage of fabrication will provide the basis to grow scalable heterostructure devices with a control over the relative interlayer crystallographic orientation, a property that is becoming increasingly important.[113,114]

4.3 Strong coupling in a tunable microcavity

The CVD-grown monolayer materials studied here have shown impressive optical quality with prominent absorption and emission resonances, with preferential properties when considering large scale opto-electronic device construction. The two devices are now tested in an optical microcavity to access the strong exciton-photon coupling regime. The design of the tunable optical microcavity is detailed in chapter 3.[43,68,155,223,230] The ground state photonic cavity mode (Laguerre-Gaussian LG_{00}), which ensures the highest light confine-

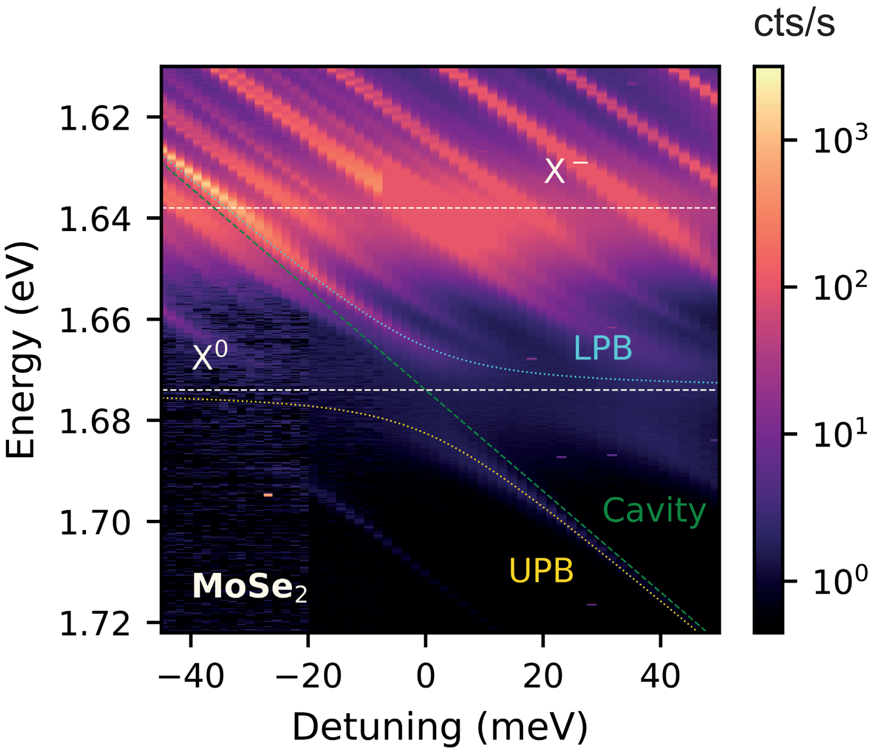

Figure 4.9: PL emission from HS1 displayed as a function of photon energy and exciton-photon detuning ($\Delta = E_c - E_{X^0}$). A clear anti-crossing of the cavity mode with the exciton is observed. PL spectra are fitted using a Lorentzian peak (see Figure 4.11) and a two level coupled oscillator model is used to extract the lower (blue curve) and upper (yellow curve) polariton branches, excitonic resonances (white horizontal lines), and LG_{00} photonic mode (green diagonal line). A Rabi splitting of 17 meV is found. The sample is optically excited using a 637 nm cw laser.

ment, is tuned in energy by increasing (or indeed decreasing) the length of the optical cavity through use of piezo nano-positioners. PL signal from the cavity-embedded heterostructures can be collected through the optical access as the cavity length is tuned. Measuring such PL response from HS1 and HS2 is shown as a function of detuning (the energy difference between the cavity mode, E_c and unperturbed exciton, X^0) in figures 4.9 and 4.10, respectively. The three dimensional optical confinement provided by the concave top mirror generates a set of transverse modes for each longitudinal mode[155,223] also visible in both figures.

When the photonic cavity mode, LG_{00} highlighted with a green diagonal dashed line in figures 4.9 and 4.10, is tuned into resonance with the excitons, light matter coupling

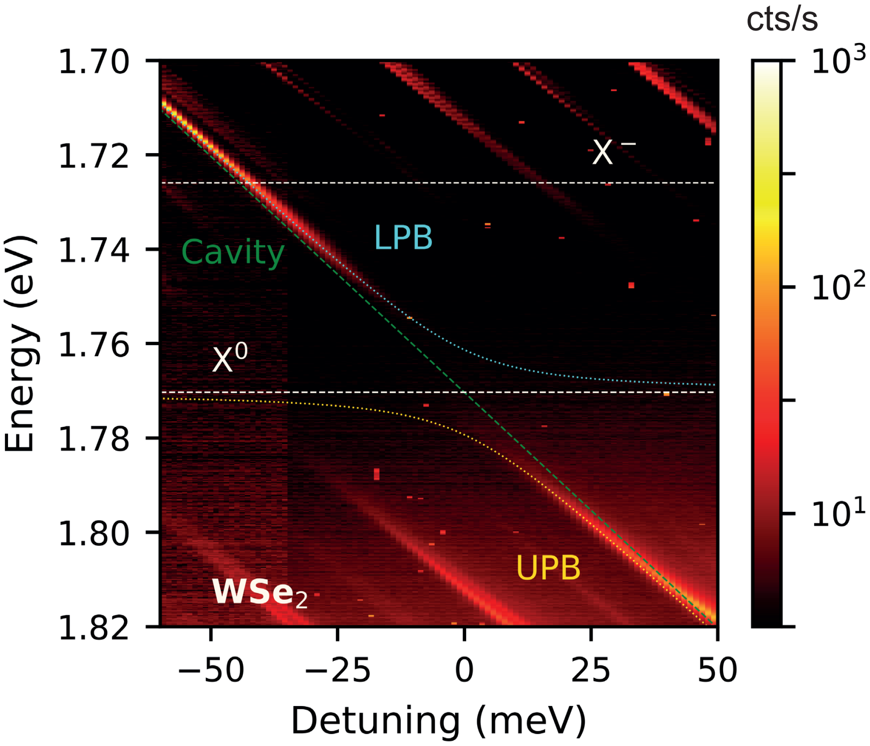

Figure 4.10: PL emission from HS2 displayed as a function of photon energy and exciton-photon detuning ($\Delta = E_c - E_{X^0}$). Clear anti-crossings of the cavity mode with the exciton are observed in both heterostructures. PL spectra are fitted using a Lorentzian peak (see Figure 4.12) and a two level coupled oscillator model is used to extract the lower (blue curve) and upper (yellow curve) polariton branches, excitonic resonances (white horizontal lines), and LG_{00} photonic mode (green diagonal line). A Rabi splitting of 17 meV is found. The sample is optically excited using a 637 nm cw laser.

manifests in one of two ways, as discussed in the introduction chapters (Chapt. 2.7). Both regimes of light-matter interaction can be seen here with $MoSe_2$ in HS1 (Fig. 4.9). At the trion resonance at 1.638 eV, the cavity mode is broadened and brightened, in a demonstration of the weak coupling[68,152,155,230] due to only a small oscillator strength associated with the $MoSe_2$ trion. The absence of such effect in HS2 (Fig. 4.10) at of 1.726 eV suggests that the oscillator strength, as indicated by the absorption peak in RC (Fig. 4.4), of the WSe_2 trion resonance is not sufficient to couple with the cavity mode.

The second regime of light-matter coupling is known as the strong coupling regime as is discussed earlier (Sec. 2.7). The coupling presents itself as a characteristic anti-crossing of the cavity mode at the exciton absorption resonance with an associated Rabi splitting $\hbar\Omega_R$.

For the first time, such behaviour can be clearly observed in both of the two CVD grown devices sampled. The resultant cavity PL spectra as the longitudinal ground state cavity mode (LG_{00}) is tuned towards the neutral excitons, situated at 1.673 eV for $MoSe_2$ in HS1 as shown in Fig. 4.9, and 1.770 eV for WSe_2 in HS2 as shown in Fig. 4.10. The peak positions of the two polariton branches (LPB: lower energy branch, UPB: higher energy branch as defined in Sec. 2.7) within the cavity PL spectra have been identified by a Lorentzian peak fitting function, and subsequently applied to a two-level coupled oscillator model (Figs. 4.11 and 4.12) in order to determine the Rabi splitting value as is shown overlaid in Figs. 4.9 and 4.10. A value of $\hbar\Omega_R = 17.2 \pm 3.3$ meV is found for HS1 and $\hbar\Omega_R = 16.8 \pm 3.1$ meV for HS2.

The Rabi splittings demonstrated here by cavity PL measurements are closely comparable to values obtained with exfoliated $MoSe_2$ and WSe_2 monolayers embedded in zero-dimensional optical microcavities.[43,68,230] This again indicates that the CVD grown encapsulated heterostructures presented here, are of high optical quality with low structural disorder and provides validation for the CVD growth technique as a fabrication method of highly scalable polaritonic devices.

4.3.1 Demonstration of the two level coupled oscillator model used to determine the Rabi splitting

To obtain the spectral data for the figures 4.9 and 4.10, photoluminescence originating from the active TMD material of each embedded heterostructures is collected at each voltage step of the piezo nano-positioner (which tunes the cavity length), and fitted using a Lorentzian peak function as to determine the central energy positions of two polariton branches as a function of tuned cavity mode energy. An example of such Lorentzian peak fitting for each heterostructure close to zero detuning, such that both polariton branches have comparable PL peak intensities (note that this is not a condition of zero detuning but typically a consequence of), is shown in figures 4.11a and 4.12a.

The Rabi splitting, calculated experimentally as the minimum energy distance between the UPB and LPB, is found to be 17.1 meV for HS1. For WSe_2 in HS2 however, the standard Lorentzian fitting procedure fails to accurately recreate the collected PL spectra at small detuning values (close to resonance) due to a low signal-to-noise ratio. This is not completely unexpected as the lowest energy spin configuration for WSe_2 at low temperature is an optically dark transition,[46] meaning that the PL intensity is significantly lower than that of $MoSe_2$. The presence of this dark transition does not impede the occurrence of strong coupling with the bright exciton, just the ability to observe the anti-crossing through PL detection. A Savitzy-Golay smoothing technique,[250] using a second order polynomial with 35 points of window, is therefore employed to increase the signal-to-noise ratio and produce a spectrum that can be accurately recreated using Lorentzian peak fitting, as shown in Fig. 4.12a. It is important to note that any peak positions found using smoothed data are not included in the two-level coupled oscillator model shown in Fig. 4.12b and that the smoothing technique is used only to demonstrate the peak fitting procedure when close to the WSe_2 X^0 resonance. The experimentally determined value of Rabi splitting which can then be extracted from the smoothed spectra is 14.2 meV.

Once the peak positions are found, the following two-level coupled oscillator model is used to fit the polariton branches:[152,156,221,251,252]

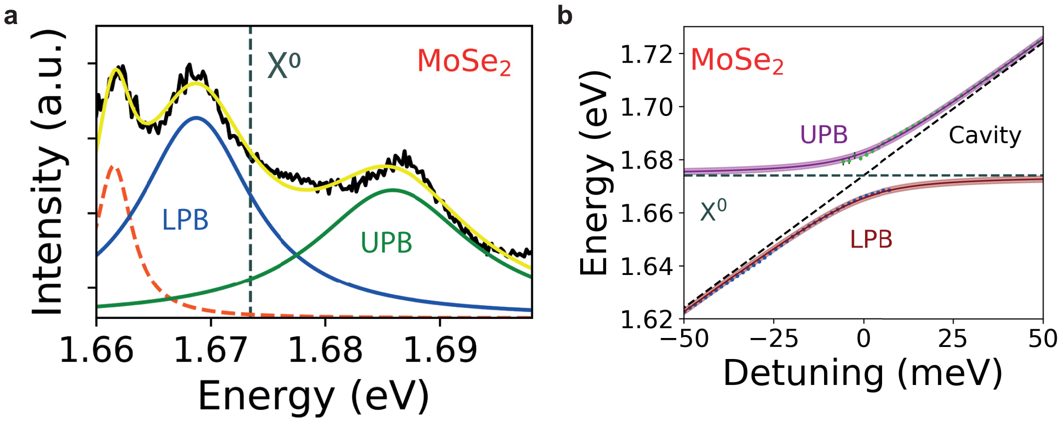

Figure 4.11: **a)** Lorentzian peak fitting of the two polariton branches when the 0D tunable cavity mode is close to resonance with the neutral exciton energy of HS1. The cavity PL emission is displayed in black, with the Lorentzian peak fit for the lower and upper polariton branch in blue and green respectively. Extra peaks fitted are shown in orange, and the overall fit is shown in yellow. **b)** The two level coupled-oscillator model is fitted to the peak positions of the corresponding polariton branch. Optimal fitting parameters are extracted, setting the expected neutral exciton energy (grey dashed lines), cavity mode (black dashed line) and Rabi splitting. In turn, these values position the fitted lower and upper polariton branches, displayed as red and purple solid lines, respectively, as a function of exciton-photon detuning ($\Delta = E_c - E_{X^0}$). Error of fitting for the peak position and the polariton branches are displayed as black error bars and a faded coloured area, respectively. Using this oscillator model, a Rabi splitting of $\hbar\Omega_R(\mathrm{MoSe_2}) = 17.2 \pm 3.3$ meV is found for HS1 in the tunable microcavity.

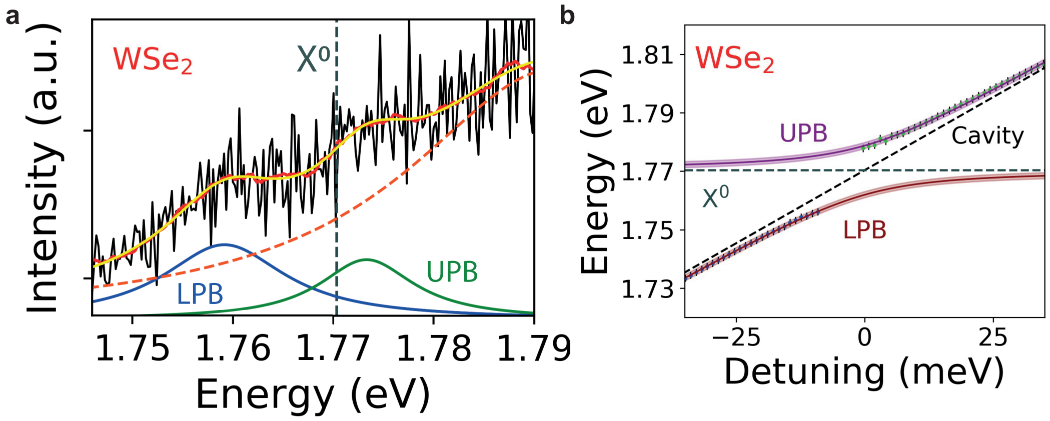

Figure 4.12: **a)** Lorentzian peak fitting of the two polariton branches when the 0D tunable cavity mode is close to resonance with the neutral exciton energy of HS2. The cavity PL emission is displayed in black, with the Lorentzian peak fit for the lower and upper polariton branch in blue and green respectively. Extra peaks fitted are shown in orange, and the overall fit is shown in yellow. The red line in a) shows the PL spectrum after a smoothing technique is applied. **b)** The two level coupled-oscillator model is fitted to the peak positions of the corresponding polariton branch. Optimal fitting parameters are extracted, setting the expected neutral exciton energy (grey dashed lines), cavity mode (black dashed line) and Rabi splitting. In turn, these values position the fitted lower and upper polariton branches, displayed as red and purple solid lines, respectively, as a function of exciton-photon detuning ($\Delta = E_c - E_{X^0}$). Error of fitting for the peak position and the polariton branches are displayed as black error bars and a faded coloured area, respectively. Using this oscillator model, a Rabi splitting of $\hbar\Omega_R(\text{WSe}_2) = 16.8 \pm 3.1$ meV for HS2 in the tunable microcavity.

$$\begin{pmatrix} E_c & V_R \\ V_R & E_{X^0} \end{pmatrix} \begin{pmatrix} \alpha \\ \beta \end{pmatrix} = E \begin{pmatrix} \alpha \\ \beta \end{pmatrix} \tag{4.1}$$

Here, the cavity mode is defined as $E_c(V) = y0 + aV + bV^2$, where V is the applied DC voltage across the piezoelectric micro-positioner stages (see Sec. 3.2) which change the cavity length, with $y0$, a, and b, fitting parameters to be found. E_{X^0} is the neutral exciton transition energy. E represents the eigenvalues corresponding to the energies of the polariton modes. α and β construct the eigenvectors, and represent the Hopfield coefficients of the cavity photon and X^0 for each polariton state, such that $|\alpha|^2 + |\beta|^2 = 1$. V_R is the exciton-photon interaction potential. The polariton branch energy eigenvalues are given by:

$$E_{U,LPB} = \frac{(E_c + E_{X^0})}{2} \pm \sqrt{\frac{1}{4}(E_c - E_{X^0})^2 + {V_R}^2} \tag{4.2}$$

where $\hbar\Omega_R = 2\sqrt{{V_R}^2 + \frac{1}{4}(E_c - E_{X^0})^2}$ is the Rabi splitting at a given detuning $\Delta = E_c - E_{X^0}$. At zero detuning, when $E_c = E_{X^0}$,

$$\hbar\Omega_R = 2V_R \tag{4.3}$$

A Rabi splitting of 17.2 ± 3.3 meV is found for HS1 and 16.8 ± 3.1 meV for HS2. Comparing the experimental values to those extracted from the above two level coupled oscillator model, a good agreement is found for HS1 suggesting the validity of the applied model, however the small discrepancy between the experimental value and the model value associated with HS2 highlights the short-comings of a relatively basic model when accurate peak positions of the polariton branches near resonance cannot be obtained. Nevertheless, the observation of strong light-matter coupling in CVD grown WSe_2 is clear, and the experimentally determined result of 14.2 meV lies within the margin of error for the model.

4.4 Monolithic cavities

Further advantages of large area TMD monolayers can be exploited with monolithic cavities, which provide a basis to form various topological designs to adapt or enhance device functionality towards polariton circuits.[239,240] While the main function of the few layer hBN films that encapsulate both HS1 and HS2 is to provide a high quality substrate for the TMD synthesis,[187,243] the protective function of the hBN layers is of particular importance for these devices as the top mirror (DBR or otherwise) would otherwise be deposited directly on top of the TMD layers[122] and can often be damaging to the atomically thin material. As a proof of concept, 98 nm of SiO_2 via e-beam deposition was grown onto HS1, followed by a semi-transparent layer of 50 nm gold, in order to fabricate a $\lambda/2$ monolithic cavity. The oxide deposition process is carried out at room temperature in order to preserve the optical integrity of the emitting materials as much as possible.[122,253]

The optimal thickness of SiO_2 to be deposited on top of $MoSe_2$ based HS1 needs to be chosen carefully to maximise the interaction between photonic cavity mode and TMD exciton. In order to do so, simulations of the electromagnetic field response of the TMD embedded cavity are performed using the transfer matrix method (TMM) which is commonly used to reproduce, with high accuracy, the behaviour of planar microcavities in strong coupling regime, given the thickness and complex refractive indexes of layers within the structure.[153] The refractive indices of the $MoSe_2$ monolayer are extracted from the experimental reflectance (RC) spectra at both 5 K and 150 K as can be seen in figure 4.13a. The imaginary part of the complex refractive index refers to the absorption strength of a given material and can be estimated from fitting the excitonic absorption resonance, as measured experimentally in RC spectra, of a TMD monolayer with a Gaussian peak function. The real part of the refractive index can then be calculated from the imaginary part following the Kramers-Kronig relations.[254] By recursively running a simulation with the goal of recreating the experimentally found RC peak by procedurally varying the imaginary part of the refractive index such that the central wavelength, amplitude, and linewidth of the Gaussian peak function are modified until the refractive index profile that provides the best match between simulated and experimental RC is found. The resultant refractive index of $MoSe_2$ at 5 K and 150 K is displayed in figure 4.13b.

The entire cavity structure, including the absorbing $MoSe_2$ layer can then be modelled by considering the tabulated refractive indices of the various materials present; sapphire, SiO_2, Ta_2O_5, and Au[255] with the following layered planar structure:

$$\text{Air / Au (50 nm) / SiO}_2\text{ spacer (}x\text{ nm) / MoSe}_2\text{ (0.9 nm) / DBR / Sapphire}$$

where the SiO_2 spacer length x is to be found, and the DBR structure, with a stopband centred at 750 nm is:

$$13\text{x [SiO}_2\text{ (129 nm) / Ta}_2\text{O}_5\text{ (89 nm)]}$$

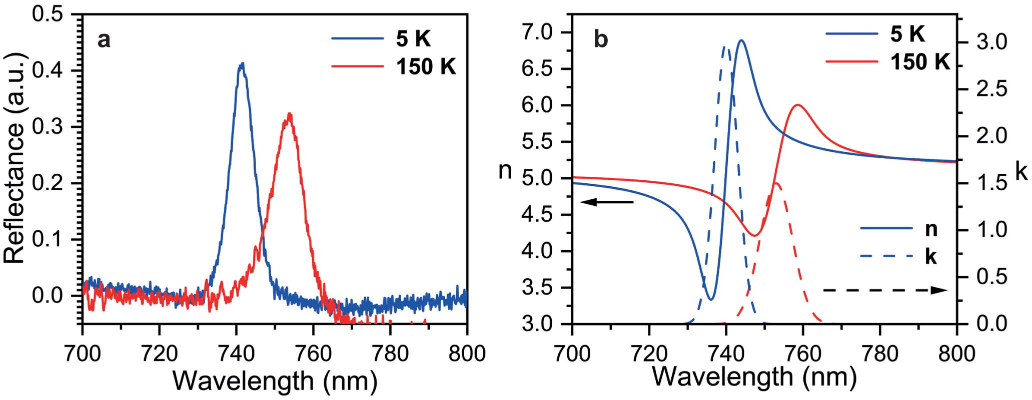

Figure 4.13: **a)** Experimental reflectance contrast of $MoSe_2$ at 5 K and 150 K. **b)** Refractive index of $MoSe_2$ at 5 K and 150 K extracted from the fit of the experimental reflectance contrast.

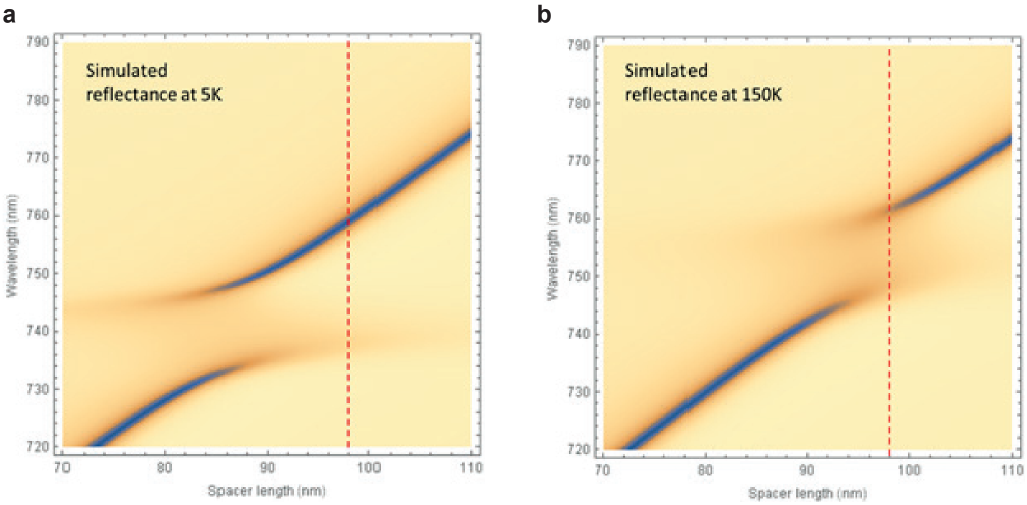

Figure 4.14: Simulated reflectance plots of the cavity as a function of the SiO_2 spacer thickness and wavelength, employing the $MoSe_2$ optical constants at both **a)** 5 K and **b)** 150 K. The red lines indicate the optimal thickness chosen for the monolithic cavity fabrication.

As such, the reflectance response of the cavity is simulated as a function of increasing SiO_2 spacer thickness and cavity mode energy, by using the $MoSe_2$ optical properties at 5 K, as shown in figure 4.14a, and 150 K in figure 4.14b. At both temperatures, the cavity mode displays a very clear anti-crossing at the neutral exciton X^0 absorption resonance wavelength, a manifestation of strong light-matter coupling. The Rabi splitting at 150 K is slightly smaller than that at 5 K due to the weaker and broader absorption of $MoSe_2$ at this temperature. From these plots, the optimal thickness for the SiO_2 spacer is determined to be 98 nm (red lines in Fig. 4.14), such that a negative detuning is to be presented by the in situ polaritonic device at 5 K, and zero detuning when the device is heated to an operating temperature of 150 K.

When considering the tunable cavity, the hemispherical design confines the photonic modes in all three spatial dimensions, resulting in a set of discrete cavity modes with $\mathrm{k}_{x,y,z} \sim 0$ as described in section 2.7. These modes are tuned in energy by modification of the optical cavity length. In contrast however, a two-dimensional monolithic cavity confines the photonic mode only in the vertical z direction. A continuous energy dispersion of the cavity mode is therefore observed in $k_{x,y}$.[152] Here, the dispersion is detected by way of angle resolved spectroscopy which detects PL as a function of emission angle as measured from the normal of the sample plane (corresponding to $\mathrm{k}_{x,y}$=0 at 0°).[152] In addition, a much greater confinement of light can be achieved using the in-situ cavity presented here,

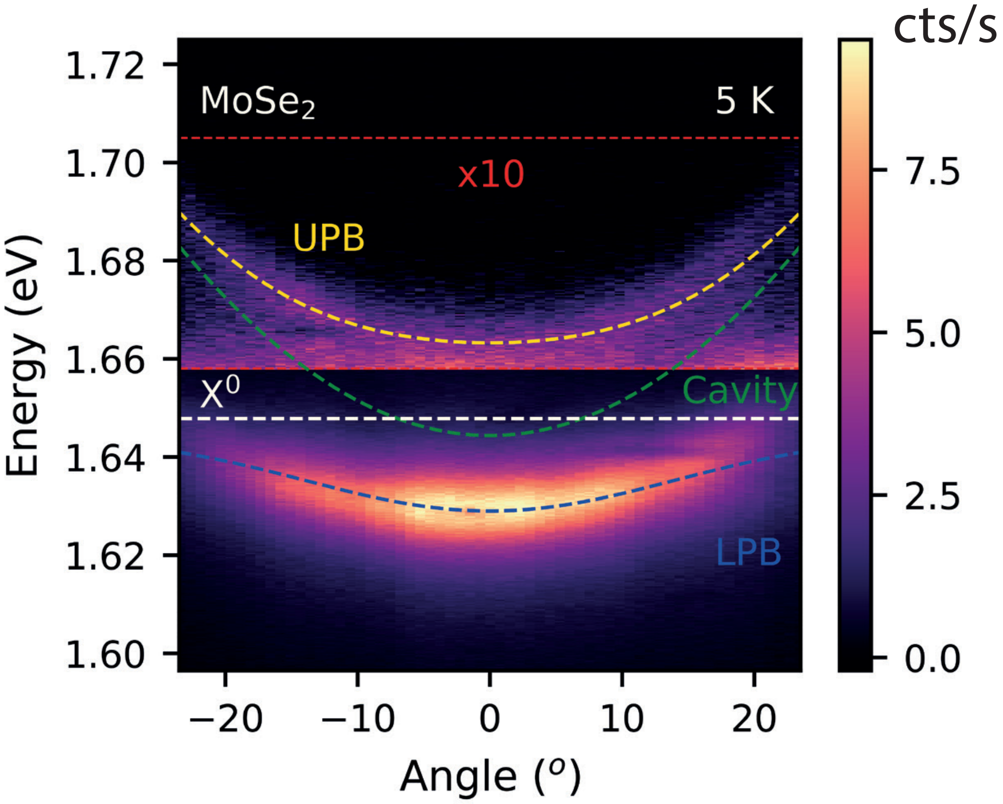

Figure 4.15: Angle resolved PL imaging of HS1 in a monolithic cavity. At 5 K, the cavity has a negative detuning at 0° of $\Delta \approx$ -3.5 meV, showing anti-crossings at ± 7°. The PL intensity in the region within the red dashed lines has been multiplied by a factor of 10 for clarity. We overlay the fitted LPB (blue) and UPB (yellow) along with the extracted parabolic cavity dispersion (green) and neutral exciton resonance (white). A Rabi splitting of $\hbar\Omega_R = 34.1 \pm 4.0$ meV is observed at 5 K. The sample is optically excited using a 660 nm cw laser at a power of 50 μW.

due to the reduced vertical size of the cavity and lower mode penetration into the Au top mirror. DBR mirrors can also be successfully used in planar monolithic cavity designs with only slightly larger mode penetration. In any case, the biggest difference to photonic mode volume is simply caused by the hemispherical geometry of the top mirror previously used (Figs. 4.9 and 4.10). As demonstrated below, the reduced mode volume and better light-matter coupling leads to an inherently increased magnitude of the observed Rabi splitting. Since a monolithic cavity is fixed (i.e. not tunable in size), we take advantage of the

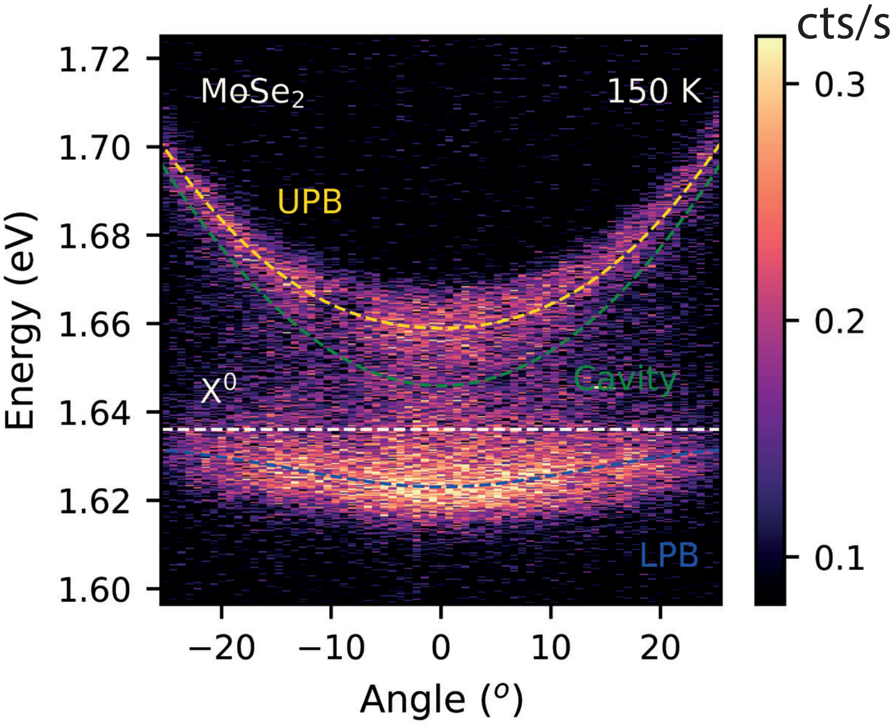

Figure 4.16: Angle resolved PL imaging of HS2 in a monolithic cavity. At 150 K, the cavity has a positive detuning at 0° of $\Delta \approx 10$ meV. We overlay the fitted LPB (blue) and UPB (yellow) along with the extracted parabolic cavity dispersion (green) and neutral exciton resonance (white). A Rabi splitting of $\hbar\Omega_R = 30.5 \pm 3.9$ meV is observed at 150 K. The sample is optically excited using a 660 nm cw laser at a power of 50 μW.

temperature dependence of the X^0 energy (Fig. 4.13), which can be used to tune the exciton into resonance with the fixed cavity photonic mode.

The MoSe$_2$ embedded monolithic cavity is optically excited using a non-resonant 660 nm cw laser operating in the linear response power regime, while the PL is collected through angle resolved PL spectroscopy as to investigate the exciton and photon states as a function of wave-number ($k_{x,y}$). Figures 4.15 and 4.16 display the cavity PL spectra whilst operating at a temperature of 5 K and 150 K respectively. At low temperatures, the exciton resonance is found at 1.648 eV, which red-shifts down to 1.636 eV at the higher temperature. At both temperatures, characteristic signatures of strong exciton-photon coupling are seen in the monolithic cavity, owing to the protective capability of the CVD grown hBN layers, which shield the active monolayers during the potentially damaging SiO$_2$ deposition process.

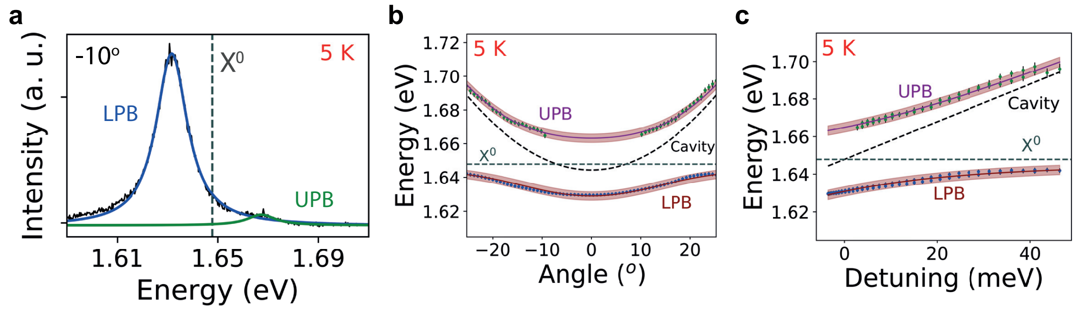

Figure 4.17: **a)** Lorentzian peak fitting of the two polariton branches at angles when the parabolic cavity mode is close to resonance with the neutral exciton energy at 5 K. Due to the large difference in intensities of the polariton branches, the two peaks are fitted individually. The resultant Lorentzian peaks fitted to the lower and upper polariton branches are displayed in blue and green solid lines respectively. **b, c)** The two level coupled-oscillator model is fitted to the peak positions of the corresponding polariton branch. Where the Lorentzian peak fitting does not provide a visually accurate fit of a spectrum (angles within ± 9.5^o for UPB at 5 K), it is excluded from the two level oscillator model. Optimal fitting parameters are extracted, setting the expected neutral exciton energy (grey dashed lines), cavity mode (black dashed line) and Rabi splitting. In turn, these values position the fitted lower and upper polariton branches, displayed as red and purple solid lines, respectively, as a function of b) collection angle, θ, and c) exciton-photon detuning ($\Delta = E_c - E_{X^0}$). Error of fitting for the peak position and the polariton branches are displayed as black error bars and a faded coloured area, respectively. The Rabi splitting is found to be $\hbar\Omega_R = 34.1 \pm 4.0$ meV at 5 K.

When the cavity device is at 5 K, the exciton is negatively detuned at 0° by - 3.5 meV, such the the UPB is significantly dimmer than the LPB. In order to display the upper polariton branch in this situation, the PL intensity is magnified 10-fold, as outlined by red dashed lines in figure 4.15.

In the case of tunable microcavity PL spectra at each voltage step is collected and fitted using a Lorentzian peak at determine the energy of the polariton branches as a function of cavity length. The same approach is applied here, as demonstrated in figures 4.17a and 4.18a, with the alteration that the PL is now collected as a function of collection angle in k-space. The coupled oscillator model (Sec. 4.3.1)[152,156,252] which finds the Rabi splitting value associated with the two fitted polariton branches also needs to be modified to accommodate the appropriate variables. This is achieved simply by changing the photonic mode energy dependence, from $E_c(V)$ to $E_c(\theta)$ such that,

$$E_c(\theta) = E_c(0^o)/\sqrt{1 - (\sin\theta/n_{eff})^2} \tag{4.4}$$

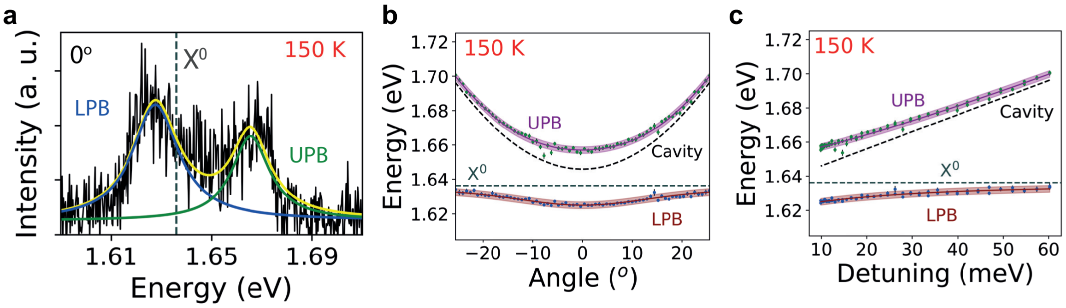

Figure 4.18: **a)** Lorentzian peak fitting of the two polariton branches at angles when the parabolic cavity mode is close to resonance with the neutral exciton energy at 150 K. The similar intensities produce fully resolvable and distinct branches across the entire angle range allowing a multiple Lorentzian peak analysis to be used on the collected spectra. The resultant Lorentzian peaks fitted to the lower and upper polariton branches are displayed in blue and green solid lines respectively, with the combined fit shown in yellow. **b, c)** The two level coupled-oscillator model is fitted to the peak positions of the corresponding polariton branch. Optimal fitting parameters are extracted, setting the expected neutral exciton energy (grey dashed lines), cavity mode (black dashed line) and Rabi splitting. In turn, these values position the fitted lower and upper polariton branches, displayed as red and purple solid lines, respectively, as a function of b) collection angle, θ, and c) exciton-photon detuning ($\Delta = E_c - E_{X^0}$). Error of fitting for the peak position and the polariton branches are displayed as black error bars and a faded coloured area, respectively. The Rabi splitting is found to be $\hbar\Omega_R = 30.5 \pm 3.9$ meV at 150 K.

where $E_c(0^o)$ is the minimum cavity photon energy at $\theta = 0^o$, and n_{eff} is the effective refractive index of the cavity.[221,251,252] This approach results in a best fitting value of $E_c(0^o)$ of 1.644 eV at 5 K, and 1.646 eV at 150 K. n_{eff} is determined to be 1.87 at 5 K, and 1.78 at 150 K, and the MoSe$_2$ X^0 absorption energy is identified as 1.648 eV at 5 K, tuned to 1.636 eV at 150 K. The two polariton branches, cavity dispersion, and exciton energy obtained from the coupled-oscillator model are shown overlaying Figs. 4.15 and 4.16, with an anti-crossing clearly seen at ± 7° when the device is at 5 K. A large Rabi splitting of 34 ± 4 meV is revealed when operating the device at 5 K. The strongly coupled cavity performs well up to a temperature of 150 K, when the excitonic mode is positively detuned ($\Delta(0^o) = +\ 10$ meV), leading to a Rabi splitting of 31 ± 5 meV being observed.

4.5 Conclusions

In this chapter, the advances made over recent years in CVD growth techniques has been demonstrated by systematically testing the optical quality of two CVD-grown TMD-based heterostructure devices. Substrate-wide $MoSe_2$, and WSe_2, semiconducting monolayers, with crystal domains exceeding 100 μm in size, encapsulated with large area hBN have been tested using PL and RC spectroscopy techniques at room and low temperatures, displaying optical properties similar to those seen in exfoliated flakes. The two devices are subsequently embedded in tunable and monolithic microcavities, where strong exciton-photon coupling is clearly displayed with interaction strengths, as described by the Rabi splitting value, shown to be similar to values demonstrated by exfoliated equivalents,[43,68,155,230] as an indication of the comparable optical qualities of the CVD grown materials on display here, with the leading fabrication process of high quality TMD based opto-electronic and polaritonic devices.

In addition, the CVD grown materials exhibit highly ordered crystallographic alignment within the ensemble of monolayer domains, due to the growth substrates, of sapphire for $MoSe_2$ and CVD-synthesised hBN for WSe_2, employed during fabrication. Confirmation of these favourable crystallographic properties is carried out through substrate-wide statistical analysis of the TMD crystal axes orientation and PL properties,[187] It is therefore decided that CVD growth offers a viable fabrication method for large scale TMD/TMD heterostructures with highly controlled interlayer twist angle,[113,114] that suitable for embedding in microcavities.

Together with further control over band structure (Chapter 5), carrier populations (Chapter 6), or through the introduction of additional 2D materials such as hBN or graphene, these structures could provide a viable route to the realisation of highly tunable and non-linear so-called dipolaritons[116,148] in large scale devices.

Further development of large scale monolayer semiconductor growth techniques, most notably directly onto hBN which provides highly co-orientated TMD domains, will inevitably lead to heterostructures that can reliably and repeatedly compete with, or outperform, those built with exfoliated flakes, with the added benefits of inherent scalability, paving the way for future scalable TMD-polaritonic circuits.

Chapter 5

Band structure engineering in TMD monolayers and beyond through alloying and hybridisation

In this chapter, the efforts towards engineering the band structure of atomically thin materials through various techniques will be explored. The opto-electronic properties of a semiconductor are entirely due to the electronic band structure, therefore by controlling the underlying electronic bands, we can control the opto-electronic properties of a material. When looking forward at potential research avenues for atomically thin semiconductors, it is often useful to look back at the successes of more conventional semiconductors. One powerful tool successfully utilised in the current generation of commercial III-V semiconductor devices and throughout semiconductor physics is alloying;[85] the process of mixing lattice elements to gently tune the band gap between that of the two pure materials. The ability to tune the optical and electronic properties of a TMD is highly beneficial, as it allows for the tailoring of properties to fit a specific application.

Homo-bilayers are composed of two individual layers of the same material stacked on top of each other. This can be done by exfoliating down to the natural bilayer, or by manually stacking two monolayers together. By exfoliating down the a natural bilayer, the interlayer electronic coupling will remain complete. This is most ideal if the natural stacking order is required, or unimportant. In order to alter the stacking order, or indeed the twist angle between layers, it is required to separate the layers and manually reconstruct the bilayer as required. A process that can introduce defects, tearing, and/or areas of sub-standard interlayer coupling.

Van der Waals heterobilayers, on the other hand, are composed of two *different* material monolayers stacked directly onto the other.[110] The ability to stack different materials on top of each other, free of lattice mismatch and dangling bonds, is one of the most exciting aspects of 2D materials. This provides an already vast collection of atomically thin materials with an unprecedented freedom of heterostructure design to produce physically engineered devices and brand new meta-materials with novel opto-electronic properties.

The optical response of vdW heterobilayers is determined by the type-II band alignment, in which the edges of conduction band (CB) and valence band (VB) are localised in the two different layers due to their band offset. The result of this is that an exciton can form with the Coulomb bound electrons and holes confined to the to constituent layers, known as an interlayer exciton (IX). The IX therefore obtains an electric dipole orientated perpendicular to the plane of the TMDs. Combined with a long radiative lifetime, this results in enhanced exciton-exciton interactions.

By carefully choosing the constituent materials, it is possible to predict the optical response. In this way the optical properties of the final structure are directly related to that of the constituent layers. While the family of layered 2D materials is large, the band structure of each individual material is exactly that, individual. This limits the potential resultant properties to a discrete set. This fundamental limitation is lifted when considering the use of alloyed monolayers. It is then possible to finely and continuously tune the energy gap, band offset, and spin-orbit coupling of heterobilayers unlocking ultimate freedom of tailored properties through chemical engineering.

In order to be able to actively select the properties that we require in a certain device, or set of devices, we need to pursue understanding of the individual layers' properties as the chemical composition is altered from one pure material to the other.

5.1 Tuning excitonic resonances in $Mo_xW_{1-x}Se_2$ monolayers and homo-bilayers

Here we will obtain basic optical characterisations of a set of 10 alloyed monolayers and bilayers, at room and low temperature. In this section, all the materials studied are exfoliated down from their respective bulk crystals, obtained from HQGraphene, onto PDMS stamps, as described in Sec. 3.1. The monolayers and bilayers are found using optical microscopy (Sec. 3.2.1) and transferred onto a 90 nm SiO_2 / Si wafer substrate and investigated without hBN encapsulation. While, hBN encapsulation has been shown to be useful (Chapt. 4), we deliberately decided not do so here to keep the fabrication process as sim-

Table 5.1: List of alloy compositions

x_{Mo}:	0.00 (WSe_2)	0.21	0.33	0.38	0.49	0.64	0.71	0.85	0.93	1.00 ($MoSe_2$)

ple as possible, minimising fabrication time and potential transfer errors, and also test the alloys in an sub-optimal dielectric environments, such that when the alloys are used within heterostructures using more complex fabrication techniques, the optical properties should not degrade beyond that which is presented here. The set of alloys being investigated are shown in table 5.1.

5.1.1 Monolayers

Due to the high binding energy inherent to excitons in monolayer TMDs, we are able to observe excitonic resonances at room temperature, without requiring cyrogenics or high vacuums, providing a very quick method to initially test the optical properties of the materials available with the setup described in Sec. 3.2.

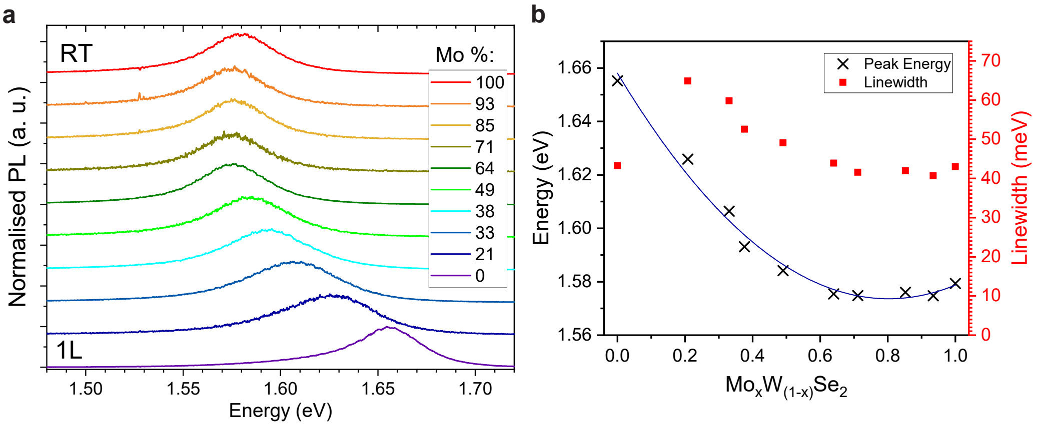

Figure 5.1: **a)** Photoluminescence from alloyed monolayers as a function of molybdenum concentration from 0% (WSe_2), as displayed in purple, to 100% ($MoSe_2$), as displayed in red. The corresponding colour and molybdenum concentration is detailed in the legend to the right. Measurements are taken at room temperature in ambient conditions with a continuous wave 630 nm laser at an excitation power of 20 μW. **b)** Peak energy (Black crosses) and linewidth (Red crosses) of neutral, X^0, exciton PL emission from alloyed monolayers at room temperature as a function of molybdenum concentration from $x = 0.0$ (WSe_2) to $x = 1.0$ ($MoSe_2$). Fitting is applied (solid line) to obtain a bowing parameter of 0.131 ± 0.012 eV.

At room temperature, the optical response of the alloyed monolayers is characterised with a single broad Gaussian-like peak centred at the emission energy. In Fig. 5.1a, the photoluminescence emission from each alloy monolayer is shown. Generally, the linewidth of an excitonic transition in TMD monolayers is strongly affected by the level of structural disorder and density of defects.[241] Figure 5.1b highlights the linewidth as a function of alloy composition, with pure WSe$_2$, MoSe$_2$ and high X$_{Mo}$ alloys displaying the narrowest at ~ 40 meV. The broadest peaks are low X$_{Mo}$ alloys, with $X_{Mo} = 0.21$ possessing a linewidth of ~ 65 meV. While the linewidths at room temperature are less significant due to thermal broadening effects, this is a trend that continues throughout the investigation. Naturally, the alloyed materials are expected to have a broader linewidth than the pure materials due to the added potential for defects within the crystalline lattice during the growth processes.

Figure 5.1b also shows the peak energy of PL emission as a function of alloy composition. At WSe$_2$, shown in purple, the emission peak is centred at 1.655 eV and is tuned through a minimum of 1.575 eV at $X_{Mo} = 0.71$, to an energy of 1.579 eV at pure MoSe$_2$. As such, this provides a continuous tuning range of 80 meV. There is a clear bowing effect that can be described using the following function:[89,90,107]

$$E_{PL}(Mo_xW_{1-x}Se_2) = xE_{PL}(MoSe_2) + (1-x)E_{PL}(WSe_2) - bx(1-x) \tag{5.1}$$

where x is the alloy composition between 0 and 1, $E_{PL}(MoSe_2)$ and $E_{PL}(WSe_2)$ is the emission energy of pure MoSe$_2$ and WSe$_2$ respectively, and b is the so-called bowing parameter. The bowing parameter is a useful metric by which to analytically describe the curve and also compare results with previous (and future) experiments. By knowing the bowing parameter of an alloy system, you can then calculate the composition required to reach a certain emission energy. Here we obtain a bowing parameter of $b = 0.131 \pm 0.012$ eV, in close agreement with previous investigations of Mo$_x$W$_{1-x}$Se$_2$ room temperature PL, where *Tongay, S., et. al.*[89] found $b = 0.14$ eV from a set of 4 alloy compositions, and *Zhang, M., et. al.*[107] found $b = 0.151$ eV from 10 compositions.

Where these previous studies are limited to room temperature spectroscopy, we cool down the alloy monolayers to liquid helium temperatures using a continuous flow cyrostat, with a cold finger at ~5 K (see Sec. 3.2). The neutral exciton resonance narrows and blue shifts when transitioning to low temperatures, and the thermal energy reduces below the trion binding energy,[33] as can be seen in figure 5.2a with the appearance of the trion emission.

The difference between the two pure materials is much more pronounced at low tem-

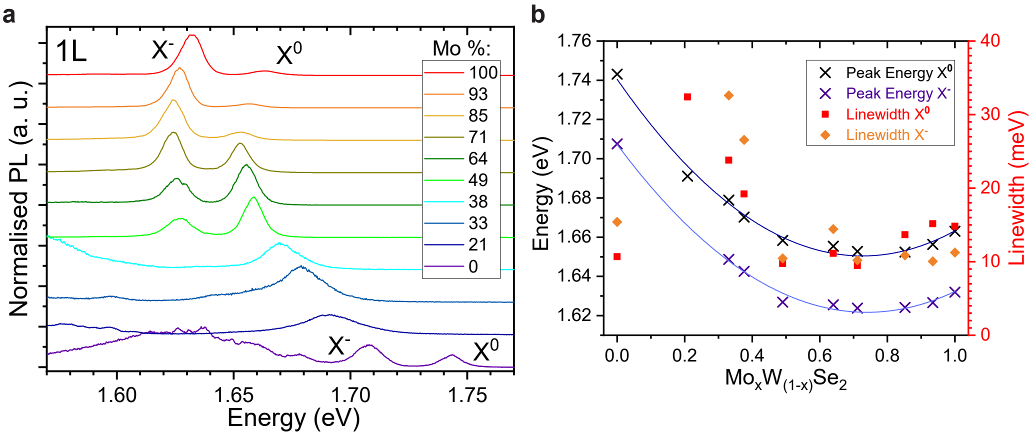

Figure 5.2: **a)** Normalised photoluminescence from alloyed monolayers as a function of molybdenum concentration from 0% (WSe_2), as displayed in purple, to 100% ($MoSe_2$), as displayed in red. The corresponding colour and molybdenum concentration is detailed in the legend to the right. Measurements are taken at liquid helium temperature in vacuum conditions with a continuous wave 630 nm laser at an excitation power of 20 μW. **b)** Peak energy (crosses) and linewidth (filled shapes) of neutral, X^0 (black crosses, red squares), and charged, X^- (purple crosses, orange diamonds), exciton PL emission from alloyed monolayers at low temperature as a function of molybdenum concentration from $x = 0.0$ (WSe_2) to $x = 1.0$ ($MoSe_2$). Fitting is applied (solid lines) to obtain a bowing parameter of 0.171 ± 0.010 eV for X^0, and 0.156 ± 0.008 eV for X^-.

perature. Now, not only in the emission energy, as was the case in figure 5.1, but across the entire spectra. $MoSe_2$ (red in Fig. 5.2) presents two clear resolvable peaks at 1.663 eV and 1.632 eV attributed to the neutral and charged excitonic emission, respectively.[33,256] WSe_2 (purple in Fig. 5.2) on the other hand, presents with the same two exciton and trion emission peaks at 1.743 eV and 1.708 eV respectively, along with a large band of emission which has previously been attributed to various excitonic complexes in WSe_2 including spin dark excitons,[246] exciton-phonon side-bands,[48] and localised states.[50] These are not a sign of reduced optical quality for WSe_2 but simply due to the dark ground state at low temperatures, and are completely expected.[39,45,210] The linewidths associated with the excitonic resonances of both pure materials are remarkably narrow, considering the samples are not encapsulated,[118,256] with $\Gamma_{X^0}(MoSe_2) = 15$ meV, $\Gamma_{X^-}(MoSe_2) = 11$ meV, $\Gamma_{X^0}(WSe_2) = 11$ meV, and $\Gamma_{X^-}(WSe_2) = 15$ meV. The linewidth is a good measure of structural quality, since the presence of defects and structural disorder will only broaden the emission linewidth.[241]

When considering the alloys, a certain amount of molybdenum atoms are replaced with tungsten, expressed as a percentage of Mo in the lattice shown in the legend on the right of figure 5.2a. Both $Mo_{0.93}W_{0.07}Se_2$ and $Mo_{0.85}W_{0.15}Se_2$ produce very similar emission spectra to that of pure $MoSe_2$, with a slight red shift due to the giant bowing effect also seen at RT analysis. Here we observe a minimum X^0 and X^- energy of 1.652 eV and 1.623 eV, respectively, at the $Mo_{0.71}W_{0.29}Se_2$ alloy monolayer, below which the exciton energies begin to blue shift. The linewidths remain similarly narrow also, as detailed by the solid shapes in figure 5.2b, suggesting a high optical quality of material. The emission linewidths actually remain low ($\sim$ 10 - 15 meV) for all alloys above $X_{Mo} \geq 0.49$ (49%). The main difference, apart from emission energy shift as a result of the giant bowing effect already explored at room temperature, is the ratio in intensities between the neutral (X^0) and charged (X^-) exciton resonances, which is heavily influenced by the free carrier densities present in the structures.[38] This can be affected at many stages of fabrication resulting in a lower doping level, and without controlled doping levels it is difficult to infer any alloy specific properties from this alone.

From $X_{Mo} \leq 0.38$, we observe a significant change in the emission spectra. It is at this concentration that the ground state of the alloy (smallest available band gap) changes from being optically bright (similar to $MoSe_2$) to being optically dark (like WSe_2) as predicted by *Wang, G., et. al.*[256] This shift is accompanied by a broadening of the excitonic peaks ($>$ 20 meV) and the trion emission disappears entirely at an alloy concentration of $X_{Mo} = 0.21$, whilst being only just resolvable for $X_{Mo} = 0.33$, and $X_{Mo} = 0.38$. The broadening of the neutral exciton and disappearance of the trion peak indicates that these alloys with high W content have a reduced optical quality compared to the pure materials. A combination of being optically dark in nature which results in an unavoidable impairment of the optical features, and that alloys are inherently more likely to form defect states during the growth process (Chapt. 2). The emission peaks are fitted with a Lorentzian function and the peak centre and linewidth are displayed in figure 5.2b. We then use Eq. 5.1 to find a bowing parameter of $b_{X^0} = 0.171 \pm 0.010$ eV and $b_{X^-} = 0.156 \pm 0.008$ eV for the neutral and charged exciton peaks, respectively. At low temperature, a continuous tuning range of 91 meV can be achieved from 1.743 eV at $X^0(WSe_2)$ to 1.652 eV $X^0(Mo_{0.71}W_{0.29}Se_2)$, or 84 meV from 1.708 eV at $X^-(WSe_2)$ to 1.624 eV $X^-(Mo_{0.71}W_{0.29}Se_2)$. The difference in tuning ranges between the neutral and charged excitons is most likely due to the difference in trion binding energy for the respective materials.[33,44]

Further insight can be obtained from reflectance contrast measurements, using a broad band white light source and comparing the reflected light from the absorbing TMD to a background measurement of the underlying 90 nm SiO_2 / Si substrate, as detailed in Sec. 3.2. Reflectance contrast measurements are much less sensitive to defect states and offer a high quality spectra, even for the optically dark materials, as displayed in figure 5.3.

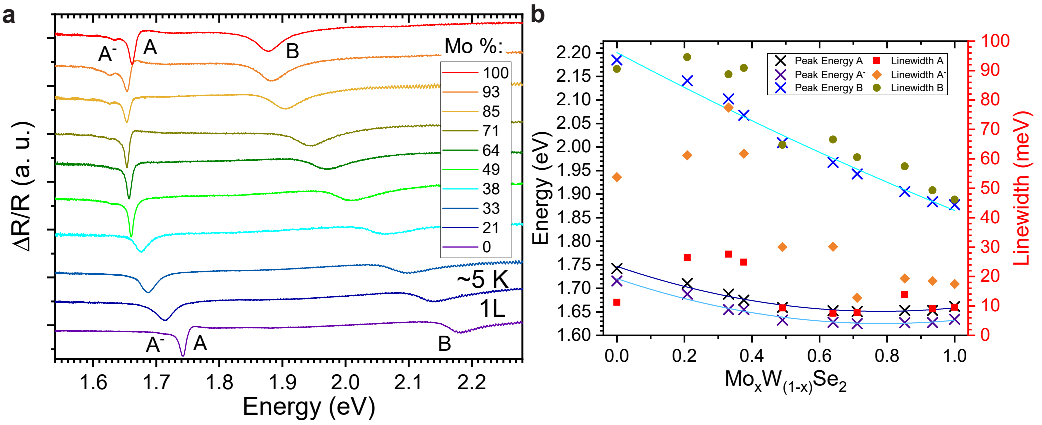

Figure 5.3: **a)** Reflectance contrast ($\Delta R/R$) of alloyed monolayers as a function of molybdenum concentration from 0% (WSe_2), as displayed in purple, to 100% ($MoSe_2$), as displayed in red. The corresponding colour and molybdenum concentration is detailed in the legend to the right. Measurements are taken at liquid helium temperature in vacuum conditions with a broad band white light source. $\Delta R/R = (R_{Flake} - R_{Sub})/(R_{Flake} + R_{Sub})$. **b)** Peak energy (crosses) and linewidth (filled shapes) of neutral A (black crosses, red squares), charged A^- (purple crosses, orange diamonds), and B (blue crosses, yellow circles), exciton absorption from alloyed monolayers at low temperature as a function of molybdenum concentration from $x = 0.0$ (WSe_2) to $x = 1.0$ ($MoSe_2$). Fitting is applied (solid lines) to obtain a bowing parameter of 0.156 ± 0.016 eV for A, and 0.143 ± 0.019 eV for A^- and 0.044 ± 0.053 eV for B.

Two features in the reflectivity spectra are immediately obvious. Firstly, a very narrow 'peak' (or dip) which bows in a similar fashion to the PL spectra shown in Fig. 5.2, from 1.661 eV for $MoSe_2$ (red), through 1.651 eV for $Mo_{0.71}W_{0.29}Se_2$ (dark yellow), to 1.742 eV in WSe_2 (purple). This peak is attributed to the A exciton absorption, and is directly related to the X^0 emission seen in PL. Secondly, a broader peak is seen at higher energies that blue shifts, without pronounced bowing, from 1.878 eV in $MoSe_2$ to 2.185 eV in WSe_2. This second peak is known as the B exciton, and represents the next optically bright exciton available at higher energies due to spin-orbit effects, along with optical selection rules.[7,33,65,256] Finally, in some spectra, it is clear a third peak, just below the A absorption peak. This is the charged A exciton, or trion, absorption resonance.[65] The oscillator strength is much weaker, as shown by the reduced peak intensity, due to the presence of an extra charge carrier.[38] The absorption peaks are fitted using a Lorentzian peak function, with the peak centre and linewidth shown in figure 5.3b. The linewidths of the neutral and charged A excitons agree well with the emission resonances in figure 5.2b, with a small stokes shift seen in the differences in peak energies.[257] Bowing parameters of 0.156 ± 0.016 eV for A, and 0.143 ± 0.019 eV for A^- and 0.044 ± 0.053 eV for B, showing good agreement with the PL results. The B resonance is not accessible with our PL experimental setup, due to an excitation wavelength of 1.96 eV.

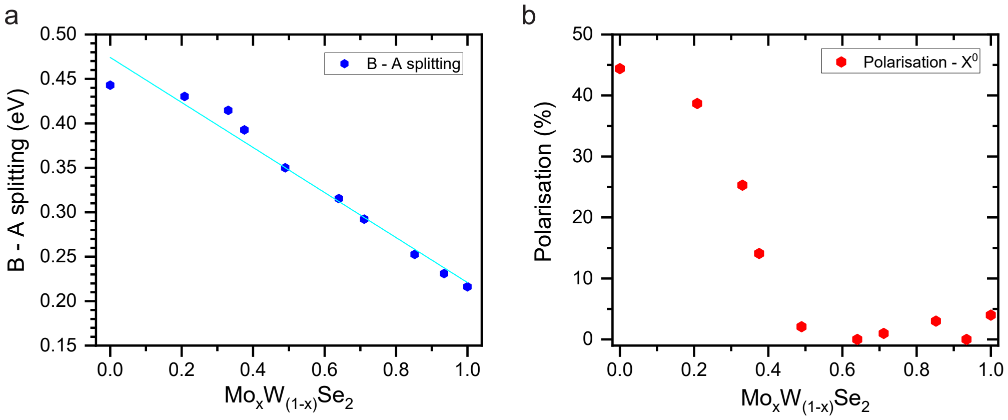

Figure 5.4: **a)** Energy splitting between the A and B monolayer absorption resonances as a function of molybdenum concentration from $x = 0.0$ (WSe_2) to $x = 1.0$ ($MoSe_2$). A linear fit (solid blue line) is applied.**b)** Degree of circular polarisation of neutral exciton PL emission as a function of alloy concentration.

Because the conduction band spin-orbit splitting is an order of magnitude smaller than that of the valence band, the difference between the A and B exciton resonances will provide a decent insight into the valence band spin-orbit splitting of the alloyed monolayers. The results of which are shown in figure 5.4a. Here, we see a linear dependence with alloy concentration in contrast to the findings of *Wang, G., et. al.*,[256] however we present more alloy concentrations and the DFT calculations used in their investigation predicts a linear trend, giving credence to our results. It is unclear exactly why their results deviate from ours, but earlier growths of alloyed materials may have introduced greater strain, or poorly distributed W-content within the Mo lattice, leading to large areas of higher, or lower, alloy concentrations.

We also present the degree of circular polarisation of alloyed monolayer neutral exciton emission as a function of Mo-content (X_{Mo}) as displayed in figure 5.4b. Polarisation is calculated by the difference between co and cross polarised detection intensity, from σ^+

excitation, normalised to the sum of co and cross emission intensity;

$$Polarisation(\%) = 100\frac{(I_{\sigma^+} - I_{\sigma^-})}{(I_{\sigma^+} + I_{\sigma^-})} \tag{5.2}$$

where I_{σ^+} (I_{σ^-}) is the detected intensity of σ^+ (σ^-) polarised light. Polarisation of the pure materials is well reported and these samples behave as expected.[56,58,64,258,259] Curiously, the dependence on alloy concentration is not smooth, with a sharp increase of valley polarisation appearing when Mo-content is reduced below 50%. This suggests that the valley polarisation present in WSe_2 and not in $MoSe_2$ is due to the optically dark nature of WSe_2 and WSe_2-like alloy monolayers inhibiting the valley relaxation of excitons, with the spin-orbit coupling switching at $X_{Mo} \approx 0.49$.[256,260]

5.1.2 Homo-bilayers

Here we investigate the optical response of alloyed homo-bilayers to accompany the monolayer results (Sec. 5.1.1) The key difference is the reduction in spatial confinement and change of dielectric environment, shifting the electronic band structure as described in chapter 2.[12,46,47,261] This results in the lowest energy exciton transition becoming one that is momentum indirect, requiring momentum-carrying phonons to assist the recombination of the carriers. This is demonstrated within the 2L PL spectra as two significant differences. Firstly, the momentum direct A exciton is shifted slightly in energy (compared to the monolayer) due to the change in dielectric environment, there is also a significant reduction in intensity as the K-K (along with the energy degenerate K'-K') exciton is no longer the ground state. Secondly, an extra emission peak appears at ~ 1.55 eV (~ 1.44 eV) in WSe_2 ($MoSe_2$), attributed to the momentum indirect transition. The momentum indirect peak is displayed as a function of alloy concentration in figure 5.5.

The PL spectra displayed in figure 5.5a is quite striking. First of all, there are multiple peaks at the indirect band gap energies for concentrations of 64% and lower. The actual band gap energy of the momentum indirect transitions are inaccessible to photons as they lie outside of the light cone in momentum space. As such, they emit photons only with the additional momentum provided by acoustic or optical phonons. Therefore, all momentum indirect transitions appear in PL as phonon replicas of their optically dark zero phonon lines.[48] Secondly, the bowing effect seen in monolayer transitions is instead replaced with an S-like trend as the alloy concentration is tuned. This can be considered as the standard bowing trend, seen previously in monolayers (Sec. 5.1.1), from $x_{Mo} = 1.0$ to $x_{Mo} \sim 0.3$ followed by a reversal at low x_{Mo} values. The excitonic transitions in bilayers of pure $MoSe_2$

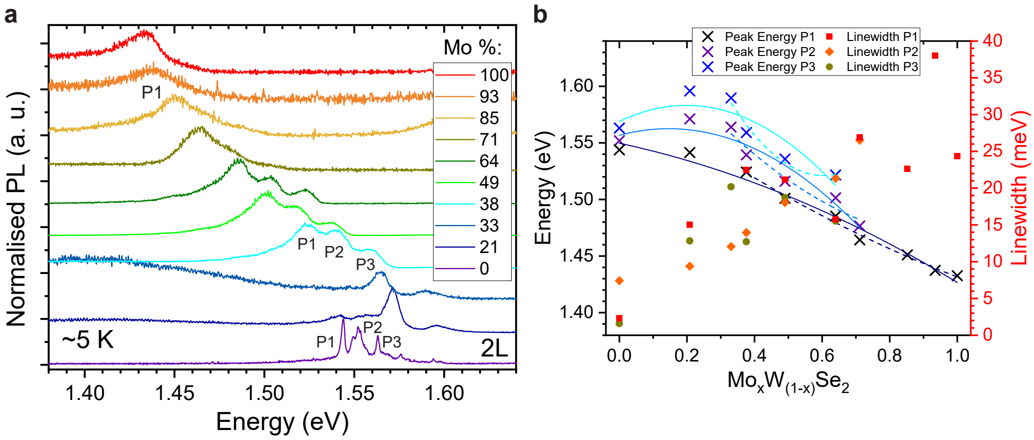

Figure 5.5: **a)** Photoluminescence from the momentum indirect transition in alloyed bilayers as a function of molybdenum concentration from 0% (WSe_2), as displayed in purple, to 100% ($MoSe_2$), as displayed in red. The corresponding colour and molybdenum concentration is detailed in the legend to the right. Three distinct peaks, labelled P1, P2 and P3, are seen for most of the alloys, attributed to phonon replicas of optically dark zero-phonon transitions. Measurements are taken at liquid helium temperature in vacuum conditions with a continuous wave 630 nm laser at an excitation power of 20 μW. **b)** Peak energy (crosses) and linewidth (filled shapes) of P1 (black crosses, red squares), P2 (purple crosses, orange diamonds), and P3 (blue crosses, yellow circles) emission from alloyed bilayers at low temperature as a function of molybdenum concentration from $x = 0.0$ (WSe_2) to $x = 1.0$ ($MoSe_2$). Fitting is applied to both the entire range available (solid lines with negative bowing), and also excluding the lowest two concentrations (dashed lines with positive bowing), highlighting the change in trend for concentrations of $x_{Mo} \leq 0.33$.

and WSe_2 are well known, and the lowest energy band gap transition (highest energy point within the valence band to the lowest energy point in the conduction band) are different for the two materials. For 2L $MoSe_2$ (WSe_2), this transition lies between the Γ_V (K_V) point in the valance band and the Q_C point in the conduction band.[48,261] These points within the electronic band structure will likely behave in different ways as the alloy concentration is tuned. By plotting the peak energies of the momentum indirect transitions as a function of alloy concentration in figure 5.5b, it is clear that this change in transition most likely occurs at a low molybdenum concentrations. To highlight this, two bowing parameters are found for each of the prominent peaks (labelled P1, P2, and P3). Firstly, across the entire alloy range where the peak exists, a negative bowing is found. And secondly, excluding the low Mo %, a positive bowing parameter is found, similar to previous results. Results of the bowing parameter fitting are detailed below in table 5.2.

Table 5.2: Bowing parameters for momentum indirect PL peaks in bilayer alloys

P1		P2		P3	
Range (x_{Mo})	b (meV)	Range (x_{Mo})	b (meV)	Range (x_{Mo})	b (meV)
0.0 → 1.0	-0.06 ± 0.02	0.0 → 0.71	-0.27 ± 0.08	0.0 → 0.64	-0.36 ± 0.16
0.38 → 1.0	0.05 ± 0.04	0.33 → 0.71	0.20 ± 0.34	0.33 → 0.64	0.86 ± 0.44

Because the momentum indirect transitions do not exist within the light cone, they are not optically accessible and therefore invisible in the absorption regime.[12] Figure 5.6a displays the reflectance contrast spectra for the ten alloys. Here we observe the absorption resonances of the momentum direct A, B, and C excitons as the alloy concentration is altered.

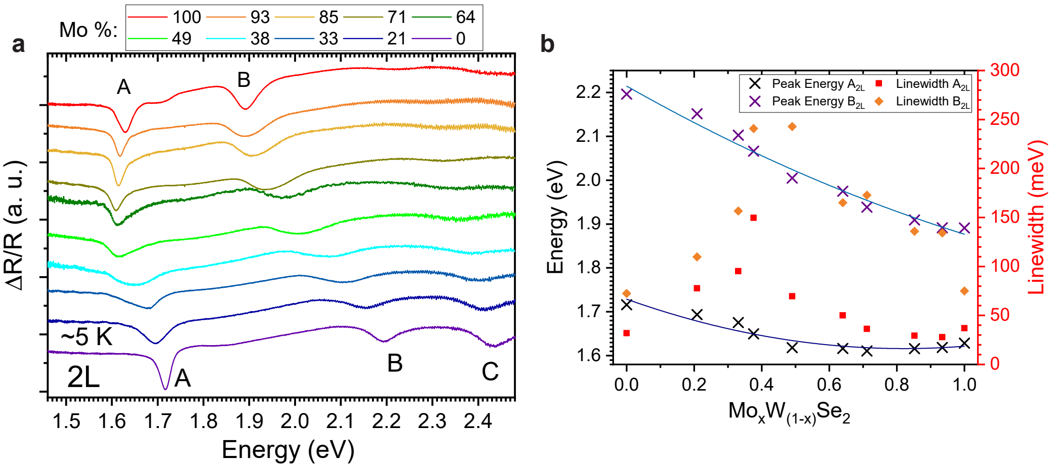

Figure 5.6: **a)** Reflectance contrast ($\Delta R/R$) of alloyed bilayers as a function of molybdenum concentration from 0% (WSe$_2$), as displayed in purple, to 100% (MoSe$_2$), as displayed in red. The corresponding colour and molybdenum concentration is detailed in the legend above. Measurements are taken at liquid helium temperature in vacuum conditions with a broadband white light source. $\Delta R/R = (R_{Flake} - R_{Sub})/(R_{Flake} + R_{Sub})$. **b)** Peak energy (crosses) and linewidth (filled shapes) of bilayer A (black crosses, red squares), and B (purple crosses, orange diamonds) exciton absorption resonances from alloyed bilayers at low temperature as a function of molybdenum concentration from $x = 0.0$ (WSe$_2$) to $x = 1.0$ (MoSe$_2$). Fitting is applied (solid lines) to obtain a bowing parameter of 0.167 ± 0.044 eV for A, 0.099 ± 0.062 eV for B.

The monolayer A and B excitons, which have been studied earlier in this chapter (Sec 5.1.1), are energetically separated by the spin-orbit splitting within the K or K' valleys.[12,17]

In a bilayer, the energy position of these excitons are shifted slightly due to the change in local dielectric environment, but are otherwise the same as the monolayer counterparts. In bilayer $MoSe_2$, the A (B) exciton peak appears at 1.629 eV (1.891 eV), compared to 1.662 eV (1.880 eV) in the monolayer limit. Similarly in WSe_2, the A (B) exciton peak appears at 1.716 eV (2.196 eV), compared to 1.742 eV (2.183 eV) in the monolayer limit (Fig. 5.3). The bilayer A exciton is $\sim$ 30 meV lower energy compared to the monolayer, whereas the bilayer B exciton is found to be $\sim$ 10 meV higher energy. This leads to an increased A-B splitting of $\sim$ 40 meV larger than the monolayer,[46,47] consistent throughout the various alloy concentrations. This highlights the complex nature of the electronic band structure, even between different thicknesses of the same material, let alone different materials and alloys. The C exciton is the next available optically bright exciton, found to exist away from the K valley.[27,262] Finally, a small peak of ambiguous origin, is seen to exist between the A and B excitons in bilayer $MoSe_2$ at $\sim$ 1.70 eV, has previously been attributed to both excited A_{2s} exciton,[47] and interlayer exciton,[263] in which the constituent charge carriers exist in two separate layers, or indeed a superposition of the two.

5.2 Polaritons in alloy monolayers

So far, the measurements have been limited to the bare flake, on a 90 nm SiO_2 / Si substrate, measured in μ-PL and μ-RC using a flow cyrostat, as described in section 3.2. From this optical spectroscopy, the alloys have demonstrated high optical quality with narrow linewidths, especially at high Mo %. We will now focus on optical spectroscopy within the strong coupling regime, using an open tunable microcavity consisting of a planar bottom mirror and a hemispherical top mirror positioned 2-3 μm above that confines the cavity mode in all three dimensions.[43,68,152,155,223,230] As described in section 3.2.3, the mirrors have full motion control using a set of piezo stages. The cavity length is tuned in small steps of the bottom mirror along the z-axis piezo stage, allowing tunable control of the cavity mode energy. To ensure the highest light confinement, the lowest order Laguerre-Gaussian mode, LG_{00}, is used (see Chapt. 2). The three dimensional optical confinement provided by the concave top mirror generates a set of transverse modes for each longitudinal mode.[152,155,223] The energy separation between these transverse mode can give an indication of the cavity mode volume, with a smaller mode volume resulting in a large separation between modes.[223]

The cavity mode can couple to the excitonic absorption resonances in two distinct manners (Detailed fully in Chapt. 2). The first, which is observed through a broadening of the cavity mode and an increase in emission intensity, is known as weak coupling occurs when the combined non-radiative losses are larger than the coupling strength. When coupled in this manner, the photonic density of states into which the excitonic state can emit photons, is increased by the presence of the resonant cavity mode, resulting in an increase of the emission intensity. The cavity mode and trion also share non-radiative loss mechanisms, resulting in an increase in observed linewidth.[152]

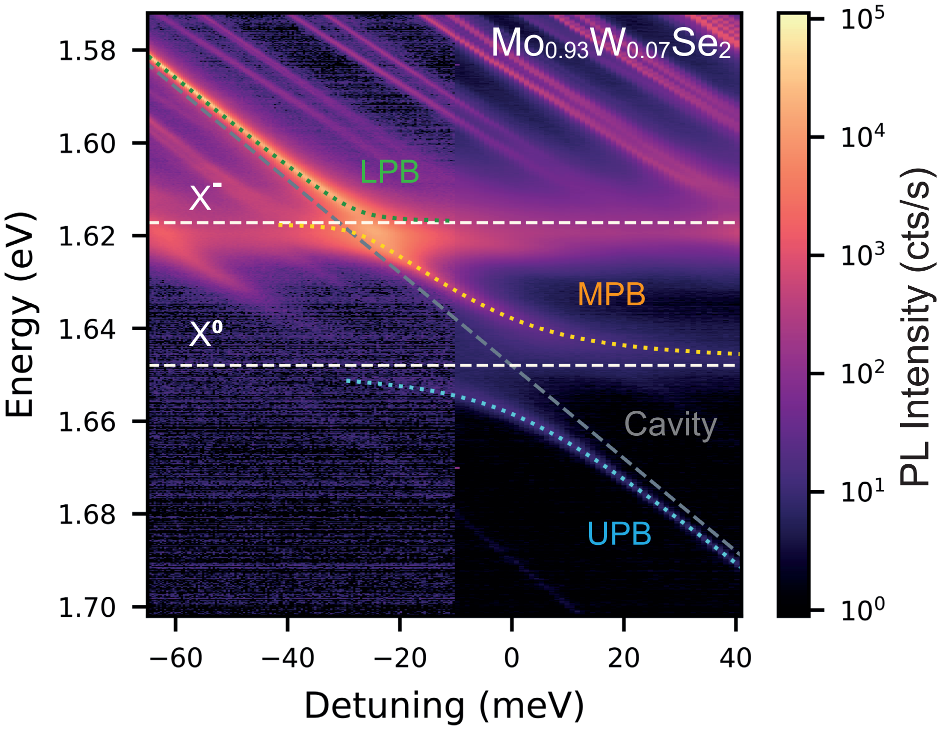

Figure 5.7: PL emission from monolayer $Mo_{0.93}W_{0.07}Se_2$ as a function of cavity photon energy and X^0 detuning. Strong light matter coupling is observed at both trion, X^-, and neutral exciton, X^0, resonances indicated here by white dashed lines at $E_{X^-} = 1.617$ eV and $E_{X^0} = 1.648$ eV respectively. PL spectra are fitted with a Lorentzian peak and are modelled with a 3 level coupled oscillator model to find the lower (LPB), middle (MPB), and upper (UPB) polariton branches are detailed here as green, orange, and blue dotted lines, respectively. The cavity mode is shown as a grey dashed line. The Rabi splitting is found to be $\hbar\Omega_R(X^0) = 20.68 \pm 0.08$ meV at the neutral exciton resonance and $\hbar\Omega_R(X^-)$ $= 5.39 \pm 0.13$ meV at the trion resonance.

The second coupling regime, associated with large oscillator strength and narrow linewidths, is strong coupling. Strong coupling occurs when the coupling strength is larger than the combined non radiative losses of the constituent states. In this regime the cyclical transfer of energy between the cavity mode and excitonic state results in a modification of the energy spectrum, opening a gap between two energy states known as the upper and lower polaritons branches. This energy gap, or Rabi splitting, is dependent on factors from both the microcavity, such as quality factor and mode volume, and the excitonic state to which the cavity mode is coupling, such as the oscillator strength and linewidth. Strong coupling is observed experimentally through a characteristic anti-crossing as the cavity mode is tuned into resonance with the excitonic absorption energy.[43,68,152,155,223,230]

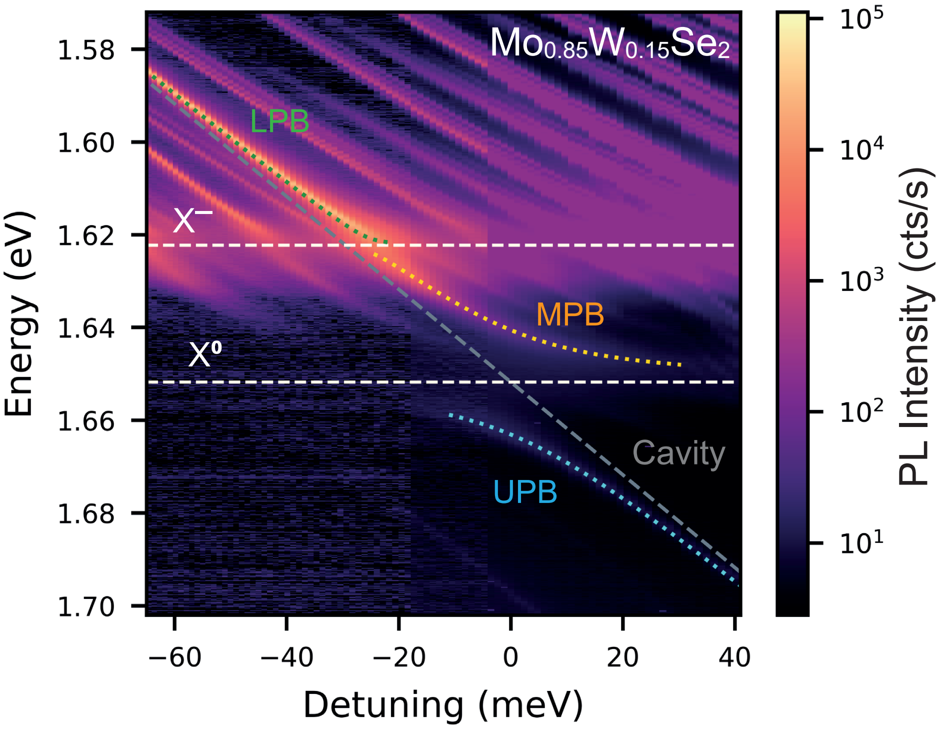

Figure 5.8: PL emission from monolayer $Mo_{0.85}W_{0.15}Se_2$ as a function of cavity photon energy and X^0 detuning. Strong light matter coupling is observed at both the neutral exciton, X^0, and at the trion resonance, X^-, indicated here by white dashed lines at E_{X^-} = 1.622 eV and E_{X^0} = 1.652 eV respectively. PL spectra are fitted with a Lorentzian peak and are modelled with a 3 level coupled oscillator model to find the lower (LPB), middle (MPB), and upper (UPB) polariton branches are detailed here as green, orange, and blue dotted lines, respectively. The cavity mode is shown as a grey dashed line. The Rabi splitting is found to be $\hbar\Omega_R(X^0) = 22.56 \pm 0.08$ meV at the neutral exciton resonance, and $\hbar\Omega_R(X^-) = 3.26 \pm 0.07$ meV at the trion resonance.

Alloy monolayers of $x_{Mo} = 0.93$ and 0.85 were exfoliated and transferred onto a planar

DBR substrate. As demonstrated by the monolayer reflectivity measurements (Fig. 5.3), high Mo % alloys show clear trion (A^-) resonances as well as the neutral (A) exciton peaks. The PL signal collected from the alloyed TMD monolayers, as the cavity length is reduced, is displayed as a colourmap in Figs. 5.7 and 5.8 as a function of detuning (the energy difference between the cavity mode and unperturbed exciton, X^0). As the cavity mode (Grey dashed lines in Figs. 5.7 and 5.8) is tuned into resonance with the neutral exciton, X^0 (White dashed lines), at 1.648 eV (1.652 eV) in $Mo_{0.93}W_{0.07}Se_2$ ($Mo_{0.85}W_{0.15}Se_2$), a large anti-crossing is observed, in both alloyed monolayers. A clear indication of the strong coupling regime. When the peak energies, gathered through a Lorentzian peak fitting analysis of the cavity modes, are fitted using a 3 level coupled oscillator model (see Chapts. 2, 4), we obtain a Rabi splitting of 20.7 ± 0.1 meV for $Mo_{0.93}W_{0.07}Se_2$ and 22.6 ± 0.1 meV for $Mo_{0.85}W_{0.15}Se_2$. These values are higher than previously seen in pure $MoSe_2$ in similar cavity structures,[43,68,170] owing to the high optical quality, narrow linewidths and large oscillator strengths that the alloy monolayers demonstrate.

Furthermore, the observation of strong coupling with the trion resonance is another demonstration of the high optical quality of the alloy monolayers. Trion absorption resonances generally have much lower oscillator strength, leading to similarly lowered coupling strength, when compared to the neutral exciton.[43,47,68,170] Often, only weak coupling is observed at the trion energy.[154,155,170] Here, we observe a characteristic anti-crossing at the trion energy, X^- (White dashed lines), of 1.617 eV (1.622 eV) for the $x_{Mo} = 0.93$ ($x_{Mo} = 0.85$) alloy monolayer, a Rabi splitting of 5.4 ± 0.1 meV (3.3 ± 0.1 meV) is found.

For the first time, strong coupling has been observed in TMD alloy monolayers. The high optical quality of TMD alloys, especially of high Mo-content, has been demonstrated in optical spectroscopy of both, the bare flake on SiO_2 (Sec. 5.1.1), and in a tunable microcavity on DBR substrates. The usage of alloying in TMDs should be considered a vital technological step forward towards fully tailored properties in polaritonic structures and devices.[171,240,264]

By employing these alloyed materials as part of a heterostructure, coupled to a pure WSe_2 monolayer as shown in figure 5.9a, it is possible to tune the long lived interlayer exciton emission energy, by varying the alloy concentration. The expectation is that the emission energy of the interlayer exciton is tuned from ~ 1.4 eV as seen in $MoSe2_2$ / WSe_2, towards the bilayer WSe_2 band gap close to 1.7 eV following the behaviour of the alloy conduction band. As is shown in figure 5.9b, what we observe instead is a hybridisation of the interlayer exciton with the momentum indirect transition reported in figure 5.5, effectively pinning the emission energy to ~ 1.55 eV, as the alloy concentration is tuned close to

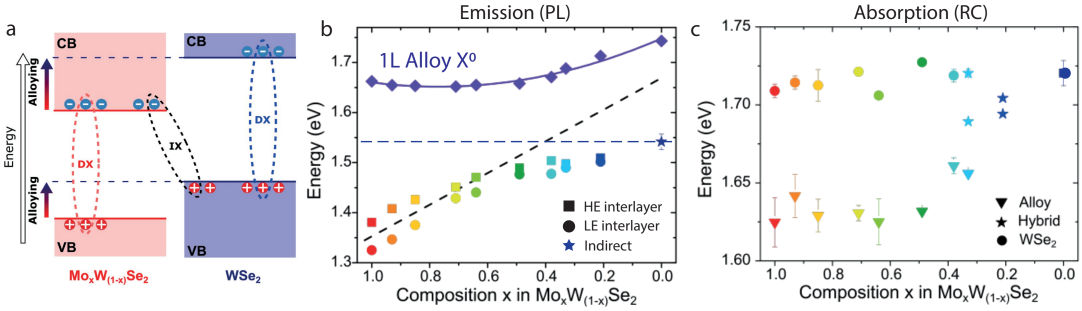

Figure 5.9: Tuning of band structure and excitonic features in $Mo_xW_{1-x}Se_2$ / WSe_2 heterostructures as a function of alloy concentration x. **a)** Schematic of the band alignment including the exciton states. As alloy concentration x_{Mo} is decreased, the band structure of the alloy tends towards WSe_2. **b, c)** Emission (b) and Absorption (c) energies of the exciton features as a function of alloy concentration. Image adapted from Catanzaro.[145] (*under embargo*)

WSe_2. Although the interlayer excitons are not observed through absorption measurements due to the very low oscillator strength of the resonance, reflectivity measurements of the two intralayer A excitons as a function of alloy concentration, as detailed in figure 5.9c, confirm the hybridisation of the conduction bands at low molybdenum concentrations. The hybridisation of resonant interlayer and intralayer excitons is therefore obtained through alloying. It is predicted that a hybridisation of intralayer and interlayer exciton would couple to a cavity photon when placed within an optical microcavity to produce highly interacting polaritons.[116,265,266,267,268] While coupling to alloy monolayers of high x_{Mo} concentrations has been displayed earlier in this chapter (Figs. 5.7 and 5.8), experiments towards the observation of dipolaritons using alloyed monolayers remain inconclusive. As such, we instead investigate this further by using $MoSe_2$ / WS_2 heterostructures that have already been shown to produce hybridised interlayer and intralayer excitons.[113,143,269]

5.3 Experimental observation of hybridised inter-intra-layer exciton-polaritons in a $MoSe_2$ / WS_2 heterostructure

The experiments discussed thus far have demonstrated the high optical quality of the alloyed TMDs and provide a unique method of tuning and engineering the band structure. One of the major benefits of TMDs, over other semiconductor materials, is the ability to stack multiple layers of material without the restrictions of lattice mismatch and dangling bonds that limit 3D alternatives. The ability to stack multiple layers of different materials, including insulating hexagonal boron nitride, and semi-metallic graphene, into structures known as van der Waals heterostructures (HS),[110] after the force that holds the layers together (see Sec. 2.6), provides a massive collection of potential structures and devices. Furthermore, by introducing the ability to further tune band gaps and excitonic resonances through alloying, an unprecedented level of control over the devices electronic and optical properties is reached.

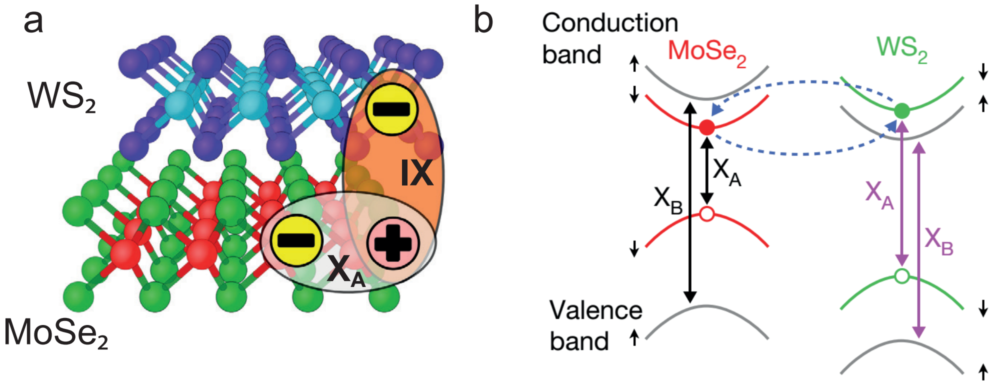

Figure 5.10: **a)** Cartoon representation of the $MoSe_2$ / WS_2 crystalline structure with the excitonic resonances being studied. **b)** Simplified electronic band structure of the two materials with the hybridisation of the resonant conduction bands. Image adapted from *Alexeev, E.M., et. el.*[113].

The promise of interlayer excitons (labelled 'IX' in figure 5.10a) stems from the larger physical separation of the composite carriers, which provides a larger dipole moment compared to their intralayer counterparts. A large dipole moment is advantageous due to the electronic interaction strength between the excitons depends on this dipole moment.[265,269] Highly interacting excitons are detected experimentally through a characteristic blueshift of PL emission,[269,270] which can, in turn, be used to estimate exciton density and study exciton transport controlled both electrostatically[271,272] and optically[273,274] leading to optically controllable excitonic transistors.[275]

Normally, these highly interacting interlayer excitons do not absorb light due to the orientation of the dipole moment perpendicular to the crystal plane does not interact with the electric field of the excitation laser, along with a smaller oscillator strength associated with reduced overlap of the electron and hole wave functions.[266] However by hybridising or coupling an interlayer exciton with an intralayer exciton, it is possible to create a hybrid quasiparticle with both large dipole moment and large oscillator strength[113,123,142,143,144,146,269] that can be coupled with a cavity photon to produce polaritons with large dipole moments.[116,148,265,266,267,268] These so-called dipolaritons build upon research into direct exciton-polaritons offering greater freedoms of control with a view towards possible new polaritonic applications including tunable single photon emission,[276] terahertz emission,[277,278,279] quantum logic gates,[280] as well as both indirect exciton[281] and dipolariton[234,282] based Bose-Einstein condensates (BEC). Research into TMD based dipolaritons has been limited to simultaneous coupling of excitons in QWs and $MoSe_2$ monolayer excitons to a shared photonic cavity mode,[234,283] while fully TMD based dipolariton devices are only just being realised.[148]

Recent studies by *Alexeev, E.M., et. al.*,[113] and *Zhang, L., et. al.*,[144] in which intralayer excitons are observed to hybridise with interlayer excitons in a TMD based $MoSe_2$ / WS_2 heterostructure due to the resonant conduction bands of the constituent materials[284] as shown in figure 5.10b. It is shown that the hybridisation strength can be tuned with interlayer twist angle due to moiré superlattice effects. Additional features present in the reflectivity spectra arise due to hybridised exciton minibands formed by the moiré superlattice. While hybridisation effects were initially thought to only exist at twist angles close to zero,[113,143] it has recently been determined that moiré superlattice effects, and hybridisation continue at large twist angles with a tuning of the resonant energies, oscillator strengths and inter-intra-layer mixing.[144]

Here, we employ the same materials, with large twist angle, in an effort to go a step further and couple cavity photons to the hybridised state with large dipole moment. A graphical representation of the heterobilayer is shown in figure 5.10a.

Figure 5.11a shows a bright-field optical microscope image (Sec. 3.2.1) of the sample being investigated, with a $MoSe_2$ / WS_2 heterobilayer (Fig. 5.10) fully encapsulated with thin hBN. The sample is built with collaborators at *The University of Manchester* and transferred onto a DBR substrate. The outlines of the materials have been highlighted and labelled accordingly. Initial optical spectroscopy (Sec. 3.2) shows a number of absorption peaks near the monolayer $MoSe_2$ intralayer exciton resonances,[47] with monolayer WS_2 intralayer excitons at ~ 2.0 eV[113,285] existing outside of our DBR stopband (1.65 eV $\pm$ 0.11 eV). Figure 5.12b details a line-scan of reflectance moving the excitation and detection focus spot in a straight line through the overlapping heterostructure (HS) region, starting outside of the HS area at 'Pos 1' (Blue circle in fig. 5.12a), through the HS, and concluding at 'Pos 7' (Red circle in fig. 5.12a), at the edge of the HS area on the opposite side. The corresponding positions are represented in circles of the same colour in figure 5.12a. A lot of information

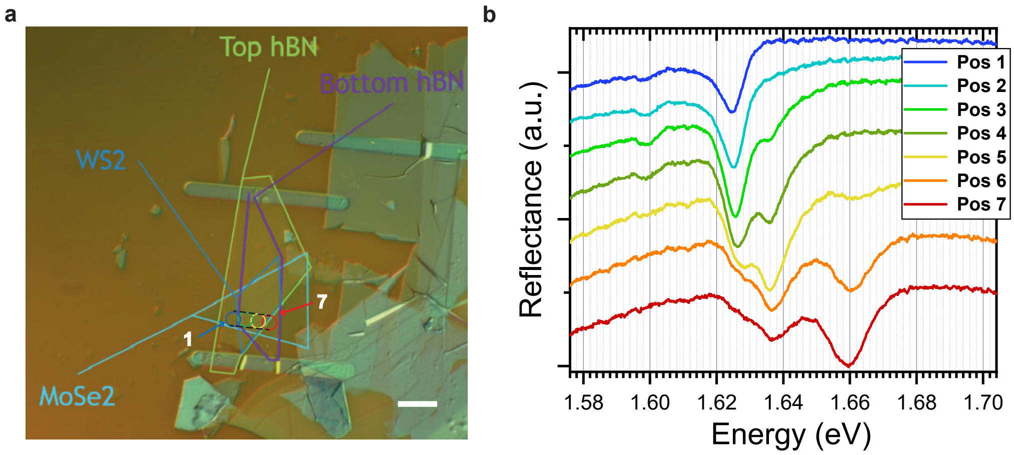

Figure 5.11: **a)** Optical microscope image of the $MoSe_2$ / WS_2 heterostructure (see 3.2.1 for details). The individual layers of the HS are outlined for clarity. Scale bar is 10 μm. **b)** Reflectance data obtained by moving the excitation/detection spot through the heterostructure area from position 1 (blue circle), to position 7 (red circle).

can be gained from performing these types of scans as it provides a rapid assessment of the entire structure. Outside of the HS area, there is a small region of uncoupled $MoSe_2$, from which we can observe the intralayer neutral and charged exciton absorption resonances, seen in the reflectivity spectrum of 'Pos 1', at 1.625 eV and 1.599 eV, respectively. As the line-scan position is moved into the coupled HS, a third peak appears at 1.635 eV. The current working theory is that this peak most likely originates from the interlayer exciton, and that the transfer of oscillator strength from peak 2 to peak 3, suggests a hybridisation of these two peaks. Finally, a fourth peak appears at 1.66 eV and continues to grow as the position is moved towards the edge of the heterostructure, most likely originating from uncoupled $MoSe_2$ in a different dielectric environment to the uncoupled absorption in 'Pos 1'. The uncoupled region of $MoSe_2$ close to 'Pos 1' is only encapsulated with top hBN, while the uncoupled region of $MoSe_2$ close to 'Pos 7' is encapsulated with only bottom hBN. The complex nature of the structure including further complications arising from multiple areas of uncoupled $MoSe_2$ is addressed later on, however the formation of an extra absorption resonance only active inside the coupled HS region, along with the observed transfer of oscillator strength provides evidence of hybridisation between the intralayer $MoSe_2$ X_A and the $MoSe_2$ / WS_2 interlayer exciton.

By placing the $MoSe_2$ / WS_2 heterostructure into a open microcavity (Sec. 3.2.3) and

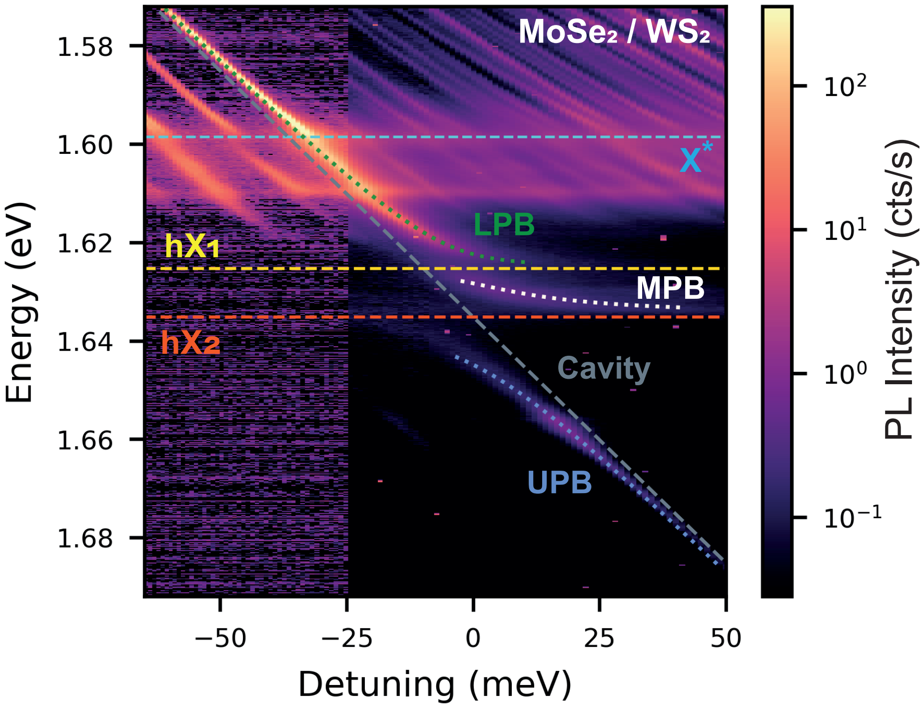

Figure 5.12: PL emission from a $MoSe_2$ / WS_2 heterostructure as a function of cavity photon energy and hX2 detuning. Strong coupling is observed at two resonances at 1.625 eV and 1.635 eV, denoted here 'hX1' and 'hX2' and displayed with yellow and orange dashed lines respectively. We also observe weak coupling with the trion, X*, resonance at 1.599 eV represented with a light blue dashed line. The LG_{00} cavity mode is displayed as a grey dashed line. The PL spectra are fitted using Lorentzian peak analysis, and a 3 level coupled oscillator model is applied to find the lower (LPB), middle (MPB), and upper (UPB) polariton branches, represented here as green, white, and blue dotted lines respectively. The Rabi splitting at hX1 is found to be $\hbar\Omega_R(hX_1) = 8.36 \pm 0.30$ meV and $\hbar\Omega_R(hX_2) = 18.52 \pm 0.20$ meV.

tuning the cavity mode into resonance with the hybridised X_A / IX excitons we can then observe strong light matter coupling with the resultant quasiparticle possessing a large dipole moment obtained from the interlayer exciton fraction. Figure 5.12 displays the PL emission of the $MoSe_2$ / WS_2 HS as the cavity mode (grey dashed line) is tuned through the excitonic resonances shown as horizontal dashed lines. At an energy of 1.599 eV, the LPB is enhanced and broadened as the cavity mode couples weakly to the $MoSe_2$ charged exciton resonance, X^*. This matches directly the lowest energy absorption peak in figure

5.11b. There is a second weak coupling at an energy of ∼ 1.61 eV to a resonance that is not observed in the RC line-scan of the HS (Fig. 5.11). The origin of this resonance is not clear. As the cavity mode is tuned towards the two main absorption peaks seen in figure 5.11b, two anti-crossings are observed, splitting the cavity mode into three distinct and resolvable polariton branches; a lower (LPB), middle (MPB) and upper (UPB) polariton branches. These characteristic anti-crossings are the experimental observation of the onset of strong coupling (Chapt. 2) of the two hybridised resonances, hX_1 and hX_2 with the cavity photons at 1.625 eV and 1.635 eV respectively. The peak energies of the three polariton branches as a function of cavity mode detuning (shown in figure 5.12 as green (LPB), white (MPB), and blue (UPB) dotted lines) are found using a Lorentzian peak fitting and fitted to a three level coupled oscillator model to determine a Rabi splitting of 8.4 ± 0.3 meV for hX_1 and 18.5 ± 0.2 meV for hX_2. The large value of Rabi splitting at hX_2 indicates a significant transfer of oscillator strength from the $MoSe_2$ intralayer X_A exciton to the interlayer exciton. Finally, weak coupling is observed again at ∼ 1.66 eV where the UPB is broadened and enhanced. This resonance corresponds with the last peak observed in figure 5.11b.

As previously mentioned, there are two areas of uncoupled $MoSe_2$ with different dielectric environments that show absorption resonances near the edges of the HS making it difficult to unambiguously identify the origins of these resonances to which the cavity mode is coupling. In an effort to reduce this ambiguity, the uncoupled regions of $MoSe_2$ are etched off using AFM. The resulting HS is displayed in figure 5.13a as an optical microscope PL image (Sec. 3.2.1). Here we see that only the quenched PL inside HS, outlined by blue dashed line, is visible while no $MoSe_2$ is observed. The bright area just above and below the HS is due to uncoupled WS_2 where the absorption resonance is not within the investigated energy range.[113,285]

Figure 5.13b shows a repeat of figure 5.11b taking a reflectivity measurement as the excitation/detection focus spot is moved through the HS region. It is instantly clear that the peak of 1.66 eV in figure 5.11b is due to the uncoupled $MoSe_2$. Interestingly, the first absorption resonance at ∼ 1.60 eV has become more pronounced, possibly due to an increase in doping during the etching process, since the trion absorption strength is influenced by the intrinsic level of dopants. Crucially however, the two resonances within the HS, previously labelled 'hX_1 and 'hX_2' are still observed within the HS region at 1.616 eV and 1.623 eV, with a redshift from figure 5.11b due to the strain induced from etching away the uncoupled $MoSe_2$. Once again, this data has not been normalised to the off-flake reflectivity because of the shifting background level as a function of excitation/detection spot position. This is most dramatic when comparing 'Pos 1', where a gentle arching spectrum is displayed, to

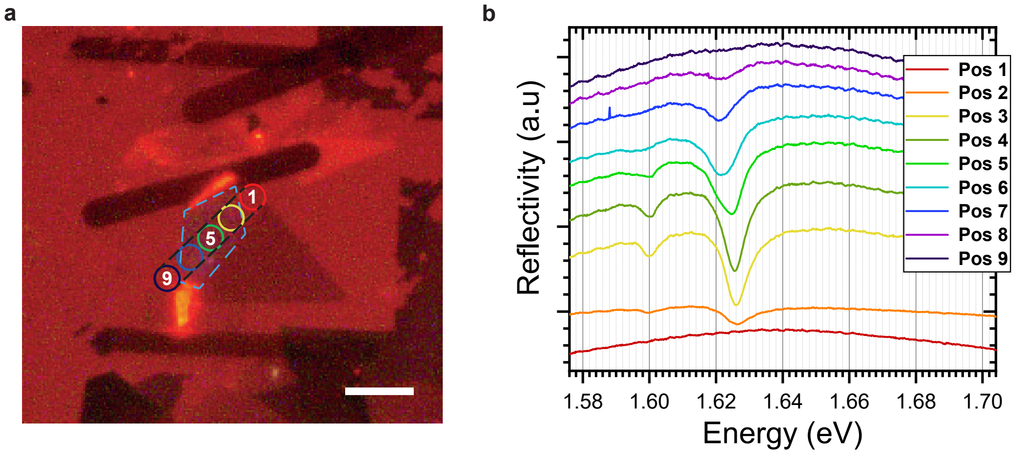

Figure 5.13: **a)** Photoluminescence image using an optical microscope (see 3.2.1 for details). This image is taken using a 20x objective lens for 10s exposure with 9.6x artificial amplification. The dim purple area outlined with a light blue dashed line is the coupled $MoSe_2$ / WS_2 heterostructure, and the brighter area just above and below the HS is from uncoupled WS_2. Scale bar is 10 μm. **b)** Reflectivity data obtained by moving the excitation spot through the heterostructure area from position 1 (highlighted in red), through position 5 (green), to position 9 (purple). The two peaks previously identified as 'hX1' and 'hX2' are still visible within the HS region at $\sim$ 1.626 eV and 1.621 eV respectively. The $MoSe_2$ X_A resonance, previously at 1.66 eV in Fig. 5.11b is no longer visible, having been removed from the sample.

'Pos 2' where the spectrum looks much flatter. While these differences could be accounted for with data processing techniques, the presentation of the unprocessed spectra as displayed here provides an intuitive insight into the HS, even without data processing.

Placing the etched sample back into the open microcavity leads to the results presented in figure 5.14. It is immediately clear that the increased absorption strength of the trion resonance at $\sim$ 1.60 eV, as observed in figure 5.13b, is now sufficient for the observation of strong coupling. The depth of an absorption resonance is inherently linked to the oscillator strength of a resonance, and therefore the photon-exciton coupling strength, where an increase in oscillator strength will lead to a larger Rabi splitting. In this case, the Rabi splitting of 6.2 meV is now sufficient to observe a clear anti-crossing at the trion resonance. Once again we observe two anti-crossings at the hX_1 and hX_2 energies. When fitting the polariton branches to a four level coupled oscillator model, a Rabi splitting of 14.9 meV (19.4 meV) is found for hX_1 (hX_2) at 1.613 eV (1.623 eV). Interestingly, the Rabi splittings

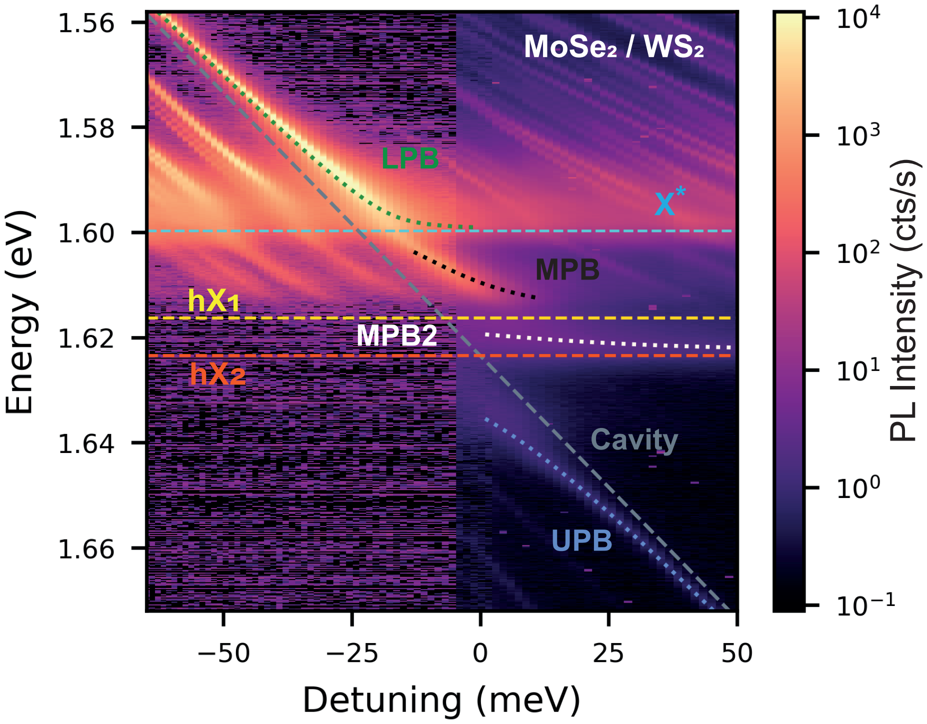

Figure 5.14: PL emission from a $MoSe_2$ / WS_2 heterostructure as a function of cavity photon energy and hX_2 detuning. Strong coupling is observed at two resonances at 1.616 eV and 1.623 eV, denoted here 'hX_1' and 'hX_2' and displayed with yellow and orange dashed lines respectively, as well as at the trion, X*, resonance at 1.600 eV represented with a light blue dashed line. The LG_{00} cavity mode is displayed as a grey dashed line. The PL spectra are fitted using Lorentzian peak analysis, and a 4 level coupled oscillator model is applied to find the lower (LPB), two middle (MPB1 and MPB2), and upper (UPB) polariton branches, represented here as green, black, white, and blue dotted lines respectively. The Rabi splitting at hX1 is found to be $\hbar\Omega_R(hX_1) = 14.82 \pm 0.55$ meV and $\hbar\Omega_R(hX_2) = 19.41 \pm 0.49$ meV. The trion resonance splitting is found to be $\hbar\Omega_R(X*) = 6.18 \pm 0.42$ meV

found in this sample are larger post-etching, compared to what is observed pre-etching. The expectation is that the absorption resonances would broaden due to thermal cycles and etching procedure damaging the integrity of the internal crystal structure, increasing the density of defects and reducing the homogeneity of the dielectric environment. The persistence of high Rabi splittings, suggests that these procedures have not damaged the heterostructure greatly. Lastly, the coupling observed at 1.66 eV in figure 5.12 is no longer seen due to the $MoSe_2$ having been etched away.

It is of course possible that the effect seen in figure 5.11b is not due to a transfer of oscillator strength but rather a shift in energy of the $MoSe_2$ X_A resonance due to the change in dielectric environment as the $MoSe_2$ layer makes contact with the WS_2 layer. However, this is not accompanied by a similar shift in trion resonance. The trion could disappear due to the expected transfer of holes into the $MoSe_2$ monolayer from the WS_2 due to the type II band alignment making the $MoSe_2$ layer charge neutral, and as such would posses no trion resonance. The issue with this idea however, is that there remains two distinct peaks within the HS area, while the trion disappears without blue-shifting, and more rapidly than the third peak at 1.635 eV appears. Comparing the spectra seen in this work to previous investigations, the main difference is the splitting between the two hybridised peak, often observed at large energy splitting of $\sim$ 40 meV,[113,143,148] whereas the splitting here is limited to $\sim$ 10 meV. This inconsistency can be explained by the large twist angle of the two monolayers, along with sub-optimal interlayer coupling reducing the hybridisation strength, and therefore energy splitting. For example, a study by *Zhang, L., et. al.*,[144] shows that a $MoSe_2$ / WS_2 with 20° twist angle, results in a splitting between the two hybridised peaks of just $\sim$ 15 meV.

The one thing that is clear, is that more data is needed. While multiple conflicting explanations exist for the same observations, an adequate conclusion cannot be reached. Therefore, more samples will be measured going forward, with great care needed over the fabrication process to make sure that $MoSe_2$ monolayer exists entirely within the hBN encapsulation, and ideally have a large enough coupled HS area, such that any uncoupled regions will not interfere with the measurements within the HS.

These experiments present a path towards strongly interacting hybridised polaritons with permanent dipole moment (dipolaritons or dipolar-polaritons), however the ambiguous origins of the exciton resonances need to be explored further. New sample heterostructures need to be constructed with great care taken with the placement of monolayers, both coupled and uncoupled. Ideally a large enough coupled region would provide sufficient distance from any uncoupled $MoSe_2$ and avoid similar issues as were encountered here. Nonetheless, the results presented here are of significant value as a proof of concept. A very recent study by *Zhang, L., et. al.*,[148] employing a planar cavity, demonstrates strong coupling to moiré excitons in a $MoSe_2$ / WS_2 heterostructure with enhanced non-linearities in the moiré polaritons, compared to $MoSe_2$ exciton-polaritons, due to moiré lattice confinement. It should be noted here that the differences in naming conventions of these polaritons in $MoSe_2$ / WS_2 is mostly due to the lack of unambiguous source in our sample, whereas the moiré theory available to *Alexeev, E.M., et. al.*[113] and *Zhang, L., et. al.*,[148] match the experimental data very well. Our efforts to observe similar non-linearities are detailed below.

5.4 Non-linear polariton-polariton interactions

Cavity reflectivity experiments were completed using 90 ps broad-band pulses with 80 MHz repetition rate and variable average power aiming to observe non-linear effects in hybridised dipolaritons. The reflectivity spectra are obtained as the cavity length is decreased, by incrementing the z-axis piezo voltage, and are normalised to a background spectrum taken at the highest voltage, after the UPB has dimmed fully. Reflectance contrast is therefore calculated as $RC(a.u.) = (R - R_{BG})/R_{BG}$ where R is the reflectivity of the active region, and R_{BG} is the reflectivity of an inactive region.

By increasing the density of excitons within a confined space, for example, a 2D material, the exciton-exciton interactions are expected to increase in a non-linear fashion.[286] Due to the large dipole moments associated with hybridised inter-intra-layer excitons, the hX-hX interaction strength is larger than standard intralayer excitons.[265,270] This manifests in an observable blueshift of the MPB originating from two complimentary processes. Firstly, the interlayer exciton resonance blue shifts as densities are increased.[270] Secondly, as the Rabi splitting decreases, the MPB will become closer to the UPB at higher energies. Both result in an observable blue-shift of the MPB.

Instead, what we observe here is a blueshift of the LPB, and redshift of the MPB as the rabi splitting of the trion resonance collapses due to the Coulomb interactions of charged excitons. These strength of the trion-trion coulomb interactions are also expected to be much larger than the standard neutral exciton-exciton, and indeed the hX-hX interactions, thanks to the presence of an extra charge carrier in the bound state. Trion polaritons share a lot of the properties that make exciton polaritons so favourable for opto-electronic applications, as well as having a higher trion-trion interaction strength leading to unique non-linear effects.[43,68,226,235] Interaction-based effects such as polariton Bose-Einstein condensation and superfluidity,[287] quantum emission,[288,289,290] along with fully optical polariton switches and transistors[240,291] have been realised outside of TMDs.

Figure 5.15 shows the cavity reflectivity experiments, as the average power is increased from a) 1000 μW, through b) 2500 μW, to c) 5000 μW. The Rabi splitting is decreased from $\sim$ 5 meV at 1 mW Av. power in 5.15a to $\sim$ 2 meV at 2.5 mW Av. power in 5.15b, before completely collapsing at 5 mW in 5.15c. The experiment is then repeated at 1 mW Av. power, where the Rabi splitting is fully restored, demonstrating that the effect is fully

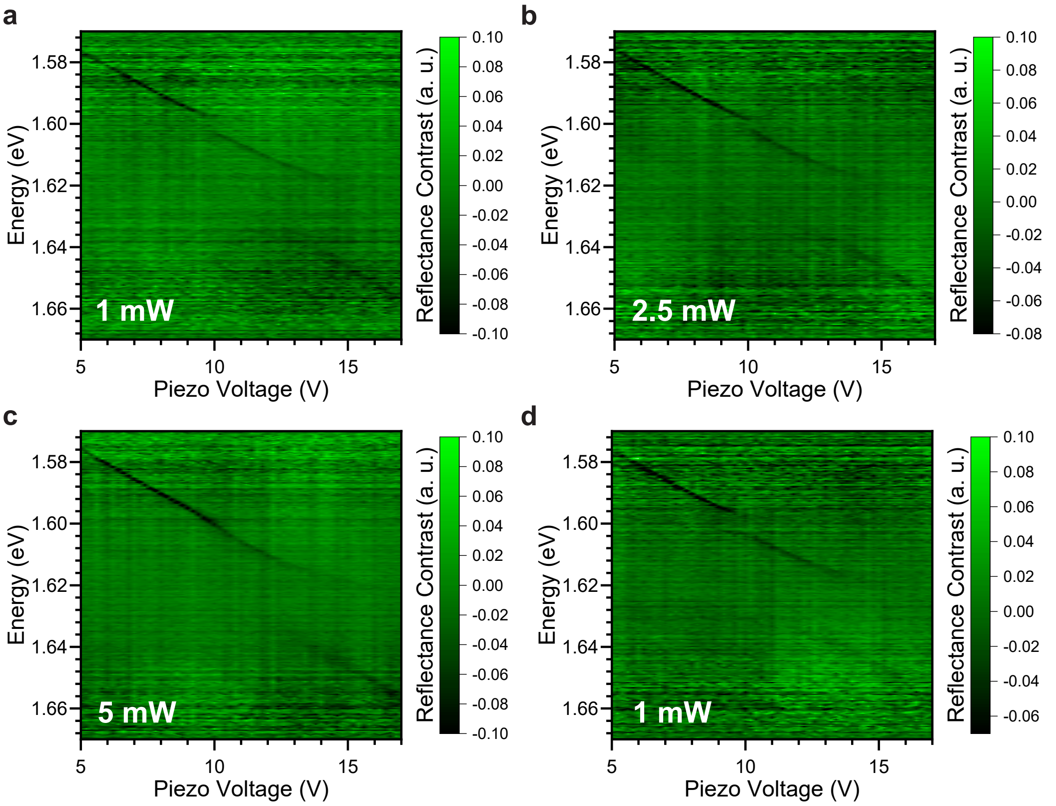

Figure 5.15: Reflectivity measurements as a function of cavity photon energy and piezo voltage at an averaged laser excitation power of a) 1 mW, b) 2.5 mW and c) 5 mW. To show that the effect is reversible, the experiment is repeated at d) 1 mW and the trion coupling is restored. As the piezo voltage is increased, the cavity length is decreased and the cavity photon energy is increased, allowing a tuning of cavity photon energy through the excitonic resonances. As the laser excitation power is increased, the Rabi splitting at the trion resonance collapses due to the trion-trion Coulomb interactions.

reversible, and not simply due to flake damage at high powers. While it is difficult to extract exact trion Rabi splittings here due to the very low signal to noise ratio, the overall effect is very clear.

The measurement is repeated at another area of the coupled $MoSe_2$ / WS_2 region to confirm the results of the experiments, where the effect is observed at a lower Av. power. Figure 5.16 shows the cavity reflectivity experiments on this second area, as the average power is increased from a) 100 μW, through b) 250 μW and c) 500 μW, to d) 1000 μW. A Rabi splitting of $\sim$ 4 meV is observed at 100 μW, to $\sim$ 2 meV at 250 μW, and $\sim$ 1

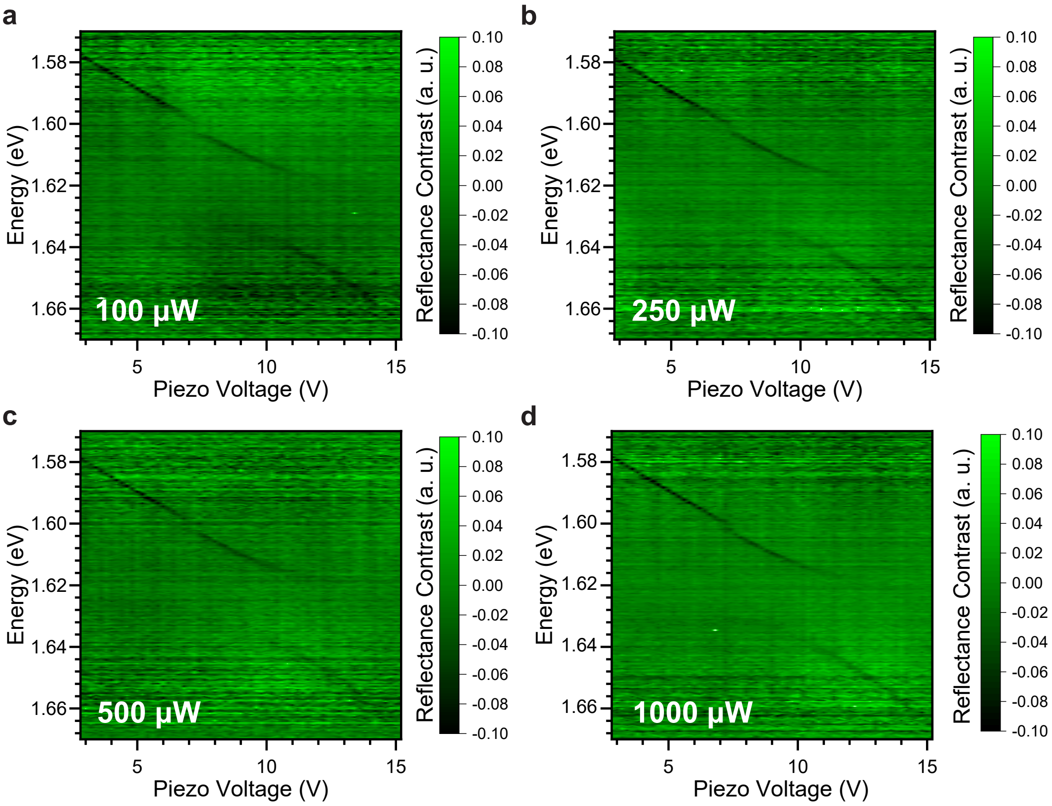

Figure 5.16: Reflectivity measurements in a second area as a function of cavity photon energy and piezo voltage at an averaged laser excitation power of a) 100 μW, b) 250 μW, c) 500 μW and d) 1 mW. The collapse of the trion coupling occurs at a lower laser excitation power than seen in 5.15.

meV at 500 μW, whereas the splitting becomes unresolvable in higher Av. powers marking a five-fold increase in effective non-linearity at this region compared to figure 5.15. It is hypothesised that the two distinct regions offer a difference in localisation of excitons, whereby an increase in locally trapped charges will result in quicker filling of phase space and observations of non-linear effects will occur at a lower excitation power.

Even at higher average powers up to 15 mW, there is no change observed in the coupling to the resonances previously labelled 'hX_1' and 'hX_2'. The lower interaction strength of neutral exciton-polaritons by a factor of 10-100[235,292] accounts for this. Dipolar polaritons produced from a cavity mode coupled with hybridised excitons should indeed possess a higher interaction strength, owing to the interlayer excitons. Estimating the power densities required to observe effects from 'hX_1' and 'hX_2' will require estimations of exciton density, which is difficult to accomplish without a control sample.

To confirm the nature of the X* resonance as a $MoSe_2$ intralayer charged exciton, it will be necessary to repeat the experiment exactly with an encapsulated $MoSe_2$ monolayer. If this experiment matches Fig. 5.16, then we can confidently attribute the intralayer charged exciton resonance. However, if more power is required to collapse the $MoSe_2$ intralayer charged exciton, then it is possible that the effects displayed here are due to a hybridised interlayer / charged intralayer exciton resonance. Ultra-fast lifetime measurements would also give an insight into the origins of the resonances. Interlayer excitons possess a longer lifetime, compared to intralayer excitons, due to the reduced electron hole wave-function overlap.

5.5 Conclusions

This investigation has demonstrated the high optical quality of alloyed monolayers, owing to the narrow linewidths of optical transitions in both emission and absorption experiments. The ability to tune the sharp excitonic resonances over a large energy range of ~ 100 meV by varying the alloy concentration is a major benefit when considering device construction. Further investigations on heterobilayers reveal a hybridisation of momentum direct interlayer exciton and momentum indirect intralayer exciton as the alloy concentration is tuned towards the pure TMD constitution.[145] (*under embargo*) Alloyed monolayers coupled to pure TMDs have also been employed in a recent investigation of spin-valley dynamics using a pump-probe experiment demonstrating the use of alloying to control valley physics in TMD based heterostructures and devices.[91]

While there is undoubtedly a need for further investigation, the potential experimental observation of dipolaritons through resonant coupling of a cavity mode with hybridised intra-inter-layer excitons in a $MoSe_2$ / WS_2 heterostructure provides an experimental proof of concept for future structures employing either the same materials with improved design or completely unexplored devices. Photo-exciting the $MoSe_2$ / WS_2 heterostructure at higher powers reveals the non-linear behaviour of trion-polaritons.

REDACTED

[redacted]

REDACTED

REDACTED

[redacted]

REDACTED

[redacted]

REDACTED

[redacted]

REDACTED

REDACTED

[redacted]

REDACTED

[redacted]

REDACTED

[redacted]

REDACTED

[redacted]

REDACTED

[redacted]

REDACTED

REDACTED

[redacted]

REDACTED

[redacted]

REDACTED

REDACTED

REDACTED

REDACTED

[redacted]

REDACTED

[redacted]

REDACTED

[redacted]

REDACTED

REDACTED

REDACTED

REDACTED

[redacted]

REDACTED

REDACTED

Chapter 7

Outlook

In this closing section, the potential avenues of research going forward are briefly discussed.

7.1 van der Waals ferromagnetic and antiferromagnetic materials

It has been shown in chapter 6 that a thin film of europium sulphide provides a TMD monolayer of $MoSe_2$ with sufficient doping to enter the polaron regime, and with an applied magnetic field, those itinerant carriers within the electronic band structure can be controlled. EuS is a ferromagnetic material, however we observed no evidence of magnetic proximity coupling with the $MoSe_2$ monolayer band structure. Previous studies[294,295] have claimed to observe such behaviour, but it seems that those results are explainable as a manifestation of the large doping as shown here. While it is expected that a thicker EuS sample may provide a suitable ferromagnetic effect, there exists materials that possess an influential degree of magnetism even at the extreme two dimensional limit.[319,320,321,322,323,324]

Many of the materials that have predicated the last century of research in solid state physics, now possess a 2D crystalline analogue,[325,326] and with the recent discovery of long range magnetic ordering persisting to the monolayer limit,[319,320,321,322,323,324] a crucial step forwards in the pursuit of van der Waals based spin- and valley-tronic devices has been realised.[321,327,328,329,330,331,332,333,334]

The family of chromium trihalides ($CrBr_3$, CrI_3, and $CrCl_3$) in particular,[324,335] which provide a unique trio of materials with both antiferromagnetic and ferromagnetic ($CrBr_3$)[336] interlayer ordering. Furthermore, the interlayer antiferromagnetic ordering can be further categorised into in-plane ($CrCl_3$)[337] and out of plane (CrI_3)[338] magnetic easy axis. $CrBr_3$

in particular has seen an expansive resurgence of interest.[323,339,340,341,342] It is seen that the interlayer exchange in exfoliated CrBr3 is ferromagnetic, although can depend on stacking order.[323,339,340,342]

In a recent study of $MoSe_2/CrBr_3$ heterostructure,[303] a three level polarisation switch (Fig. 7.1a) was realised through an interplay of spin proximity effects, and spin-dependent charge transfers. It was also shown that TMD monolayers can be used as an optical proxy to view the magnetic spin behaviour of the underlying $CrBr_3$ (Fig. 7.1b). Other antiferromagnetic materials such as $MnPX_3$ (X=Se,S), and $NiPS_3$ also look promising as layered magnetic materials for use in nanoscale information processing,[333] although further studies are required.

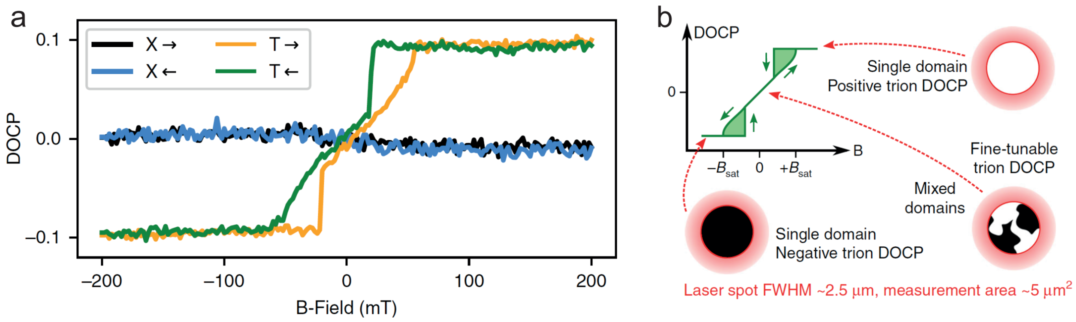

Figure 7.1: **a)** Degree of circular polarisation, $DOCP = (I_{\sigma^+} - I_{\sigma^-})/(I_{\sigma^+} + I_{\sigma^-})$, exhibited by the $MoSe_2$ trion (T), and neutral exciton (X) as the external magnetic field is ramped up (→) and back down (←) between ± 200 mT. Across this range, the nominal valley Zeeman effect in $MoSe_2$ monolayers in negligible as shown by the neutral exciton. **b)** The trion DOCP behaviour is shown to be an exact match of the underlying magnetic domain behaviour in the $CrBr_3$ layer. Image from Ref.[303]

The incorporation of this emerging family of magnetic materials with optically active TMDs is shown to combine the advantageous chiral optical selection rules and spin-valley locking of $MoSe_2$ (and other TMDs), with the highly correlated and field-responsive long range ordering inherent to magnets, such as $CrBr_3$.[8,329,343,344] Macroscopic multi-layers of ferromagnet-semiconductor pairs have previously proven ripe systems for both advanced spintronics research and real-world applications in information technology. As such, devices such as $MoSe_2$ / $CrBr_3$ represent the building blocks for future generations of nanoscale information technologies.[113,141,345,346,347,348]

7.2 Automation of micro-mechanical exfoliation and flake search

There is no question about the optical properties of TMDs and their potential for use in a variety of applications. This missing piece for TMDs overall success is the fabrication methods. Chapter 4 highlights the progress of chemical vapour deposition, by demonstrating for the first time, strong exciton-photon coupling in CVD grown encapsulated $MoSe_2$ and WSe_2 monolayers.[170] While CVD growth techniques strive to produce monolayers of equal, or perhaps greater, optical quality than those fabricated through micromechanical exfoliation, reports have surfaced of a fully automated multilayer heterostructure fabrication

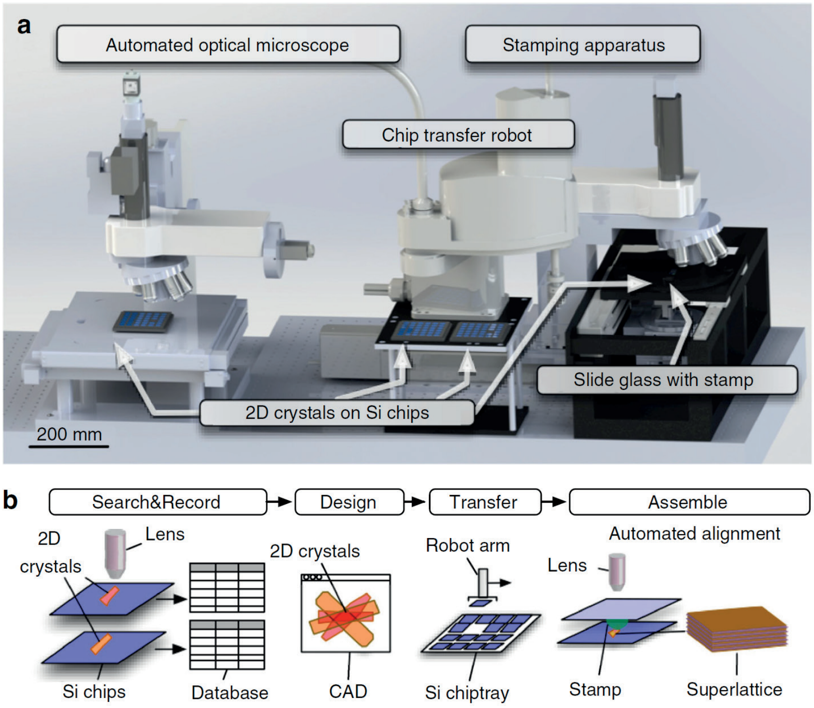

Figure 7.2: **a)** The robotic system is comprised of an automated optical microscope, stamping apparatus, and Si chip transfer robot, all placed within a glovebox and fully automated. **b)** Schematic of the heterostructure fabrication process. The optical microscope with automated XY scanning stage scans the surface of the Si chips. When a flake is detected, the position and shape are recorded to a database. A customised CAD software allows the researcher to design the heterostructure and provides the building information to the system. Finally, the robots build the vdW heterostructure, layer by layer onto a polymer stamp as directed by the computer-vision algorithm. Image from Ref.[349]

process using exfoliated flakes.[349] The glovebox enclosed system (Fig. 7.2) claims to detect 400 monolayer graphene flakes per hour, and stack four cycles of a given 2D materials per hour, with minimal human intervention per stack cycle. As such, a 29 layer superlattice of alternating graphene and hBN layers is built to demonstrate the system's capability. This provides a ground breaking step forward to scalable TMD based devices, with only one small, or actually rather large, concern... the price it takes to build such a system.

Thankfully, there is one part of the fully automated fabrication system that is much more accessible for the average 2D materials research group. An automated XYZ scanning stage is fairly easy to construct with stepper motors, while it is possible to use open source software to design an automated flake search program. In doing so *Millard, T.S., et. al.*[187] designed a simple automated flake search system, that does a very similar job as described in the above fully automated system. This system was used to perform a substrate wide crystallographic orientation analysis on a variety of CVD grown samples.

Automation of a fabrication process is required to make TMD based devices commercially viable, the cost needs to be reasonable however.

7.3 Optical waveguides

The results presented in chapter 4 are of particular note when considering the realisation of scalable devices. CVD grown monolayers embedded into a monolithic cavity can be used as the starting point for the construction of a large array of polariton circuits. A key milestone towards implementation of opto-valleytronics would be long range valley transport between distant systems. In combination with the previously discussed automated flake search system to map the entire active area of a sample, before growing the top mirror. It will be fairly straightforward to design and etch a waveguide and coupler to specific flakes on the substrate.

Excitons being charge neutral particles free to move through the lattice are quite suitable for valley transport. Indeed, exciton integrated circuits have been demonstrated in other material systems.[139] However, in TMDs, the exciton propagation length is severely limited by their short lifetime.[68,230] One potential solution is to use strongly coupled exciton-polaritons as a method of valley pseudospin transportation. The reduced effective mass and high propagation speed, owing to their photonic component, is ideal for particle mobility, while polaritons have been shown to maintain a robust polarisation.[75] Similar device designs have been constructed for use with quantum wells.[350]**? ?**

A first step experiment would be to test the polariton diffusion through such a waveguide by connecting two distinct TMD flakes by a 1D waveguide, and optically excite one of them. If a matching valley pseudospin is detected at the second flake, then valley transportation has been realised. Further investigation could involve a Y shaped waveguide to act as polariton routers, such that polaritons created at the bottom of the Y, will travel towards the junction and, depending on valley pseudospin, will preferentially travel down one arm or the other, owing to the finite Berry curvature inherited from the exciton component, in a polariton valley Hall effect. Exploiting this mechanism will lead to controllable polariton valley circuits.

Bibliography

1. Novoselov, K. S., Geim, A. K., Morozov, S. V., Jiang, D., Zhang, Y., Dubonos, S. V., Grigorieva, I. V., and Firsov, A. A. *Science* **306**(5696), 666–669 (2004).

2. Yu, H., Liu, G. B., Gong, P., Xu, X., and Yao, W. *Nature Communications* **5**(May), 1–7 (2014).

3. Chhowalla, M., Shin, H. S., Eda, G., Li, L.-J., Loh, K. P., and Zhang, H. *Nature Chemistry* **5**(4), 263–275 apr (2013).

4. Mattheiss, L. F. *Physical Review B* **8**(8), 3719–3740 (1973).

5. Manzeli, S., Ovchinnikov, D., Pasquier, D., Yazyev, O. V., and Kis, A. *Nature Reviews Materials* **2**(8), 17033 aug (2017).

6. Xiao, D., Liu, G. B., Feng, W., Xu, X., and Yao, W. *Physical Review Letters* **108**(19), 1–5 (2012).

7. Schaibley, J. R., Yu, H., Clark, G., Rivera, P., Ross, J. S., Seyler, K. L., Yao, W., and Xu, X. *Nature Reviews Materials* **1**(11), 1–15 (2016).

8. Xu, X., Yao, W., Xiao, D., and Heinz, T. F. *Nature Physics* **10**(5), 343–350 (2014).

9. Zeng, H. and Cui, X. *Chemical Society Reviews* **44**(9), 2629–2642 (2015).

10. Splendiani, A., Sun, L., Zhang, Y., Li, T., Kim, J., Chim, C. Y., Galli, G., and Wang, F. *Nano Letters* **10**(4), 1271–1275 (2010).

11. Kittel, C. *Introduction to solid state physics*. John Wiley & Sons, New York, 7 edition, (1996).

12. Mak, K. F., Lee, C., Hone, J., Shan, J., and Heinz, T. F. *Physical Review Letters* **105**(13), 2–5 (2010).

13. Coehoorn, R., Haas, C., and De Groot, R. A. *Physical Review B* **35**(12), 6203–6206 (1987).

14. Silva-Guillén, J., San-Jose, P., and Roldán, R. *Applied Sciences* **6**(10), 284 oct (2016).

15. Ridolfi, E., Le, D., Rahman, T. S., Mucciolo, E. R., and Lewenkopf, C. H. *Journal of Physics Condensed Matter* **27**(36) (2015).

16. Liu, G. B., Shan, W. Y., Yao, Y., Yao, W., and Xiao, D. *Physical Review B - Condensed Matter and Materials Physics* **88**(8), 1–10 (2013).

17. Zhu, Z. Y., Cheng, Y. C., and Schwingenschlögl, U. *Physical Review B - Condensed Matter and Materials Physics* **84**(15), 1–5 (2011).

18. Wang, G., Chernikov, A., Glazov, M. M., Heinz, T. F., Marie, X., Amand, T., and Urbaszek, B. *Reviews of Modern Physics* **90**(2) (2018).

19. Mak, K. F., He, K., Shan, J., and Heinz, T. F. *Nature Nanotechnology* **7**(8), 494–498 (2012).

20. Hsu, W. T., Chen, Y. L., Chen, C. H., Liu, P. S., Hou, T. H., Li, L. J., and Chang, W. H. *Nature Communications* **6**, 1–8 (2015).

21. Yao, W., Xiao, D., and Niu, Q. *Physical Review B - Condensed Matter and Materials Physics* **77**(23), 1–7 (2008).

22. Frenkel, J. *Physical Review* **37**(1), 17–44 (1931).

23. Wannier, G. H. *Physical Review* **52**(3), 191–197 (1937).

24. Mott, N. F. *Transactions of the Faraday Society* **34**, 500–506 (1938).

25. Fox, M. *Optical Properties of Solids*. Oxford University Press, 2 edition, (2010).

26. Chernikov, A., Berkelbach, T. C., Hill, H. M., Rigosi, A., Li, Y., Aslan, O. B., Reichman, D. R., Hybertsen, M. S., and Heinz, T. F. *Physical Review Letters* **113**(7), 1–5 (2014).

27. Qiu, D. Y., Da Jornada, F. H., and Louie, S. G. *Physical Review Letters* **111**(21), 1–5 (2013).

28. Ugeda, M. M., Bradley, A. J., Shi, S. F., Da Jornada, F. H., Zhang, Y., Qiu, D. Y., Ruan, W., Mo, S. K., Hussain, Z., Shen, Z. X., Wang, F., Louie, S. G., and Crommie, M. F. *Nature Materials* **13**(12), 1091–1095 (2014).

29. Kumar, N., Cui, Q., Ceballos, F., He, D., Wang, Y., and Zhao, H. *Physical Review B - Condensed Matter and Materials Physics* **89**(12), 1–6 (2014).

30. Kozawa, D., Kumar, R., Carvalho, A., Kumar Amara, K., Zhao, W., Wang, S., Toh, M., Ribeiro, R. M., Castro Neto, A. H., Matsuda, K., and Eda, G. *Nature Communications* **5**, 1–7 (2014).

31. Li, X., Tao, L., Chen, Z., Fang, H., Li, X., Wang, X., Xu, J. B., and Zhu, H. *Applied Physics Reviews* **4**(2) (2017).

32. Stier, A. V., McCreary, K. M., Jonker, B. T., Kono, J., and Crooker, S. A. *Nature Communications* **7**, 1–8 (2016).

33. Ross, J. S., Wu, S., Yu, H., Ghimire, N. J., Jones, A. M., Aivazian, G., Yan, J., Mandrus, D. G., Xiao, D., Yao, W., and Xu, X. *Nature Communications* **4**, 1473–1476 (2013).

34. McCreary, K. M., Hanbicki, A. T., Sivaram, S. V., and Jonker, B. T. *APL Materials* **6**(11) (2018).

35. Berkelbach, T. C., Hybertsen, M. S., and Reichman, D. R. *Physical Review B - Condensed Matter and Materials Physics* **88**(4), 1–6 (2013).

36. Mak, K. F. and Shan, J. *Nature Photonics* **10**(4), 216–226 (2016).

37. Yu, H., Cui, X., Xu, X., and Yao, W. *National Science Review* **2**(1), 57–70 mar (2015).

38. Mak, K. F., He, K., Lee, C., Lee, G. H., Hone, J., Heinz, T. F., and Shan, J. *Nature Materials* **12**(3), 207–211 (2013).

39. Li, Z., Wang, T., Lu, Z., Jin, C., Chen, Y., Meng, Y., Lian, Z., Taniguchi, T., Watanabe, K., Zhang, S., Smirnov, D., and Shi, S. F. *Nature Communications* **9**(1), 1–7 (2018).

40. Ye, Z., Waldecker, L., Ma, E. Y., Rhodes, D., Antony, A., Kim, B., Zhang, X. X., Deng, M., Jiang, Y., Lu, Z., Smirnov, D., Watanabe, K., Taniguchi, T., Hone, J., and Heinz, T. F. *Nature Communications* **9**(1), 6–11 (2018).

41. Chen, S. Y., Goldstein, T., Taniguchi, T., Watanabe, K., and Yan, J. *Nature Communications* **9**(1), 1–8 (2018).

42. Barbone, M., Montblanch, A. R. P. P., Kara, D. M., Palacios-Berraquero, C., Cadore, A. R., De Fazio, D., Pingault, B., Mostaani, E., Li, H., Chen, B., Watanabe, K., Taniguchi, T., Tongay, S., Wang, G., Ferrari, A. C., and Atatüre, M. *Nature Communications* **9**(1) (2018).

43. Sidler, M., Back, P., Cotlet, O., Srivastava, A., Fink, T., Kroner, M., Demler, E., and Imamoglu, A. *Nature Physics* **13**(3), 255–261 (2017).

44. Courtade, E., Semina, M., Manca, M., Glazov, M. M., Robert, C., Cadiz, F., Wang, G., Taniguchi, T., Watanabe, K., Pierre, M., Escoffier, W., Ivchenko, E. L., Renucci, P., Marie, X., Amand, T., and Urbaszek, B. *Physical Review B* **96**(8), 1–12 (2017).

45. Koperski, M., Molas, M. R., Arora, A., Nogajewski, K., Slobodeniuk, A. O., Faugeras, C., and Potemski, M. *Nanophotonics* **6**(6), 1289–1308 (2017).

46. Arora, A., Koperski, M., Nogajewski, K., Marcus, J., Faugeras, C., and Potemski, M. *Nanoscale* **7**(23), 10421–10429 (2015).

47. Arora, A., Nogajewski, K., Molas, M., Koperski, M., and Potemski, M. *Nanoscale* **7**(48), 20769–20775 (2015).

48. Lindlau, J., Selig, M., Neumann, A., Colombier, L., Förste, J., Funk, V., Förg, M., Kim, J., Berghäuser, G., Taniguchi, T., Watanabe, K., Wang, F., Malic, E., and Högele, A. *Nature Communications* **9**(1), 1–8 dec (2018).

49. Li, Z., Wang, T., Jin, C., Lu, Z., Lian, Z., Meng, Y., Blei, M., Gao, S., Taniguchi, T., Watanabe, K., Ren, T., Tongay, S., Yang, L., Smirnov, D., Cao, T., and Shi, S.-F. *Nature Communications* **10**(1), 2469 dec (2019).

50. Jadczak, J., Kutrowska-Girzycka, J., Kapuściński, P., Huang, Y. S., Wójs, A., and Bryja, L. *Nanotechnology* **28**(39), 395702 sep (2017).

51. Sortino, L., Brooks, M., Zotev, P. G., Genco, A., Cambiasso, J., Mignuzzi, S., Maier, S. A., Burkard, G., Sapienza, R., and Tartakovskii, A. I. *ACS Photonics* **7**(9), 2413–2422 (2020).

52. Branny, A., Kumar, S., Proux, R., and Gerardot, B. D. *Nature Communications* **8**(1), 15053 aug (2017).

53. Kumar, S., Brotóns-Gisbert, M., Al-Khuzheyri, R., Branny, A., Ballesteros-Garcia, G., Sánchez-Royo, J. F., and Gerardot, B. D. *Optica* **3**(8), 882 aug (2016).

54. Kormányos, A., Burkard, G., Gmitra, M., Fabian, J., Zólyomi, V., Drummond, N. D., and Fal'Ko, V. *2D Materials* **2**(4) (2015).

55. Qiu, D. Y., Cao, T., and Louie, S. G. *Physical Review Letters* **115**(17), 1–5 (2015).

56. Li, Y., Ludwig, J., Low, T., Chernikov, A., Cui, X., Arefe, G., Kim, Y. D., van der Zande, A. M., Rigosi, A., Hill, H. M., Kim, S. H., Hone, J., Li, Z., Smirnov, D., and Heinz, T. F. *Physical Review Letters* **113**(26), 266804 dec (2014).

57. Macneill, D., Heikes, C., Mak, K. F., Anderson, Z., Kormányos, A., Zólyomi, V., Park, J., and Ralph, D. C. *Physical Review Letters* **114**(3), 1–5 (2015).

58. Jones, A. M., Yu, H., Ghimire, N. J., Wu, S., Aivazian, G., Ross, J. S., Zhao, B., Yan, J., Mandrus, D. G., Xiao, D., Yao, W., and Xu, X. *Nature Nanotechnology* **8**(9), 634–638 (2013).

59. Wang, G., Marie, X., Liu, B. L., Amand, T., Robert, C., Cadiz, F., Renucci, P., and Urbaszek, B. *Physical Review Letters* **117**(18), 1–5 (2016).

60. Hao, K., Moody, G., Wu, F., Dass, C. K., Xu, L., Chen, C. H., Sun, L., Li, M. Y., Li, L. J., MacDonald, A. H., and Li, X. *Nature Physics* **12**(7), 677–682 (2016).

61. Schmidt, R., Arora, A., Plechinger, G., Nagler, P., Granados Del Águila, A., Ballottin, M. V., Christianen, P. C., Michaelis De Vasconcellos, S., Schüller, C., Korn, T., and Bratschitsch, R. *Physical Review Letters* **117**(7), 1–6 (2016).

62. Glazov, M. M., Amand, T., Marie, X., Lagarde, D., Bouet, L., and Urbaszek, B. *Physical Review B - Condensed Matter and Materials Physics* **89**(20), 1–5 (2014).

63. Yu, T. and Wu, M. W. *Physical Review B - Condensed Matter and Materials Physics* **89**(20), 1–7 (2014).

64. Zhang, A., Fan, J., Li, Y., Ji, J., Zhao, G., Xia, T., Yan, T., Zhang, X., Zhang, W., Wang, X., and Zhang, Q. (2015).

65. Glazov, M. M., Ivchenko, E. L., Wang, G., Amand, T., Marie, X., Urbaszek, B., and Liu, B. L. *Physica Status Solidi (B) Basic Research* **252**(11), 2349–2362 (2015).

66. Cadiz, F., Courtade, E., Robert, C., Wang, G., Shen, Y., Cai, H., Taniguchi, T., Watanabe, K., Carrere, H., Lagarde, D., Manca, M., Amand, T., Renucci, P., Tongay, S., Marie, X., and Urbaszek, B. *Physical Review X* **7**(2), 1–12 (2017).

67. Maialle, M. Z., de Andrada e Silva, E. A., and Sham, L. J. *Physical Review B* **47**(23), 15776–15788 jun (1993).

68. Dufferwiel, S., Lyons, T. P., Solnyshkov, D. D., Trichet, A. A., Withers, F., Schwarz, S., Malpuech, G., Smith, J. M., Novoselov, K. S., Skolnick, M. S., Krizhanovskii, D. N., and Tartakovskii, A. I. *Nature Photonics* **11**(8), 497–501 (2017).

69. Zhu, C. R., Zhang, K., Glazov, M., Urbaszek, B., Amand, T., Ji, Z. W., Liu, B. L., and Marie, X. *Physical Review B - Condensed Matter and Materials Physics* **90**(16), 1–5 (2014).

70. Aivazian, G., Gong, Z., Jones, A. M., Chu, R. L., Yan, J., Mandrus, D. G., Zhang, C., Cobden, D., Yao, W., and Xu, X. *Nature Physics* **11**(2), 148–152 (2015).

71. Srivastava, A., Sidler, M., Allain, A. V., Lembke, D. S., Kis, A., and Imamoglu, A. *Nature Physics* **11**(2), 141–147 (2015).

72. Wang, G., Bouet, L., Glazov, M. M., Amand, T., Ivchenko, E. L., Palleau, E., Marie, X., and Urbaszek, B. *2D Materials* **2**(3) (2015).

73. Kormányos, A., Zólyomi, V., Drummond, N. D., Rakyta, P., Burkard, G., and Fal'Ko, V. I. *Physical Review B - Condensed Matter and Materials Physics* **88**(4), 1–8 (2013).

74. Lundt, N., Klaas, M., Sedov, E., Waldherr, M., Knopf, H., Blei, M., Tongay, S., Klembt, S., Taniguchi, T., Watanabe, K., Schulz, U., Kavokin, A., Höfling, S., Eilenberger, F., and Schneider, C. *Physical Review B* **100**(12), 121303 sep (2019).

75. Lyons, T. P., Dufferwiel, S., Brooks, M., Withers, F., Taniguchi, T., Watanabe, K., Novoselov, K. S., Burkard, G., and Tartakovskii, A. I. *Nature Communications* **10**(1), 1–8 (2019).

76. Efimkin, D. K. and MacDonald, A. H. *Physical Review B* **95**(3), 1–10 (2017).

77. Back, P., Sidler, M., Cotlet, O., Srivastava, A., Takemura, N., Kroner, M., and Imamoğlu, A. *Physical Review Letters* **118**(23), 1–5 (2017).

78. Ossau, W. and Suris, R. *Optical Properties of 2D Systems with Interacting Electrons*. Springer Netherlands, Dordrecht, (2003).

79. Suris, R., Kochereshko, V., Astakhov, G., Yakovlev, D., Ossau, W., N\"{u}rnberger, J., Faschinger, W., Landwehr, G., Wojtowicz, T., Karczewski, G., and Kossut, J. *physica status solidi (b)* **227**(2), 343–352 oct (2001).

80. Baeten, M. and Wouters, M. *Physical Review B - Condensed Matter and Materials Physics* **91**(11), 1–10 (2015).

81. Baeten, M. and Wouters, M. *Physical Review B - Condensed Matter and Materials Physics* **89**(24), 1–8 (2014).

82. Smoleński, T., Cotlet, O., Popert, A., Back, P., Shimazaki, Y., Knüppel, P., Dietler, N., Taniguchi, T., Watanabe, K., Kroner, M., and Imamoglu, A. *Physical Review Letters* **123**(9), 097403 aug (2019).

83. Tan, L. B., Cotlet, O., Bergschneider, A., Schmidt, R., Back, P., Shimazaki, Y., Kroner, M., and İmamoğlu, A. *Physical Review X* **10**(2), 021011 apr (2020).

84. Lyons, T. P., Gillard, D. J., Leblanc, C., Puebla, J., Solnyshkov, D. D., Klompmaker, L., Akimov, I. A., Louca, C., Muduli, P., Genco, A., Bayer, M., Otani, Y., Malpuech, G., and Tartakovskii, A. I. , 1–8 sep (2021).

85. Yin, Z. and Tang, X. *Solid-State Electronics* **51**(1), 6–15 (2007).

86. Gan, L. Y., Zhang, Q., Zhao, Y. J., Cheng, Y., and Schwingenschlögl, U. *Scientific Reports* **4**(1), 6691 (2014).

87. Wei, X. L., Zhang, H., Guo, G. C., Li, X. B., Lau, W. M., and Liu, L. M. *Journal of Materials Chemistry A* **2**(7), 2101–2109 (2014).

88. Zhang, M., Wu, J., Zhu, Y., Dumcenco, D. O., Hong, J., Mao, N., Deng, S., Chen, Y., Yang, Y., Jin, C., Chaki, S. H., Huang, Y. S., Zhang, J., and Xie, L. *ACS Nano* **8**(7), 7130–7137 (2014).

89. Tongay, S., Narang, D. S., Kang, J., Fan, W., Ko, C., Luce, A. V., Wang, K. X., Suh, J., Patel, K. D., Pathak, V. M., Li, J., and Wu, J. *Applied Physics Letters* **104**(1) (2014).

90. Chen, Y., Xi, J., Dumcenco, D. O., Liu, Z., Suenaga, K., Wang, D., Shuai, Z., Huang, Y. S., and Xie, L. *ACS Nano* **7**(5), 4610–4616 (2013).

91. Kravtsov, V., Liubomirov, A. D., Cherbunin, R. V., Catanzaro, A., Genco, A., Gillard, D., Alexeev, E. M., Ivanova, T., Khestanova, E., Shelykh, I. A., Tartakovskii, A. I., Skolnick, M. S., Krizhanovskii, D. N., and Iorsh, I. V. *2D Materials* **8**(2), 025011 jan (2021).

92. Rasmussen, F. A. and Thygesen, K. S. *Journal of Physical Chemistry C* **119**(23), 13169–13183 (2015).

93. Kang, J., Tongay, S., Zhou, J., Li, J., and Wu, J. *Applied Physics Letters* **102**(1), 22–25 (2013).

94. Xie, L. M. *Nanoscale* **7**(44), 18392–18401 (2015).

95. Fu, Q., Yang, L., Wang, W., Han, A., Huang, J., Du, P., Fan, Z., Zhang, J., and Xiang, B. *Advanced Materials* **27**(32), 4732–4738 (2015).

96. Mann, J., Ma, Q., Odenthal, P. M., Isarraraz, M., Le, D., Preciado, E., Barroso, D., Yamaguchi, K., Von Son Palacio, G., Nguyen, A., Tran, T., Wurch, M., Nguyen, A., Klee, V., Bobek, S., Sun, D., Heinz, T. F., Rahman, T. S., Kawakami, R., and Bartels, L. *Advanced Materials* **26**(9), 1399–1404 (2014).

97. Kobayashi, Y., Mori, S., Maniwa, Y., and Miyata, Y. *Nano Research* **8**(10), 3261–3271 (2015).

98. Feng, Q., Mao, N., Wu, J., Xu, H., Wang, C., Zhang, J., and Xie, L. *ACS Nano* **9**(7), 7450–7455 (2015).

99. Feng, Q., Zhu, Y., Hong, J., Zhang, M., Duan, W., Mao, N., Wu, J., Xu, H., Dong, F., Lin, F., Jin, C., Wang, C., Zhang, J., and Xie, L. *Advanced Materials* **26**(17), 2648–2653 (2014).

100. Kang, J., Tongay, S., Li, J., and Wu, J. *Journal of Applied Physics* **113**(14), 1–7 (2013).

101. Komsa, H. P. and Krasheninnikov, A. V. *Journal of Physical Chemistry Letters* **3**(23), 3652–3656 (2012).

102. Yang, L., Fu, Q., Wang, W., Huang, J., Huang, J., Zhang, J., and Xiang, B. *Nanoscale* **7**(23), 10490–10497 (2015).

103. Wang, X., Feng, H., Wu, Y., and Jiao, L. *Journal of the American Chemical Society* **135**(14), 5304–5307 (2013).

104. Eichfeld, S. M., Hossain, L., Lin, Y. C., Piasecki, A. F., Kupp, B., Birdwell, A. G., Burke, R. A., Lu, N., Peng, X., Li, J., Azcatl, A., McDonnell, S., Wallace, R. M., Kim, M. J., Mayer, T. S., Redwing, J. M., and Robinson, J. A. *ACS Nano* **9**(2), 2080–2087 (2015).

105. Duan, X., Wang, C., Fan, Z., Hao, G., Kou, L., Halim, U., Li, H., Wu, X., Wang, Y., Jiang, J., Pan, A., Huang, Y., Yu, R., and Duan, X. *Nano Letters* **16**(1), 264–269 (2016).

106. Rigosi, A. F., Hill, H. M., Rim, K. T., Flynn, G. W., and Heinz, T. F. *Physical Review B* **94**(7), 1–6 (2016).

107. Zhang, M., Wu, X. J., Zhu, X. Y., Dumcenco, X. D. O., Hong, J., Mao, N., Deng, S., Chen, Y., Yang, Y., Jin, C., Chaki, S. H., and Huang, Y.-s. *ACS Nano* **8**(7), 7130–7137 (2014).

108. Tit, N., Obaidat, I. M., and Alawadhi, H. *Journal of Physics Condensed Matter* **21**(7) (2009).

109. Castellanos-Gomez, A., Buscema, M., Molenaar, R., Singh, V., Janssen, L., Van Der Zant, H. S., and Steele, G. A. *2D Materials* **1**(1), 1–34 (2014).

110. Geim, A. K. and Grigorieva, I. V. *Nature* **499**(7459), 419–425 (2013).

111. Novoselov, K. S., Mishchenko, A., Carvalho, A., and Castro Neto, A. H. *Science* **353**(6298), aac9439 jul (2016).

112. Frisenda, R., Navarro-Moratalla, E., Gant, P., Pérez De Lara, D., Jarillo-Herrero, P., Gorbachev, R. V., and Castellanos-Gomez, A. *Chemical Society Reviews* **47**(1), 53–68 (2018).

113. Alexeev, E. M., Ruiz-Tijerina, D. A., Danovich, M., Hamer, M. J., Terry, D. J., Nayak, P. K., Ahn, S., Pak, S., Lee, J., Sohn, J. I., Molas, M. R., Koperski, M., Watanabe, K., Taniguchi, T., Novoselov, K. S., Gorbachev, R. V., Shin, H. S., Fal'ko, V. I., and Tartakovskii, A. I. (2019).

114. Tartakovskii, A. I. *Nature Reviews Physics* **2**(1), 8–9 jan (2020).

115. Kasprzak, J., Richard, M., Kundermann, S., Baas, A., Jeambrun, P., Keeling, J. M. J. J., Marchetti, F. M., Szymánska, M. H., André, R., Staehli, J. L., Savona, V., Littlewood, P. B., Deveaud, B., and Dang, L. S. *Nature* **443**(7110), 409–414 (2006).

116. Cristofolini, P., Christmann, G., Tsintzos, S. I., Deligeorgis, G., Konstantinidis, G., Hatzopoulos, Z., Savvidis, P. G., and Baumberg, J. J. *Science* **336**(6082), 704–707 may (2012).

117. Mueller, T. and Malic, E. *npj 2D Materials and Applications* **2**(1), 1–12 (2018).

118. Ajayi, O. A., Ardelean, J. V., Shepard, G. D., Wang, J., Antony, A., Taniguchi, T., Watanabe, K., Heinz, T. F., Strauf, S., Zhu, X.-Y., and Hone, J. C. *2D Materials* **4**(3), 031011 jul (2017).

119. Dean, C. R., Young, A. F., Meric, I., Lee, C., Wang, L., Sorgenfrei, S., Watanabe, K., Taniguchi, T., Kim, P., Shepard, K. L., and Hone, J. *Nature Nanotechnology* **5**(10), 722–726 (2010).

120. Wang, L., Meric, I., Huang, P. Y., Gao, Q., Gao, Y., Tran, H., Taniguchi, T., Watanabe, K., Campos, L. M., Muller, D. A., Guo, J., Kim, P., Hone, J., Shepard, K. L., and Dean, C. R. *Science* **342**(6158), 614–617 nov (2013).

121. Lee, G. H., Cui, X., Kim, Y. D., Arefe, G., Zhang, X., Lee, C. H., Ye, F., Watanabe, K., Taniguchi, T., Kim, P., and Hone, J. *ACS Nano* **9**(7), 7019–7026 (2015).

122. Del Pozo-Zamudio, O., Genco, A., Schwarz, S., Withers, F., Walker, P. M., Godde, T., Schofield, R. C., Rooney, A. P., Prestat, E., Watanabe, K., Taniguchi, T., Clark, C., Haigh, S. J., Krizhanovskii, D. N., Novoselov, K. S., and Tartakovskii, A. I. *2D Materials* **7**, 31006 (2020).

123. Tran, K., Moody, G., Wu, F., Lu, X., Choi, J., Kim, K., Rai, A., Sanchez, D. A., Quan, J., Singh, A., Embley, J., Zepeda, A., Campbell, M., Autry, T., Taniguchi, T., Watanabe, K., Lu, N., Banerjee, S. K., Silverman, K. L., Kim, S., Tutuc, E., Yang, L., MacDonald, A. H., and Li, X. *Nature* **567**(7746), 71–75 (2019).

124. Rivera, P., Schaibley, J. R., Jones, A. M., Ross, J. S., Wu, S., Aivazian, G., Klement, P., Seyler, K., Clark, G., Ghimire, N. J., Yan, J., Mandrus, D. G., Yao, W., and Xu, X. *Nature Communications* **6**, 4–9 (2015).

125. Rigosi, A. F., Hill, H. M., Li, Y., Chernikov, A., and Heinz, T. F. *Nano Letters* **15**(8), 5033–5038 (2015).

126. Ceballos, F., Bellus, M. Z., Chiu, H. Y., and Zhao, H. *Nanoscale* **7**(41), 17523–17528 (2015).

127. Yu, Y., Hu, S., Su, L., Huang, L., Liu, Y., Jin, Z., Purezky, A. A., Geohegan, D. B., Kim, K. W., Zhang, Y., and Cao, L. *Nano Letters* **15**(1), 486–491 (2015).

128. Nagler, P., Plechinger, G., Ballottin, M. V., Mitioglu, A., Meier, S., Paradiso, N., Strunk, C., Chernikov, A., Christianen, P. C., Schüller, C., and Korn, T. *2D Materials* **4**(2), 1–12 (2017).

129. Rivera, P., Yu, H., Seyler, K. L., Wilson, N. P., Yao, W., and Xu, X. *Nature Nanotechnology* **13**(11), 1004–1015 (2018).

130. Alexeev, E. M., Catanzaro, A., Skrypka, O. V., Nayak, P. K., Ahn, S., Pak, S., Lee, J., Sohn, J. I., Novoselov, K. S., Shin, H. S., and Tartakovskii, A. I. *Nano Letters* **17**(9), 5342–5349 sep (2017).

131. Miller, D. A., Chemla, D. S., Damen, T. C., Gossard, A. C., Wiegmann, W., Wood, T. H., and Burrus, C. A. *Physical Review Letters* **53**(22), 2173–2176 (1984).

132. Charbonneau, S., Thewalt, M. L. W., Koteles, E. S., and Elman, B. *Physical Review B* **38**(9), 6287–6290 sep (1988).

133. Chen, Y. J., Koteles, E. S., Elman, B. S., and Armiento, C. A. *Physical Review B* **36**(8), 4562–4565 (1987).

134. Combescot, M., Combescot, R., and Dubin, F. *Reports on Progress in Physics* **80**(6), 066501 jun (2017).

135. Butov, L. V. *Journal of Physics Condensed Matter* **16**(50) (2004).

136. Butov, L. V. *Journal of Physics Condensed Matter* **19**(29) (2007).

137. Rapaport, R. and Chen, G. *Journal of Physics Condensed Matter* **19**(29) (2007).

138. Golub, J. E., Kash, K., Harbison, J. P., and Florez, L. T. *Physical Review B* **41**(12), 8564–8567 (1990).

139. High, A. A., Novitskaya, E. E., Butov, L. V., Hanson, M., and Gossard, A. C. *Science* **321**(5886), 229–231 (2008).

140. Fogler, M. M., Butov, L. V., and Novoselov, K. S. *Nature Communications* **5**(May), 1–5 (2014).

141. Yu, H., Liu, G. B., Tang, J., Xu, X., and Yao, W. *Science Advances* **3**(11) (2017).

142. Jin, C., Regan, E. C., Yan, A., Iqbal Bakti Utama, M., Wang, D., Zhao, S., Qin, Y., Yang, S., Zheng, Z., Shi, S., Watanabe, K., Taniguchi, T., Tongay, S., Zettl, A., and Wang, F. *Nature* **567**(7746), 76–80 (2019).

143. Ruiz-Tijerina, D. A. and Fal'Ko, V. I. *Physical Review B* **99**(12), 30–32 (2019).

144. Zhang, L., Zhang, Z., Wu, F., Wang, D., Gogna, R., Hou, S., Watanabe, K., Taniguchi, T., Kulkarni, K., Kuo, T., Forrest, S. R., and Deng, H. *Nature Communications* **11**(1), 1–8 (2020).

145. Catanzaro, A. *Fabrication and characterization of transition metal dichalcogenide alloys and their heterostructures.* Thesis, University of Sheffield, oct (2019).

146. Seyler, K. L., Rivera, P., Yu, H., Wilson, N. P., Ray, E. L., Mandrus, D. G., Yan, J., Yao, W., and Xu, X. *Nature* **567**(7746), 66–70 (2019).

147. Brotons-Gisbert, M., Baek, H., Molina-Sánchez, A., Scerri, D., White, D., Watanabe, K., Taniguchi, T., Bonato, C., and Gerardot, B. D. , 1–11 (2019).

148. Zhang, L., Wu, F., Hou, S., Zhang, Z., Chou, Y.-h., Watanabe, K., Taniguchi, T., Forrest, S. R., and Deng, H. *Nature* **591**(7848), 61–65 mar (2021).

149. Kavokin, A., Malpuech, G., and Gil, B. *MRS Internet Journal of Nitride Semiconductor Research* **8**(January 1998), e3 jun (2003).

150. Sheppard, C. J. *Pure and Applied Optics: Journal of the European Optical Society Part A* **4**(5), 665–669 (1995).

151. Bienstman, P. *Rigorous and efficient modelling of wavelength scale photonic componants.* PhD thesis, Universiteit Gent, (2001).

152. Kavokin, A., Baumberg, J. J., Malpuech, G., and Laussy, F. P. *Microcavities.* Oxford University Press, dec (2007).

153. Novotny, L. and Hecht, B. *Principles of Nano-Optics.* Cambridge University Press, Cambridge, (2012).

154. Dufferwiel, S., Fras, F., Trichet, A., Walker, P. M., Li, F., Giriunas, L., Makhonin, M. N., Wilson, L. R., Smith, J. M., Clarke, E., Skolnick, M. S., and Krizhanovskii, D. N. *Applied Physics Letters* **104**(19), 192107 may (2014).

155. Dufferwiel, S., Schwarz, S., Withers, F., Trichet, A. A. P. P., Li, F., Sich, M., Del Pozo-Zamudio, O., Clark, C., Nalitov, A., Solnyshkov, D. D., Malpuech, G., Novoselov, K. S., Smith, J. M., Skolnick, M. S., Krizhanovskii, D. N., and Tartakovskii, A. I. *Nature Communications* **6**(May), 1–7 (2015).

156. Kavokin, A. and Malpuech, G. *Cavity polaritons.* Elsevier, 2nd editio edition, (2003).

157. Bandres, M. A. and Gutiérrez-Vega, J. C. *Journal of the Optical Society of America A* **21**(5), 873 (2004).

158. Murshid, S. H. *Optical Fiber Multiplexing and Emerging Techniques: SDM and OAM.* IOP Publishing, (2019).

159. Freise, A. and Strain, K. *Living Reviews in Relativity* **13**(February 2010) (2010).

160. Allen, L., Beijersbergen, M. W., Spreeuw, R. J. C., and Woerdman, J. P. In *Optical Angular Momentum*, volume 45, 31–35. IOP Publishing Ltd (1992).

161. Schneider, C., Glazov, M. M., Korn, T., Höfling, S., and Urbaszek, B. *Nature Communications* **9**, 2695 (2018).

162. Hopfield, J. J. *Physical Review* **112**(5), 1555–1567 (1958).

163. Agranovich, V. M. and Faidysh, A. *Optika i Spektroskopiya* **1**(7), 885–895 (1957).

164. Pekar, S. *Journal of Physics and Chemistry of Solids* **5**(1-2), 11–22 jan (1958).

165. Weisbuch, C., Nishioka, M., Ishikawa, A., and Arakawa, Y. *Physical Review Letters* **69**(23), 3314–3317 (1992).

166. Ivchenko, E. L. *Optical Spectroscopy of Semiconductor Nanostructures.* Alpha Science, (2005).

167. Schneider, C., Winkler, K., Fraser, M. D., Kamp, M., Yamamoto, Y., Ostrovskaya, E. A., and Höfling, S. (2017).

168. Purcell, E. M. *Physical Review B* **69**, 681 (1946).

169. Glazov, M. M., Ivchenko, E. L., Poddubny, A. N., and Khitrova, G. *Physics of the Solid State* **53**(9), 1753–1760 (2011).

170. Gillard, D. J., Genco, A., Ahn, S., Lyons, T. P., Yeol Ma, K., Jang, A.-R., Severs Millard, T., Trichet, A. A. P., Jayaprakash, R., Georgiou, K., Lidzey, D. G., Smith, J. M., Suk Shin, H., and Tartakovskii, A. I. *2D Materials* **8**(1), 011002 nov (2020).

171. Sanvitto, D. and Kéna-Cohen, S. *Nature Materials* **15**(10), 1061–1073 (2016).

172. Jiang, Z., Ren, A., Yan, Y., Yao, J., and Zhao, Y. S. *Advanced Materials* **34**(4), 2106095 jan (2022).

173. Ouyang, C., Li, Y., Fu, X., Zeng, Z., Huang, L., Liu, S., Wang, X., Gao, T., and Pan, A. *Applied Physics Letters* **117**(22) (2020).

174. Su, R., Fieramosca, A., Zhang, Q., Nguyen, H. S., Deleporte, E., Chen, Z., Sanvitto, D., Liew, T. C. H., and Xiong, Q. *Nature Materials* **20**(10), 1315–1324 oct (2021).

175. Su, R., Ghosh, S., Wang, J., Liu, S., Diederichs, C., Liew, T. C. H., and Xiong, Q. *Nature Physics* **16**(3), 301–306 mar (2020).

176. Spencer, M. S., Fu, Y., Schlaus, A. P., Hwang, D., Dai, Y., Smith, M. D., Gamelin, D. R., and Zhu, X.-Y. *Science Advances* **7**(49), 1–9 dec (2021).

177. Zhang, S., Shang, Q., Du, W., Shi, J., Wu, Z., Mi, Y., Chen, J., Liu, F., Li, Y., Liu, M., Zhang, Q., and Liu, X. *Advanced Optical Materials* **6**(2), 1–9 (2018).

178. Lundt, N., Klembt, S., Cherotchenko, E., Betzold, S., Iff, O., Nalitov, A. V., Klaas, M., Dietrich, C. P., Kavokin, A. V., Höfling, S., and Schneider, C. *Nature Communications* **7**, 13328 (2016).

179. Zhang, L., Gogna, R., Burg, W., Tutuc, E., and Deng, H. *Nature Communications* **9**(1), 1–8 (2018).

180. Liu, X., Galfsky, T., Sun, Z., Xia, F., Lin, E.-c., Lee, Y.-H., Kéna-Cohen, S., and Menon, V. M. *Nature Photonics* **9**(1), 30–34 jan (2014).

181. Novoselov, K. S., Jiang, D., Schedin, F., Booth, T. J., Khotkevich, V. V., Morozov, S. V., and Geim, A. K. *Proceedings of the National Academy of Sciences of the United States of America* **102**(30), 10451–10453 (2005).

182. Huang, Y., Sutter, E., Shi, N. N., Zheng, J., Yang, T., Englund, D., Gao, H. J., and Sutter, P. *ACS Nano* **9**(11), 10612–10620 (2015).

183. Cai, Z., Liu, B., Zou, X., and Cheng, H. M. *Chemical Reviews* **118**(13), 6091–6133 (2018).

184. Yu, J., Li, J., Zhang, W., and Chang, H. *Chemical Science* **6**(12), 6705–6716 (2015).

185. Liu, Y., Zhang, S., He, J., Wang, Z. M., and Liu, Z. *Nano-Micro Letters* **11**(1), 1–24 (2019).

186. Zhao, Q., Puebla, S., Zhang, W., Wang, T., Frisenda, R., and Castellanos-Gomez, A. *Advanced Photonics Research* **1**(2), 2000025 (2020).

187. Severs Millard, T., Genco, A., Alexeev, E. M., Randerson, S., Ahn, S., Jang, A.-R., Shin, H. S., and Tartakovskii, A. I. *npj 2D Materials and Applications* **4**, 12 (2020).

188. Meitl, M. A., Zhu, Z. T., Kumar, V., Lee, K. J., Feng, X., Huang, Y. Y., Adesida, I., Nuzzo, R. G., and Rogers, J. A. *Nature Materials* **5**(1), 33–38 (2006).

189. Frisenda, R., Navarro-Moratalla, E., Gant, P., Pérez De Lara, D., Jarillo-Herrero, P., Gorbachev, R. V., and Castellanos-Gomez, A. *Chemical Society Reviews* **47**(1), 53–68 (2017).

190. Haigh, S. J., Gholinia, A., Jalil, R., Romani, S., Britnell, L., Elias, D. C., Novoselov, K. S., Ponomarenko, L. A., Geim, A. K., and Gorbachev, R. *Nature Materials* **11**(9), 764–767 (2012).

191. Liu, Y., Weiss, N. O., Duan, X., Cheng, H. C., Huang, Y., and Duan, X. *Nature Reviews Materials* **1**(9) (2016).

192. Frisenda, R., Navarro-Moratalla, E., Gant, P., Pérez De Lara, D., Jarillo-Herrero, P., Gorbachev, R. V., and Castellanos-Gomez, A. *Chemical Society Reviews* **47**(1), 53–68 (2018).

193. Pizzocchero, F., Gammelgaard, L., Jessen, B. S., Caridad, J. M., Wang, L., Hone, J., Bøggild, P., and Booth, T. J. *Nature Communications* **7**(May) (2016).

194. Gass, M. H., Bangert, U., Bleloch, A. L., Wang, P., Nair, R. R., and Geim, A. K. *Nature Nanotechnology* **3**(11), 676–681 (2008).

195. Withers, F., Del Pozo-Zamudio, O., Mishchenko, A., Rooney, A. P., Gholinia, A., Watanabe, K., Taniguchi, T., Haigh, S. J., Geim, A. K., Tartakovskii, A. I., and Novoselov, K. S. *Nature Materials* **14**(3), 301–306 (2015).

196. Shree, S., George, A., Lehnert, T., Neumann, C., Benelajla, M., Robert, C., Marie, X., Watanabe, K., Taniguchi, T., Kaiser, U., Urbaszek, B., and Turchanin, A. *2D Materials* **7**(1), 15011 (2019).

197. Sun, L., Yuan, G., Gao, L., Yang, J., Chhowalla, M., Gharahcheshmeh, M. H., Gleason, K. K., Choi, Y. S., Hong, B. H., and Liu, Z. *Nature Reviews Methods Primers* **1**(1), 5 dec (2021).

198. Teal, G. K., Fisher, J. R., and Treptow, A. W. *Journal of Applied Physics* **17**(11), 879–886 nov (1946).

199. Carlson, D. E. and Wronski, C. R. *Applied Physics Letters* **28**(11), 671–673 jun (1976).

200. Knights, J. C. In *AIP Conference Proceedings*, volume 31, 296–300. AIP, (1976).

201. Manasevit, H. *Journal of Crystal Growth* **55**(1), 1–9 oct (1981).

202. Tsang, W. T. *Journal of Applied Physics* **58**(3), 1415–1418 aug (1985).

203. Shi, Y., Li, H., and Li, L. J. *Chemical Society Reviews* **44**(9), 2744–2756 (2015).

204. Zhang, Y., Yao, Y., Sendeku, M. G., Yin, L., Zhan, X., Wang, F., Wang, Z., and He, J. *Advanced Materials* **31**(41), 1901694 oct (2019).

205. Lee, Y.-H., Yu, L., Wang, H., Fang, W., Ling, X., Shi, Y., Lin, C.-T., Huang, J.-K., Chang, M.-T., Chang, C.-S., Dresselhaus, M., Palacios, T., Li, L.-J., and Kong, J. *Nano Letters* **13**(4), 1852–1857 apr (2013).

206. Zhang, Y., Zhang, Y., Ji, Q., Ju, J., Yuan, H., Shi, J., Gao, T., Ma, D., Liu, M., Chen, Y., Song, X., Hwang, H. Y., Cui, Y., and Liu, Z. *ACS Nano* **7**(10), 8963–8971 oct (2013).

207. Shaw, J. C., Zhou, H., Chen, Y., Weiss, N. O., Liu, Y., Huang, Y., and Duan, X. *Nano Research* **7**(4), 511–517 apr (2014).

208. Zhou, H., Wang, C., Shaw, J. C., Cheng, R., Chen, Y., Huang, X., Liu, Y., Weiss, N. O., Lin, Z., Huang, Y., and Duan, X. *Nano Letters* **15**(1), 709–713 jan (2015).

209. Okada, M., Okada, N., Chang, W. H., Endo, T., Ando, A., Shimizu, T., Kubo, T., Miyata, Y., and Irisawa, T. *Scientific Reports* **9**(1), 1–10 (2019).

210. Liu, H. J., Jiao, L., Xie, L., Yang, F., Chen, J. L., Ho, W. K., Gao, C. L., Jia, J. F., Cui, X. D., and Xie, M. H. *2D Materials* **2**(3), 034004 jun (2015).

211. Marx, M., Nordmann, S., Knoch, J., Franzen, C., Stampfer, C., Andrzejewski, D., Kümmell, T., Bacher, G., Heuken, M., Kalisch, H., and Vescan, A. *Journal of Crystal Growth* **464**(November 2016), 100–104 apr (2017).

212. Jiang, J., Li, N., Zou, J., Zhou, X., Eda, G., Zhang, Q., Zhang, H., Li, L. J., Zhai, T., and Wee, A. T. *Chemical Society Reviews* **48**(17), 4639–4654 (2019).

213. Xie, S., Tu, L., Han, Y., Huang, L., Kang, K., Lao, K. U., Poddar, P., Park, C., Muller, D. A., DiStasio, R. A., and Park, J. *Science* **359**(6380), 1131–1136 (2018).

214. Gong, Y., Lin, J., Wang, X., Shi, G., Lei, S., Lin, Z., Zou, X., Ye, G., Vajtai, R., Yakobson, B. I., Terrones, H., Terrones, M., Tay, B. K., Lou, J., Pantelides, S. T., Liu, Z., Zhou, W., and Ajayan, P. M. *Nature Materials* **13**(12), 1135–1142 (2014).

215. Huang, C., Wu, S., Sanchez, A. M., Peters, J. J. P., Beanland, R., Ross, J. S., Rivera, P., Yao, W., Cobden, D. H., and Xu, X. *Nature Materials* **13**(12), 1096–1101 dec (2014).

216. Zhang, X.-Q., Lin, C.-H., Tseng, Y.-W., Huang, K.-H., and Lee, Y.-H. *Nano Letters* **15**(1), 410–415 jan (2015).

217. Zhang, Q., Xiao, X., Zhao, R., Lv, D., Xu, G., Lu, Z., Sun, L., Lin, S., Gao, X., Zhou, J., Jin, C., Ding, F., and Jiao, L. *Angewandte Chemie International Edition* **54**(31), 8957–8960 jul (2015).

218. Duan, X., Wang, C., Shaw, J. C., Cheng, R., Chen, Y., Li, H., Wu, X., Tang, Y., Zhang, Q., Pan, A., Jiang, J., Yu, R., Huang, Y., and Duan, X. *Nature Nanotechnology* **9**(12), 1024–1030 dec (2014).

219. Cui, F., Feng, Q., Hong, J., Wang, R., Bai, Y., Li, X., Liu, D., Zhou, Y., Liang, X., He, X., Zhang, Z., Liu, S., Lei, Z., Liu, Z., Zhai, T., and Xu, H. *Advanced Materials* **29**(46), 1–9 (2017).

220. Dathbun, A., Kim, Y., Kim, S., Yoo, Y., Kang, M. S., Lee, C., and Cho, J. H. *Nano Letters* **17**(5), 2999–3005 (2017).

221. Liu, X., Galfsky, T., Sun, Z., Xia, F., Lin, E. C., Lee, Y. H., Kéna-Cohen, S., and Menon, V. M. *Nature Photonics* **9**(1), 30–34 (2014).

222. Dolan, P. R., Hughes, G. M., Grazioso, F., Patton, B. R., and Smith, J. M. *Optics Letters* **35**(21), 3556 nov (2010).

223. Schwarz, S., Dufferwiel, S., Walker, P. M., Withers, F., Trichet, A. A. P. P., Sich, M., Li, F., Chekhovich, E. A., Borisenko, D. N., Kolesnikov, N. N., Novoselov, K. S., Skolnick, M. S., Smith, J. M., Krizhanovskii, D. N., and Tartakovskii, A. I. *Nano Letters* **14**(12), 7003–7008 (2014).

224. Boher, P., Leroux, T., Bignon, T., and Collomb-Patton, V. *Stereoscopic Displays and Applications XXIII* **8288**(February 2012), 82880S (2012).

225. He, K., Kumar, N., Zhao, L., Wang, Z., Mak, K. F., Zhao, H., and Shan, J. *Physical Review Letters* **113**(2), 1–5 (2014).

226. Dhara, S., Chakraborty, C., Goodfellow, K. M., Qiu, L., O'Loughlin, T. A., Wicks, G. W., Bhattacharjee, S., and Vamivakas, A. N. *Nature Physics* **14**, 130–133 (2018).

227. Low, T., Chaves, A., Caldwell, J. D., Kumar, A., Fang, N. X., Avouris, P., Heinz, T. F., Guinea, F., Martin-Moreno, L., and Koppens, F. *Nature Materials* **16**(2), 182–194 (2017).

228. Krol, M., Rechcinska, K., Nogajewski, K., Grzeszczyk, M., Lempicka, K., Mirek, R., Piotrowska, S., Watanabe, K., Taniguchi, T., Molas, M. R., Potemski, M., Szczytko, J., and Pietka, B. *2D Materials* **7**, 15006 (2020).

229. Chen, Y.-J., Cain, J. D., Stanev, T. K., Dravid, V. P., and Stern, N. P. *Nature Photonics* **11**, 431–435 (2017).

230. Dufferwiel, S., Lyons, T. P., Solnyshkov, D. D., Trichet, A. A. P., Catanzaro, A., Withers, F., Malpuech, G., Smith, J. M., Novoselov, K. S., Skolnick, M. S., Krizhanovskii, D. N., and Tartakovskii, A. I. *Nature communications* **9**(1), 4797 (2018).

231. Qiu, L., Chakraborty, C., Dhara, S., and Vamivakas, A. N. *Nature Communications* **10**, 1513 (2019).

232. Barachati, F., Fieramosca, A., Hafezian, S., Gu, J., Chakraborty, B., Ballarini, D., Martinu, L., Menon, V., Sanvitto, D., and Kéna-Cohen, S. *Nature nanotechnology* **13**(10), 906–909 (2018).

233. Lundt, N., Dusanowski, Ł., Sedov, E., Stepanov, P., Glazov, M. M., Klembt, S., Klaas, M., Beierlein, J., Qin, Y., Tongay, S., and Others. *Nature nanotechnology* **14**(8), 770–775 (2019).

234. Waldherr, M., Lundt, N., Klaas, M., Betzold, S., Wurdack, M., Baumann, V., Estrecho, E., Nalitov, A., Cherotchenko, E., Cai, H., Ostrovskaya, E. A., Kavokin, A. V., Tongay, S., Klembt, S., Höfling, S., and Schneider, C. *Nature Communications* **9**(1), 3286 dec (2018).

235. Emmanuele, R. P. A., Sich, M., Kyriienko, O., Shahnazaryan, V., Withers, F., Catanzaro, A., Walker, P. M., Benimetskiy, F. A., Skolnick, M. S., Tartakovskii, A. I., Shelykh, I. A., and Krizhanovskii, D. N. *Nature Communications* **11**(1), 3589 dec (2020).

236. Christopoulos, S., Von Högersthal, G. B. H., Grundy, A. J. D. D., Lagoudakis, P. G., Kavokin, A. V., Baumberg, J. J., Christmann, G., Butté, R., Feltin, E., Carlin, J. F., and Grandjean, N. *Physical Review Letters* **98**(12), 126405 (2007).

237. Bhattacharya, P., Frost, T., Deshpande, S., Baten, M. Z., Hazari, A., and Das, A. *Physical Review Letters* **112**(23), 236802 (2014).

238. Amo, A., Lefrère, J., Pigeon, S., Adrados, C., Ciuti, C., Carusotto, I., Houdré, R., Giacobino, E., and Bramati, A. *Nature Physics* **5**(11), 805–810 (2009).

239. Liew, T. C. H., Kavokin, A. V., Ostatnický, T., Kaliteevski, M., Shelykh, I. A., and Abram, R. A. *Physical Review B* **82**(3), 033302 jul (2010).

240. Ballarini, D., De Giorgi, M., Cancellieri, E., Houdré, R., Giacobino, E., Cingolani, R., Bramati, A., Gigli, G., and Sanvitto, D. *Nature Communications* **4**(1), 1778 jun (2013).

241. Gebhardt, C., Förg, M., Yamaguchi, H., Bilgin, I., Mohite, A. D., Gies, C., Florian, M., Hartmann, M., Hänsch, T. W., Högele, A., and Hunger, D. *Scientific Reports* **9**(1), 13756 dec (2019).

242. Roch, J. G., Froehlicher, G., Leisgang, N., Makk, P., Watanabe, K., Taniguchi, T., and Warburton, R. J. *Nature Nanotechnology* **14**(5), 432–436 may (2019).

243. Zhang, X., Zhang, F., Wang, Y., Schulman, D. S., Zhang, T., Bansal, A., Alem, N., Das, S., Crespi, V. H., Terrones, M., and Redwing, J. M. *ACS Nano* **13**(3), 3341–3352 mar (2019).

244. Yu, H., Yang, Z., Du, L., Zhang, J., Shi, J., Chen, W., Chen, P., Liao, M., Zhao, J., Meng, J., Wang, G., Zhu, J., Yang, R., Shi, D., Gu, L., and Zhang, G. *Small* **13**(7), 1603005 feb (2017).

245. Okada, M., Sawazaki, T., Watanabe, K., Taniguch, T., Hibino, H., Shinohara, H., and Kitaura, R. *ACS Nano* **8**(8), 8273–8277 (2014).

246. Robert, C., Amand, T., Cadiz, F., Lagarde, D., Courtade, E., Manca, M., Taniguchi, T., Watanabe, K., Urbaszek, B., and Marie, X. *Physical Review B* **96**(15), 1–8 oct (2017).

247. Lippert, S., Schneider, L. M., Renaud, D., Kang, K. N., Ajayi, O., Kuhnert, J., Halbich, M.-U., Abdulmunem, O. M., Lin, X., Hassoon, K., Edalati-Boostan, S., Kim, Y. D., Heimbrodt, W., Yang, E.-H., Hone, J. C., and Rahimi-Iman, A. *2D Materials* **4**(2), 025045 mar (2017).

248. Dumcenco, D., Ovchinnikov, D., Marinov, K., Lazić, P., Gibertini, M., Marzari, N., Sanchez, O. L., Kung, Y.-C., Krasnozhon, D., Chen, M.-W., Bertolazzi, S., Gillet, P., Fontcuberta i Morral, A., Radenovic, A., and Kis, A. *ACS Nano* **9**(4), 4611–4620 apr (2015).

249. Zhang, X., Choudhury, T. H., Chubarov, M., Xiang, Y., Jariwala, B., Zhang, F., Alem, N., Wang, G.-C., Robinson, J. A., and Redwing, J. M. *Nano Letters* **18**(2), 1049–1056 feb (2018).

250. Savitzky, A. and Golay, M. J. E. *Analytical Chemistry* **36**(8), 1627–1639 (1964).

251. Nishimura, T., Yamashita, K., Takahashi, S., Yamao, T., Hotta, S., Yanagi, H., and Nakayama, M. *Optics Letters* **43**(5), 1047 (2018).

252. Savona, V., Andreani, L. C., Schwendimann, P., and Quattropani, A. *Solid State Communications* **93**(9), 733–739 (1995).

253. Genco, A., Giordano, G., Carallo, S., Accorsi, G., Duan, Y., Gambino, S., and Mazzeo, M. *Organic Electronics* **62**, 174–180 (2018).

254. Mukherjee, B., Tseng, F., Gunlycke, D., Amara, K. K., Eda, G., and Simsek, E. *Optical Materials Express* **5**(2), 447 feb (2015).

255. Palik, E. D. *Handbook of Optical Constants of Solids*. Number v. 3 in Academic Press handbook series. Elsevier, (1985).

256. Wang, G., Robert, C., Suslu, A., Chen, B., Yang, S., Alamdari, S., Gerber, I. C., Amand, T., Marie, X., Tongay, S., and Urbaszek, B. *Nature Communications* **6**, 1–7 (2015).

257. Zhao, W., Ghorannevis, Z., Chu, L., Toh, M., Kloc, C., Tan, P. H., and Eda, G. *ACS Nano* **7**(1), 791–797 (2013).

258. Smolenski, T., Goryca, M., Koperski, M., Faugeras, C., Kazimierczuk, T., Bogucki, A., Nogajewski, K., Kossacki, P., and Potemski, M. *Physical Review X* **6**(2), 1–7 (2016).

259. Wang, G., Palleau, E., Amand, T., Tongay, S., Marie, X., and Urbaszek, B. *Applied Physics Letters* **106**(11) (2015).

260. Bragança, H., Riche, F., Qu, F., Lopez-Richard, V., and Marques, G. E. *Scientific Reports* **9**(1), 1–14 (2019).

261. Liu, G.-B. B., Xiao, D., Yao, Y., Xu, X., and Yao, W. *Chem. Soc. Rev.* **44**(9), 2643–2663 (2015).

262. Li, Y., Chernikov, A., Zhang, X., Rigosi, A., Hill, H. M., Van Der Zande, A. M., Chenet, D. A., Shih, E. M., Hone, J., and Heinz, T. F. *Physical Review B - Condensed Matter and Materials Physics* **90**(20), 1–6 (2014).

263. Horng, J., Stroucken, T., Zhang, L., Paik, E. Y., Deng, H., and Koch, S. W. *Physical Review B* **97**(24), 241404 jun (2018).

264. Amo, A., Liew, T. C., Adrados, C., Houdré, R., Giacobino, E., Kavokin, A. V., and Bramati, A. *Nature Photonics* (2010).

265. Byrnes, T., Kolmakov, G. V., Kezerashvili, R. Y., and Yamamoto, Y. *Physical Review B - Condensed Matter and Materials Physics* **90**(12), 1–10 (2014).

266. Wilkes, J. and Muljarov, E. A. *Physical Review B* **94**(12), 1–9 (2016).

267. Rosenberg, I., Mazuz-Harpaz, Y., Rapaport, R., West, K., and Pfeiffer, L. *Physical Review B* (2016).

268. Rosenberg, I., Liran, D., Mazuz-Harpaz, Y., West, K., Pfeiffer, L., and Rapaport, R. *Science Advances* (2018).

269. Li, W., Lu, X., Dubey, S., Devenica, L., and Srivastava, A. , 1–25 oct (2019).

270. Negoita, V., Snoke, D., and Eberl, K. *Physical Review B - Condensed Matter and Materials Physics* **61**(4), 2779–2783 (2000).

271. Winbow, A. G., Leonard, J. R., Remeika, M., Kuznetsova, Y. Y., High, A. A., Hammack, A. T., Butov, L. V., Wilkes, J., Guenther, A. A., Ivanov, A. L., Hanson, M., and Gossard, A. C. *Physical Review Letters* **106**(19), 1–4 (2011).

272. Dorow, C. J., Kuznetsova, Y. Y., Leonard, J. R., Chu, M. K., Butov, L. V., Wilkes, J., Hanson, M., and Gossard, A. C. *Applied Physics Letters* **108**(7) (2016).

273. Hammack, A. T., Griswold, M., Butov, L. V., Smallwood, L. E., Ivanov, A. L., and Gossard, A. C. *Physical Review Letters* **96**(22), 1–4 (2006).

274. Alloing, M., Lemaître, A., Galopin, E., and Dubin, F. *Scientific Reports* **3**, 1–6 (2013).

275. Andreakou, P., Poltavtsev, S. V., Leonard, J. R., Calman, E. V., Remeika, M., Kuznetsova, Y. Y., Butov, L. V., Wilkes, J., Hanson, M., and Gossard, A. C. *Applied Physics Letters* **104**(9) (2014).

276. Kyriienko, O., Shelykh, I. A., and Liew, T. C. *Physical Review A - Atomic, Molecular, and Optical Physics* (2014).

277. Kyriienko, O., Kavokin, A. V., and Shelykh, I. A. *Physical Review Letters* **111**(17), 1–5 (2013).

278. Li, J. Y., Duan, S. Q., and Zhang, W. *Epl* **108**(6) (2014).

279. Seedhouse, A., Wilkes, J., Kulakovskii, V. D., and Muljarov, E. A. *Optics Letters* **44**(17), 4339 (2019).

280. Kyriienko, O. and Liew, T. C. *Physical Review B* **93**(3) (2016).

281. Shahnazaryan, V., Kyriienko, O., and Shelykh, I. A. *Physical Review B - Condensed Matter and Materials Physics* **91**(8), 1–8 (2015).

282. Su, J. J., Kim, N. Y., Yamamoto, Y., and Macdonald, A. H. *Physical Review Letters* **112**(11), 1–5 (2014).

283. Wurdack, M., Lundt, N., Klaas, M., Baumann, V., Kavokin, A. V., Höfling, S., and Schneider, C. *Nature Communications* **8**(1), 1–6 (2017).

284. Kozawa, D., Carvalho, A., Verzhbitskiy, I., Giustiniano, F., Miyauchi, Y., Mouri, S., Castro Neto, A. H., Matsuda, K., and Eda, G. *Nano Letters* **16**(7), 4087–4093 (2016).

285. Hill, H. M., Rigosi, A. F., Roquelet, C., Chernikov, A., Berkelbach, T. C., Reichman, D. R., Hybertsen, M. S., Brus, L. E., and Heinz, T. F. *Nano Letters* **15**(5), 2992–2997 (2015).

286. Brichkin, A. S., Novikov, S. I., Larionov, A. V., Kulakovskii, V. D., Glazov, M. M., Schneider, C., Höfling, S., Kamp, M., and Forchel, A. *Physical Review B* **84**(19), 195301 nov (2011).

287. Proukakis, N. P., Snoke, D. W., and Littlewood, P. B. *Universal Themes of Bose-Einstein Condensation.* (2017).

288. Muñoz-Matutano, G., Wood, A., Johnsson, M., Vidal, X., Baragiola, B. Q., Reinhard, A., Lemaître, A., Bloch, J., Amo, A., Nogues, G., Besga, B., Richard, M., and Volz, T. (2019).

289. Delteil, A., Fink, T., Schade, A., Höfling, S., Schneider, C., and İmamoğlu, A. (2019).

290. Cuevas, Á., Carreño, J. C. L., Silva, B., De Giorgi, M., Suárez-Forero, D. G., Muñoz, C. S., Fieramosca, A., Cardano, F., Marrucci, L., Tasco, V., Biasiol, G., Del Valle, E., Dominici, L., Ballarini, D., Gigli, G., Mataloni, P., Laussy, F. P., Sciarrino, F., and Sanvitto, D. *Science Advances* (2018).

291. Sturm, C., Tanese, D., Nguyen, H. S., Flayac, H., Galopin, E., Lemaître, A., Sagnes, I., Solnyshkov, D., Amo, A., Malpuech, G., and Bloch, J. *Nature Communications* (2014).

292. Kravtsov, V., Khestanova, E., Benimetskiy, F. A., Ivanova, T., Samusev, A. K., Sinev, I. S., Pidgayko, D., Mozharov, A. M., Mukhin, I. S., Lozhkin, M. S., Kapitonov, Y. V., Brichkin, A. S., Kulakovskii, V. D., Shelykh, I. A., Tartakovskii, A. I., Walker, P. M., Skolnick, M. S., Krizhanovskii, D. N., and Iorsh, I. V. *Light: Science & Applications* **9**(1), 56 dec (2020).

293. Allain, A., Kang, J., Banerjee, K., and Kis, A. *Nature Materials* **14**(12), 1195–1205 (2015).

294. Norden, T., Zhao, C., Zhang, P., Sabirianov, R., Petrou, A., and Zeng, H. *Nature Communications* **10**(1) (2019).

295. Zhao, C., Norden, T., Zhang, P., Zhao, P., Cheng, Y., Sun, F., Parry, J. P., Taheri, P., Wang, J., Yang, Y., Scrace, T., Kang, K., Yang, S., Miao, G. X., Sabirianov, R., Kioseoglou, G., Huang, W., Petrou, A., and Zeng, H. *Nature Nanotechnology* **12**(8), 757–762 (2017).

296. Keller, J., Parker, J., Stankiewicz, J., Read, D., Stampe, P., Kennedy, R., Xiong, P., and von Molnar, S. *IEEE Transactions on Magnetics* **38**(5), 2673–2675 sep (2002).

297. Grzeszczyk, M., Molas, M. R., Nogajewski, K., Bartoš, M., Bogucki, A., Faugeras, C., Kossacki, P., Babiński, A., and Potemski, M. *Scientific Reports* **10**(1), 4981 dec (2020).

298. Klein, J., Hötger, A., Florian, M., Steinhoff, A., Delhomme, A., Taniguchi, T., Watanabe, K., Jahnke, F., Holleitner, A. W., Potemski, M., Faugeras, C., Finley, J. J., and Stier, A. V. *Physical Review Research* **3**(2), L022009 apr (2021).

299. Lin, T. N., Santiago, S. R., Caigas, S. P., Yuan, C. T., Lin, T. Y., Shen, J. L., and Chen, Y. F. *npj 2D Materials and Applications* **3**(1) (2019).

300. Imamoglu, A., Cotlet, O., and Schmidt, R. *Comptes Rendus. Physique* **15**(6), 1–8 feb (2021).

301. Efimkin, D. K. and Macdonald, A. H. *Physical Review B* **97**(23), 1–12 (2018).

302. Roch, J. G., Miserev, D., Froehlicher, G., Leisgang, N., Sponfeldner, L., Watanabe, K., Taniguchi, T., Klinovaja, J., Loss, D., and Warburton, R. J. *Physical Review Letters* **124**(18), 187602 (2020).

303. Lyons, T. P., Gillard, D., Molina-Sánchez, A., Misra, A., Withers, F., Keatley, P. S., Kozikov, A., Taniguchi, T., Watanabe, K., Novoselov, K. S., Fernández-Rossier, J., and Tartakovskii, A. I. *Nature Communications* **11**(1), 6021 dec (2020).

304. Scharf, B., Xu, G., Matos-Abiague, A., and Žutić, I. *Physical Review Letters* **119**(12), 127403 sep (2017).

305. Jauregui, L. A., Joe, A. Y., Pistunova, K., Wild, D. S., High, A. A., Zhou, Y., Scuri, G., de Greve, K., Sushko, A., Yu, C. H., Taniguchi, T., Watanabe, K., Needleman, D. J., Lukin, M. D., Park, H., and Kim, P. *Science* **366**(6467), 870–875 nov (2019).

306. Damen, T. C., Via, L., Cunningham, J. E., Shah, J., and Sham, L. J. *Physical Review Letters* **67**(24), 3432–3435 (1991).

307. Ozawa, T., Price, H. M., Amo, A., Goldman, N., Hafezi, M., Lu, L., Rechtsman, M. C., Schuster, D., Simon, J., Zilberberg, O., and Carusotto, I. *Reviews of Modern Physics* **91**(1), 15006 (2019).

308. Li, M., Sinev, I., Benimetskiy, F., Ivanova, T., Khestanova, E., Kiriushechkina, S., Vakulenko, A., Guddala, S., Skolnick, M., Menon, V. M., Krizhanovskii, D., Alù, A., Samusev, A., and Khanikaev, A. B. *Nature Communications* **12**(1) (2021).

309. Liu, W., Ji, Z., Wang, Y., Modi, G., Hwang, M., Zheng, B., Sorger, V. J., Pan, A., and Agarwal, R. *Science* **370**(6516), 600–604 (2020).

310. Wang, Z., Chong, Y., Joannopoulos, J. D., and Soljačić, M. *Nature* **461**(7265), 772–775 oct (2009).

311. Lu, L., Joannopoulos, J. D., and Soljačić, M. *Nature Photonics* **8**(11), 821–829 nov (2014).

312. Langer, F., Schmid, C. P., Schlauderer, S., Gmitra, M., Fabian, J., Nagler, P., Schüller, C., Korn, T., Hawkins, P. G., Steiner, J. T., Huttner, U., Koch, S. W., Kira, M., and Huber, R. *Nature* **557**(7703), 76–80 may (2018).

313. Bahari, B., Ndao, A., Vallini, F., El Amili, A., Fainman, Y., and Kanté, B. *Science* **358**(6363), 636–640 nov (2017).

314. Nalitov, A. V., Solnyshkov, D. D., and Malpuech, G. *Physical Review Letters* **114**(11), 116401 mar (2015).

315. Klembt, S., Harder, T. H., Egorov, O. A., Winkler, K., Ge, R., Bandres, M. A., Emmerling, M., Worschech, L., Liew, T. C. H., Segev, M., Schneider, C., and Höfling, S. *Nature* **562**(7728), 552–556 oct (2018).

316. Song, W., Sun, W., Chen, C., Song, Q., Xiao, S., Zhu, S., and Li, T. *Physical Review Letters* **123**(16), 165701 (2019).

317. Karzig, T., Bardyn, C.-E., Lindner, N. H., and Refael, G. *Physical Review X* **5**(3), 031001 jul (2015).

318. Solnyshkov, D. D., Malpuech, G., St-Jean, P., Ravets, S., Bloch, J., and Amo, A. , 1–19 nov (2020).

319. Gong, C., Li, L., Li, Z., Ji, H., Stern, A., Xia, Y., Cao, T., Bao, W., Wang, C., Wang, Y., Qiu, Z. Q., Cava, R. J., Louie, S. G., Xia, J., and Zhang, X. *Nature* **546**(7657), 265–269 (2017).

320. Huang, B., Clark, G., Navarro-Moratalla, E., Klein, D. R., Cheng, R., Seyler, K. L., Zhong, D., Schmidgall, E., McGuire, M. A., Cobden, D. H., Yao, W., Xiao, D., Jarillo-Herrero, P., and Xu, X. *Nature* **546**(7657), 270–273 (2017).

321. Fei, Z., Huang, B., Malinowski, P., Wang, W., Song, T., Sanchez, J., Yao, W., Xiao, D., Zhu, X., May, A. F., Wu, W., Cobden, D. H., Chu, J. H., and Xu, X. *Nature Materials* **17**(9), 778–782 (2018).

322. Lee, J. U., Lee, S., Ryoo, J. H., Kang, S., Kim, T. Y., Kim, P., Park, C. H., Park, J. G., and Cheong, H. *Nano Letters* **16**(12), 7433–7438 (2016).

323. Kim, M., Kumaravadivel, P., Birkbeck, J., Kuang, W., Xu, S. G., Hopkinson, D. G., Knolle, J., McClarty, P. A., Berdyugin, A. I., Ben Shalom, M., Gorbachev, R. V., Haigh, S. J., Liu, S., Edgar, J. H., Novoselov, K. S., Grigorieva, I. V., and Geim, A. K. *Nature Electronics* **2**(10), 457–463 oct (2019).

324. Molina-Sánchez, A., Catarina, G., Sangalli, D., and Fernández-Rossier, J. *Journal of Materials Chemistry C* **8**(26), 8856–8863 (2020).

325. Zhou, J., Lin, J., Huang, X., Zhou, Y., Chen, Y., Xia, J., Wang, H., Xie, Y., Yu, H., Lei, J., Wu, D., Liu, F., Fu, Q., Zeng, Q., Hsu, C. H., Yang, C., Lu, L., Yu, T., Shen, Z., Lin, H., Yakobson, B. I., Liu, Q., Suenaga, K., Liu, G., and Liu, Z. *Nature* **556**(7701), 355–359 (2018).

326. Haastrup, S., Strange, M., Pandey, M., Deilmann, T., Schmidt, P. S., Hinsche, N. F., Gjerding, M. N., Torelli, D., Larsen, P. M., Riis-Jensen, A. C., Gath, J., Jacobsen, K. W., Mortensen, J. J., Olsen, T., and Thygesen, K. S. *2D Materials* **5**(4) (2018).

327. Huang, B., Clark, G., Klein, D. R., MacNeill, D., Navarro-Moratalla, E., Seyler, K. L., Wilson, N., McGuire, M. A., Cobden, D. H., Xiao, D., Yao, W., Jarillo-Herrero, P., and Xu, X. *Nature Nanotechnology* **13**(7), 544–548 (2018).

328. Gong, C. and Zhang, X. *Science* **363**(6428) (2019).

329. Burch, K. S., Mandrus, D., and Park, J. G. *Nature* **563**(7729), 47–52 (2018).

330. Seyler, K. L., Zhong, D., Klein, D. R., Gao, S., Zhang, X., Huang, B., Navarro-Moratalla, E., Yang, L., Cobden, D. H., McGuire, M. A., Yao, W., Xiao, D., Jarillo-Herrero, P., and Xu, X. *Nature Physics* **14**(3), 277–281 (2018).

331. Gibertini, M., Koperski, M., Morpurgo, A. F., and Novoselov, K. S. *Nature Nanotechnology* **14**(5), 408–419 (2019).

332. Jiang, S., Li, L., Wang, Z., Mak, K. F., and Shan, J. *Nature Nanotechnology* **13**(7), 549–553 (2018).

333. Mak, K. F., Shan, J., and Ralph, D. C. *Nature Reviews Physics* **1**(November) (2019).

334. Zhong, D., Seyler, K. L., Linpeng, X., Wilson, N. P., Taniguchi, T., Watanabe, K., McGuire, M. A., Fu, K. M. C., Xiao, D., Yao, W., and Xu, X. *Nature Nanotechnology* **15**(3), 187–191 (2020).

335. Dillon, J. F., Kamimura, H., and Remeika, J. P. *Journal of Physics and Chemistry of Solids* **27**(9), 1531–1549 (1966).

336. Tsubokawa, I. *Journal of the Physical Society of Japan* **15**(9), 1664–1668 sep (1960).

337. Klein, D. R., MacNeill, D., Song, Q., Larson, D. T., Fang, S., Xu, M., Ribeiro, R. A., Canfield, P. C., Kaxiras, E., Comin, R., and Jarillo-Herrero, P. *Nature Physics* **15**(12), 1255–1260 (2019).

338. Huang, F. *Journal of Physical Chemistry C* **123**(12), 7440–7446 (2019).

339. Ghazaryan, D., Greenaway, M. T., Wang, Z., Guarochico-Moreira, V. H., Vera-Marun, I. J., Yin, J., Liao, Y., Morozov, S. V., Kristanovski, O., Lichtenstein, A. I., Katsnelson, M. I., Withers, F., Mishchenko, A., Eaves, L., Geim, A. K., Novoselov, K. S., and Misra, A. *Nature Electronics* **1**(6), 344–349 (2018).

340. Ciorciaro, L., Kroner, M., Watanabe, K., Taniguchi, T., and Imamoglu, A. *Physical Review Letters* **124**(19), 197401 (2020).

341. Zhang, Z., Shang, J., Jiang, C., Rasmita, A., Gao, W., and Yu, T. *Nano Letters* **19**(5), 3138–3142 may (2019).

342. Chen, W., Sun, Z., Wang, Z., Gu, L., Xu, X., Wu, S., and Gao, C. *Science* **366**(6468), 983–987 (2019).

343. Zhong, D., Seyler, K. L., Linpeng, X., Cheng, R., Sivadas, N., Huang, B., Schmidgall, E., Taniguchi, T., Watanabe, K., Mcguire, M. A., Yao, W., Xiao, D., Fu, K.-m. C. M. C., and Xu, X. *Science Advances* **3**(5), 1–7 (2017).

344. Tong, Q., Chen, M., and Yao, W. *Physical Review Applied* **12**(2), 1 (2019).

345. Jin, C., Kim, J., Iqbal Bakti Utama, M., Regan, E. C., Kleemann, H., Cai, H., Shen, Y., Shinner, M. J., Sengupta, A., Watanabe, K., Taniguchi, T., Tongay, S., Zettl, A., and Wang, F. *Science* **360**(6391), 893–896 (2018).

346. Cao, Y., Fatemi, V., Fang, S., Watanabe, K., Taniguchi, T., Kaxiras, E., and Jarillo-Herrero, P. *Nature* **556**(7699), 43–50 (2018).

347. Hunt, B., Taniguchi, T., Moon, P., Koshino, M., and Ashoori, R. C. *Science* **340**(June), 1427–1431 (2013).

348. Sharpe, A. L., Fox, E. J., Barnard, A. W., Finney, J., Watanabe, K., Taniguchi, T., Kastner, M. A., and Goldhaber-Gordon, D. *Science* **365**(6453), 605–608 (2019).

349. Masubuchi, S., Morimoto, M., Morikawa, S., Onodera, M., Asakawa, Y., Watanabe, K., Taniguchi, T., and Machida, T. *Nature Communications* **9**(1), 1413 (2018).

350. Walker, P. M., Tinkler, L., Skryabin, D. V., Yulin, A., Royall, B., Farrer, I., Ritchie, D. A., Skolnick, M. S., and Krizhanovskii, D. N. *Nature Communications* **6**, 1–7 (2015).


Disce Doce
RERVM COGNOSCERE CAVSAS